Fall 12-2021

The Investigations of NPS Modulated Immunity and Immunometabolism

Brittney Leigh Ruedlinger
Old Dominion University, brued@outlook.com

THE INVESTIGATIONS OF NPS MODULATED IMMUNITY AND IMMUNOMETABOLISM

by

Brittney Leigh Ruedlinger
B.S. May 2017, Old Dominion University
M.S. December 2018, Old Dominion University

A Dissertation Submitted to the Faculty of
Old Dominion University in Partial Fulfillment of the
Requirements for the Degree of

DOCTOR OF PHILOSOPHY

BIOMEDICAL SCIENCES, BIOELECTRICS

OLD DOMINION UNIVERSITY
December 2021

Approved by:

Stephen J. Beebe (Director)

Lesley H. Greene (Member)

Siqi Guo (Member)

Piotr Kraj (Member)

ABSTRACT

THE INVESTIGATIONS OF NPS MODULATED IMMUNITY AND IMMUNOMETABOLISM

Brittney Leigh Ruedlinger
Old Dominion University, 2021
Director: Dr. Stephen J. Beebe

Cancers remain in the top noncommunicable diseases responsible for premature mortality. The heterogeneity among cancers and within tumors makes treating them ever more challenging. Our misfortune for developing cures is mocked by cancer, with the lowest probability of success (PoS) through clinical trials and FDA approval. At the basic level, there are generally two broad gaps impeding cancer eradication: the unidentified shared mechanism(s) exploited by all cancers and the therapeutic approach to intervene. Nanosecond pulse stimulation (NPS) offers a unique approach since its broad impacts intersect those often hijacked by oncogenesis. Metabolic pathways, known for dysfunctions among cancers, share a common intersection at the mitochondria, where signaling molecules impact cellular homeostasis. The concept of immunometabolism recognizes shifts in metabolism coincide with phenotypic expression of certain immune cells. Thus, the effects of NPS were investigated in vitro for mechanistic impacts on mitochondria and in vivo for efficacy, immunity, and immunometabolism.

In vitro, the NPS-induced dissipation of the mitochondrial membrane potential ($\Delta\Psi_m$), a determinant of mitochondrial fitness, was probed for calcium dependence, mitochondrial reactive oxygen species (mROS) generation, and sensitivity to cyclophilin D inhibition (CypD) by cyclosporin A. The results showed that $\Delta\Psi_m$ dissipation was calcium and mROS dependent and

sensitive to CypD inhibition, indicating that NPS activated the permeability transition pore, known for its physiological role in cellular homeostasis.

In vivo, the efficacy of NPS induced tumor regression was cancer type dependent since in some cancer models it was more (murine breast cancer) or less (murine melanoma) successful at inducing primary tumor clearance and protection. Thus, the NPS induced effects on immunity and the immunometabolism of CD4+ T cells were investigated in the murine B16-F10 melanoma model. The results indicated that while NPS indeed induced an immune response, the persistence of suppressor cells was likely responsible for the lack of efficacy. Furthermore, in vivo NPS induced metabolic reprogramming of CD4+ T cells which was supported phenotypically. These were the first investigations into the NPS induced effects on immunometabolism.

This dissertation is dedicated to my daughters, Ellie and Alexy Lu, who have learned that a meaningful life is one spent in pursuit of undeniable passions.

ACKNOWLEDGMENTS

Many individuals have contributed to the successful completion of this dissertation and the research investigations detailed within these pages. I am extremely grateful for my committee members for their extensive time contributions, relentless guidance, and patience throughout these investigations and in preparation of this manuscript. The compassion, grace, humility, generosity, and perseverance exemplified by my committee chair are of the highest caliber, for which I consider myself privileged to have been his mentee.

I would also like to extend my deepest gratitude to the SoBran Vivarium staff and veterinarians for teaching me so many things and taking such good care of my girls. Their talents and dedication are exceptional in addition to their highest regard for the ethical treatment of animals.

Finally, I am exceptionally grateful for Dr. Yu Jing and Dr. Guilan Shi for their tireless efforts to teach me flow cytometry.

The dissertation research of B.L.R. was supported in part by funding from Pulse Biosciences, Inc., and The Catalyst- Virginia Biosciences Health Research Corporation.

NOMENCLATURE

AB	Antibody
ACK	Ammonium-Chloride-Potassium
ANT	Adenine Nucleotide Translocase
ATP	Adenosine Triphosphate
BALB/cJ	Balbc Mouse Strain
BAX	BCL2 Associated X
BCL2	B-cell Lymphoma-2
BCL-XL	B-cell lymphoma-extra large
BID	BH3 Interacting Domain Death Agonist
BSS	Buffered Saline Solution
BVM	Blumlein line versus MOSFET experiments
BL6	C56BL/6J Mouse Strain
cAMP	Cyclic Adenosine Monophosphate
CD	Cluster of Differentiation (human, h; mouse, m)
CDX	Cell-line Derived Xenograft
CHARMM	Chemistry at Harvard Macromolecular Mechanics
CM	Central Memory
CsA	Cyclosporin A
CSF2	Colony Stimulating Factor 2, gene
CTLs	Cytotoxic T Lymphocytes
CypD	Cyclophilin D

DC	Dendritic Cells
DIDS	Diisothiocyanatostilbenedisulphonic acid
dLN	Draining (tumor) Lymph Node(s)
DNA	Deoxyribonucleic acid
DOB	Day/ Date of Birth
DOC	Day/ Date of Challenge
DOE	Day/ Date of HCB CD34+ HSC Engraftment
DOT	Day/ Date of Tumor Initiation
DPBS	Dulbecco's Phosphate Buffered Saline
ED	Effective Dose
EM	Effector Memory
EP	Electroporation
ER	Endoplasmic Reticulum
ET	Electrotransfer
ETC	Electron Transport Chain
FC	Flow Cytometry
F-RFT	Fast Rise and Fall Time
GET	Gene Electrotransfer
GM-CSF	Granulocyte/ Macrophage- Colony Stimulating Factor, protein
GROMACS	GROningen MAchine for Chemical Simulations
GVHD	Graft-Versus-Host Disease
HCB	Human (Umbilical) Cord Blood
HIS	Human Immune System

HMGB1	High Mobility Group Box Protein 1
HSC	Hematopoietic Stem Cells
ICD	Immunogenic Cell Death
IF	Interfemoral
IHC	Immunohistochemistry
IL3; IL-3	Interleukin-3, gene; protein
IL-7Rα	Interleukin-7 Receptor α
IMM	Inner Mitochondrial Membrane
IO	Intraosseous
IP	Intraperitoneal
IVIS	In Vivo Imaging System
KITLG	Human Steel Factor, gene
KLRG1	Killer Cell Lectin Like Receptor G1
LUC	Luciferin and/ or Luciferase
$\Delta\Psi_m$	Mitochondrial Membrane Potential
Macs	Macrophages
MD	Molecular Dynamics
MDSC	Myeloid Derived Suppressor Cells
MFP	Mammary Fat Pad
MM	Master Mix
MOSFET	Metal-Oxide-Semiconductor Field-Effect Transistor
mPTP	Mitochondrial Permeability Transition Pore
mROS	Mitochondrial Reactive Oxygen Species

ms	Millisecond
MSOX	MitoSOX-Red
MVB	Mandibular Vein Bleed
NAC	N-acetyl cysteine
NAMD	Nanoscale Molecular Dynamics
NK	Natural Killer cells
NKG2D	Natural Killer Group 2D
NK-T	Natural Killer-T cells
NPS	Nanosecond Pulsed Stimulation
ns	Nanosecond
N-SCM	Naïve/ Stem-Cell like Memory
NSG	NOD.Cg-Prkdc^{scid} Il2rg$^{tm\ 1Wjl}$/SzJ mouse
NSGM3	NOD.Cg-*Prkdc^{scid} Il2rg^{tm1Wjl}* Tg (CMV-IL3, CSF2, KITLG) 1Eav/MloySzJ
nsPEFs	Nanosecond pulsed electric fields
OMM	Outer Mitochondrial Membrane
OSCP	Oligomycin Sensitivity Conferral Protein
OX-PHOS	Oxidative-phosphorylation
p53	Tumor Protein 53
PBS	Phosphate Buffered Saline
PEPCAT	Peptide Conformational Analysis Tool
PI	Propidium Iodide
PiC	Phosphate Carrier
pIL-12	Plasmid Interleukin 12

PKA	Protein Kinase A
PM	Plasma Membrane
PME	Particle Mesh Ewald
PMF	Proton Motive Force
PS	Phosphatidylserine
PVDF	Polyvinylidene difluoride
RBC	Red Blood Cells
RCD	Regulated Cell Death
ROS	Reactive Oxygen Species
SASA	Solvent Accessible Surface Area
SCF	Stem Cell Factor, protein
SDS-PAGE	Sodium Dodecyl-Sulfate Polyacrylamide Gel Electrophoresis
SEER	Survival, Epidemiology, and End Result
SHAKE	“Shake-ing” bond algorithm
SH-XFA	Seahorse Extracellular Flux Assay
STRIDE	Structural identification algorithm
TAMs	Tumor Associated Macrophages
TILs	Tumor Infiltrating Lymphocytes
TMRE	Tetramethylrhodamine, ethyl ester, perchlorate
TNBC	Triple-Negative Breast Cancer
Tx	Treatment
VDAC	Voltage-dependent anion channel
VMD	Visual Molecular Dynamics

XFA	Extracellular Flux Analysis/Analyzer
X-PLOR	exploration of conformational space of macromolecules restrained to regions allowed by combinations of empirical energy functions and experimental data / exploration of modern concepts of structured programming in macromolecular simulation

TABLE OF CONTENTS

Page

LIST OF TABLES

LIST OF FIGURES

Figure Page

CHAPTER I

INTRODUCTION

Section 1.1. The Problem and Significance of Research

The development for an effective treatment against therapeutically resistant cancers, like triple negative breast cancer (TNBC), and progressed stages of cancers, like melanoma skin cancer, remains an elusive goal. TNBC is referred to as such due to the lack of three receptors considered in the triple negative phenotype, including the estrogen receptor, progesterone receptor, and the human epidermal growth factor receptor 2 [1,2]. This lack of receptor expression, grants TNBC evasion of our currently available treatments which target them [1,2]. Breast cancer is the 2nd most commonly diagnosed disease, contributing to 24.5% of new cancer diagnoses in women with 15% succumbing to premature mortality [3]. According to Foulkes *et al*, TNBC and basal-like tumors account for 15% of invasive breast cancers, significantly effecting underrepresented populations of young black and Hispanic females over young women of other racial and ethnic decent [2]. Skin cancers are by far the most prominent of cancers and are most often curable, except for progressive and metastatic stages, especially those of melanomas [4]. According to the Survival, Epidemiology, and End Result (SEER) stages of melanoma, regional and distant stages are associated with 65% and 25% 5-year survival rates, respectively, which is far less than the 99% 5-year survival rate of localized melanoma [4]. Thus, an innovative approach for treating these deadly cancers is in order.

What is it about cancer that makes it such a hard target to hit? Why is it that despite our efforts, cancer drugs have the lowest succession rates through clinical trials [5]? The answer to these questions is one in the same, as cancer defies the laws governing healthy bodies in multiple

ways. We refer to these avenues of evasion as the hallmarks of cancer, of which at least ten have been identified (Figure 1) [6]. These include mechanisms of evasion from growth suppressors and resisting cell death, as well as avoidance of immune destruction and manipulation of bioenergetic, genomic repair, and proliferative pathways [6]. Essentially, cancer enhances survival and growth via upregulation of proteins and biomolecules, while simultaneously suppressing those that would lead to detection and destruction. The tumor microenvironment is heterogeneous, consisting of many cell types, and, when coupled with the great variety of mutations and dysfunctional attributes, we can begin to appreciate the gravity of cancer [6,7]. However, these hallmarks are merely the tip of the iceberg, as we discover increasing complexities that give cancer cells unlimited potential for evasion [8,9]. These aspects can be viewed as modular components, referred to as epigenetic modifications, that cancer cells can exploit to modify gene products [7,8,10].

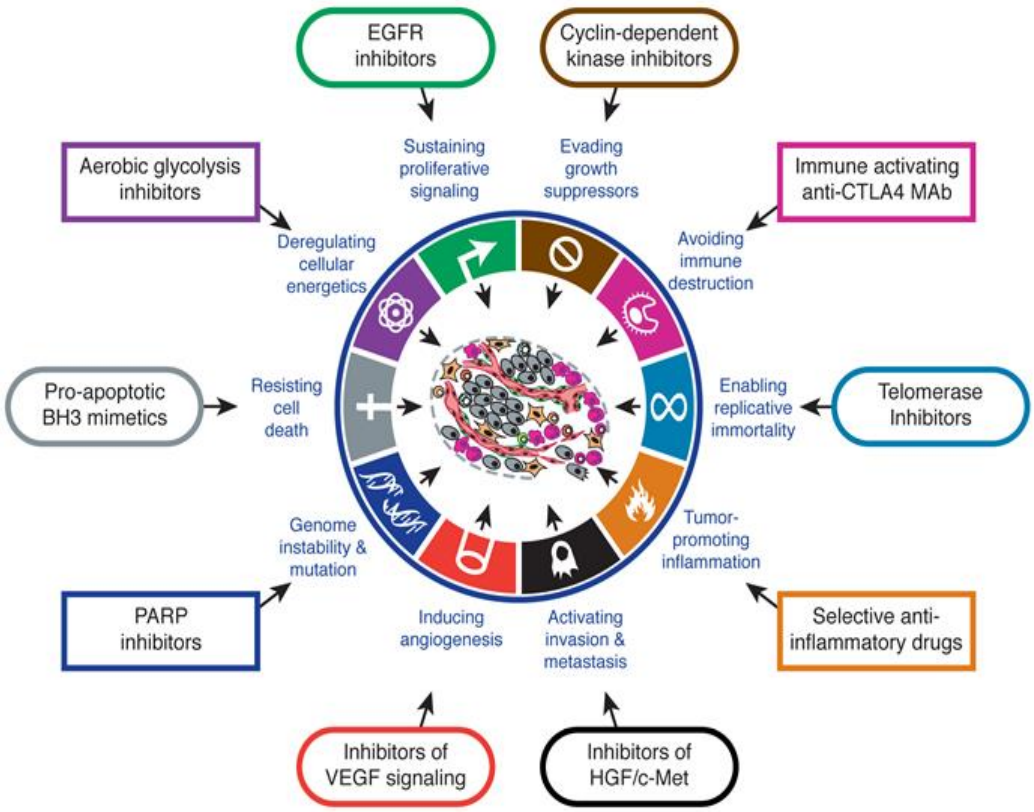

Figure 1. Illustrates the hallmarks of cancer. The ten hallmarks of cancer are indicated as well as the drugs and/or potential avenues for compromising them. Figure adapted from [6] used with permission from Elsevier (license no. 5131580253289 issued on 08/17/2021).

The complexity of cancer and the tumor microenvironment requires the broad, multifactorial perspective of the genome-centric concept [7,10]. In support of this concept, one might consider how under both normal and pathological states differentiated cells can alter their phenotype, or change their identity, displaying cellular plasticity [9]. This is also referred to as stemness since the cells exhibit stem-cell-like behavior. Figure 2 is an adapted version of the stem cell differentiation model proposed in the 1950's [11]. Although we now understand that

cells can regain stemness, it requires selective pressures and can be considered analogous to a ball being pushed back up the hill. T cells, for example, are known for having such plasticity under normal physiological conditions in which they differentiate from naïve T cells into subsets of effector, memory stem cells, central memory, etc. [12]. In more recent years, we have learned that the tumor microenvironment also consists of stem-like cells, or cancer stem cells [13]. Perhaps even more alarming, is that normal healthy immune cells, infiltrating the tumor microenvironment fall into the trap of disguising the tumor as it suppresses their proper functional roles [14,15]. Now, we can easily identify the problem with cancer, which is that the multidimensional, enchantingly uncanny nature of the tumor microenvironment is much more analogous to fractal network theory than biology. Thus, the multidimensional fractal network of the tumor microenvironment may only yield when matched with an innovative multidimensional approach, and we may have just the tool for the job.

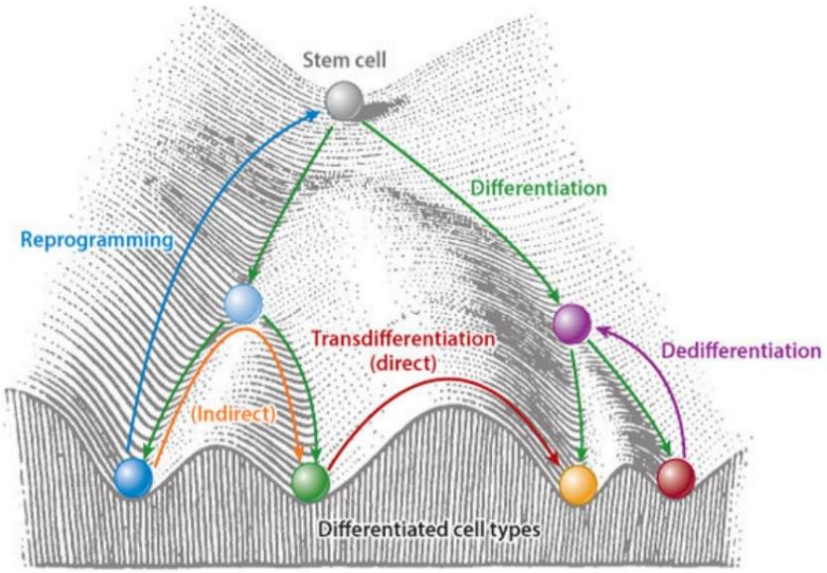

Figure 2. Stem cell differentiation. Illustrates stem cell differentiation into specific cell types as a ball rolling down a landscape. The pathways of differentiation, transdifferentiation, dedifferentiation, and reprogramming are indicated. Figure reproduced from [9,11] with permission from Annual Reviews, Inc. (order license ID 1147792-1, 09/14/2021).

Advances in biotechnology of nanoscale proportions have proven their macroscopic potential in the treatment of diseased states. The biomedical application of electricity is a concept dating back to 50AD, when electric torpedo fish were used to treat neurological ailments and headaches [16]. The concept remained elusive until sparking again in the mid- to late- 1900's, when electropermeabilization became a novel avenue for bacterial deactivation and targeted therapies [17]. The advent of nanosecond bioelectrics occurred towards the end of the last century and remains the focus of many investigations [18]. Nanosecond pulse stimulation (NPS) differs from traditional electroporation (EP) in that it has intracellular affects [19]. The

technology utilizes high power, low energy, and nonthermal pulses to capitalize and exploit the biochemical pathways of cancer cells [20-28]. Variations in pulse number, duration, intensity, and frequency induce a variety of cellular responses, including regulated cell death (RCD) mechanisms [20-27]. Nanosecond pulsed electric fields (nsPEFs), have been used for effectively ablating cancer cells both *in vitro* and *in vivo* [20,21,23-27,29-34]. *In vitro* investigations have aimed to elucidate the multitude of cellular effects induced by NPS, while *in vivo* models have aimed to investigate the observable effects on the organism as well as the phenotypic signatures of the innate and adaptive immune response in animal models [20-27,29-35]. From its conception in the late 1990's, this technology has been used against numerous oncogenic cell lines in culture, including HeLa cells, breast cancers, melanomas, leukemias, and many more [18,19,36-57]. Recent in vivo investigations have proven to induce tumor cell death in murine liver and breast cancer models [29,30,58,59]. Additionally, this technology has been enhanced with drug, thermal and gene delivery for targeting therapeutically resistant cancers, such as melanomas [47,60-62].

The emerging concept of immunometabolism presents some unique insights into the over-lapping mechanisms exploited by cancers and harnessed by NPS [63-66]. Several investigations have looked at the metabolic signatures of activation and memory statuses of immune cells, including natural killer (NK), T cell subsets and macrophages [65,67-69]. Activation of these immune cells was accompanied by altered metabolism for ATP energy and metabolite production required by the onset of their new status [68]. For both T cells and macrophages, this means switching their primary energy pathway from the slow, efficient mechanism of oxidative-phosphorylation (OX-PHOS) to the faster, metabolite yielding mechanism of glycolysis to fuel the demands of rapid proliferation [67,68,70]. Once the

threatening pathogen is cleared, the metabolism shifts back to OX-PHOS, endowing efficiency for long-term memory [64,67,68,71]. While these immunometabolic signatures have been investigated in response to pathogen and cytokine induced activation, they have yet to be observed in response to NPS [72]. Therefore, part of this investigation aims to determine the NPS-induced modulation of immunometabolic and phenotypic signatures in T cells. It is also worthwhile to investigate the NPS-induced effects on the centralized hub of metabolism, the mitochondria, to examine the correlation between phenotypic and immunometabolic profiles with respect to mitochondrial function [73-75]. Should a novel avenue present itself in this manner, this would broaden our knowledge of immunity in cancer and provide key insights for governing the translational use of NPS for treating human cancers [43,44].

Section 1.2. Innovation

The innovative approach of investigating mitochondrial fitness as well as immunometabolism in correlation with phenotypic signatures of immunity induced by NPS in mouse breast and melanoma models provided novel insights into the underlying mechanisms through which cancers evade current therapies and NPS works to resolve oncogenesis. These investigations proposed to explore the mitochondrial function in immune cells, or rather specifically, isolated CD4+ T cells, which are often proponents of the suppressive tumor microenvironment. Additionally, the correlation between phenotypic and metabolic signatures associated with activation and memory statuses of the NPS induced immune response were the first of its kind.

CHAPTER II

BACKGROUND

Section 2.1. Intracellular Effects of NPS

Since the advent of nsPEFs, investigations to elucidate their effects on biological systems have been launched. Since nsPEFs induce stimulatory effects, the term NPS is generally used. On the macroscopic scale, NPS has been shown to ablate oncogenic tissues, including melanomas, T-cell leukemia, hepatic carcinomas, and breast cancer tumors, among others. On the microscopic scale, intracellular mechanisms elicited by NPS were observed on the endoplasmic reticulum (ER), mitochondria, and nucleus, among other intracellular organelles and structures; however, insights into their direct mode of action remain controversial. It has been widely accepted that NPS, unlike classical EP, have significant effects on intracellular components, while the outer membrane effects are targets for both NPS and EP. Intracellular effects have been shown on small signaling molecules, nucleic acids, and proteins. Yet, the nature of these interactions remains a topic of uncertainty but can be characterized as direct effects or indirect effects that are secondary to activated biology. Direct effects include channel-like lipid pore formation in the plasma membrane and on intracellular membranes such as ER. Indirect effects occur with other cellular components such as intracellular signaling transduction responses to stress and/or repair mechanisms as well as regulated cell death mechanisms as defaults when recovery fails. There are also considerations for effects on nucleic acids and proteins, including enzymes. Thus, a review of these intracellular effects became the scope of this review with aims to compile published information as well as methods and instrumentation commonly employed by these investigations.

NPS debuted in 1997, when Schoenbach et al., revealing that by decreasing pulse duration into the nanosecond range and less than the membrane charging time constant, negation of the outer membrane could be achieved [18]. The effects of ns pulses were correlated with fundamental empirical laws from which insights are gained in the governance of physical science [18]. Experimental investigations in 2001, supported this idea of intracellular electromanipulation, when observations were reported of "sparkler cells" among human eosinophils contaminating a population of enriched neutrophils [76]. Free, cytosolic calcein penetrated the membranes of some intracellular granules after ns pulse stimulation, appearing to leave the outer membrane intact [76]. The implications for use of NPS became clear, as this observation opened the door to biomedical applications as well as in treating cancer [23] in addition to their initial intended use in water and food processing [18,76,77]. Shortly after, intracellular effects of ns pulses on human cells and leukemia cells were published, followed by additional triumph on the cancer front [23,24,78]. In 2006, ns pulses were shown to ablate melanomas in a self-destructive manner [47]. Efforts to understand the intricacies of ns pulse interactions with these underlying mechanisms of self-destruction, or RCD, proceed relentlessly, albeit much is yet to be gained. Thus, the remaining focus aims into a comprehensive review of known intracellular effects of ns pulses. Furthermore, investigation methods and key instrumentation will be identified with aims to aid in future experimental designs.

Effects on nucleic acids. It was speculated that ns pulses had direct effects on deoxyribonucleic acid (DNA) in 2000, as electromagnetic field interactions of electrons traveling stacked base pairs was explored as a mechanism of gene regulation [77]. As investigations continue to elucidate electrochemical interactions and mechanisms of redox chemistry, this postulate becomes more relevant [79]. In 2003, Stacey et al investigated the genotoxic effects of ns pulses

on adherent and nonadherent cell lines [35]. Cell cycle analysis and DNA damage analysis (comet assay) revealed that the effects were cell type specific [35]. Furthermore, results revealed that DNA damage and chromosomal aberrations were sustained albeit not extensively [35]. This indicates that the cell responses or mechanisms may be dissimilar than those observed by other genotoxic stimuli [35]. Another potential for DNA damage could be from reactive oxygen species (ROS) generated by NPS, as ROS formation/ accumulation may be one possible initial step in RCD [46,80].

Effects on the poration of intracellular membranes. Ns pulses have been shown to directly affect poration of intracellular membranes [76]. In 2001, Schoenbach et al., demonstrated that the granules of human eosinophils became selectively permeable to calcein with increasing pulse application [76]. The preparation from human blood yielded a polymorphonuclear suspension; however, with subsequent purification, a suspension of $\geq$65% eosinophils was achieved [76]. The remaining percentage of nucleated cells included neutrophils, serving as an advantageous contaminant [76]. It was noted that the neutrophils appeared unaffected by the pulse applications while affectively porating the intracellular granules of the eosinophils [76]. Thus, identifying another important property of ns pulse application: that applications would be cell specific [76]. Such specificity opened the door to potential uses in broad biomedical applications [76].

Effects on the poration of plasma/cytoplasmic membranes. Propidium iodide (PI), a red-fluorescent nuclear and chromosome counterstain, is often employed to detect the viability of cells as defined by plasma membrane permeabilization. Under stable physiological conditions, the stain is impermeant; however, with compromised cellular membranes, the stain gains access. Thus, PI became an asset in discovering the permeabilization of membranes from pulsed electric field applications. In 1998, Rols and Teissie used PI to demonstrate that for micro- and milli-

second pulses, longer pulses permeabilized the outer cell membrane with greater efficiency than shorter pulses in Chinese hamster ovary cells with preservation of cell viability [51]. In 2002-2003, experiments by Schoenbach and co-workers showed a delayed response to permeability of PI with the application of ns pulses in Jurkat cells and HL-60 cells [55,81]. These experiments supported the immediate permittivity of PI with μs pulses; however, they also showed delayed uptake with increasing time after ns pulses [55,81]. This suggested that the mortality was not a direct result of the external stimuli, but rather the initiation of apoptosis as a newly defined mechanism of cell death within the cell [24,82].

An interesting publication was released in 2006, when experimentation was coupled with computation to explore nanopore formation of cytosolic membranes [83]. On the experimental side, PI was employed as previously described in addition to YO-PRO-1, similar in physical properties, yet slightly lower molecular weight [83]. Microscopic observations indicate that YO-PRO-1 permeates the cytosolic membrane before PI under the same pulse parameters [83]. This suggests two ideas: (1) field-driven activation of a specified channel (P2X7 receptor) or (2) nanopores formed from the induced field are smaller than PI yet large enough for YO-PRO-1 [83]. However, there are several points to consider (1) an understanding of YO-PRO-1 interaction with cell structures is not well defined (2) the baseline threshold fluorescence for YO-PRO-1 detection with epifluorescence microscopy is much lower than that of PI and (3) the fluorescence intensity is subjective to interpretation, rather than calculated numerical fluorescence intensity [83].

In a later study by Sozar et al., 2018, the authors compared the electropermeabilization of two cations, PI (1+) and YO-PRO-1 (2+), both with increased fluorescence after internalization with nucleotides, and an anion, calcein (4-), which does not bind to nucleotides [84]. The authors

considered several factors that determine post pulse transport of the ions. These included the Born energy, which is determined by the electrostatic energies in the media and the lower permittivity of the interior media [85]. The membrane dipole should also be considered, which is on the order of several hundred millivolts positive [85]. This means that the membrane dipole potential increases the transport energy barrier for cations and lowers it for anions [85] Another factor that is generally not considered was the post pulse transmembrane potential, which recovers a resting membrane potential within seconds after electropermeabilization and before the barrier defects have been repaired [86,87]. The study showed that YO-PRO-1 entered more rapidly than PI and calcein entry was the slowest [84]. However, calcein efflux was faster than its influx and similar to the influx of YO-PRO-1 and PI [84,86].

On the computational side, GROningen MAchine for Chemical Simulations (GROMACS) version 3.2.1 was used for assembly and simulation of the lipid bilayers and Visual Molecular Dynamics (VMD) was used for generating graphics [83]. Several algorithms were used to set molecular boundaries, restricting the molecular dynamic simulation to certain molecular conditions with the added applied electric field [83]. While these included electrostatic torques and attraction-repulsion interactions on the molecular level, mechanical forces were neglected [83]. The results indicated that phosphatidylserine (PS) electrophoretically traverses the hydrophilic pore wall towards the positive anode after several nanoseconds [83]. Interestingly, nanopore formation in the phospholipid bilayer preferentially occurs at the opposite side of the cell, nearest the more negative cathode [83]. Thus, the experimental and computational observations leave the potential for variable interactions at the cell membrane, including the possibility and/or probability of direct effects on other charged cellular components [83].

Effects on regulated cell death. In 2003, an in-depth analysis of intracellular effects was released [24]. This investigation combined classic biochemistry techniques with modern instrumentation, including immunoblot analysis and flow cytometry coupled with fluorescent molecular probes [24]. Human Jurkat cells, HL-60 cells and 3T3-L1 cells were employed to study the effects of ns pulses on apoptotic cell markers [24]. Apoptotic cells would exemplify annexin-V binding, caspase activation, decrease in cell size, and the release of cytochrome c from mitochondria into the cytosol [24]. Furthermore, secondary necrotic cells, or rather cells that died, from membrane rupturing *in vitro* after apoptosis, were identified by the diminished integrity of the cytosolic membrane [24]. Ethidium homodimer-1, an impermeant DNA stain, and fluorochrome labeled annexin-V, an impermeant with preferential binding of externalized PS, were used to distinguish apoptotic states with flow cytometry [24]. The results indicated that the number of apoptotic cells and post-apoptotic secondary necrotic cells increased with time after pulse application, and no signs of primary necrosis were observed [24]. It is now known that NPS can externalize PS as a voltage-driven, nanopore-facilitated translocation in lipid membranes [83,88-90], making it a risky apoptosis marker, unless determined 30 minutes after NPS treatment [91]. Flow cytometry was also used to investigate caspase activation by detecting fluorescence of a labeled permeant caspase inhibitor with affinity for active caspase enzymes. However, determination of catalytically active caspase [24,76,82], was used as the favored assay for active caspases as apoptosis markers [48]. The results showed that caspase activation was dose-dependent, post-treatment time- dependent, and energy independent [24]. Immunoblot analysis of cytochrome c and cytochrome c oxidase required extracted fractions of the cytosol and mitochondria preparation for separation with sodium dodecyl-sulfate polyacrylamide gel electrophoresis (SDS-PAGE) [24]. Targeted molecular weight proteins were transferred to polyvinylidene difluoride

(PVDF) membranes treated with monoclonal anti-cytochrome c antibody and monoclonal anti-bovine cytochrome c oxidase subunit IV [24]. The results indicated that the mitochondrial fractions contained both, while the ns pulse treated cytosolic fractions contained cytochrome c, untreated samples had neither cytochrome c oxidase nor cytochrome c [24]. In this manner, Beebe et al., revealed that ns pulses can initiate apoptosis defined by caspase activation and in a mitochondrial cytochrome release -dependent manner [24]; however, NPS does not induce apoptosis in all cell types [92-94].

Subsequent investigations used many of the same methods and supported previous findings [43,44,48]. Employment of additional targets, including B-cell Lymphoma-2 (BCL2) and BCL2 Associated X (BAX), RCD proteins, provided support for mitochondrial-independent apoptosis, as activation occurred with or without tumor protein 53 (p53) and BAX [44]. To further characterize the apoptotic mechanisms induced by NPS, various molecular probes and inhibitors were used to gain insights on the mitochondrial membrane potential ($\Delta\Psi_m$) as well as explore the mechanisms of calcium in response to the applied field [48]. The results indicated that along with PI externalization, caspase activation, calpain activation, and with or without cytochrome c release, they could add decreases in BH3 Interacting Domain Death Agonist (BID), decreases in $\Delta\Psi_m$, and no changes in ROS, BCL2, and B-cell lymphoma-extra-large (BCL-XL) to observed cellular effects of NPS [48]. Cleavage of BID, an RCD protein, was found to exemplify involvement of both calcium and caspase activity [48]. Ultimately, cell death mechanisms were found to be variable, with indications of elicitation of various RCD mechanisms [48] that calcium dependence and time post-treatment dependence of the $\Delta\Psi_m$ dissipation implicates potential involvement of the mitochondrial permeability transition pore (mPTP) [22].

Effects on proteins. In 2005, Budi et al., employed classical molecular dynamics (MD) to understand the effects of static electric fields and oscillating electric fields on the α-helical region of the insulin chain-B protein structure [95]. Nanoscale Molecular Dynamics (NAMD) and Chemistry at Harvard Macromolecular Mechanics (CHARMM) 27 force field were used for setting the boundaries of classical MD and atomic interactions, along with several others including, 'SHAKE-ing" bond algorithm (SHAKE) and Particle Mesh Ewald (PME) summation [95]. VMD use of the structural identification algorithm (STRIDE) was employed to establish the evolution of secondary protein structure [95]. Additionally, the Peptide Conformational Analysis Tool (PEPCAT) was used to classify conformation states of the protein, root-mean-square deviation (RMSD) and STRIDE were used for structure stability, and the programming system for computational structural biology, exploration of modern concepts of structured programming in macromolecular simulation (X-PLOR), was used to calculate the solvent accessible surface area (SASA) [95]. The results indicated that oscillating electric fields destabilized protein conformation and damaged secondary structures more than static electric fields [95]. Subsequent investigations utilized similar methods to determine the effects of NPS on myoglobin [96]. The results indicated that to induce unfolding of a protein, the externally applied electric field must be between 10^8-10^9 V/m, albeit lower fields may polarize and induce protein conformation changes [96]. Furthermore, bipolar pulses, with rapid positive and negative intensities, were shown to shift protein conformation beyond the intermediate state and that discontinuation did not induce renaturation [97].

In 2015, Stephen Beebe revealed his investigation on the direct effects of ns pulses on proteins, specifically the catalytic subunit (C-subunit) of the cyclic adenosine monophosphate (cAMP)-dependent protein kinase or protein kinase A (PKA) [32]. While he had cloned the

alpha (α), beta (β), and gamma (γ) C-subunit isoforms from a human testis library [98], in this investigation, he used a recombinant mouse C_α-subunit, which was most commonly used in PKA experiments C_α was expressed in bacteria and purified by affinity and size exclusion chromatography yielding a pure C_α -subunit protein [32]. The paper filter assay with bound phosphorylated substrate was used to quantify the catalytic activity of the enzyme [32].

The results indicated that the catalytic subunit activity could be significantly inactivated by NPS conditions [32]. The inactivation of C_α was independent of energy density, suggesting that the inactivation could be caused by high frequency components due to the short rise-fall times of the short duration pulses [32]. In molecular dynamic simulations, high intensity short duration pulses were shown to disrupt secondary structures of myoglobin, the soybean hydrophobic protein, and the insulin B-chain [32,99]. This direct effect of NPS on C_α-subunit inactivation suggests effects to disrupt the active catalytic structure of the enzyme [32]. While the specific mechanism(s) of NPS-induced inactivation of C_α-subunit catalysis remain to be determined, these data do show that NPS can have nonthermal, inactivation effects on this prototype kinase [32]. That the basic catalytic mechanisms for protein kinase phosphorylation are highly conserved, suggests the possibility that NPS can have effects on one of the largest protein families, which are involved in essentially all cell function. Kinases account for 2% of the mammalian genome, of which, 47% are associated with disease loci or cancer amplicons [32,100]. It is also possible that lipid–protein pore complexes embedded in cell membranes could be affected by NPS to account to other observed effects that are now attributed to effects on cell lipid membranes only [32]. It was suggested that damage to voltage-gated channel proteins or disruption of the phospholipid by layer could be involved in inhibition of voltage-gated channels by nsPEFs [101-103].

While NPS may affect proteins, it is highly unlikely that a direct charging effect on a protein is a lone action given what we know about the breadth of effects of the ultrashort, fast rise-time electric effects on cell membranes and ultracellular structures such as cytoskeleton, endoplasmic reticulum, mitochondria, nucleus, and other organelles. The influx of Ca^{2+} and the elevation of ROS modulate Ca^{2+}-dependent and oxidative functions.

Summary of intracellular effects. In summary, various experimentation methods and MD simulations have provided insights into the intracellular effects of ns pulses. It has been shown that the cell cycle can be disrupted and that RCD mechanisms can be elicited [24,35,43,44,82]. Cell impermeant molecules have shown variable degrees of uptake, showing a dose-like treatment dependence [22,43,76]. Calcium has been identified as a key player, as one would assume, given the multitude of pivotal interactions within the cell and throughout the body [24,26,78,104]. MD simulations provide insights unseen by microscopic observations, including ns pulse interactions with water, lipids, and proteins [78,83,104]. It seems that the consensus is that nanopore formation of lipids is the only direct effect, while effects on nucleic acids and proteins are indirectly affected; however, it is likely that nucleic acids and proteins are directly affected [18,76,77]. Perhaps one may reason to think that all charged atoms within the load range could be affected. In support of this theory, it is proposed to consider the following: (1) electrons have been shown to traverse the base pairs of DNA, playing a role in signal transduction in DNA repair [35,46,79], (2) the MD simulations of nanopore formation include polar water molecules, amphiphilic phospholipids and one amphiphilic phosphatidylserine, a phospholipid bound to a polar amino acid, serine [55,76], (3) proteins consist of amino acids with amphipathic, polar and electrically charged side chains on the primary level, not to mention essential coordination of ions and metals in their tertiary and quaternary levels (4) it has been shown that poration of

intracellular membranes occurs before the cytosolic membrane, perhaps this can be attributed to membrane composition differences, such as cholesterol levels, proteins and lipids, which could also account for the effective variance among cell types in response to ns pulse stimulation [105]. Thus, the intracellular effects of ns pulses are becoming more defined, yet their intrinsic nature remains a topic of discourse.

Section 2.2. The mPTP is a Sensor of NPS

As previously discussed, NPS is a technology advanced from pulsed power physics, which stores and rapidly releases high voltage, short duration pulses into cells and/or tissues [18,19,22,52,55]. Compared to conventional EP effects on the PM, these ultrashort electric pulses have distinct permeability effects, forming a higher density of nanopores in the PM as well as the membranes of all subcellular structures [83,106,107]. Of particular interest for NPS are the unique structural and functional effects on subcellular organelles, including the ER, nucleus, mitochondria, and cytoskeletal components [19,26,32,78,86]. While many studies have focused on the permeabilization of cellular membranes and resultant ionic fluxes, other effects could directly or indirectly alter proteins [32,101,102,108]. The NPS theory for higher probabilities of effects on intracellular constituents, rests with the model of the PM charging time constant, which is approximately 75 ns for cells in suspensions, or perhaps more fitting, the inverse of that constant in the frequency domain, Hz=1/time(s) [20,22,25,76,109-111]. The model states that intracellular effects occur as high-frequency components during the short, fast rise and fall times (F-RFT) of nanosecond duration pulses, while PM effects occur during the pulse plateau. This was supported for short duration pulses by analyzing calcium mobilization in the ER, the dissipation of the $\Delta\Psi_m$ and cell death [22,25,112].

This technology also has practical biomedical/clinical merit, as it was shown to induce immune system mediated vaccine-like effects, or *in situ* vaccination, in murine mammary (mouse, 4T1-Luc) and liver (rat, H1-N1) cancer models [30,60,113]. Interestingly, the NPS conditions that induced *in situ* vaccination in these murine cancer models, did not exhibit caspase activation *in vitro*, suggesting that the NPS induced cell death mechanisms that elicit immunity was not through apoptosis [30,60,114]. Such immunogenic tropism exploited by tumors and intersected by NPS demanded refinement of our experimental efforts to examine their convergent paths. When comparing the notorious hallmarks of cancer with cellular effects of NPS, the mitochondria became the obvious candidate [6,64,65,115]. Not only are mitochondria responsible for providing essential energy and metabolites but they play pivotal roles in many cellular processes, including a variety of signaling pathways as well as cell death [6,64,116]. While cancers aim to manipulate many of these processes to proliferate and avoid death, NPS has a high probability of targeting mitochondria for two main reasons. First, compared to the nucleus and ER, they are small organelles that exhibit extremely high electric fields across their membranes generating a high resting $\Delta\Psi_m$ [106]. Mitochondrial chemiosmotic coupling from redox reactions of the electron transport chain (ETC) generates a $\Delta\Psi_m$ of -150 mV to -200 mV. Thus, the effects of multiple nanosecond duration (60 ns) pulses, with delivery of F-RFT (5-10 ns), superimpose voltages across the high resting $\Delta\Psi_m$, having significant impacts on mitochondrial function [106,107,116]. Second, is that mitochondria serve as a sensitive centralized energy hub for the cell in that they regulate metabolites, control metabolic and energetic functions, crosstalk with other organelles, and impinge on many survival and RCD mechanisms [116]. Mitochondria also store and regulate calcium homeostasis as well as generate and utilize adenosine triphosphate (ATP) to maintain the $\Delta\Psi_m$, which is a sensitive indicator of

functional cell status and fate [64,74,116]. The $\Delta\Psi_m$ is established by oxidizing substrates that maintain a proton motive force (PMF) to synthesize ATP for cellular activities, regulate metabolism, and oversee survival and death [116,117]. Thus, mitochondrial targeting of NPS can have significant impacts on cell function and survival.

A significant event at the induction of RCD is often through the mPTP, a protein complex which reversibly or irreversibly opens, bridging the IMM and outer mitochondrial membrane (OMM) [118,119]. The consensus on the mPTP is that it is a large non-selective pore (~ 2.3 nm diameter), which allows ions and small molecules (~ 1.5 kDa) to pass between the mitochondrial matrix and cytosol [119-126]. Opening the mPTP dissipates the $\Delta\Psi_m$, attenuates oxygen consumption, and inhibits ATP synthesis via OX-PHOS. ATP-synthases can hydrolyze ATP to maintain the $\Delta\Psi_m$; however, sustained openings allow equilibration of small molecules and ions, dissipating the $\Delta\Psi_m$ and leading to RCD [119,126]. The mechanism(s) of RCD depends on the content of these small molecules, such as ATP, ROS, and the ratio of proapoptotic to antiapoptotic proteins, among other cellular metabolites and substrates. Although the exact constituents that complex to form the mPTP have been debated for decades, cyclophilin D (CypD), a Ca^{2+}-dependent and cyclosporin A (CsA)-sensitive protein, is a well-accepted regulator of the mPTP [118,127,128].

Our previous investigations established that (1) NPS-induced loss of $\Delta\Psi_m$ is Ca^{2+}-dependent and coincided with cell death, (2) that NPS induces cell death in Jurkat cells by caspase-dependent (apoptotic) and caspase-independent (non-apoptotic) RCD, and (3) that NPS induces Ca^{2+}-dependent loss of $\Delta\Psi_m$ in all cell types examined [49]; thus, peremptorily compelling these investigations into the NPS induced effects on the mitochondria. Although it may appear counterintuitive at first, since our broad interests are around cancer and immunity,

cancer cells and/or immune cells were not used for examining the fundamental mechanisms at the mitochondrial level. Cancer cells with manipulated, dysfunctional mitochondria, and immune cells which are rather small and have low metabolic rates, would complicate experimental procedures therefore, impeding the mission to gain fundamental insights which likely are broadly applicable. To circumvent these issues, rat cardiomyocytes (H9C2 cells) were selected for unraveling the effects of NPS on the mitochondria. These cells offer advantages over cancer and/or immune cells because they have a surfeit of metabolically active mitochondria, as one might assimilate muscle cells would need for proper function. Thus, H9C2 cells were used to show that NPS activates the mPTP by sensitizing the pore constituents to CypD and Ca^{2+}-influx through nanopores in the PM and NPS-generated Ca^{2+}-dependent elevation of mROS; therefore, suggesting that the mPTP is a sensor of NPS.

Section 2.3. Brief History of Immuno-oncology

The association between the immune system and cancer has been explored for approximately 130-years. In 1881, the German pathologist, Rudolf Virchow, hypothesized that cancers arise at sites of chronic inflammation when he observed inflammatory infiltrates in solid tumors [129,130]. In the late 19^{th} / early 20^{th} century, Paul Ehrlich, a Polish/ German physician and biologist, proposed that the immune system could be employed to target tumors [130,131]. This concept was investigated by William Coley, an American surgeon and cancer researcher, when he observed spontaneous and sustained tumor regression in postoperative cancer patients that developed infections at the tumor site [130,132]. This led him to treat patients with Streptococcus pyogenes inflammatory infiltrates albeit this was highly controversial [130,132]. Anomalously, the histopathological characteristics of carcinomas and chronically inflamed

and/or injured tissues are quite similar [130]. Taken together, these considerably contradictory observations elucidated the dichotomy of the immune system in cancer by revealing that the immune system can facilitate and target tumorigenesis [130].

Since these early revelations, our understanding of the immune system and cancer has immensely improved. As a result, our modalities for therapeutically intersecting cancer are approached from targeting the cancer and/or targeting the immune system [130]. Immune checkpoint inhibitors target immune cells with aims to reveal the cancer and restore order; however, prodigious challenges impede advancement in the field of immuno-oncology [130]. Primarily, our understanding of the biological and/ or immunological mechanisms of these immunomodulatory strategies is failing to keep pace with their use in clinical trials [130,133].

In 1889, an English surgeon, Stephen Paget, identified what is perhaps our greatest challenge in treating cancer when he proposed the "seed and soil" theory on metastasis [130,134]. In his theory, Paget postulated that (1) crosstalk occurs between cancer cells and their microenvironment which regulates the metastasis, (2) the colonization of metastasizing cancer cells depends on properties of the distant organ/tissue, thus (3) metastatic tropism, tissue/organ specific homing of cancer cells, patterns were the result of the "dependence of the seed" (or cancer cell) "on the soil" (or abscopal tissue/ organ) [130,134]. Certainly, Paget's cognizance of metastasis laid the foundation for the more recent revelations that primary tumors can actually induce distant changes, creating premetastatic niches [130]. Albeit the challenges with metastasis remain one of our greatest challenges in fighting cancer as it is attributed for about 90% of cancer related mortality [130,135].

The cancer-cell-intrinsic view continued to dominate cancer research in leu of Paget's prescient hypothesis [130,136,137]. Nearly 100-years later, a paradigm shift in the field of

cancer research emerged when metastatic progression could not be sufficiently supported by cancer-cell-intrinsic mechanisms and macrophages were found to infiltrate the tumor microenvironment (TME) [130,136-140]. Now, Paget's revolutionary "seed and soil" theory on metastasis dominates cancer research. The metastatic potential of the TME has been described for (1) interactions between immune cells and malignant cells and (2) interference with inter-immune-cell crosstalk [130,141-143]. Taken together, it is understood that the effects of tumorigenesis extend far beyond the primary tumor location and, therefore, the TME encompasses local and systemic tissues and/or organs [130].

Section 2.4. Gene Electrotransfer and NPS

Perhaps the most established use of electricity in biomedical applications is electroporation (EP), which considers cells in parallel with a generalized electric circuit whereby the cytoplasm is considered as the conductive body and the cell surface membrane is considered the dielectric barrier [19]. When cells are placed between two electrodes in a conductive medium and unipolar voltage pulses are applied, such current causes the cell membrane to accumulate the electric charges and, consequently, voltage [19]. EP occurs when the membrane voltage exceeds the norm, or rather the threshold voltage, and pores traverse the transmembrane space [19]. These effects can be irreversible, with high doses leading to cell death, as well as reversible, with low doses leading to cell recovery [19]. The latter of which is often used for temporarily porating cell membranes for drug and gene delivery [19,106].

Conventional EP typically involves pulses with a magnitude of about 0.1<1 kV/cm and durations greater than 100 μs [106]. These conditions permeabilize the plasma membrane (PM)

of cells which allows the exchange of small molecules and ions, fluxing with the concentration gradient, via pores in the lipid bilayer and voltage-sensitive channels [18]. The application of pulses with durations between 10-300 ns and magnitudes of about 360<10 kV/cm, are much shorter in duration yet with much greater magnitude than EP [24,76,82,144,145]. As previously discussed, these ns duration pulses have a multitude of cellular effects, and their application is referred to as NPS.

The relevant differences between EP and NPS are the effects on pore size and density [106,107]. With EP, pores form in the PM relatively quickly and increase in size with increased electric field; however, with NPS, pores continue to form with increased electric field exposure, yet the pore sizes remain relatively stable [106,107]. As part of these investigations, EP and NPS were used in vivo to induce tumor cell death.

Gene electrotransfer (GET) is considered one of the most efficient means of transferring genetic material across the PM [146]. In this approach, plasmid vectors encoding genetic material are transferred into cells by reversible EP [146,147]. Clinically, GET offers the advantage of targeting tissues, like tumors, while mitigating the adverse side effects of systemic therapeutic approaches [146]. In order to stimulate an appropriate immune response in the host, a balance between transgene expression and tissue damage must be achieved [148]. The efficacy of GET depends on the pulse parameters, including the duration, number, frequency, and magnitude, as well as the applicator electrodes, including parallel plate, or caliper electrodes, and various configurations of needle arrays [148]. To achieve the desired expression levels and outcomes, the GET parameters should be prudently considered for optimal delivery, especially considering the impartiality between stimulation and suppression of the immune system [148]. In these investigations, GET was used to deliver plasmid Interleukin 12 (IL-12, p-IL12) [148].

Antigen presenting cells (APC) produce this proinflammatory cytokine which stimulates T cell and NK cell proliferation [148]. Regarding cancer, IL-12 was shown to have anti- angiogenic and metastatic effects, thus limiting resources and progression [148]. Interestingly, IL-12 induces expression of interferon gamma production (IFN-γ), which serves as an anti-tumor mediator; however, there is a caveat to the expression levels of IL-12, since high expression levels assist tumors with immune system evasion [148]. Nevertheless, the pIL12-GET was used as previously described [61,148].

Additionally, pIL12-GET was examined in combination with NPS. Guo et al., showed that cells treated first with NPS and then with GET significantly increased gene expression [149]. This makes sense when considering the effects of NPS and EP on pore formation. Since NPS induces a high density of pores and EP expands them, then when NPS is immediately followed by EP this could, in theory, facilitate enhanced gene delivery. Therefore, the combined approach of GET and NPS was examined for treatment efficacy.

Section 2.5. Specific Aims

Cancers remain in the top noncommunicable diseases responsible for premature mortality [3,150]. Advances in our understanding of cancers has led to improvements of disease prevention as well as therapies and cures for some types of cancer. Unfortunately, the heterogeneity among cancers and within tumors makes treating them ever more challenging [6,8]. Our misfortunes for developing cures is mocked by cancer, with the lowest probability of success (PoS) through clinical trials and FDA approval [5,151-154]. At the very basic level,

there are generally two broad gaps holding us back from eradicating cancer: the unidentified shared mechanism(s) exploited by all cancers and the therapeutic approach to intervene.

The broad goal aimed to explore cancer mechanisms from a new angle with nanosecond pulse stimulation (NPS). These ultrashort, powerful pulses offer advances over traditional interventions with localized treatments, flexible parameters, and the potential for combining therapeutic approaches, like targeted drug delivery and gene electrotransfer (GET) [20,56,106]. The ultrashort pulse duration penetrates the cell, offering the unique ability to bypass the gatekeepers of the cell and impact nearly all its components. Cancers, too, impact nearly all cellular components, hijacking a multitude of cellular pathways and stressing key organelles. The approach of these investigations was to examine the molecular hallmarks of cancer intersection in vitro and anticancer immunity in vivo in response to NPS. A junction where the established NPS effects and the hallmarks of cancer overlap is at the multifaceted mitochondria [155]. Therefore, the in vitro investigations aimed to gain a deeper understanding of the mitochondrial effects of NPS and revealed that NPS induced dissipation of the mitochondrial membrane potential ($\Delta\Psi_m$), which is pivotal to metabolic homeostasis and regulated cell death (RCD) pathways. These investigations showed that dissipation of the $\Delta\Psi_m$ was dependent on the presence of calcium (Ca^{2+}) and sensitive to cyclosporin A (CsA), which inhibits cyclophilin D (CypD), a known regulator of the mitochondrial permeability transition pore (mPTP). This indicated activation of the mPTP rather than simply nanoporating the inner mitochondrial membrane (IMM). There were still a few mechanistic questions regarding the role of mitochondrial reactive oxygen species (mROS) remaining and were investigated as part of *aim 1* [156]. Regardless of the subsequent findings, the observations indicated NPS manipulated mitochondrial function, which was also demonstrated to play essential roles in immune cell

status and were investigated as part of *aim 2*. The in vivo investigations revealed several aspects of antitumor immunity, including the clearance of primary tumors, distal secondary tumors (untreated), and a vaccine effect with certain NPS parameters [30]. Tumor specific efficacy of NPS was also observed, meaning that the NPS parameters that worked for one type of tumor (4T1-Luc murine breast cancer) was less effective on a different type (B16-F10 murine melanoma). These investigations were continued as part of *aim 2* where the phenotypic expression and metabolism in immune activation and memory induced by NPS were explored [157-159]. The central hypothesis was that *NPS modulates mitochondrial function and fitness which induces metabolic shifts in immune cells consistent with the immunometabolic and phenotypic profiles associated with their suppressive and activation statuses in antitumor immunity.* To investigate this hypothesis, the following two aims were proposed:

Aim 1. *To elucidate the roles of Ca^{2+}, mROS, $\Delta\Psi_m$, CypD, and mPTP formation in response to NPS in a model cell line.*

Cardioblasts (H9C2 cells) with robust mitochondrial functions, served as the model cell for investigating the NPS-cancer hallmark junction at the mitochondria, including the roles of Ca^{2+}, mROS, $\Delta\Psi_m$, CypD, and the mPTP. These investigations were conducted with mitochondrial assays optimized for flow cytometry. The hypothesis was that NPS would activate the mPTP by dissipating the $\Delta\Psi_m$ in a Ca^{2+} and mROS dependent manner in H9C2 cells. Furthermore, these findings indicated the potential for NPS effects on mitochondrial function in immune cells, albeit their small stature and low metabolic activity limited gaining the mechanistic insights in this manner and required the more sensitive approach of aim 2.

Aim 2. *To examine the NPS-induced resolution of immunosuppression and the activation of the innate and adaptive immune response.*

The preliminary investigations revealed that NPS-induced antitumor immunity with greater efficacy in mouse 4T1-Luc breast cancer than in B16-F10 melanoma. The hypothesis was that the immune profiles and immunometabolic signatures would be different between these two cancer models. The immunosuppressive and activation markers of the innate and adaptive immune responses were compared by phenotypic profiling with flow cytometry. Additionally, the metabolism of isolated CD4+ T cells were analyzed by extracellular flux analyses to determine their functional status [160]. The comparative analysis of the NPS modulated effects on phenotype and immunometabolism were expected to support current literature findings on drug-induced immune activation and memory.

Fulfillment of these aims will contribute to an improved understanding of the mitochondrial and metabolic roles of immunity in cancer. In the long-term, they have the potential of providing new insights for the development of cancer interventive therapies and supportive evidence for the biomedical applications of NPS.

CHAPTER III

METHODOLOGY

Section 3.1. Overview of Research Design

The effects of nanosecond pulses were considered on four levels. First, the intracellular effects of NPS were examined for their impact on the mitochondria. Second, NPS and/or pIL12-GET were used in vivo to examine their efficacy on tumor clearance and induced immunity. Third, the NPS-induced immune response was analyzed phenotypically for signs of activation and memory. Finally, the NPS-induced metabolic response of isolated CD4+ T cells was examined.

The mitochondrial effects of NPS were examined in rat derived cardiomyocytes, H9C2 cells, as they are relatively large cells containing multiple mitochondria, which made them a desirable selection for probing aspects of such a small organelle. The primary focus here was to examine the effects of NPS on the mitochondrial membrane potential $\Delta\Psi_m$ as this might indicate activation and opening of the mPTP. While the constituents of the complex remain elusive, CypD has been accepted as its primary regulator. Aside from that, the mPTP has calcium dependent mechanisms for activation and sensitivities to ROS. To test NPS as an activator for the mPTP, a NPS dose response was conducted to determine the optimal range which activated intracellularly RCD. The CCK8 viability assay was employed for this preliminary task and was conducted 24-hours post-treatment with NPS. NPS parameters slightly greater than half of the maximal inhibitory effects were used for examining the NPS-induced dissipation of the $\Delta\Psi_m$. To examine whether such dissipation was resultant of mPTP activation, the key influencers were manipulated, including the calcium concentration and CypD inhibition. The effects of variable

calcium concentrations were examined in parallel with CypD inhibition via CsA. In those experiments, the cells were incubated with and/or without CsA and treated with NPS suspended in their respective calcium concentration containing medium. Shortly after treatment, flow cytometry was used to examine the percentage of cells that were maintaining $\Delta\Psi_m$. The relationship of $\Delta\Psi_m$ and mROS generation was examined by conducting a NPS dose response. In these experiments, a single sample from each dose was probed for $\Delta\Psi_m$ and mROS. In this manner, one could examine the dissipation in parallel with mROS accumulation. Taken together, the NPS-induced effects of $\Delta\Psi_m$ dissipation and mROS generation were thoroughly examined for their roles in the potential mechanism of NPS-induced mPTP activation. Furthermore, the insights gained in these experiments showed that NPS affects mitochondria, which led to the notion that it might also affect mitochondrial metabolism, an aspect later explored in immune cells.

While the mitochondrial experiments were underway, NPS was investigated for therapeutic efficacy in several in vivo cancer models. These experiments were approached on three levels: (1) examine the efficacy of different NPS pulse forming network configurations on primary tumor clearance and protection, (2) examine the most efficient NPS treatment for abscopal tumor clearance/ rejection in addition to primary tumor clearance and protection, (3) examine the efficacy of NPS, pIL12-GET, and pIL12-GET-NPS on primary tumor clearance and protection, and (4) examine the efficacy of the most efficient NPS treatment on human tumors. First, the 100ns Blumlein line (BL) pulser was compared with a 200ns BL pulser and 200ns metal-oxide-semiconductor field-effect transistor (MOSFET) pulser. The electric field parameters for voltage and frequency of the 200ns BL and MOSFET pulsers were matched to examine potential differences in primary tumor clearance and protection between the two

configurations. For these experiments, murine mammary cancer (4T1-Luc) and melanoma (B16-F10) tumors were initiated in mice, Balb/cJ and C57BL/6J, respectively. When tumors reached a treatable size for using pinch electrodes, usually within 8-11 days, they were treated with NPS. Weights and tumor volumes were measured regularly until clearance was observed. In the 4T1-Luc model, IVIS live imaging was used to detect the luciferase expressing cancer cells. In this manner, images of the tumors as well as early detection of metastasis were gained. Images of the B16-F10 tumors were also acquired albeit without the detection of luminescence. Mice that were successfully treated with NPS, as evident by complete tumor clearance, were challenged with the same cancer to examine whether the treatment granted protection from subsequent exposure. It is important to point out that untreated control mice were primarily employed at the challenge. The rationale behind this was (1) that all mice were naïve before receiving the first tumor inoculant and would/ did develop tumors as a result, (2) that naïve mice should be employed at the challenge to ensure viability of the cells being used in the challenge, and (3) to comply with the "Three R's" of The Animal Welfare Act for reducing the number of animals employed by these experiments, which was supported by points 1 and 2. Mice that rejected tumor development were considered to have immune protection; thus, NPS was considered to have a vaccine-like effect referred to as *in situ* vaccination. Obtaining tumor measurements, weights, and imaging, as applicable, were standard for all cancer/ tumor models and should be assumed where not explicitly defined. Second, the 4T1-Luc model was examined for abscopal tumor clearance. In these experiments, a second tumor was initiated on the opposite side of the mouse before treatment at various time points. These experiments aimed to examine the treatment efficacy on distant, or distal, tumor sites, as well as primary treated tumors and subsequent protection, and to explore possible scenarios for the findings in the event NPS efficacy proved dependent on the

number of days the tumor was initiated prior to treatment. Third, the B16-F10 model was used to examine the efficacy of NPS, pIL12-GET, and the combination of pIL12-GET-NPS on primary tumor clearance and protection. In these experiments, tumors were treated with the 100ns BL pulses, pIL12-GET, or pIL12-GET and 100ns BL pulses. Although a thorough explanation was previously described, one of the important differences between ns pulses and ms pulses, as employed by GET, is the variation in the generation of pore density and size. The ns pulses generate multiple nano-sized pores, while the ms pulses generate larger pores in the PM. With that in mind, the rationale for developing the order of treatment events was that the application of ns pulses could enhance GET. Thus, NPS was applied first, to generate a high density of nanopores in the PM, followed by ms pulses, which would then yield a high density of larger sized pores, which could facilitate an enhanced plasmid uptake by the treated tumor cells. That said, pIL12-GET was delivered on days 0, 3, and 7 for both pIL12-GET and pIL12-GET-NPS treatment groups. Forth, and final, NPS was used to treat human breast cancers in immunocompromised mice, NSG and NSG-SGM3, to examine the efficacy for clearing treated tumors. In this model, the 100ns BL pulser was used to treat triple negative breast cancer patient derived xenografts (TNBC-PDX) and a metastatic mammary cancer, MDA-MB-231 VIM RFP/ HTB-26MET, cell line derived xenografts (BC-CDX) to examine the differences in efficacy between the two models. Mice that cleared primary tumors were not challenged in this model as per the model host lacked a competent immune system and therefore not likely to have developed immune memory. The original aims of this model included the reconstitution of these mice with a human immune system (HIS) by engrafting them at an early age with human umbilical cord derived CD34+ hematopoietic stem cells (HCB CD34+ HSC), which would expand and differentiate into a chimeric human immune system within the mouse in a tolerable

manner. After about 10-12 weeks, tumors were started in these mice so that the tumor volume and HIS would be optimal at the same time for treatment. In addition, it was hypothesized that the cytokines and growth factors associated with the tumor might have a stimulatory effect on the engrafted immune system and lead to chimeric enhancement, which could then be used to examine the human-like immune response after NPS. However, this model was plagued with challenges and no mouse was ever successfully engrafted with both. Thus, the insights into the NPS-induced human immune response were not achievable and subsequent investigations refocused on the murine cancer models.

The murine immune response induced by NPS was previously examined in the 4T1-Luc model [30,60]; however, differences observed in the treatment efficacy in the B16-F10 model begged for a comparison of the induced immune response. For these experiments, B16-F10 tumors were treated with the 100ns BL parameters and tissues were examined for immunity on days 0 (untreated), 1, 2, 3, and 7 post-treatment and post-challenge when tumor status and immunity became evident. Multi-fluorescence flow cytometry antibody panels were designed to examine the phenotypes of immune cells, including macrophages, dendritic cells, T cells, and natural killer cells, circulating in the peripheral blood, tumors, tumor draining lymph nodes, and spleens. Flow cytometric gating strategies were used to gain insights into more specific designations such as activation and memory statuses.

Recently, the activation and memory statuses of certain immune cells, like macrophages and T cells, have been investigated for metabolic shifts, a concept referred to as immunometabolism [64,116,161,162]. Those associated with naïve, quiescent, and memory statuses were shown to predominantly rely on mitochondrial respiration, while those associated with activated statuses predominantly rely on glycolysis [64,68,116,162]. To determine whether

NPS could induce metabolic shifts in immune cells, CD4+ T cells were magnetically isolated from lymph nodes of naïve BL6 mice and the tumor draining lymph node (dLN) of B16-F10 tumor bearing BL6 mice that were untreated and NPS treated (NPS-TX) on day 1 and 3 post-treatment. The enriched CD4+ T cells were then examined by Seahorse extracellular flux analyses (SH-XFA) to examine the impacts of NPS on metabolic statuses. In parallel, flow cytometry was used to examine the activation and memory statuses phenotypically for comparison with the metabolic statuses.

Taken together, these investigations aimed to examine aspects of NPS in vitro, in vivo and ex vivo via the detailed methods in the forthcoming sections.

Section 3.2. In Vitro Materials and Methods

Cells and culturing. Rat derived cardiomyocytes, H9C2 cells, were cultured in Dulbecco's Modified Eagle Medium (DMEM) containing 4 mM L-glutamine, 4500 mg/L glucose, 1 mM sodium pyruvate, and 1500 mg/L sodium bicarbonate (Corning, 10-013-CV), supplemented with 10 % fetal bovine serum (FBS; HyClone Laboratories, SH30396.03) and 1 % penicillin-streptomycin (pen-strep; Corning, 30-002-CI). Cell cultures were incubated at 37℃ in a 95 % air, 5 % CO_2 incubator. Adherent, H9C2 cells were harvested with 0.25 % (w/v) Trypsin- 0.53 mM EDTA solution (Corning, MT25053CI). Cells were subcultured/ passaged no more than 25-30 times for *in vitro* experimental use. Initial cell counts and viability were obtained using 0.4 % trypan blue exclusion viability assay (Corning, 25900CI). Cells with greater than 95% viability were washed with PBS, centrifuged at 300_{RCF} for 5 min at room temperature, and resuspended at a concentration of $1x10^5$ cells/ 100 µL for NPS treatments.

CCK-8 viability assay. The Cell Counting Kit 8 (CCK-8) viability assay (Dojindo, CK04-13), which employs the highly water-soluble, tetrazolium salt WST-8 [2-(2-methoxy-4-nitrophenyl)-3-(4-nitrophenyl)-5-(2,4-disulfophenyl)-2H-tetrazolium, monosodium salt] (Patent No. WO97/38985), was used according to the manufacturer instructions for determining cell viability after NPS. This kit offered advantages over other viability assays in that it is highly sensitive and does not require mixing, circumventing issues with inconsistent preparations. First, the assay was used to predetermine the cell densities required for properly filling the surface area of the culture well, which is about 0.32 cm^2/ well of a 96-FBWP, while maintaining viability by following the procedure for conducting a cell proliferation assay. The calibration curve was prepared by plotting the cell densities against the measured absorbances, and the limits of linearity, which, in this case, were the points where the highest cell densities and absorbances before the curve plateau were observed, indicated the cell concentrations/ densities that were used for subsequent employment of the cytotoxicity assay protocol. The cytotoxicity assay protocol was slightly modified for examining the NPS dose response on viability in H9C2 cells as per NPS treatment does not require the addition of cytotoxic agents; thus, the well volumes were adjusted such that the final volume remained consistent with that indicated by the manufacturer. In short, after NPS, 5 µL of cells, suspended according to the previously determined cell densities, were used to inoculate wells of a 96-FBWP (clear bottom and white walls), containing 95 µL of complete media. The cells were incubated overnight in their usual manner. The following day, 10 µL of CCK-8 reagent was added to each well and incubated for 1-3 hours before obtaining the absorbance measurements at 450 nm. The NPS dose response viability curve was prepared by plotting the NPS doses against the measured absorbances. The dose at which 25% of the cells remained viable 24 hours after NPS was employed for subsequent experiments as it was most

likely to induce RCD mechanisms within the post-treatment observation timeframe (*preliminary data not shown*).

Experimental mediums. Corning Cell Culture Phosphate Buffered Saline, 1X (PBS, MT21040CV) and Dulbecco's Phosphate Buffered Saline, 1X (DPBS, 21-030-CM) were used for $\Delta\Psi_m$ and mROS experiments without and with calcium, respectively. When stated, 1.8 mM EGTA was added to ensure removal of extracellular calcium. Mitochondrial Respiration Medium Kit (Oroboros MiR05-Kit, 60101-01) was prepared according to the kit protocol except for the omission of EGTA and the addition of calcium at the following concentrations: 0, 10, 33, 50, 75, 100, 150, 200, 250, and 1800 µM [163].

Experimental inhibitors. The NPS-induced effects on the mPTP were investigated by pretreating cells with the CypD inhibitor, 5 µM cyclosporin A (CsA; Tocris, 1101), and/or calcium scavenger, 1.8 mM ethylene glycol-bis(β-aminoethyl ether)-N,N,N′,N′-tetraacetic acid (EGTA; Sigma, E3889-10G). For each pretreatment, the cells were suspended at a concentration of $1x10^5$ cells/100 µL of required medium and incubated in the dark at room temperature for 30-60 min. Then, for the NPS dose response experiments, the cells were ready for the experiment; however, for the $\Delta\Psi_m$-CsA-Ca^{2+} experiments, the cells were centrifuged and resuspended at the same cell and inhibitor concentrations in experimental medium with variable calcium concentrations.

Flow Cytometry, fluorescent indicators, and labeling. Tetramethylrhodamine, ethyl ester, perchlorate (TMRE; Immunochemistry Technologies LLC, Bloomington, MN), was used at a concentration of 0.2 µM for detecting $\Delta\Psi_m$ [25,48], and MitoSOX-Red (MSOX; Invitrogen, Molecular Probes, Inc., Eugene, OR), mitochondrial superoxide indicator, was used at a concentration of 1 µM for probing mROS with flow cytometry in live H9C2 cells [156].

Untreated and/or unstained samples were used as negative controls for treatment and fluorescence, respectively. H_2O_2 was regularly used as the negative (TMRE) or positive (MSOX) control but was not included in the figures since a dose response was observed for both molecular probes.

$\Delta\Psi_m$ and CypD inhibition experiments. H9C2 cells were harvested, counted, and resuspended as previously described. Then, 200 µL samples were centrifuged (1 min, 800_{RCF}) and resuspended in modified MiR05 as previously described. Each sample was then split into two aliquots of 100 µL for TMRE staining and CsA inhibition (5 µM). The samples were protected from light and incubated at room temperature for 15 min. Samples were treated with 25, 60ns pulses at 40 kV/cm at a frequency of 1 Hz, protecting from light as permitted. TMRE fluorescence was detected 10-20 min post-treatment with a Miltenyi MacsQuant Analyzer 10 flow cytometer.

$\Delta\Psi_m$ and mROS experiments. Since TMRE and MSOX indicators exhibit similar emission spectra, they were measured in parallel by treating a sample with NPS and then dividing into two aliquots, one for TMRE and one for MSOX. The samples were incubated at room temperature, protected from light, for 15-20 min before acquiring flow cytometric data (Miltenyi MacsQuant Analyzer 10).

In vitro NPS treatment parameters. A 60ns custom built Blumlein (BL) line pulser was used throughout these investigations as previously described [23,48,76,164]. Cells were treated in 100-µL pulser cuvettes while in suspension.

Section 3.3. In Vivo Mouse Models

Mouse models. BALB/cJ, or Balbc, (Jackson Laboratory, 000651) and C57BL/6J, or BL6, (Jackson Laboratory, 000664) female, 6-8-week-old mice were used for the 4T1-Luc and B16-F10 cancer models, respectively. 4T1-Luc tumors were initiated via subcutaneous injection into the posterior layer of the mammary fat pad (MFP), abscopal and/or challenge injections were delivered into the opposite MFP. Abscopal tumors were initiated prior to treatment as indicated by the experiment. B16-F10 tumors were initiated via subcutaneous injection into the right flank, and challenge injections were delivered into the opposite flank. Challenges in both tumor models took place > 3-7 weeks post-treatment. Transgenic Foxp3^{GFP} C57BL/6J mice were generously provided by Dr. Piotr Kraj [165]. These mice were employed for *ex vivo* investigations into the metabolic effects of NPS on immune cells.

Specific pathogen-free female NOD.Cg-Prkdc^{scid} Il2rg$^{tm\ 1Wjl}$/SzJ mice, commonly referred to as NSG, purchased from The Jackson Laboratory (catalog no. 005557), were employed by this investigation due to their extreme immunodeficiencies, carrying two mutations on the NOD/ShiLtj genetic background: severe combined immune deficiency, scid, and a complete null allele of the IL2 receptor common gamma chain, IL2rg^{null}. These mutations render the mice B and T cell deficient as well as deficient of functional NK cells. Such immunodeficiencies make the NSG mouse a model organism for immune reconstitution via HCB CD34+ HSC engraftment. However, advances to this model in transgenic expression led to the advent of the NOD.Cg-*Prkdc^{scid} Il2rg^{tm1Wjl}* Tg (CMV-IL3, CSF2, KITLG) 1Eav/MloySzJ mouse, referred to as NSG-SGM3, NSGS, or NSGM3. This model offered advanced human immune system engraftment as they express human IL3, GM-CSF (CSF2), and SCF (KITLG), which enhance stable and chimeric engraftment of myeloid lineages as well as regulatory T cells. This

model became the more ideal candidate for examining the NPS-induced human immune response. Furthermore, females were previously shown to have superior engraftment to males. Thus, female NSG-SGM3 mice, purchased from The Jackson Laboratory (catalog no. 013062), were employed for the later experiments, and presented within this manuscript.

All mice were housed under specific pathogen-free conditions and used according to the guidelines from the IACUC of Old Dominion University (specifics can be found in Section 3.12. Vertebrate Animals).

Humanizing mice. On the day of engraftment, isolated HCB CD34+ HSCs were carefully thawed in a warm water bath set to 37℃ and washed three times for ample dilution of DMSO. Warmed media (RPMI-1640, 10% FBS and 1% penicillin-streptomycin) and centrifugation parameters of 1500_{RCF} for 5 min at room temperature are used under aseptic conditions for this process. The HSCs were suspended at 300,000 HSCs/ 100 µL, according to the pre-cryo reported cell count, in cold preferred media (as defined by the isolation kit protocol) and stored at 4℃ until the post-cryo cell count and purity were confirmed via flow cytometry. Pure samples underwent a second round of washing with cold, un-supplemented PBS to dilute the serum levels associated with inducing a host immune response in immunocompetent mouse strains. While the strains employed for this investigation are of the NOD *scid* background, a common misconception is that their genetic engineering renders their immune system completely suppressed; however, this is not entirely accurate. Most subsets of the innate and all subsets of the adaptive immune system are lacking albeit, granulocytes of the innate immune system, functioning in allergic responses, remain competent. Thus, it was essential to keep with best practices and ensure adequate serum removal for optimal engraftment in these mice. HCB CD34+ HSC, with confirmed purity, as

shown in Figure 3, were suspended at a concentration of 100,000 cells/ 100µL in PBS and transported on ice for injection delivery.

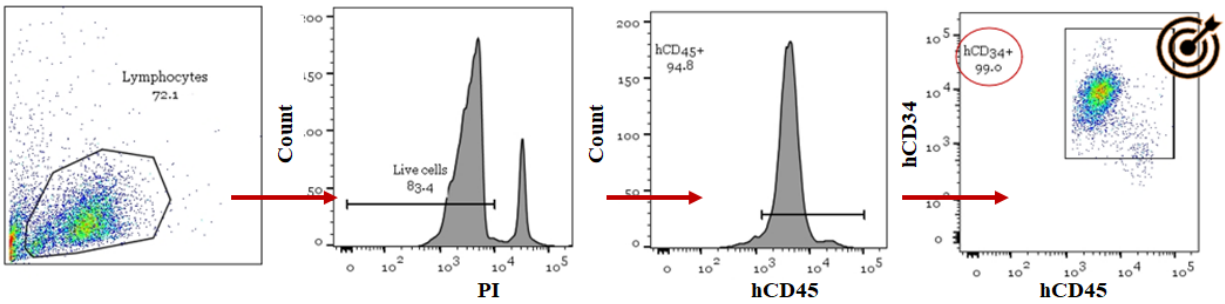

Figure 3. Representative analysis of HCB CD34+ HSC pre-engraftment. After cryopreservation, flow cytometry was used to confirm the viability and purity of the isolated cells prior to engrafting mice. Viable HCB CD34+ HSC were considered PI negative, hCD45 positive and hCD34 positive. Only samples with high purity, as shown above, were used for engrafting mice. FC plots were produced with FlowJo™ Software (Windows) Version 10 (Ashland, OR: Becton, Dickinson and Company; 2019).

An aliquot of approximately 300,000 isolated HCB CD34+ HSCs, based on the pre-cryo report, was vetted for impurities via flow cytometric analysis (Figure 4). Human antibodies were used to probe the sample for progenitor cell contaminants like T cells (CD3, CD4 and CD8), B cells (CD19) and myelomonocytic cells (CD33) in addition to confirming the abundance of HSCs (CD34). While positive selection via magnetic isolation inhibits the binding of antibodies

to a portion of the hCD34 receptor, several clones are available for binding allosterically. It was essential that HCB CD34+ HSC samples were keenly analyzed for impurities, negating the use of any sample with greater than 1% excess of viable progenitor cells as such impurities may induce the early onset of graft-verse-host disease (GVHD). Therefore, HCB CD34+ HSCs were analyzed at least twice, once before and after cryopreservation, prior to their engraftment in NSG/ NSG-SGM3 mice. Viability of the hCD34+ population, among others, was also measured using propidium iodide (PI) staining and flow cytometry. In this manner, comparison analyses of pre-cryo with post-cryo isolates, supported published evidence indicating decreased viability of progenitor cells yet sustained viability of HCB CD34+ HSC after cryopreservation (data not shown). It is also noteworthy to mention that the anticipated viability was around 70% or greater, which was obtainable as shown in Figure 4, with a viability of about 83%. The robust nature of HCB CD34+ HSCs coupled with the mortality of progenitors renders cryopreservation preferred to the engraftment of freshly isolated cells with similar, yet viable progenitor frequencies capable of inducing GVHD. Furthermore, the post-cryo cell count consists of HCB CD34+ HSCs with increased accuracy as remaining debris and necrotic progenitors are discarded in the supernatant of washes and decreasing the number of spectator events collected during flow cytometric data acquisition.

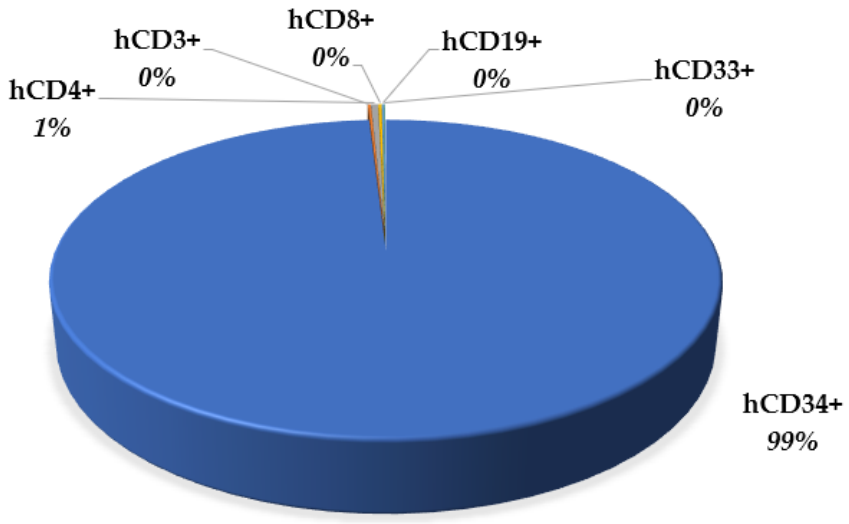

Figure 4. hCD34+ post-cryopreservation purity assessment. Percentages of lymphocyte subsets of the hCD45+ population post-cryopreservation. The hCD34+ population makes up 99% of all hCD45+ cells, and with less than 1% of progenitor cells remaining in the sample, cells were used for engraftment.

Once the HCB CD34+ HSC purity was confirmed and the post-cryo cell count obtained, the HCB CD34+ HSCs were suspended at a concentration of 100,000 hCD34+ cells/ 100 µL PBS and maintained on ice until injection delivery. Approximately 4-8 hours prior to HSC engraftment, 4-6-week-old female NSG and/or NSG-SGM3 mice were treated with sublethal irradiation dosed according to their age as shown in Figure 5. Generally, the HCB CD34+ HSCs were resurrected from cryopreservation during the waiting period, that is, mice were treated with irradiation and then the cells were prepared. In earlier experiments, mice received two injections of 50,000 hCD34+ cells/ 50 µL PBS. The first 50 µL aliquot was delivered into the femur, referred to as interfemoral (IF) and/or intraosseous (IO) infusion whereby the cells were directly

injected into the marrow of the femoral bone. This required that, first, a pilot hole be made into the femur with a 25-G needle before injecting cells with a 27-G needle, not to mention a very steady hand and keen sight. The second 50 µL injection was given intraperitoneally (IP), whereby the cells were directly injected into the peritoneal cavity. The rationale behind implementing this two-injection method was that IF/IO delivery would place the cells into the tissue of origin, as in the tissue where naïve immune cells start, and that IP delivery would enhance immune cell chimerism, in that the naïve cells would be carried to their primary location of differentiation, i.e., lymphocytes to the thymus for T cell differentiation. However, the process of delivering both injections was lengthy, and no benefits were observed, so a single 100,000 HCB CD34+ HSCs/ 100 µL IP injection was used for the experiments shown.

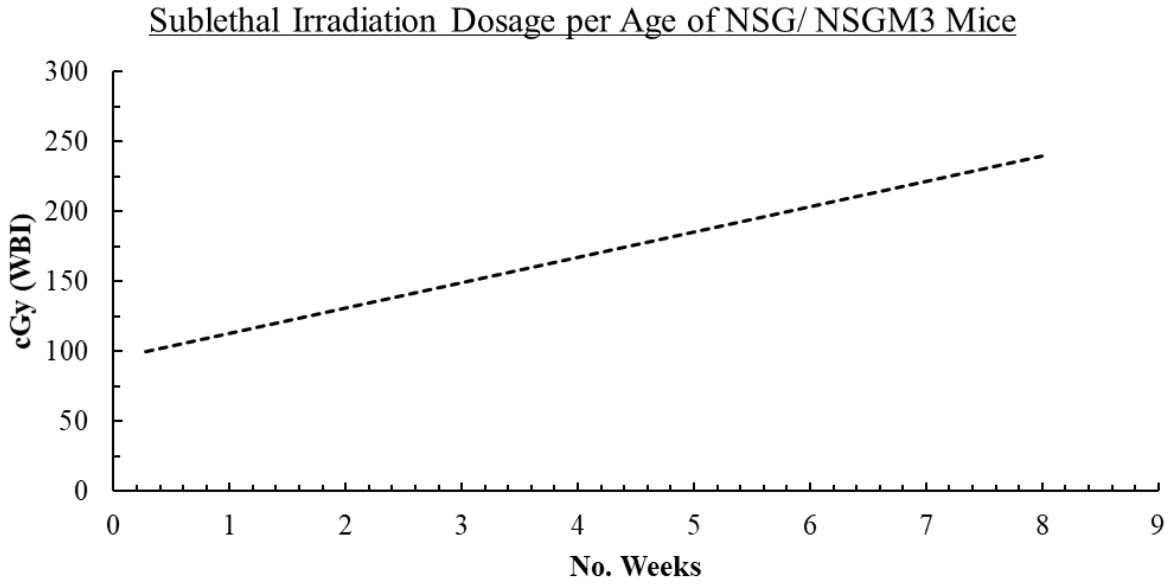

Figure 5. Sublethal irradiation dosage per age of NSG/NSGM3 mice. The line graph indicates the irradiation dosage for priming the mouse hosts to accommodate the human immune cell xenograft without inducing adverse effects of irradiation.

To monitor the humanization progression, blood was collected via mandibular vein bleeds (MVB) every 4-5-weeks after the engraftment of HCB CD34+ HSC to examine the presence of mature phenotypes. Collected blood samples were treated with red blood cell lysis (RBC) buffer to reduce the RBC content. White blood cells were then stained with the antibodies as shown in Table 1, to identify T cells, B cells, myelomonocytic cells, and HSC. In short, cells were incubated with antibodies at 4℃ in the dark for 15 min. They were washed with BSS, 1x, three times and fixed with 4% paraformaldehyde. Stained samples were incubated overnight, protected from light, at 4℃. Data was acquired with a Miltenyi MacsQuant Analyzer 10 (Miltenyi) and/ or FACSCanto (BD Biosciences) flow cytometer and analyzed with FlowJo™

Software (Windows) Version 10 (Ashland, OR: Becton, Dickinson and Company; 2019). While all mice in an experiment received the same cocktail of pooled HCB CD34+ HSCs, their expansion was highly variable, and therefore, no statistics were reported for immune cell phenotypes.

Table 1 HCB CD34+ HSC purity and differentiation antibody panel.

Voltage Channel	**Fluorophore**	**Human Antibody**	**Lineage**
V1	VioBlue	*hCD3*	T cell
V2	VioGreen	*hCD33*	Myelomonocytic
B1	FIT-C	*hCD4*	T cell
B2	PE	*hCD34*	HSC
B3	PerCP-Vio700	*hCD19*	B cell
B4	PE-Vio770	*hCD45*	Lymphocyte
R1	APC	*hCD8*	T cell
R2	APC-Vio770	*hCD90*	Thy 1.1

The oncohu-mouse. Approximately 10-14-weeks into the humanization process, tumors were started in either the flank or MFP of hu-mice via cell injection or tumor section implantation; thus, becoming oncohu-mice. All procedures were conducted under aseptic conditions and while recipient mice were anesthetized as described. For the TNBC-CDX oncohu-mice, the injection region was shaved and recipients of the MDA-MB-231 VIM-RFP cells (CDX) were inoculated in the MFP with $1x10^6$ cells/ 50µL injection. For producing TNBC-PDX oncohu-mice, the

implantable region was shaved and/or briefly treated with Nair to remove fur prior to thoroughly cleansing the skin with two 1 min alcohol and Betadine swabs. Sterile surgical Killner scissors were used to make a small incision, about 5mm long, into the epidermis of the flank or breast. The scissors were then inserted between the epidermal and subcutis tissue and gently opened to form a subcutaneous pocket. Mcpherson angled forceps were used to insert the $2mm^2$ tumor sections into the pocket. Once the tumor was placed and the forceps removed, the pocket closed and VetBond was used to reseal the incision.

Section 3.4. In Vivo Materials and Methods

Cells and culturing. Murine mammary cancer cells, 4T1-Luc, were purchased from Dr. Gary Sahagian (Tufts University, 2013) and maintained in high-glucose DMEM (ATCC, 30–2002) supplemented with 10% FBS (ATCC, 30-2020), 1% nonessential amino acids (NEAA; Corning, 25-025-CI) and 1% pen-strep. Murine melanoma, B16-F10, cells were purchased from ATCC (ATCC, CRL-6475) and cultured in DMEM (ATCC, 30-2002) supplemented with 10% FBS (ATCC, 30-2020) and 1% pen-strep. Cell cultures were maintained in a humidified 5 % CO_2, 95 % air, incubator at 37℃.

The human breast cancer cell line, MDA-MB-231 VIM-RFP, was purchased from ATCC (ATCC®, HTB-26MET™). In vivo use of this human cell line is referred to as the breast cancer cell line derived xenograft (BC-CDX). Cells were cultured in Eagle's Minimum Essential Medium (EMEM; ATCC®, 30-2003), supplemented with 10% FBS (ATCC®, catalog no. 30-2020), 0.01 mg/mL human recombinant insulin (Thermo Fisher, 12585014), 10 µg/mL Blasticidin S HCl (Gibco, A11139-03), and 1% pen-strep. Cell cultures were incubated at 37℃

in a 95% air, 5% CO_2, humidified incubator and maintained according to the manufacturer instructions.

In vivo tumor inoculant preparations. Adherent cancer cells, including 4T1-Luc, B16-F10, and MDA-MB-231 VIM-RFP, were harvested with 0.25 % (w/v) Trypsin- 0.53 mM EDTA (Corning, MT25053CI) solution and subcultured/ passaged no more than 15 times for *in vivo* experimental use. Initial cell counts and viability were obtained using 0.4 % trypan blue exclusion viability assay (Corning, 25900CI). Cells with greater than 95 % viability were washed with PBS, centrifuged at 300_{RCF} for 5 min at room temperature. Breast cancer cells, including 4T1-Luc and MDA-MB-231 VIM-RFP, were resuspended at a concentration of $1x10^6$ cells/ 50 µL PBS for inoculation. Melanoma cells, B16-F10, were resuspended at a concentration of $5x10^5$ cells/ 50 µL PBS or $2.5x10^5$ cells/ 50 µL Matrigel at 5 mg/mL (Corning, 354234). Cells were transported and maintained on ice until injected into the MFP (breast cancer) or flank (melanoma) of the mouse.

In vivo human tumor patient derived xenograft. An NSG mouse was purchased bearing a human triple negative breast cancer patient derived xenograft (TNBC-PDX) from Jackson Laboratory. Once the tumor reached the maximum burden, about 1500 mm^3, the mouse was euthanized and tumor sections, about 2 mm^2, were transplanted into additional mice under aseptic technique, or cryopreserved in Corning RPMI-1640 supplemented with 10 % FBS, 1 % penicillin-streptomycin and 5 % DMSO to maintain viability. When cryopreserved tumor sections were used, they were quickly thawed and washed with unsupplemented Corning RPMI-1640. Tumor sections were maintained in unsupplemented Corning RPMI-1640 on ice for transport and until they were implanted into the flank or MFP of the mouse.

In vivo NPS treatment parameters (ns). Three different pulsers, with two different delivery configurations, were used throughout these investigations, including custom built 100ns and 200ns BL line pulsers, and a MOSFET pulser (Pulse BioSciences) used to deliver 200ns pulses [166]. Unlike the BL pulsers, with fixed pulse durations at 100ns and/or 200ns, respectively according to their network configuration, the pulse durations of the MOSFET pulser are not fixed and were adjusted to an average of 200ns prior to treatment. In each case, 1000 pulses were delivered at a frequency of 3Hz. The electric field was adjusted to 50kV/cm for the 100ns BL pulser and 30kV/cm for the 200ns BL and MOSFET pulsers. The profiles of the BL pulses were monitored by a digital Tektronix oscilloscope (Tektronix, OR, TDS2024C), while the power was generated by a Glassman high voltage power supplier (Glassman High Voltage, Inc., NJ, EH series). Table 2 indicates the referenced NPS treatment, pulse duration, the network configuration/ type of pulser, and the electric field of the pulse. This table should be recalled while examining this manuscript as the first column indicates how each set of NPS treatment parameters will be referenced throughout these investigations. The addition of Tx, i.e., 100ns BL-Tx, will delineate that an experimental group had been treated with that set of NPS parameters. The term NPS-Tx also refers to the 100ns BL-Tx.

Table 2 In vivo NPS treatment parameters.

Referenced Treatment	Pulse duration	Pulser Type	Electric Field
100ns BL	100ns	BL	50 kV/cm
200ns BL	200ns	BL	30 kV/cm
200ns MOSFET	200ns	MOSFET	30 kV/cm

In vivo pUCMV3-IL-12 GET treatment parameters. The pUMVC3-mIL-12 plasmid (pIL12) was purchased from Aldevron (Fargo, ND) at a concentration of 2mg/mL saline and endotoxin levels <100EU/mg [148]. The CMV promoter was responsible for driving the expression of the IL-12 from the plasmid. In preparation of pIL12-GET, the concentration was reduced to 1mg/mL sterile physiological saline of which, 50µL were injected directly into the center of each tumor with a 25-G needle and syringe; thus, corresponding to 50µg pIL12/tumor per treatment [148].

Gene electrotransfer (GET) was performed with an ECM 830 Square Wave Electroporation System (BTX, Harvard Apparatus, MA) to deliver 5ms pulses [148]. Each treatment delivered 10 unipolar pulses at 60V/mm [148]. Parallel plate caliper electrodes, consisting of two adjustable plates, were coated with KY lubricant to ensure the electric field was delivered to the tumor without arching [148]. For GET treatments, pIL12 was injected into the tumor prior to ms electrical stimulation [148]. For the combination of NPS and GET (NPS-GET) treatments, the pIL12 was injected into the tumor before treating with the 100ns BL pulse conditions previously described and subsequent stimulation with ms pulses. This order of events

was shown to enhance gene delivery [149]. GET and NPS-GET treatment groups received three GET treatments on days 0, 3, and 7.

Data collection. Mice were weighed and tumors were measured twice a week with digital calipers until complete tumor clearance was observed or the mouse was euthanized. Tumor volumes were calculated by the following equation: $V=\pi ab^2/6$, where *a* is the longest diameter and *b* is the shortest diameter, perpendicular to *a*. All other experimental data was acquired via instrumentation according to protocols detailed within this manuscript.

Xenogen IVIS 100 Spectrum System. D-Luciferin, potassium salt (Gold Biotechnology, LUCK) was prepared at a concentration of 47mM, or rather 15mg/mL DPBS without Ca^{2+} and Mg^{2+} (Corning, 21031CV) according to the manufacturer. Mice with 4T1-Luc tumors were intraperitoneally injected with 10µL D-luciferin/g body weight for in vivo live imaging of tumors and detection of metastasis with Xenogen IVIS 100 Spectrum system (Caliper Life Sciences). Mice were imaged under anesthesia with 2-3% isoflurane approximately 15 min after receiving the injection before and after NPS treatment, and until complete tumor regression was observed or termination.

Section 3.5. Ex Vivo Tissues and Processing

As part of these investigations, mouse tissues were harvested and processed into single cells for flow cytometric analysis and/or subsequent isolation processes. These tissues included peripheral blood, lymph nodes, spleens, and tumors, which were processed according to the following methods.

Peripheral blood was collected via cardiac puncture, under 2.5-3% isoflurane anesthesia, with a 25-G needle and heparin coated syringe to mitigate coagulation while drawing the blood. At best, approximately 500-800µL of blood was collected via this method and used only when immediately followed by euthanasia via cervical dislocation. The blood was transferred into K_2EDTA coated tubes and inverted to ensure adequate mixing with the anticoagulant. Blood was either treated with Ammonium-Chloride-Potassium (ACK) RBC lysis buffer or layered onto Ficoll-Paque density gradient to remove, reduce and/or separate the RBC from the white blood cells. When ACK RBC lysis buffer was used, aliquots of blood less than 100µL were transferred into wells of a 96-well RBWP. About 200µL of ACK buffer was added and incubated for 3-7 min, monitoring the sample for clarity. Once the samples appeared more translucent, rather than opaque, they were centrifuged at 1200_{RCF} for 1 min at 23℃. Samples were wash with 200µL aliquots of BSS 2-3 times to remove the lysis buffer. The same centrifugation parameters were used throughout washing and antibody staining processes. When Ficoll-Paque was used to separate the blood cells, whole blood was layered onto 2-3mL of Ficoll-Paque in 5mL polystyrene tubes and centrifuged at 800_{RCF} for 10 min at 23℃ with the brake off. The white blood cell layer, referred to as the buffy coat, was carefully transferred into new polystyrene tubes for washing, counting, and staining.

Lymph nodes and/or tumor draining lymph nodes (LN/ dLN) were collected from euthanized mice and stored in RPMI-1640 on ice until processing. Lymph nodes were inserted into the open-end of micro-mesh pouches, made from 40 µm nylon mesh material. Single cells were obtained by teasing the cells through the mesh into RPMI-1640 or another suitable buffer. To ensure single cell suspension, as required for FC, the cells were filtered through a prewet sterile 40 µm filter (Falcon) and washed through with PBS into 50 mL conical tubes. Aliquots of

each sample were used for counting cells with FC, while the remaining were centrifuged at 800_{RCF} for 5-10 min at 23℃. The leukocytes were then suspended for subsequent processes, as previously described for blood. Mouse spleens were processed similarly to lymph nodes; additionally, ACK RBC lysis was often included.

Tumors were collected from euthanized mice and maintained in RPMI-1640 on ice until processing, mechanically and enzymatically. The Miltenyi Mouse Tumor Dissociation Kit (130-096-730) was used according to the manufacturer protocol for dissociating soft, B16-F10, and hard, 4T1-Luc, tumors (0.04–1 g). In short, tumors were sectioned into 2-4 mm pieces and placed into gentleMACS C Tubes (130-093-237, 130-096-334) with 2.35 mL of RPMI-1640, 100 µL of Enzyme D, 10 µL of Enzyme R (this was reduced from the original 50 µL volume to preserve lymphocyte populations as recommended by the manufacturer), and 12.5 µL of Enzyme A. The gentleMACS Octo Dissociator with Heaters was used to run program *37C_m_TDK_1* (B16-F10) or *37C_m_TDK_2* (4T1-Luc). Once complete, the cell suspensions were filtered through a prewet 70 µm sterile filter into a 50 mL conical tube, washed with 10 mL of RPMI-1640, and centrifuged at 300_{RCF} for 7 minutes. The supernatant was completely aspirated, and the cells were resuspended in 1-2 mL of BSS. Samples that appeared to have substantial amounts of RBC and/or tumor cells, were either treated with ACK RBC lysis buffer or subjected to further separation by Ficoll-Paque density gradient, as previously described.

Once tissues were processed into single cell suspensions, the number of cells were counted with FC and suspended at a concentration of 300,000 $<1x10^9$ cells/ 100µL, depending on subsequent FC staining and/or processing.

Section 3.6. Ex Vivo Cell Isolation Processes

Ex vivo isolation and preservation of HCB CD34+ HSC. Human umbilical cord blood (HCB) was obtained under written consent (unidentified specimen exemption) and collected in K_2·EDTA blood collection tubes to mitigate clot formation and maintained at 4℃. Within 24-hours of birth, samples were pooled for processing to circumvent inadequate reconstitution in NSG and/or NSG-SGM3 mice. The Human Umbilical Cord Blood CD34+ Cell Isolation Kit II (StemCell, 17896) from StemCell™ was used for isolating HCB CD34+ HSCs with several modifications to the manufacturers protocol. Initially, blood samples were carefully pooled and, when necessary, filtered through 200 µm and 40 µm sterile filters to ensure single cell suspension and removal of blood clots associated with decreased yields and sample purity. The pooled HCB was evenly distributed into 50 mL conical tubes and centrifuged at 300_{RCF} for 15 min at 4℃ with full acceleration and deceleration, i.e., brake on. This served as a preliminary method for limiting red blood cell (RBC) lysis often contaminating the mononuclear cell layer observed with strict adherence to the manufacturer protocol. Thus, this preliminary separation technique required the careful transfer of the buffy coat with aims of limiting RBC transfer and circumvent this contamination issue altogether. With such a significant decrease in RBCs, the volume of Pre-Enrichment Cocktail was decreased by at least half of that recommended by the manufacturer. Subsequent processing for HCB CD34+ HSC isolation adhered with the manufacturer's protocol. The isolated cells were cryopreserved in RPMI-1640 supplemented with 10% FBS and 5% DMSO to maintain viability. Isolated HSCs were slowly frozen to -80℃ and transfered for long-term storage under liquid nitrogen until experimental proceedings.

Murine CD4+ T cell isolation. The StemCell magnetic isolation kit for CD4+ T cells (StemCell, 19852) was used according to the manufacturer instructions except that they were isolated from

the LN and/or dLN, rather than the spleen. This not only simplified the procedure, since RBC and other cellular components were negligible, but facilitated gaining meaningful insights nearest the tumor. In short, dLN were processed into to single cell suspensions as previously detailed. The total cell count was obtained by flow cytometry and then the cells were suspended at $1x10^8$ nucleated cells/ mL before incubation with the kit components and subjection to magnetic separation, whereby the undesired cells were positively selected for by the magnet and the CD4+ T cells were negatively obtained in the eluent. The purity of the CD4+ T cells was checked with flow cytometry (Figure 6) before preparing them for Seahorse XFA.

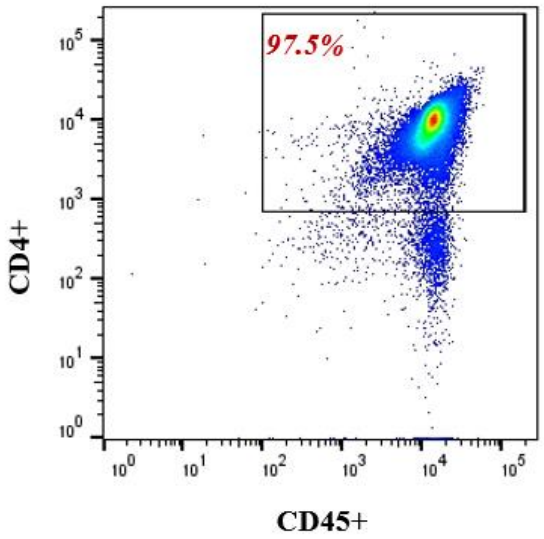

Figure 6. Purity of magnetically isolated CD4+ T cells. This representative pseudocolor flow cytometry plot indicates the isolated CD4+ T cells were obtainable with a high level of purity with a 97.5% double positive CD45+ CD4+ population. This FC plot was produced with FlowJo™ Software (Windows) Version 10 (Ashland, OR: Becton, Dickinson and Company; 2019).

Section 3.7. Flow Cytometry and Antibodies

Flow cytometry buffer preparation. Balanced salt solutions (BSS) were prepared for use with sample preparation and flow cytometry. BSS-A, 20x, was prepared by combining 20g glucose, 1.2g KH_2PO_4, and 3.8g Na_2HPO_4 with 1 L of milliQ water followed with 0.22 µm vacuum filtration. BSS-B, 20x, was prepared by combining 3.8g $CaCl_2{\cdot}2H_2O$, 8.0g KCl, 160.0g NaCl, 4.0g $MgCl_2{\cdot}6H_2O$, and 2.0g $MgSO_4$ with 1 L of milliQ water and autoclaved. The working buffer, BSS, 1x, was prepared by combining 50 mL BSS-A, 50 mL BSS-B, 20 mL FBS, and 1g

NaN_3 (sodium azide) with 1 L of milliQ water, and filtering with sterile 0.22µm 500mL Vacuum Filter/Storage Bottle Systems (Corning, 431097). The pH of all three buffers were adjusted to 7.2 prior to sterilization and were stored at 4℃.

Miltenyi MacsQuant Analyzer 10 flow cytometer. A Miltenyi MacsQuant Analyzer 10 flow cytometer was used for flow cytometric data acquisition. FlowJo™ Software (Windows) Version 10 (Ashland, OR: Becton, Dickinson and Company; 2019) was used for analyzing flow cytometric data.

Antibodies and staining for FC. Fluorescently conjugated antibodies (AB) were used to phenotypically distinguish leukocyte populations in murine and human tissues. Prior to experimentation, antibodies were titrated to determine the dilution ratio for proper staining. A 1:100 dilution ratio was found to provide appropriate levels of fluorescence detection and applicable for use with all antibodies; while many antibodies provided adequate detection at even lower dilutions (1:400), employment of a single dilution aided in maintaining a consistent workflow. AB master mixes (AB-MM) were previously prepared by combining the AB with the volume of BSS required for staining all samples in an experiment to maintain consistency.

The anti-mouse antibodies included: Brilliant-Violet 510-CD3 (BioLegend Cat# 100233, RRID:AB_2561387), APC-CD3 (BioLegend Cat# 100235, RRID:AB_2561455), FITC-CD4 ((Miltenyi Biotec Cat# 130-120-819, RRID:AB_2752205) (BioLegend Cat# 100406, RRID:AB_312691) (Miltenyi Biotec Cat# 130-120-819, RRID:AB_2752205)), PE/Cy7-CD4 (BioLegend Cat# 100421, RRID:AB_312706), APC-CD4 ((Miltenyi Biotec Cat# 130-123-207, RRID:AB_2811460) (BioLegend Cat# 100411, RRID:AB_312696)), APC-CD8a ((BioLegend Cat# 100712, RRID:AB_312751) (Miltenyi Biotec Cat# 130-102-540, RRID:AB_2659887)),

APC/Cy7-CD8a ((BioLegend Cat# 100714, RRID:AB_312753) (BioLegend Cat# 100713, RRID:AB_312752), APC-Vio770-CD8a (Miltenyi Biotec Cat# 130-102-305, RRID:AB_2659897), PE-CD11b ((BioLegend Cat# 101207, RRID:AB_312790) (BioLegend Cat# 101208, RRID:AB_312791)), PE-Vio770-CD11b (Miltenyi Biotec Cat# 130-113-236, RRID:AB_2726046), VioBlue-CD11c (Miltenyi Biotec Cat# 130-102-413, RRID:AB_2660158) (Miltenyi Biotec Cat# 130-102-797, RRID:AB_2660157), FITC-CD14 (BD Biosciences Cat# 561710, RRID:AB_10896324), APC-CD25 (BioLegend Cat# 102012, RRID:AB_312861), FITC-CD27 (BioLegend Cat# 124207, RRID:AB_1236463), PE-CD38 (Miltenyi Biotec Cat# 130-102-607, RRID:AB_2657877), APC-CD40 (Miltenyi Biotec Cat# 130-102-547, RRID:AB_2660762), VioBlue-CD44 (Miltenyi Biotec Cat# 130-116-531, RRID:AB_2727594), VioGreen-CD45 (Miltenyi Biotec Cat# 130-110-803, RRID:AB_2658224), PerCP/Cy5.5-CD62L ((BioLegend Cat# 104432, RRID:AB_2285839) (BioLegend Cat# 104431, RRID:AB_2187123)), VioBlue-CD68 (Miltenyi Biotec Cat# 130-112-861, RRID:AB_2659027), APC-Vio770-CD80 (Miltenyi Biotec Cat# 130-116-463, RRID:AB_2727560), PE/Cy7-CD86 ((BioLegend Cat# 105013, RRID:AB_439782) (BioLegend Cat# 105014, RRID:AB_439783)), APC/Cy7-CD86 (BioLegend Cat# 105029, RRID:AB_2074993), PE/Cy7-CD127/ IL-7Rα (BioLegend Cat# 135014, RRID:AB_1937265), PerCP-Vio700-CD161/NK1.1 (Miltenyi Biotec Cat# 130-103-963, RRID:AB_2660599), PE-CD279/ PD-1 (BioLegend Cat# 135206, RRID:AB_1877231), PE-Vio770-CD314/ NKG2D (Miltenyi Biotec Cat# 130-102-730, RRID:AB_2657380), VioBlue-CD335/ NKp46 (Miltenyi Biotec Cat# 130-112-365, RRID:AB_2657606), PerCP-Vio700-F4/80 (Miltenyi Biotec Cat# 130-102-161, RRID:AB_2651711), APC/Cy7-Gr-1/ Ly-6G/ Ly-6C (BioLegend Cat# 108424, RRID:AB_2137485), FITC-IA-IE/ MHC II (Miltenyi Biotec Cat# 130-102-168,

RRID:AB_2660054), and 0.125 µg APC-Erg2 (Thermo Fisher Scientific Cat# 17-6691-82, RRID:AB 11151502).

The anti-human antibodies included: VioBlue-CD3 (Miltenyi Biotec Cat# 130-114-519, RRID:AB_2726687), VioGreen-CD33 (Miltenyi Biotec Cat# 130-111-025, RID:AB_2657563), FITC-CD4 (Miltenyi Biotec Cat# 130-114-531, RRID:AB_2726690), PE-CD34 (Miltenyi Biotec Cat# 130-113-179, RRID:AB_2726006), PerCP-Vio700-CD19 (Miltenyi Biotec Cat# 130-114-174, RRID:AB_2726478), PE-Vio770-CD45 (Miltenyi Biotec Cat# 130-110-634, RRID:AB_2658249), APC-CD8 (Miltenyi Biotec Cat# 130-110-679, RRID:AB_2659237), and APC-Vio770-CD90 (Miltenyi Biotec Cat# 130-114-863, RRID:AB_2726814).

For cell surface labeling, cells were suspended at concentrations between $0.1 < 1.5x10^6$ cells in 20 < 100 µL AB-MM and incubated for 15 min at 4℃, protected from light. Then, samples were washed three times with BSS to remove excess AB and resuspended at their original concentration. For fixing non-intracellularly stained samples, an additional aliquot of 4% paraformaldehyde was added at equal volume. For intracellular staining, cells were fixed after cell surface staining and permeabilized using the Foxp3 Staining Buffer Set (Thermo Fisher Scientific, 00-5523-00) according to the manufacturer protocol, then cells were intracellularly stained as required.

Section 3.8. Seahorse Extracellular Flux Analyses

The Seahorse Extracellular Flux Analyzer Mini (SH-XFA; Agilent Technologies, USA) was used for examining the NPS-induced effects on metabolism in immune cells. The isolated immune cells were plated at a concentration of 400,000 cells/ 100 µL in Seahorse XF HS poly-D-

lysine (PDL) miniplates and incubated at room temperature for approximately 10 min to allow cells to settle into a monolayer. To ensure cells adhered to the PDL-coated mini plate, they were centrifuged at 300_{RCF} for 5 min at 23℃. The remaining steps were carried out according to the manufacturer protocol for the Seahorse XF Glycolysis Stress Test Kit (Agilent, 103017-100) and/or Seahorse XF Cell Mito Stress Test Kit (Agilent, 103010-100). Data Analysis was performed using Agilent's cloud-based data analysis software, Seahorse Analytics (https://seahorseanalytics.agilent.com) (Agilent Technologies, USA).

Section 3.9. Statistical Analyses

FlowJo™ Software (Windows) Version 10 (Ashland, OR: Becton, Dickinson and Company; 2019) was used for analyzing flow cytometric data. All experiments were conducted at least three times and data were expressed as mean ± standard error (S.E.). The Student's t-test was used to analyze statistical differences between groups. P-values were calculated with MedCalc Software Ltd. Comparison of means calculator, https://www.medcalc.org/calc/comparison_of_means.php (Version 20.014; accessed 2019-2021) and were considered significant when $p \leq 0.05$ and/or as indicated within the figure legend. GraphPad Prism version 9.2.0 for Windows, GraphPad Software, San Diego, California USA, www.graphpad.com, was used to conduct statistical analyses of Kaplan-Meier survival curves as well as one-way and/or two-way analysis of variance (one-way or two-way ANOVA).

Section 3.10. Human Subjects Protection

As required by federal regulations (45 CFR 46) and NIH policy, the following statements aim to disclose human subject involvement in this investigation. Human subject involvement was limited to *unidentifiable biospecimens*, including human umbilical cord derived blood. No personal health information was obtained with the specimens. There were no human risks associated with this investigation as the collected tissues would have otherwise been discarded following standard operating procedures. A subject consent form was provided and explained to all participants: Adverra IRB Approval Version 24 Jan 2019. While there were no direct benefits to the participants, we hope that the information gained will help those with cancer in the future.

Section 3.11. Inclusion of Woman and Minorities

Human umbilical cord blood was collected from females at the time of birth without regard for race and/or ethnicity. The nature of this investigation required employment of women and minority populations.

Section 3.12. Vertebrate Animals

Ethics statement. These studies were carried out in strict accordance with the recommendations in the Guide for the Care and Use of Laboratory Animals of the National Institute of Health. The protocols were approved by the Old Dominion University Institutional Animal Care and Use Committee (protocol no. 16-018, 16-024, 16-028, 18-008, 19-018, and 19-030). All blood collections, surgeries, injections, and treatments were performed while mice were under

continuous 2-3% isoflurane in oxygen anesthesia, and all efforts were made to minimize any pain, distress, and/or suffering. Specifically, mice were monitored by Sobran Inc. vivarium staff and humanely euthanized when (1) a loss of 10% bodyweight was observed, (2) tumor burden approached 1500 mm^3, or (3) when the outermost tumor epithelium became ulcerated.

Analgesics and antibiotics. Balb/cJ and/or C57BL/6J mice were given a 50 µL subcutaneous injection of carprofen (branded name, Rimadyl), proportional to approximately 5 mg/kg body weight, as a non-steroidal anti-inflammatory drug for minimizing pain and/or discomfort on the day of treatment and 1/day as needed for up to 3 days after. The carprofen was freshly prepared at a 1:10 dilution in warm saline. Hu-mice did not receive carprofen as this could be detrimental to the engrafted human immune system and post-treatment pain associated with NPS treatments was minimal. All mice were monitored for post-operative/treatment recovery and returned to their respective mouse suites when normal behavior was observed, i.e., grooming, eating, drinking, etc.

NSG and/or NSG-SGM3 mice were given 8 mg/kg bupivacaine, a local anesthetic, via subcutaneous injection near the injection site when interfemoral delivery of HCB CD34+ HSC was employed in the humanization process [167-173]. To circumvent adverse effects of sublethal irradiation, mice received Baytril, an antimicrobial, in their drinking water, dosed at 25.5 mg/kg body weight for 3-5 days before and 2-weeks after humanization [167,168]. Humanization refers to the process of reconstituting NSG and/or NSG-SGM3 mice with a human immune system (HIS).

Survival surgeries. For survival surgeries, mice were first placed into an induction chamber charged with a 3-5% isoflurane in oxygen for several minutes to ensure sedation. Then mice were fitted with a standard rodent mask and kept under general anesthesia using 2-3% isoflurane.

Surgeries were performed on a heated surgical table and/or warming pad to maintain body temperature throughout the procedure and into recovery. Carprofen was administered subcutaneously at 5 mg/kg within 15-min prior to the surgical procedure and for up to 3-5-days after as needed depending on observations of pain and/or distress.

The tumor region was prepared for excision by shaving and/or briefly treating the region with Nair to remove fur prior to thoroughly cleansing the skin with two 1 min alcohol and Betadine swabs. Sterile surgical Killner scissors were used to make an incision, about 10mm long, into the epidermis near the tumor. Then, the scissors were inserted between the epidermal and subcutis tissue and gently opened to reveal the tumor tissue within the subcutaneous pocket. Mcpherson angled forceps were used to retrieve tumor sections. Once the tumor was removed, the skin was closed with 3-5 sutures and VetBond.

After surgery, mice were kept warm and monitored for recovery. They were returned to their respective mouse suites when they were alert and normal behavior was observed, i.e., grooming, eating, drinking, etc. Postoperative statuses and wound healing were monitored daily for the first week.

Endpoints. Mice were closely monitored to ensure that there were no untoward effects as defined by the body analysis criteria that is “not healthy”. Unhealthy was defined as any condition that resulted in (a) a loss of 8-12% of body weight, unkempt and/or dull fur, (2) unclear, sunken and/or protruding eyes, (3) hypoactivity, and (4) isolation from cage mates. Additionally, unhealthy tumor burden included (1) volumes of about 1500mm^3 and (2) ulceration of the outermost epithelium. The veterinarian was consulted for appropriate treatments whenever applicable. All mice deemed unhealthy by these determinants were humanely euthanized.

Euthanasia. Mice were euthanized by cervical dislocation under heavy anesthesia, 3% isoflurane, whenever tissue recovery was necessary. Thoracotomy served as the secondary measure of euthanasia. Alternatively, mice were exposed to 20% CO_2 per minute until eyes were fixed and mice remained motionless for approximately 5-min. Cervical dislocation was the means of secondary euthanasia.

CHAPTER IV

RESULTS

Section 4.1. The mPTP is a Sensor of NPS

NPS induces Ca^{2+}-dependent, CsA sensitive dissipation of $\Delta\Psi_m$ in H9C2 cells. NPS-induced dissipation of the $\Delta\Psi_m$ was previously demonstrated to be primarily Ca^{2+}-dependent [25,32]. Since membrane permeabilization is Ca^{2+}-independent and Ca^{2+}-mechanisms are most often mediated by proteins, we suggest that the NPS-induced loss of $\Delta\Psi_m$ is likely due to effects on proteins, including the elusive constituents of the mPTP [32]. This poses a likely scenario for NPS as it could potentially affect the voltage sensitive components like the voltage-dependent anion channel (VDAC) and ATP-synthase, which remain central to many investigations for their potential role(s) in regulating the mPTP [127]. Previously, we tested agents that modulate several possible components of the mPTP, including 4,4-diisothiocyanatostilbenedisulphonic acid (DIDS) to inhibit VDAC, bongkrekic acid to inhibit adenine nucleotide translocase (ANT), and CsA to inhibit CypD, and found that none of these appeared to alter the effects of NPS on the $\Delta\Psi_{m[32].}$ While the ambiguity of the mPTP constituents remains debated, a well vetted, well accepted, regulator has been identified as a Ca^{2+}-dependent protein, CypD [174]. CypD plays the role as a principal monitor of mitochondrial function, regulating and regulated by mitochondrial function [119,175]. Furthermore, CypD has several binding partners, including ANT, phosphate carrier (PiC), and oligomycin sensitivity conferral protein (OSCP), which supports the hypothesis that CypD modulates the mPTP through ATP synthase [119,175,176]. The most recent models for the mPTP propose monomeric and dimeric ATP synthases form the pore, albeit both require vetting [128,177,178]. Since CypD regulates the mPTP and ATP synthase,

these CypD sensors could have matching identities. Nevertheless, given that CypD's Ca^{2+}-dependence could be lost at saturated Ca^{2+} concentrations, we determined the Ca^{2+} dose-dependent effects of NPS-induced loss of $\Delta\Psi_m$ in the presence and absence of CsA, a well-characterized inhibitor of CypD, using highly aerobic, mitochondria rich, H9C2 rat cardiomyoblasts.

Figure 7 shows a detailed approach as we increased the calcium concentration in the presence and absence of CsA and determined the effects of NPS on the $\Delta\Psi_m$ in H9C2 cells. In preliminary experiments (not shown), NPS conditions with 60 ns durations and 40 kV/cm induced a pulse number dependent decrease on $\Delta\Psi_m$ in the presence of calcium. The results of several experiments are displayed under the NPS parameters (25, 60 ns, pulses at 40 kV/cm, 0.012 V·s/cm), such that about 75% of the cells would lose $\Delta\Psi_m$ in the presence of calcium. Concentrations of calcium were increased as indicated, ranging from 0 µM to 1800 µM, and the effects of NPS on the $\Delta\Psi_m$ were determined in the presence or absence of CsA. Increasing the concentrations of calcium induced progressive loss of $\Delta\Psi_m$, further defining the Ca^{2+}-dependence for loss of $\Delta\Psi_m$; however, in the presence of CsA, the loss of $\Delta\Psi_m$ was significantly inhibited. These experiments demonstrated the Ca^{2+}-dependent, CsA-sensitive dissipation of $\Delta\Psi_m$, which are precise diagnostics for NPS effects on CypD as a mPTP regulator.

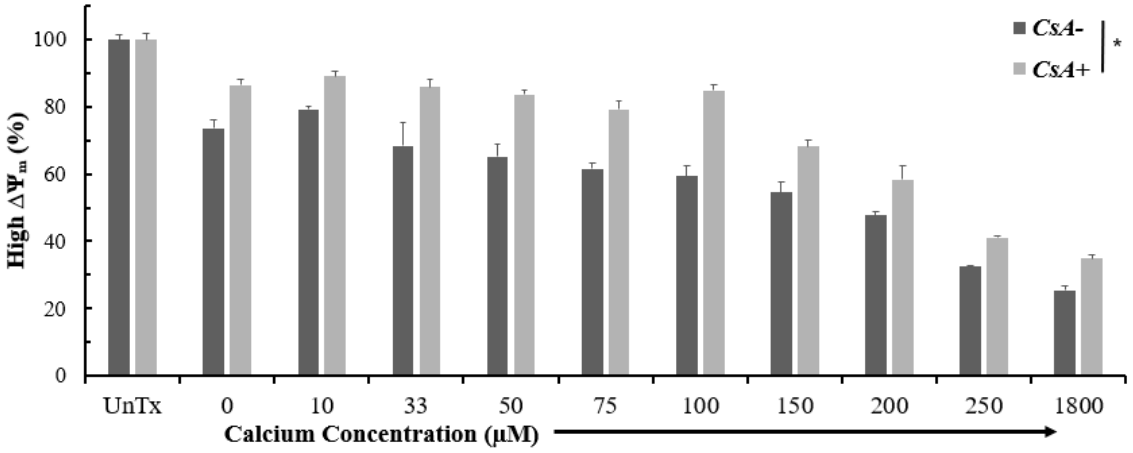

Figure 7. NPS-induced dissipation of $\Delta\Psi_m$ is calcium dependent and CsA sensitive in H9C2 cells. Cells were treated with 25, 60 ns pulses at 40 kV/cm in increasing concentrations of calcium (0-1800μM Ca^{2+}) with and without CypD inhibition with 5 μM CsA. Data values were normalized to untreated controls and represent the mean ± SE (n=9). The two-way ANOVA was performed using GraphPad Prism version 9.2.0 for Windows, GraphPad Software, San Diego, California USA, www.graphpad.com, and indicated significance (*), $p<0.000002$.

NPS induces Ca^{2+}-dependent increases in ROS in H9C2 cells. The second hit of the 'two-hit' hypothesis, as previously discussed, considers the roles of the Ca^{2+}-dependent mechanism(s) and mROS generation on NPS-induced mitochondrial sensitization [179,180]. NPS has been shown to induce increases in ROS in several cell types using nonspecific ROS detectors such as H2DCFDA (dichlorodihydrofluorescein diacetate) and carboxy-H2DCFDA (carboxy-2',7'-dichlorofluorescein diacetate), as well as with more specific detectors like Amplex-Red (N-

acteyl-3,7-dihydroxyphenoxazine), which detects H_2O_2, and DHE (dihydroethidium), which may be primarily sensitive to superoxide radicals [25,181]. NPS was also shown to induce ROS in a Ca^{2+}-dependent manner in human pancreatic cancer cells (BcPC-3) using carboxy-H2DCFDA [46]. While some of these detectors may sense ROS unselectively in mitochondria, we used MitoSOX-Red (MSOX), a DHE that contains a triphenylphosphonium moiety that increases mitochondrial accumulation of the compound [182]. However, like DHE, MSOX may not be as specific to sole detection of superoxide radicals [156,182,183]. To circumvent issues with nonspecific staining, MSOX was titrated before using it to determine if NPS-induced mROS in H9C2 cells [156]. We treated cells by increasing the number of applied pulses with 60ns durations at 40 kV/cm with or without calcium. These results indicate that NPS-induced Ca^{2+}-dependent increases in mROS (Figure 8). In the absence and presence of calcium, mROS increased by about 20% and 75%, respectively, compared to the untreated cells. The Ca^{2+}-dependent increase of mROS tended to be higher at lower pulse numbers. For example, with delivery of 20 and 50 pulses, the Ca^{2+}-dependent increase in mROS was about 65% and 42% respectively. This difference could be because there is a limit to calcium induction, perhaps based on saturation of the Ca^{2+}-mediated mechanism(s), while the NPS-induced mechanisms by themselves continue to increase with pulse number.

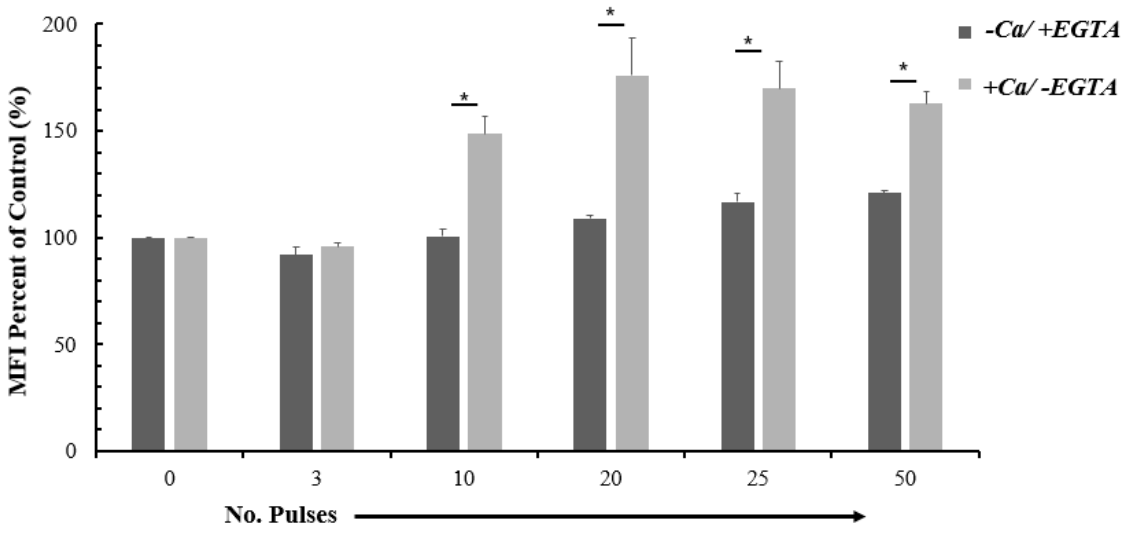

Figure 8. NPS induced mROS in H9C2 cells in a calcium and dose dependent manner. Cells were treated with 60ns pulses at 40 kV/cm with increasing pulse number from 0 to 50, with and without the presence of calcium. Data values were normalized to untreated controls and represent the mean ± S.E. (n=3). The unpaired t test was performed using GraphPad Prism version 9.2.0 for Windows, GraphPad Software, San Diego, California USA, www.graphpad.com, and indicated significance (*), $p<0.000002$.

NPS induced loss of ΔΨm requires both calcium and ROS. The NPS-induced dissipation of the $\Delta\Psi_m$ in H9C2 cells was Ca^{2+}-dependent (Figure 7); however, because calcium necessary although not sufficient, for decreasing the $\Delta\Psi_m$, another component remains undefined. Since the elevation of mROS in H9C2 cells in response to NPS is Ca^{2+}-dependent (Figure 8), we determined the dual effects of NPS on mROS and $\Delta\Psi_m$ in H9C2 cells. As shown in Figure 9, the dissipation of the $\Delta\Psi_m$ and increase in mROS are inversely proportional with increased pulsed

number. Taken together, these studies show that NPS opens the mPTP by sensitizing CypD to calcium and mROS. Furthermore, the effects on the $\Delta\Psi_m$ are abrogated by calcium chelation and NPS induces mROS accumulation only in the presence of calcium.

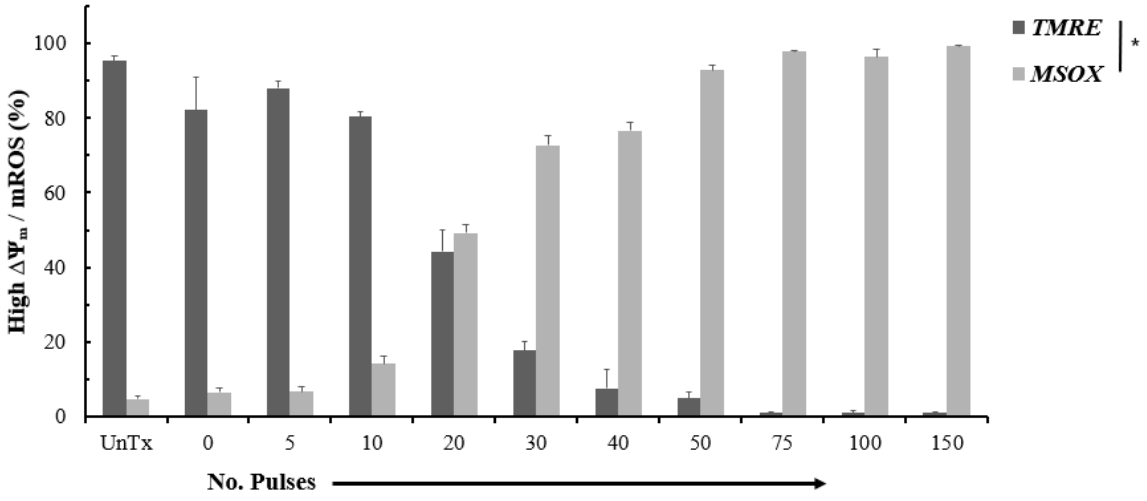

Figure 9. Dose dependence of NPS induced dissipation of $\Delta\Psi_m$ and mROS generation. NPS induced the dissipation of $\Delta\Psi_m$ and mROS generation in H9C2 cells in a dose dependent manner. The $\Delta\Psi_m$ and mROS generation were probed with TMRE and MitoSOX-Red, respectively. Cells were treated with 60 ns pulses at 60 kV/cm by increasing the number of pulses. Since $\Delta\Psi_m$ dissipation and mROS generation are Ca^{2+}-dependent, cells were treated in the presence of calcium. The values from each point represent the mean $\pm$ S.E. (n=3). The two-way ANOVA was performed using GraphPad Prism version 9.2.0 for Windows, GraphPad Software, San Diego, California USA, www.graphpad.com, and indicated significance (*), $p<0.000002$.

Section 4.2. In Vivo: The Murine Breast Cancer Model

BVM in the 4T1-Luc cancer model. The 4T1-Luc breast cancer model was used to compare the treatment efficacy between the 100ns BL pulser with the 200ns BL pulser and 200ns MOSFET, in experiments referred to as BL versus MOSFET (BVM). Tumors were initiated by inoculating the left mammary fat pad (MFP) of female Balbc/J mice with $1x10^6$ 4T1-Luc cells about 10-days prior to treatment with NPS. The Xenogen IVIS 100 Spectrum system was used for capturing in vivo live images (Figure 10) of the tumors by injecting the Balbc/J mice, interperitoneally, with 10µL D-luciferin/g body weight and capturing bioluminescence images after 15 minutes. The region of interest (ROI) was drawn to circle the tumors and the luminescence, measured in radiance ($p/sec/cm^2/sr$), provided preliminary insights into the tumor burden, including detection of metastasis. Those with stable primary tumors and no signs of metastasis at the time of pre-treatment imaging, usually 1-day prior, were placed into treatment groups by evenly distributing tumor volumes. After treatment, IVIS live imaging was used to examine the tumor statuses, i.e., progression or regression. For the 100ns BL and 200ns BL NPS treatment groups, tumor clearance was typically observed within the first week or two, as evident by lack of luminescence and scab formation. Mice that successfully cleared the primary tumors after NPS treatment were challenged 7-weeks later. At that time, imaging was used to confirm complete primary tumor clearance before initiating the challenge tumor via injecting $5x10^5$ 4T1-Luc cells into the opposite (right) MFP. IVIS live imaging was then used to examine the progression and/or rejection of the second tumor inoculant, the outcome of which, was usually evident within the first week or two.

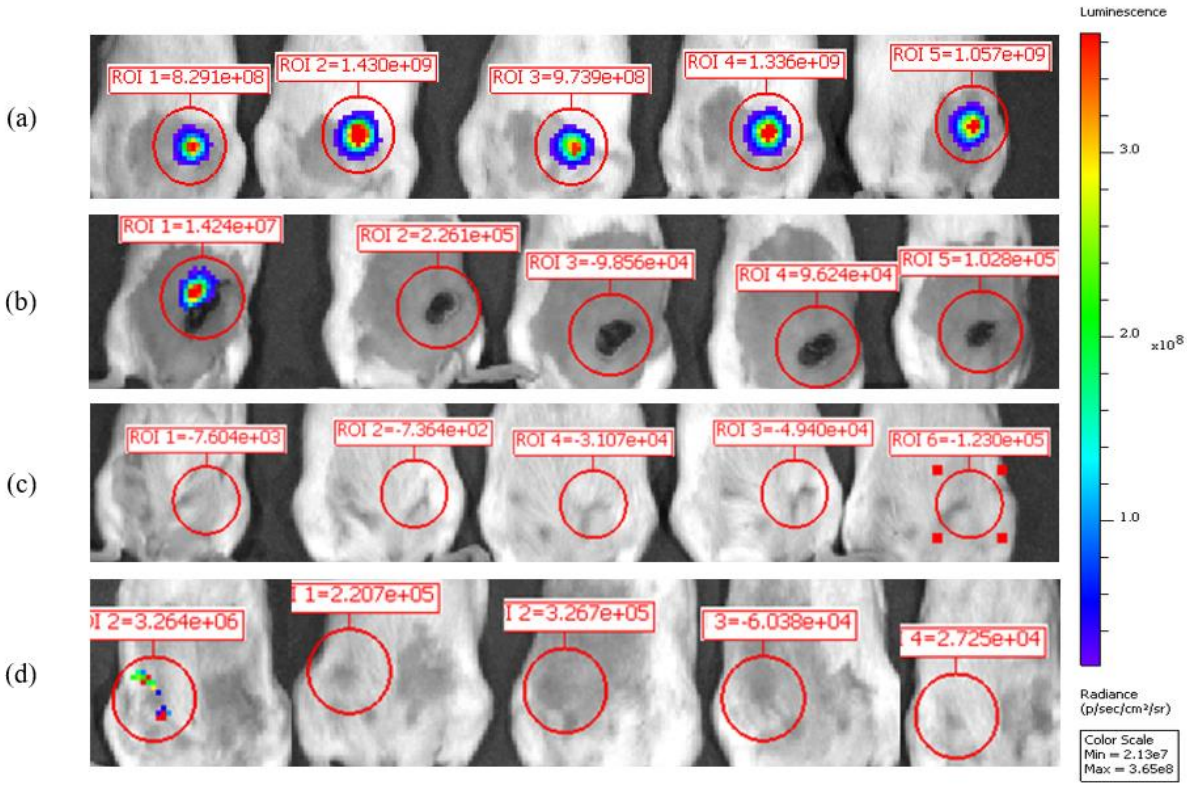

Figure 10. Representative IVIS live imaging of 4T1-Luc tumors in the BVM model. The 4T1-Luc tumors were visualized by intraperitoneally injecting Balbc/J mice with 10µL D-luciferin/g body weight and capturing bioluminescence images after 15 minutes with Xenogen IVIS 100 Spectrum system (Caliper Life Sciences). The representative images were obtained (a) before and (b) after, 1-week, treatment with NPS. Mice that successfully cleared the primary tumor after NPS were challenged with a second inoculant of $5x10^5$ 4T1-Luc cells 7-weeks later. The Xenogen IVIS 100 Spectrum system was used to capture images shortly (c) before and (d) 1-week after the challenge to examine tumor progression and/or rejection. Luminescence was measured in radiance (p/sec/cm^2/sr), as indicated for each tumor region of interest (ROI).

The primary 4T1-Luc tumor volumes were also obtained before treatment, for group distribution, and after treatment to monitor their statuses for regression and clearance or progression and increasing tumor burden. The primary 4T1-Luc tumor volumes were plotted for each treatment group from the day of treatment (day 0), as displayed by the tumor growth curves in Figure 11. For all NPS treatment parameters, tumor regression was observed following NPS. The 100ns BL (n=12) and 200ns BL (n=9) NPS parameters were successful (100%) at inducing complete tumor regression and clearance, usually within the first 2-3-weeks. While those successfully treated with the 200ns MOSFET (n=9) NPS parameters cleared tumors (67%) within the same time frame as the Blumlein treatment groups, others were unsuccessful (3:9) at clearing the treated tumor, reaching tumor burden within 38 days of treatment.

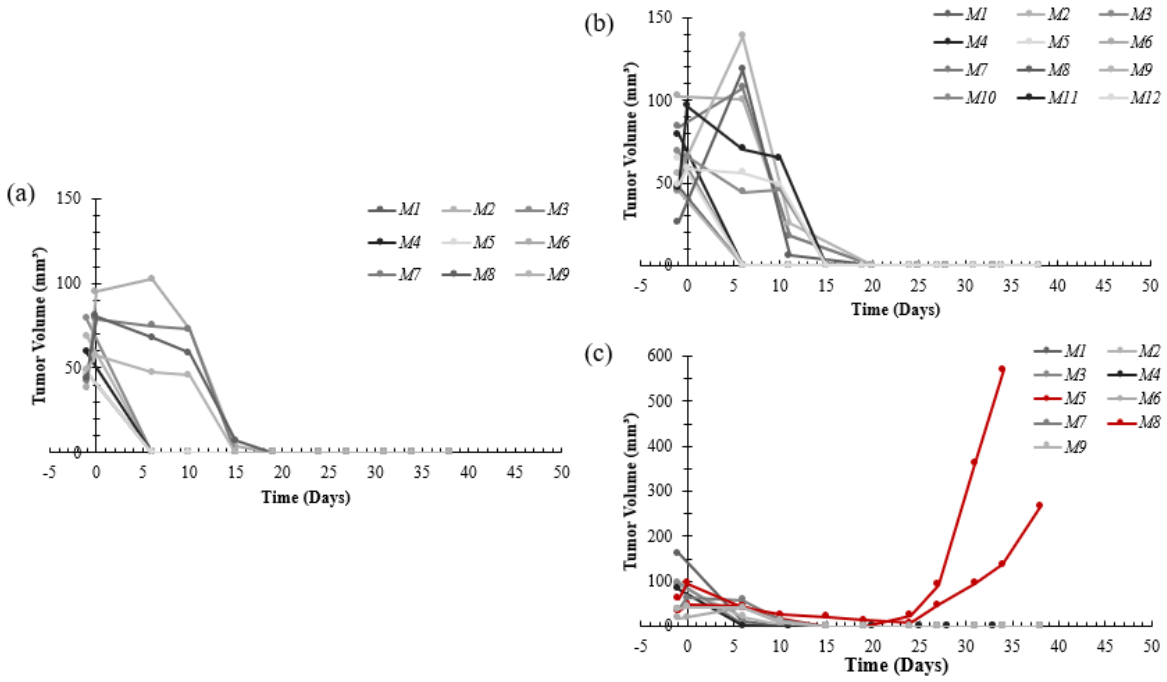

Figure 11. 4T1-Luc BVM model primary tumor growth curves. Balbc/J mice were inoculated with $1x10^6$ 4T1-Luc cells 10-days before the day of treatment (day 0). The day before treatment, the tumors were measured, and mice (M) were divided into treatment groups such that the average tumor volumes were evenly distributed. The NPS treatment groups included those treated with the (a) 100ns Blumlein line (BL) pulser (n=12), (b) 200ns BL pulser (n=9), and (c) 200ns MOSFET pulser (n=9). Tumors that regressed are displayed in the grey monochromatic scheme, while those that progressed after NPS treatment are shown in red.

In this BVM challenge model, the Balbc mice that successfully cleared the primary NPS treated tumors were challenged with a second inoculant of $5x10^5$ 4T1-Luc cells in the opposite MFP (right) about 7-weeks later. An age-matched untreated group of naïve Balbc mice was employed at this time for comparison with the NPS treatment groups and to ensure cellular viability. The resultant 4T1-Luc tumor growth curves were plotted for the untreated (n=15) group and the 100ns BL (n=12), 200ns BL (n=9), and 200ns MOSFET (n=6) NPS treatment groups from the day of the challenge inoculation (Figure 12). While tumor progression was observed for all untreated controls (15:15), tumor progression was often rejected by mice previously treated with NPS, indicating that NPS induced a vaccine-like effect on immunity. Interestingly, the unprotected 100ns BL (4:12) and 200ns MOSFET (2:6) NPS treated mice developed tumors similarly to the untreated mice, while impeded tumor progression was observed in the unprotected mice previously treated with the 200ns BL (2:9) NPS parameters.

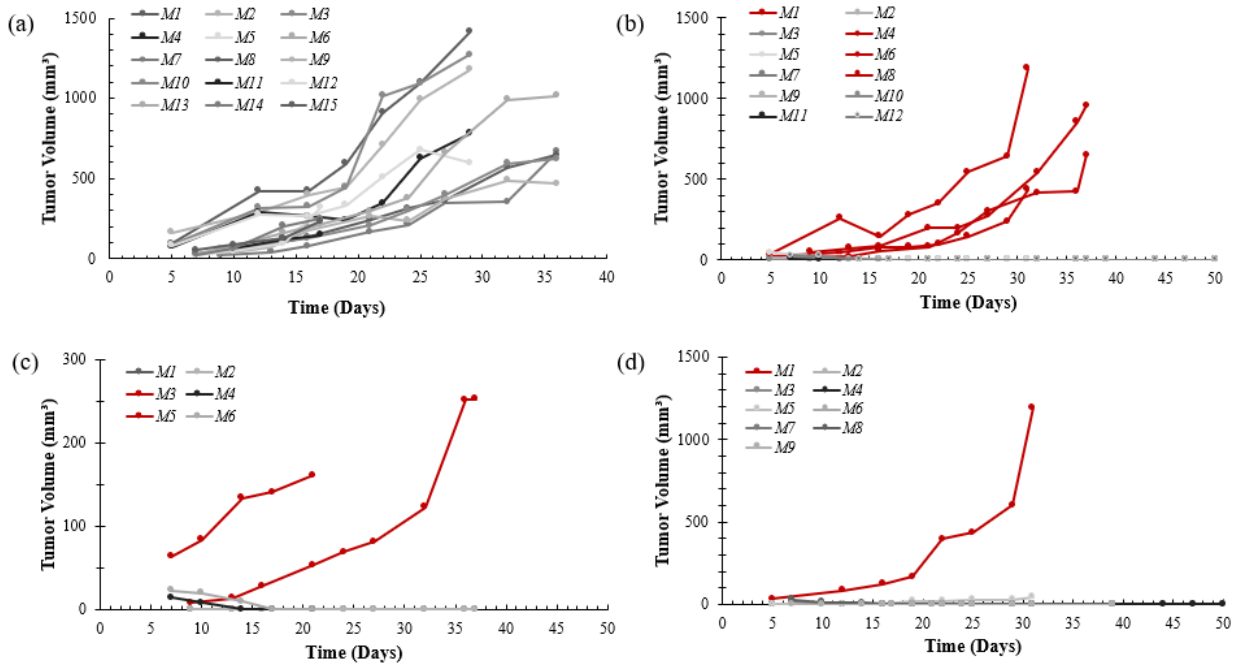

Figure 12. 4T1-Luc BVM model challenge tumor growth curves. The Balbc/J mice that successfully cleared the primary tumors after NPS treatment were challenged with a second inoculation of $5x10^5$ 4T1-Luc cells into the opposite MFP (right) about 7-weeks after NPS treatment. An age-matched group of naïve Balbc/J mice were employed as untreated controls at this time to ensure cellular viability. The resultant tumor volumes in mice (M) for the (a) untreated (n=15), (b) 100ns BL (n=12), (c) 200ns BL (n=9), and (d) 200ns MOSFET (n=6) treatment groups were plotted from the day of the challenge inoculation (day 0). Tumors that regressed are displayed in the grey monochromatic scheme, while those that progressed after NPS treatment are shown in red.

The treatment efficacy of NPS was also considered in terms of survival of the Balbc/J mice in the 4T1-Luc BVM model. Kaplan-Meier probability/ percent of survival curves for the 100ns BL (n=12), 200ns BL (n=9), and 200ns MOSFET (n=9) NPS treatment groups and for the untreated (n=15) control group of the 4T1-Luc BVM model were examined with GraphPad Prism software (Figure 13). The log-rank (Mantel-Cox) and Gehan-Breslow-Wilcoxon tests were performed to determine the p-values between and among groups. For the null hypothesis, this was less than 0.0001, which indicated significance among the 4T1-Luc BVM groups. The significance level was set using the Bonferroni method to compare the multiple pairs of BVM groups. Since we previously defined significance as $p<0.05$, and there were 8 comparisons, the Bonferroni-correction threshold for these analyses was $p<0.0063$. Therefore, the differences between the untreated control group and each NPS treatment group were considered statistically significant using the family-wise significance level of 5%. Comparisons between NPS treatment groups were not considered significant by these measures.

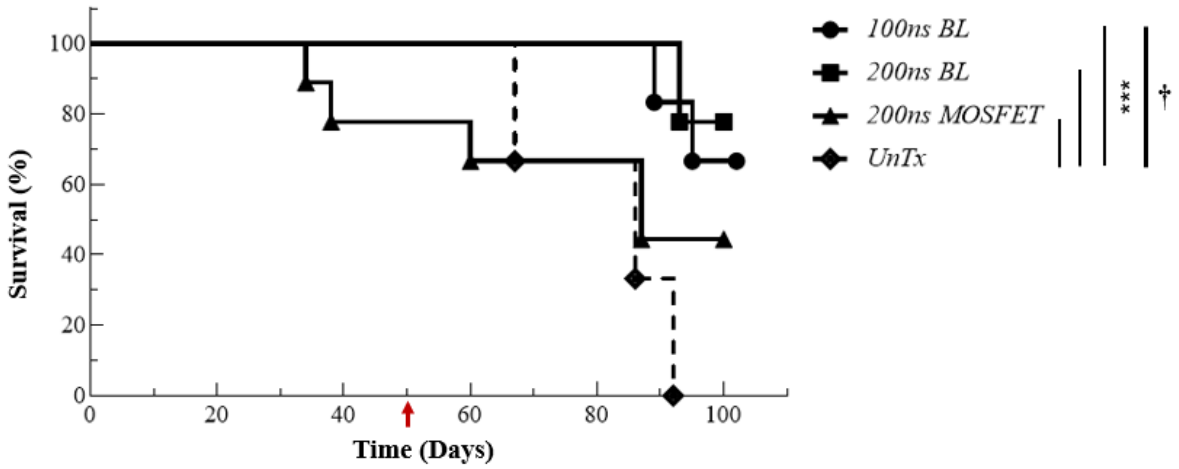

Figure 13. 4T1-Luc BVM model Kaplan-Meier survival curves. Tumors were initiated in Balbc/J mice via inoculation of $1x10^6$ 4T1-Luc cells into the left mammary fat pad (MFP) 10-days before the day of treatment (day 0). The mice were placed into treatment groups such that the average tumor volumes were evenly distributed. The NPS treatment groups, indicated as solid black lines, included those treated with the 100ns Blumlein line (BL) pulser (round markers), the 200ns BL pulser (square markers), and the 200ns MOSFET pulser (triangle markers). Mice that successfully cleared the primary tumor after NPS and survived were challenged with a second inoculation of $5x10^5$ 4T1-Luc cells into the opposite (right) MFP about 7-weeks later (red arrow) and monitored for an additional 7-weeks. An age-matched untreated control group (dashed line, diamond marker) (n=15) was included at that time to ensure viability of the 4T1-Luc cell inoculant. The log-rank (Mantel-Cox) and Gehan-Breslow-Wilcoxon tests were performed using GraphPad Prism version 9.2.0 for Windows, GraphPad Software, San Diego, California USA, www.graphpad.com, and the null hypothesis (†) was significant, $p< 0.0001$. The family-wise significance level of 5%, using the Bonferroni-corrected threshold method for p-values, indicated significance between groups (*), $p<0.0063$.

The survival ratios and percentages were also examined after treatment and after the challenge for the 4T1-Luc BVM model (Table 3). In this manner, the survival percentages account for the number of mice remaining 7-weeks after NPS and were available to challenge. The 100ns BL (12:12) and 200ns BL (9:9) NPS parameters were most efficient at inducing primary tumor clearance as evident by 100% survival after treatment. Although the parameters of the 200ns BL and 200ns MOSFET NPS treatments were matched, treatment with the 200ns MOSFET NPS parameters were less successful at inducing primary tumor clearance and protection as evident by 67% survival after treatment and after the challenge (net survival of 44%). Interestingly, the 200ns BL NPS parameters were most successful at inducing immunity with 78% (7:9) survival after the challenge, while 67% survived from the 100ns BL (8:12) and 200ns MOSFET (4:6) NPS treatment groups.

Table 3 4T1-Luc BVM survival ratios and percentages.

4T1-Luc Treatment Group	**Survival (Ratio)**		**Survival (%)**	
	After Treatment	*After Challenge*	*After Treatment*	*After Challenge*
Untreated	NA	0:15	NA	0%
100ns BL	12:12	8:12	100%	67%
200ns BL	9:9	7:9	100%	78%
200ns MOSFET	6:9	4:6	67%	67%

The abscopal effect in the 4T1-Luc cancer model. The 4T1-Luc breast cancer model was also used to investigate the efficacy of NPS at inducing abscopal tumor clearance in addition to clearing the primary NPS treated tumor in experiments referred to as the abscopal effect (AE). Primary tumors (α) were initiated by inoculating the left MFP of Balbc mice with $1x10^6$ 4T1-Luc cells. The secondary/ abscopal tumors (β) were initiated on days 0, -3, and -7 (AE_0, AE_{-3}, and AE_{-7}, respectively) before treatment by inoculating the opposite (right) MFP with $5x10^5$ 4T1-Luc cells. Figure 14 shows the primary and abscopal tumor growth curves for the mice inoculated on the same day as treatment (AE_0, n=7). Three of the seven mice in this group were unable to clear either tumor, while one was unable to clear the primary and another unable to clear the abscopal. With two mice successfully clearing both tumors, the NPS treatment efficacy was 29% when abscopal tumors were started on the same day as treatment.

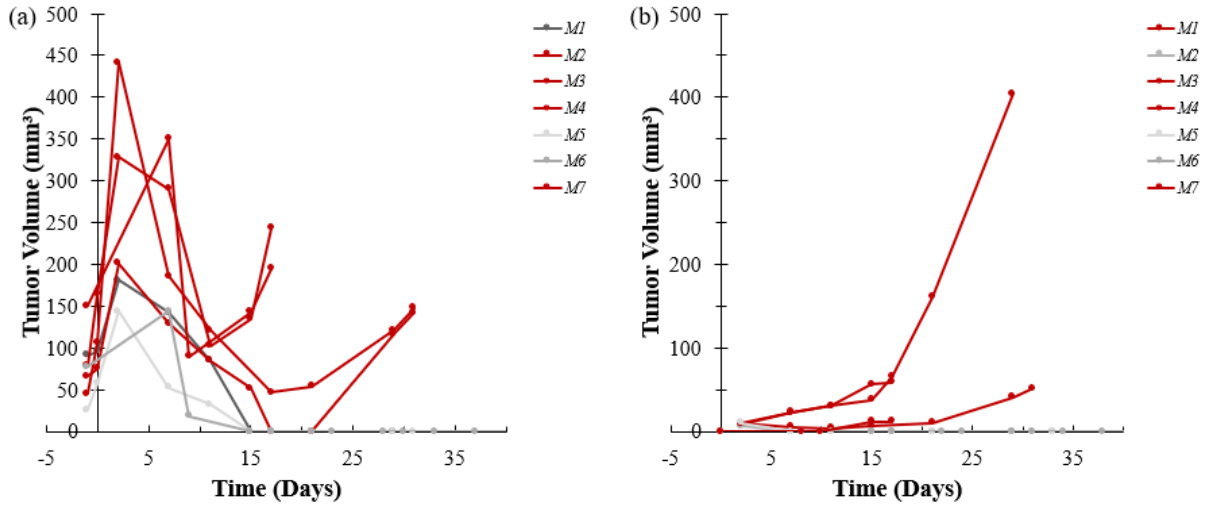

Figure 14. AE_0 primary and abscopal 4T1-Luc tumor growth curves. Balbc/J mice were inoculated with $1x10^6$ 4T1-Luc cells (primary tumor) 10-days before and $5x10^5$ 4T1-Luc cells (abscopal tumor) on the same day (AE_0, n=7) as treatment with NPS. The primary tumors were treated with NPS (100ns BL, 1000 pulses, 50kV/cm, 3Hz). The resultant (a) primary and (b) abscopal tumor growth curves for these mice (M) were plotted from the day of treatment (day 0). Tumors that regressed are displayed in the grey monochromatic scheme, while those that progressed after NPS treatment are shown in red.

The Balbc mice that received the abscopal inoculation three days before (AE_{-3}, n=12) NPS treatment, were more successful at clearing both tumors (Figure 15). Complete primary and abscopal tumor clearance was observed in five of the twelve mice (42%). However, seven mice (58%) failed after treatment, including five (42%) which were unable to clear neither the primary nor abscopal tumors, and two (16%) which were unable to clear the abscopal tumor.

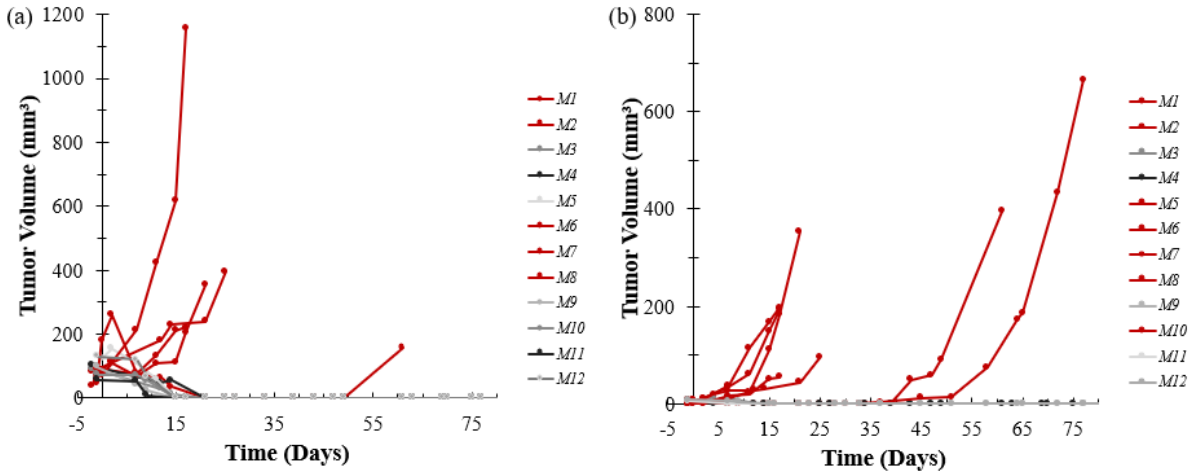

Figure 15. AE_{-3} primary and abscopal 4T1-Luc tumor volumes. Balbc/J mice were inoculated with $1x10^6$ 4T1-Luc cells (primary tumor) 10-days before and $5x10^5$ 4T1-Luc cells (abscopal tumor) three days (AE_{-3}, n=12) before treatment with NPS. The primary tumors were treated with NPS (100ns BL, 1000 pulses, 50kV/cm, 3Hz). The resultant (a) primary and (b) abscopal tumor growth curves in these mice (M) were plotted from the day of treatment (day 0). Tumors that regressed are displayed in the grey monochromatic scheme, while those that progressed after NPS treatment are shown in red.

The Balbc mice that received the abscopal inoculation seven days before (AE_{-7}, n=10) NPS treatment were more successful at clearing the primary tumors albeit abscopal tumor clearance was far less common (Figure 16). Primary tumor clearance was observed in nine of ten mice (90%) however, 90% of the mice failed to clear the abscopal tumor. Primary and abscopal tumor clearance was observed in only one mouse (10%) from this group.

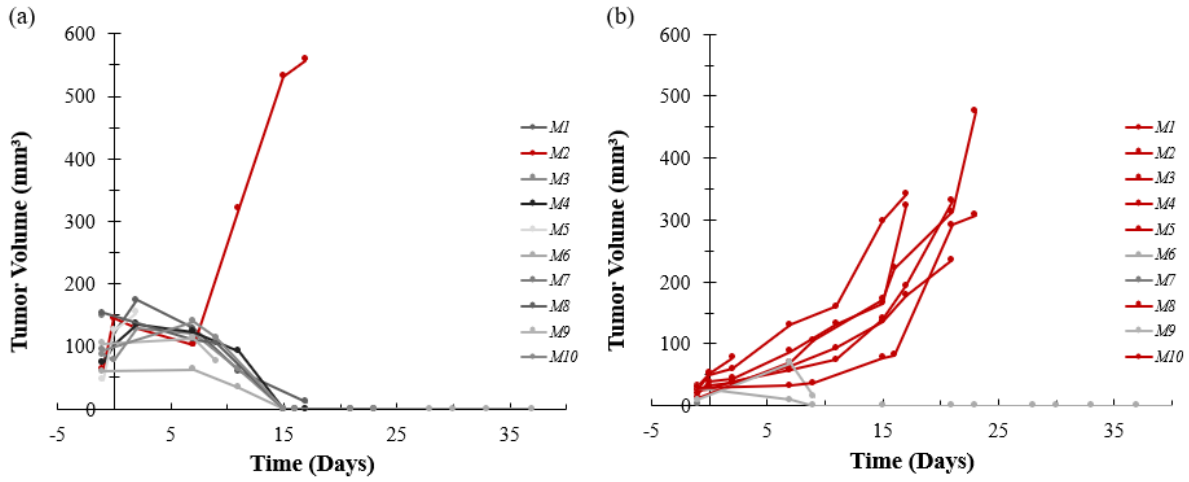

Figure 16. AE_{-7} primary and abscopal 4T1-Luc tumor volumes. Balbc/J mice were inoculated with $1x10^6$ 4T1-Luc cells (primary tumor) 10-days before and $5x10^5$ 4T1-Luc cells (abscopal tumor) seven days (AE_{-7}, n=10) before treatment with NPS. The primary tumors were treated with NPS (100ns BL, 1000 pulses, 50kV/cm, 3Hz). The resultant (a) primary and (b) abscopal tumor growth curves in these mice (M) were plotted from the day of treatment (day 0). Tumors that regressed are displayed in the grey monochromatic scheme, while those that progressed after NPS treatment are shown in red.

The Balbc mice from all AE groups which successfully cleared both the primary (α) and abscopal (β) tumors were challenged at least 7-weeks after treatment with NPS. At that time, a third tumor (θ) was initiated in a total of eight mice, including two from AE_0, five from AE_{-3}, and one from AE_{-7}, by inoculating the adjacent (lower right) MFP with $5x10^5$ 4T1-Luc cells. Due to the limited survival in the AE_0 and AE_{-7} groups, a comparative analysis at this point would lack validity; however, these mice did receive the same NPS treatment and cleared both tumors, so it was worthwhile to investigate whether they were protected, i.e., tumor rejection, indicative of NPS induced immunity. Therefore, these mice were collectively challenged (n=8), and tumor growth curves were examined in unison. Figure 17 shows the resultant tumor (θ) growth curves from these AE experiments. Of the eight mice challenged, 25% were unprotected and developed tumors (one from AE_0 and AE_{-3} groups). Thus, cumulative protection was observed in 75% as evident by tumor rejection. The AE_{-3} group contributed the majority of mice for the challenge (n=5); of which, rejection of the challenge tumor and protection was observed in 80% for that group alone.

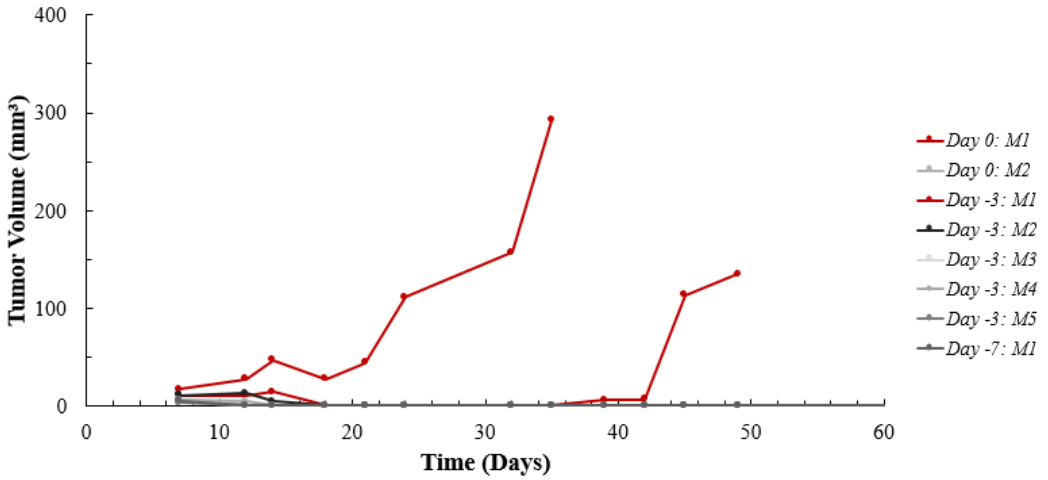

Figure 17. AE model 4T1-Luc challenge tumor growth curves. All Balbc mice that successfully cleared the primary and abscopal tumors after treatment with the 100ns BL NPS parameters were challenged for immunity. This required a third inoculation of $5x10^5$ 4T1-Luc cells in the adjacent (lower right) MFP at least 7-weeks after treatment. Since the remaining number of Balbc mice in each AE group was limited due to failed tumor clearance after treatment with the same NPS parameters, this tumor progression was collectively examined (n=8). Tumors that regressed in these mice (M) are displayed in the grey monochromatic scheme, while those that progressed are shown in red.

The NPS treatment efficacy for inducing primary (α) and abscopal (β) tumor clearance as well as immunity was also considered in terms of survival of the Balbc/J mice in the 4T1-Luc AE model. The Kaplan-Meier probability/ percent of survival curves (Figure 18**)** for the day 0 (AE_0, n=7), day -3 (AE_{-3}, n=12), and day -7 (AE_{-7}, n=10) abscopal (β) tumor recipients treated with the 100ns BL NPS parameters (day 0) and for the untreated (UnTx-α, n=4; UnTx- θ, n=3) control groups of the 4T1-Luc AE model were examined with GraphPad Prism software. The log-rank (Mantel-Cox) and Gehan-Breslow-Wilcoxon tests were performed to determine the p-values between and among groups. For the null hypothesis, this was less than 0.0001, which indicated significance among the 4T1-Luc AE groups. The significance level was set using the Bonferroni method to compare the multiple pairs of AE groups. Since we previously defined significance as $p<0.05$, and there were 10 comparisons, the Bonferroni-correction threshold for these analyses was $p<0.005$. Therefore, the differences between the untreated control groups and the day -3 abscopal tumor recipient group (AE_{-3}) treated with NPS were considered statistically significant using the family-wise significance level of 5%. Comparisons between NPS treatment groups were not considered significant by these measures; however, the difference between the day -3 and day -7 abscopal tumor recipient groups treated with NPS would have been considered significant without consideration of the Bonferroni-correction threshold since $p<0.05$.

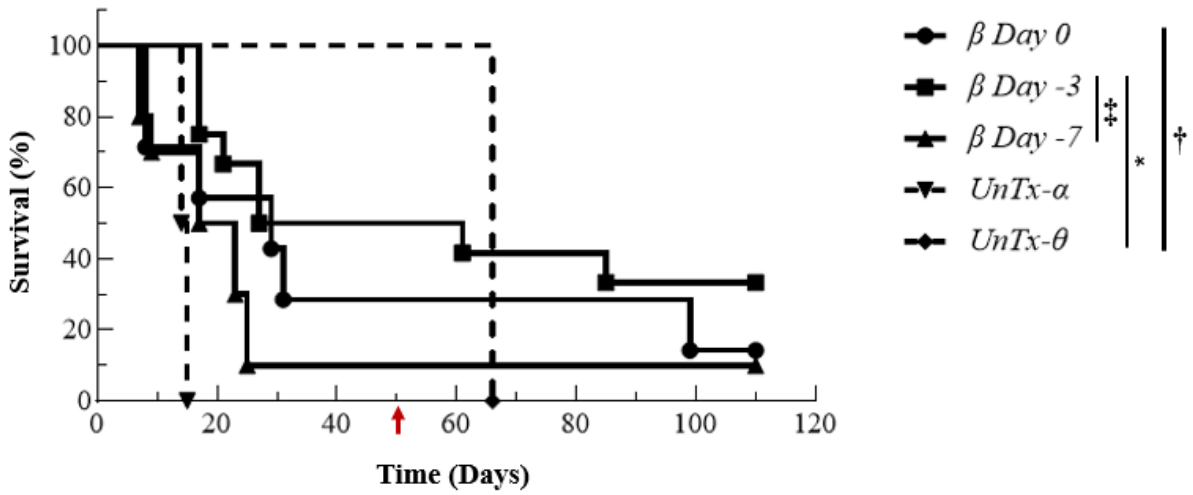

Figure 18. 4T1-Luc AE model Kaplan-Meier survival curves. The primary tumors were initiated in Balbc mice via inoculation of the left mammary fat pad (MFP) with $1x10^6$ 4T1-Luc cells 10-days before the day of treatment (day 0), and the abscopal tumors (β) were initiated via inoculation of the opposite (upper right) MFP with $5x10^5$ 4T1-Luc cells on days 0, -3, and -7 (n=7, 12, and 10, respectively). Those that survived, clearing both tumors after treatment with NPS (100ns BL, 1000 pulses, 50kV/cm, 3Hz), were challenged with a third inoculation of $5x10^5$ 4T1-Luc cells in the adjacent (lower right) MFP about 7-weeks later, indicated by the red arrow. Two age-matched untreated control groups were employed for these investigations, with α denoting the first and θ denoting the second. The log-rank (Mantel-Cox) and Gehan-Breslow-Wilcoxon tests were performed using GraphPad Prism version 9.2.0 for Windows, GraphPad Software, San Diego, California USA, www.graphpad.com, and the null hypothesis (†) was significant, $p< 0.0001$. A family-wise significance level of 5%, using the Bonferroni-corrected threshold method for p-values, indicated significance between groups (*), $p<0.005$. It is also worth mentioning that the significance between the day -3 and day -7 abscopal tumor recipient groups treated with NPS was 0.03 (‡) before application of the Bonferroni method.

The survival ratios and percentages were also examined after treatment and after the challenge for the 4T1-Luc AE model (Table 4). In this manner, the survival percentages for after the challenge account for the number of mice remaining 7-weeks after NPS. NPS was more efficient at inducing primary and abscopal tumor clearance in the C57BL6/J mice inoculated with the abscopal tumor on day -3 as evident by 42% (5:12) survival. When inoculated on the same day (day 0) and seven days (day -7) prior to treatment, NPS was less effective at inducing complete tumor clearance as evident by 20% (2:7) and 10% (1:10) survival, respectively. Mice from all AE groups which survived after NPS treatment, clearing both primary and abscopal tumors, were cumulatively challenged at least 7-weeks later. Collectively, 75% of the NPS treated AE mice survived, rejecting the challenge tumor, and indicating that NPS induced immunity in these mice.

Table 4 AE 4T1-Luc survival ratios and percentages.

Abscopal Treatment Group	**Survival (Ratio)**		**Survival (%)**	
	After Treatment	*After Challenge*	*After Treatment*	*After Challenge*
Untreated	0:4	0:3	0%	0%
Day 0	2:7	1:2	29%	*75%*
Day -3	5:12	4:5	42%	
Day -7	1:10	1:1	10%	

Section 4.3. In Vivo: The Murine Melanoma Model

BVM in the B16-F10 cancer model. The B16-F10 melanoma model was also used to compare the BL and MOSFET NPS parameters for treatment efficacy. C57BL6/J mice were inoculated with $5x10^5$ B16-F10 cells in the left flank to initiate primary tumors. The mice were allocated into groups such that the average tumor volumes were evenly distributed among the treatment groups. In addition to the previously discussed 100ns BL (n=11), 200ns BL (n=12), and 200ns MOSFET (n=12) NPS treatment groups, a surgery group (n=7) was included as the standard of care control for this model. Figure 19 shows the resultant B16-F10 tumor growth curves after treatment (day 0). For the surgery group, adequate surgical removal was not always obtained, and 57% (4:7) continued to develop tumors. In this model, the 100ns BL NPS parameters induced tumor regression and complete clearance in 64% (7:11) of mice in this group, while the resultant tumor clearance from treatment with the 200ns BL NPS parameters was 50% (6:12). Successful tumor clearance resulting from treatment with the 200ns MOSFET NPS parameters occurred less frequently than those observed for the BL pulsers, with complete tumor regression occurring in only 17% (2:12) of mice in this group. Unfortunately, due to the COVID19 pandemic, experimental measures were limited and experiments and/or participants were terminated somewhat prematurely albeit not before tumor statuses were evident.

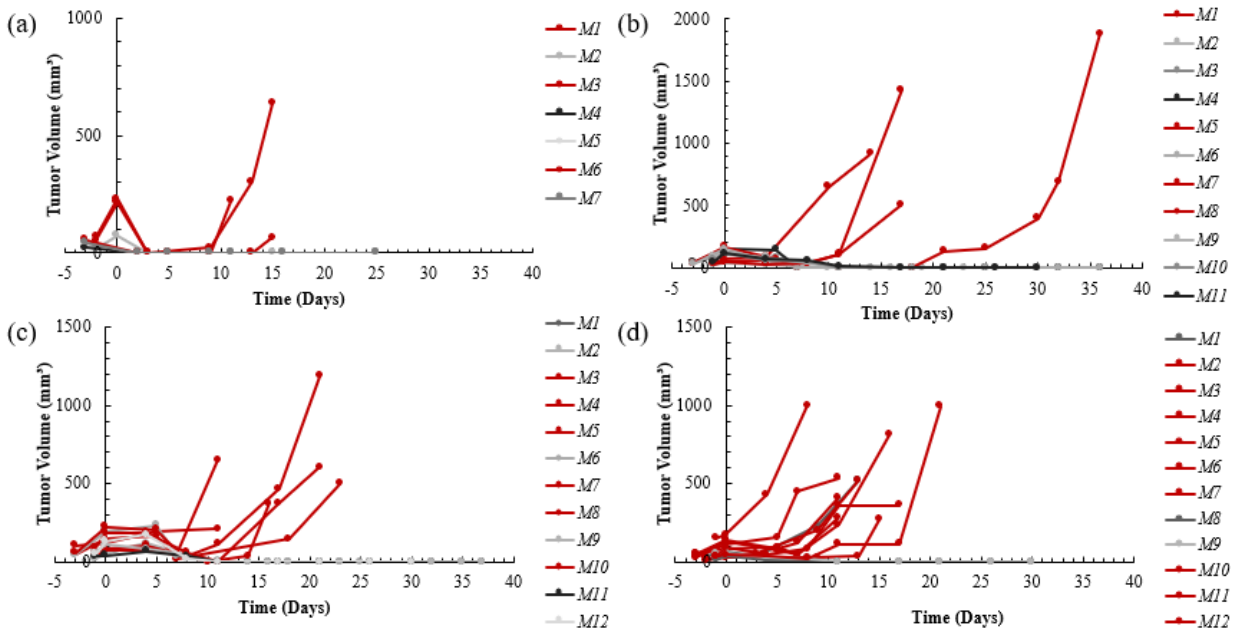

Figure 19. B16-F10 BVM model primary tumor growth curves. Primary tumors were initiated in C57BL6/J mice via inoculation of the left flank with $5x10^5$ B16-F10 cells approximately 10-days before the day of treatment (day 0). The day before treatment, the tumors were measured, and mice were divided into treatment groups such that the average tumor volumes were evenly distributed. The treatment groups included a (a) surgery group in addition to those treated with the (b) 100ns Blumlein line (BL) (n=11), (c) 200ns BL (n=12), and (d) 200ns MOSFET (n=12) NPS parameters. Tumors that regressed are displayed in the grey monochromatic scheme, while those that progressed after NPS treatment are shown in red.

As part of the BVM model, mice that were successful at clearing the primary tumors after treatment were challenged for immunity. The challenge tumors were initiated by subcutaneously inoculating the opposite (right) flank of the C57BL6/J mice with $2.5x10^5$ B16-F10 cells. At this time, a group of age-matched, previously naïve, C57BL6/J mice were employed as untreated controls to ensure cellular viability and for comparison with the treated mice. The resultant tumor growth curves were plotted from the day of the challenge, Figure 20. All untreated (n=12) and surgery (n=3) mice developed tumors from the challenge inoculant. For the surgery group, this indicated that the previous surgical removal of the primary tumor did not result in immunity to B16-F10 melanoma. Those previously treated with the 100ns BL NPS parameters were only 14% (1:7) successful at rejecting the challenge tumor, while those previously treated with the 200ns BL NPS parameters were more successful, with tumor rejection observed in 50% (3:6) of the mice in this treatment group. Those previously treated with the 200ns MOSFET NPS parameters were unsuccessful at rejecting the challenge tumor, albeit these NPS treatment parameters lacked efficiency in clearing the primary tumor resulting in an extremely limited number of mice available to challenge (0:2).

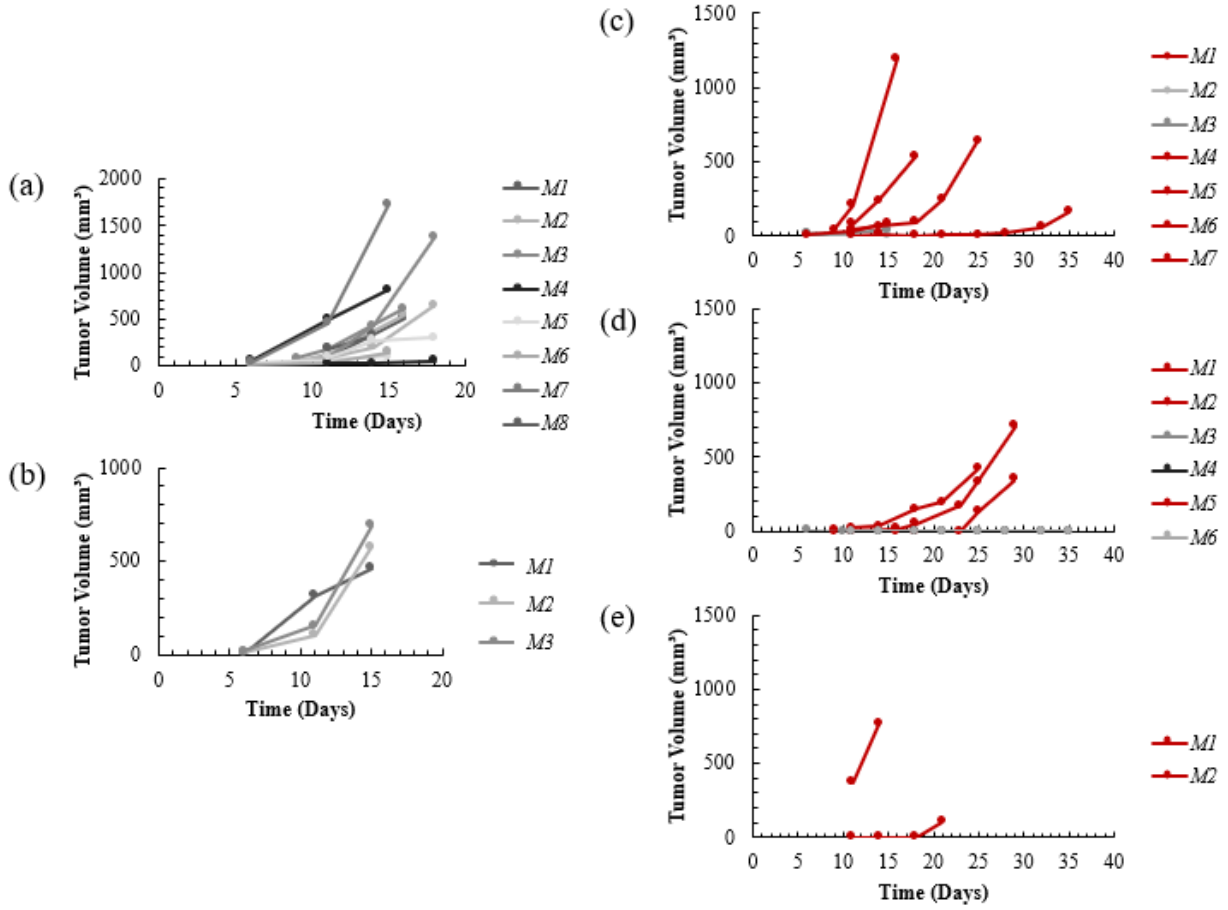

Figure 20. B16-F10 BVM challenge tumor growth curves. The C57BL6/J mice that successfully cleared the primary tumors after treatment were challenged via a second subcutaneous inoculation of $2.5x10^5$ B16-F10 cells into the opposite (right) flank about 7-weeks after treatment (day 0). An age-matched group of naïve C57BL6/J mice were employed as untreated controls at this time. The resultant tumor growth curves for these mice (M) were plotted for the (a) untreated (n=12) and (b) surgery (n=3) control groups as well as for the (c) 100ns BL (n=7), (d) 200ns BL (n=6), and (e) 200ns MOSFET (n=2) NPS treatment groups. Tumors that regressed are displayed in the grey monochromatic scheme, while those that progressed after NPS treatment are displayed in red.

The treatment efficacy of NPS was also considered in terms of survival of the C57BL6/J mice in the B16-F10 BVM model. Kaplan-Meier probability/ percent of survival curves for the 100ns BL (n=11), 200ns BL (n=12), and 200ns MOSFET (n=12) NPS treatment groups and for the untreated (n=12) and surgery (n=7) control groups of the B16-F10 BVM model were examined with GraphPad Prism software (Figure 21). The log-rank (Mantel-Cox) and Gehan-Breslow-Wilcoxon tests were performed to determine the p-values between and among groups. For the null hypothesis, this was less than 0.0001, which indicated significance among the B16-F10 BVM groups. The significance level was set using the Bonferroni method to compare the multiple pairs of BVM groups. Since we previously defined significance as $p<0.05$, and there were 10 comparisons, the Bonferroni-correction threshold for these analyses was $p<0.005$. Therefore, the differences between the 100ns BL and 200ns MOSFET NPS treatment groups as well as between the 200ns BL and 200ns MOSFET NPS treatment groups were considered statistically significant using the family-wise significance level of 5%. Comparisons between other groups were not considered significant by these measures; however, the difference between the surgery group and the 200ns BL NPS treatment group would have been considered significant without consideration of the Bonferroni-correction threshold since $p<0.05$. Since the other NPS treatment groups were not statistically observed to offer advantages over the standard of care (surgery group) for this cancer model, the uncorrected significance between the surgery and 200ns BL NPS treatment groups ($p=0.03$) was worth mentioning.

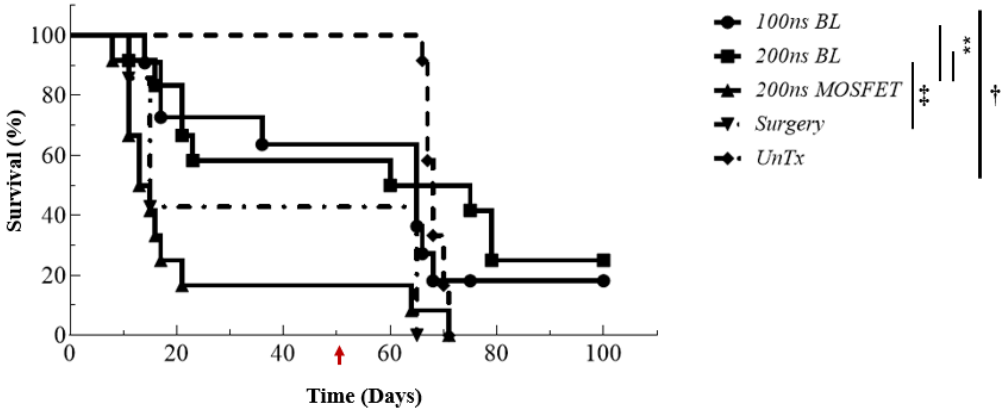

Figure 21. B16-F10 BVM model Kaplan-Meier survival curves. Tumors were initiated in C57BL6/J mice via subcutaneous inoculation of the left flank with $5x10^5$ B16-F10 cells approximately 10-days before the day of treatment (day 0). The average tumor volumes were evenly distributed among groups. Treatment groups (solid lines) included 100ns BL (round) (n=12), 200ns BL (square) (n=9), and 200ns MOSFET (triangle) (n=9) NPS parameters, as well as a surgery group (dashed line, inverted triangle) (n=7). Mice that survived, clearing the primary tumor, were challenged with a second subcutaneous inoculation of $2.5x10^5$ B16-F10 cells into the opposite (right) flank about 7-weeks later, indicated by the red arrow. An age-matched untreated control group (dashed line, diamond) (n=12) was included at that time to ensure viability of the cell inoculant. The log-rank (Mantel-Cox) and Gehan-Breslow-Wilcoxon tests were performed using GraphPad Prism version 9.2.0 for Windows, GraphPad Software, San Diego, California USA, www.graphpad.com, and the null hypothesis (†) was significant, $p< 0.0001$. The family-wise significance level of 5%, using the Bonferroni-corrected threshold method for p-values, indicated significance between groups (*), $p<0.005$. It is also worth mentioning that the significance between the surgery and 200ns BL treatment groups was 0.05 (‡) before application of the Bonferroni method.

The survival ratios and percentages were also examined after treatment and after the challenge for the B16-F10 BVM model (Table 5). The 100ns BL and 200ns BL NPS parameters were most efficient at inducing primary tumor clearance as evident by their 64% (7:11) and 50% (6:12), respectively, survival after treatment. Surgical removal was less effective than the BL NPS parameters at primary tumor clearance, as evident by the 43% (3:7) survival. Although the parameters of the 200ns BL and 200ns MOSFET NPS treatments were matched, treatment with the 200ns MOSFET NPS parameters were much less successful at inducing primary tumor clearance as evident by a mere 17% (2:12) survival after treatment. Furthermore, the 200ns MOSFET NPS parameters were completely unsuccessful at inducing immunity as evident by 0% (0:2) survival after the challenge. Interestingly, the 200ns BL NPS parameters were most successful at inducing immunity with 50% (3:6) survival after the challenge, while only 14% (1:7) survived from the 100ns BL NPS treatment group.

Table 5 B16-F10 BVM survival ratios and percentages.

B16-F10 Treatment Group	**Survival (Ratio)**		**Survival (%)**	
	After Treatment	*After Challenge*	*After Treatment*	*After Challenge*
Untreated	NA	0:12	NA	0%
Surgery	3:7	0:3	43%	0%
100ns BL	7:11	1:7	64%	14%
200ns BL	6:12	3:6	50%	50%
200ns MOSFET	2:12	0:2	17%	0%

NPS vs. pIL-12 GET in the B16-F10 cancer model. Due to the poor treatment efficacy of NPS in the B16-F10 melanoma model, we decided to examine the effects of a combination approach in experiments referred to as the GET-NPS model. In this model, the 100ns BL NPS parameters (NPS) (n=10), pIL-12 GET (GET) (n=10), and the combination of pIL-12 GET and the 100ns BL NPS parameters (GET-NPS) (n=10) were examined for their efficacy at inducing primary tumor clearance and protection when challenged. Primary tumors were initiated in C57BL6/J mice by inoculating the left flank with $5x10^5$ B16-F10 cells about 10 days before treatment. The mice were allocated into groups such that the average tumor volumes were evenly distributed among the treatment groups, including an untreated control group (n=5). Untreated mice were humanely euthanized due to tumor progression within 1-week after the other groups were treated, about 2-3-weeks after tumors were initiated. For the NPS treatment group, the B16-F10 tumors were treated on day 0 with the100ns BL NPS parameters as previously discussed. For the pIL12-GET treatment group, tumors were treated by injecting 50µg pIL-12 directly into the B16-F10 tumor, intratumorally, which was immediately followed by electroporation (EP) (5ms, 10 pulses, 60V/mm). When the combined approach was employed (GET-NPS), intratumoral delivery of pIL-12 was immediately followed by treatment with the 100ns BL NPS parameters and then treatment with EP on the first day (day 0) of treatment. Both the GET and GET-NPS groups were also treated with pIL12-GET on days 3 and 7. Figure 22 shows the resultant primary B16-F10 tumor growth curves for each treatment group from the first day of treatment (day 0). Treatment with NPS and/or GET-NPS typically induced tumor regression within the first week after treatment; however, in some mice, the tumors appeared to regress but resurfaced about 3 weeks later (2:10/group). Some of the tumors in mice from these groups, as well as in the pIL12-GET group, appeared unphased as they continued to progress within the first week of treatment

(NPS 2:10, GET 3:10, GET-NPS 2:10). Primary tumor clearance was observed for the NPS and GET-NPS treatment groups, with successful clearance in 60% (6:10) and 50% (5:10), respectively. Interestingly, while pIL12-GET was not observed to induce complete tumor regression, it was observed to have a stabilizing effect on tumors, with 40% (4:10) of the mice in this group maintaining reduced tumor burdens.

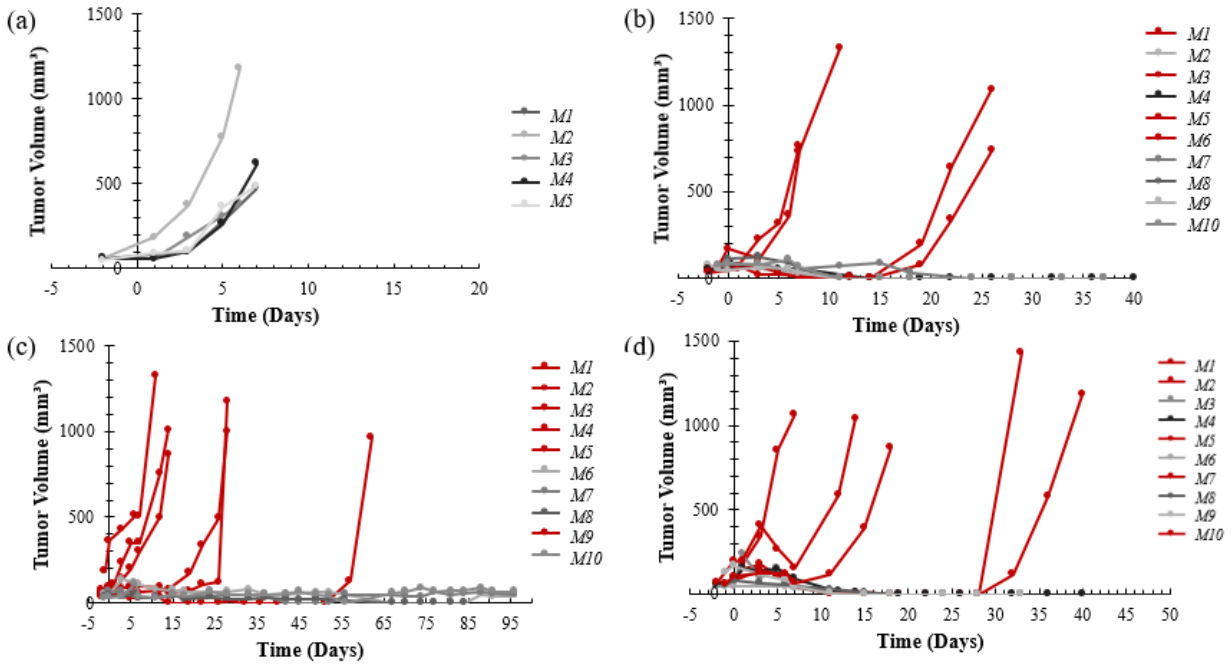

Figure 22. B16-F10 GET-NPS model primary tumor growth curves. Primary tumors were initiated in C57BL6/J mice via inoculation of the left flank with $5x10^5$ B16-F10 cells approximately 10-days before the day of treatment (day 0). The day before treatment, the tumors were measured, and mice were divided into treatment groups such that the average tumor volumes were evenly distributed. The treatment groups included (a) an untreated control group (n=5) in addition to those treated with (b) NPS (100ns BL, 1000 pulses, 50kV/cm) (n=10) on day 0, (c) pIL12-GET (intratumoral injection of 50µg pIL-12 followed by electroporation (5ms, 10 pulses, 60V/mm)) (n=10) on days 0, 3, and 7, and (d) the combination of pIL12-GET and NPS (GET-NPS) (n=10). For the combination, pIL-12 was injected into the tumor before treatment with NPS and subsequent treatment with EP on day 0; additionally, this group was treated on days 3 and 7 with pIL12-GET. Tumors that regressed in these mice (M) are displayed in the grey monochromatic scheme, while those that progressed after treatment are shown in red.

As part of the GET-NPS model, the C57BL6/J mice that had either cleared the primary tumor or had small stable tumors were challenged for immunity. The challenge tumors were initiated about 7-weeks after treatment via subcutaneous inoculation of the opposite (right) flank with $2.5x10^5$ B16-F10 cells. At this time, a group of age matched C57BL6/J mice were employed as untreated controls to ensure cellular viability and for comparison with the treated mice. The resultant tumor growth curves were plotted from the day of the challenge (Figure 23). As shown, all untreated mice (n=10) developed tumors within the 3-weeks. Unprotected mice in the NPS (4:6), pIL12-GET (2:5), and GET-NPS (4:5) treatment groups developed tumors similarly to the untreated controls, with tumor rejection occurring in 33% (2:6), 75% (3:4), and 20% (1:5), respectively, of those challenged.

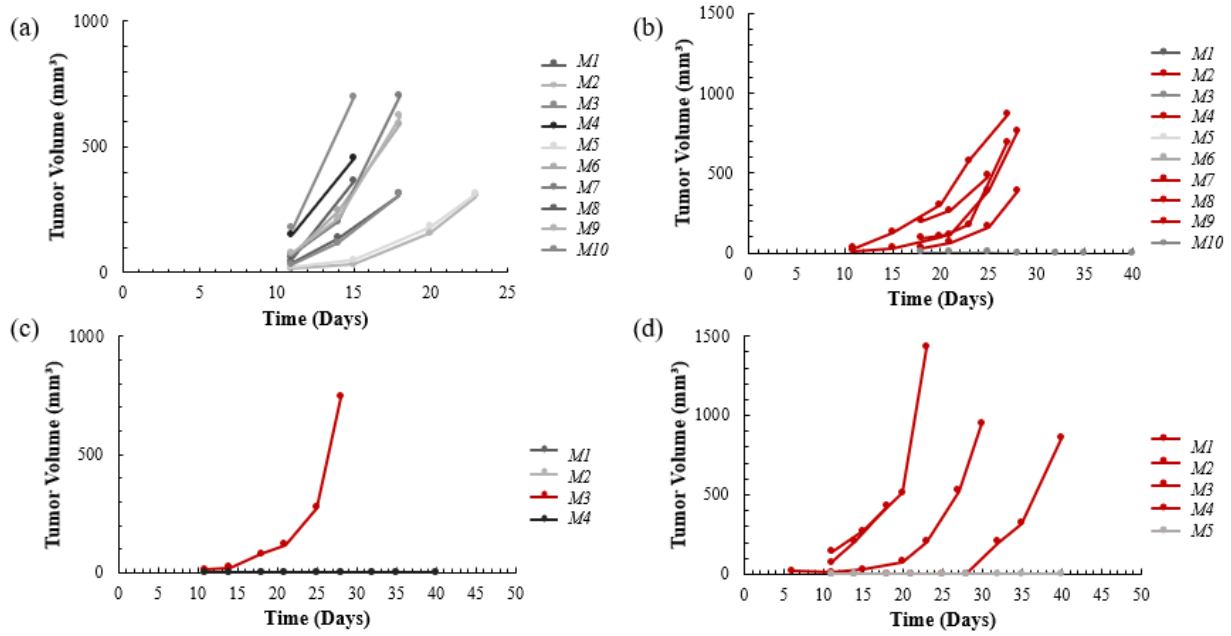

Figure 23. B16-F10 GET-NPS challenge tumor growth curves. The C57BL6/J mice that successfully cleared and/or had stable the primary tumors after treatment were challenged via a second subcutaneous inoculation of $2.5x10^5$ B16-F10 cells into the opposite (right) flank about 7-weeks after treatment (day 0). An age-matched group of C57BL6/J mice were employed as untreated controls at this time. The resultant challenge tumor growth curves were plotted for the (a) untreated control group (n=10) in addition to those previously treated with (b) NPS (100ns BL, 1000 pulses, 50kV/cm) (n=6), (c) pIL12-GET (intratumoral injection of 50µg pIL-12 followed by electroporation (5ms, 10 pulses, 60V/mm)) (n=4), and (d) the combination of pIL12-GET and NPS (GET-NPS) (n=5). Tumors that regressed in these mice (M) are displayed in the grey monochromatic scheme, while those that progressed after NPS treatment are displayed in red.

The treatment efficacy of NPS was also considered in terms of survival of the C57BL6/J mice in the B16-F10 GET-NPS model. Kaplan-Meier probability/ percent of survival curves for the 100ns BL NPS (n=10), pIL12-GET (n=10), and the combined GET-NPS (n=10) treatment groups and for the primary (n=5) and challenge (n=10) untreated control groups of the B16-F10 GET-NPS model were analyzed with GraphPad Prism software (Figure 24). The log-rank (Mantel-Cox) and Gehan-Breslow-Wilcoxon tests were performed to determine the p-values between and among groups. For the null hypothesis, this was less than 0.0001, which indicated significance among the B16-F10 GET-NPS groups. The significance level was set using the Bonferroni method to compare the multiple pairs of GET-NPS groups. Since we previously defined significance as $p<0.05$, and there were 10 comparisons, the Bonferroni-correction threshold for these analyses was $p<0.005$. Therefore, the differences between the 100ns BL NPS treatment group and untreated control groups as well as between the combined GET-NPS treatment group and primary untreated control group were considered statistically significant using the family-wise significance level of 5%. Comparisons between other groups were not considered significant by these measures.

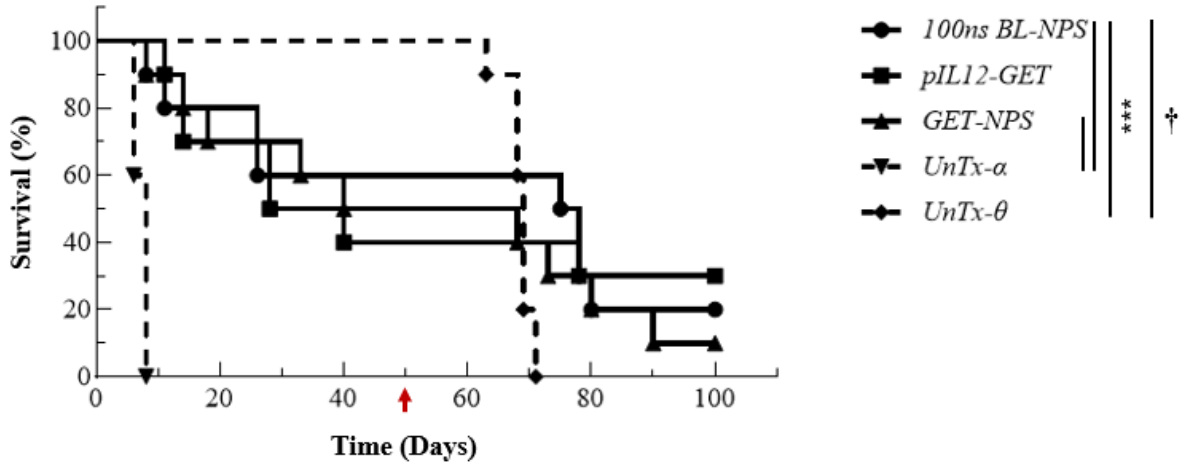

Figure 24. The B16-F10 GET-NPS model Kaplan-Meier survival curves. Tumors were initiated in C57BL6/J mice via subcutaneous inoculation of the left flank with $5x10^5$ B16-F10 cells approximately 10-days before the day of treatment (day 0). The average tumor volumes were evenly distributed. The treatment groups (solid lines) included those treated with 100ns BL NPS (round) (n=10), pIL12-GET (square) (n=10), and pIL12-GET and 100ns BL NPS (GET-NPS) (triangle) (n=10). Mice that survived, clearing the primary tumor, were challenged with a second subcutaneous inoculation of $2.5x10^5$ B16-F10 cells into the right flank about 7-weeks later (red arrow). Groups of age-matched C57BL6/J mice were employed as untreated controls at the time of treatment (dashed line, inverted triangle) (UnTx-α, n=5) and challenge (dashed line, diamond) (UnTx-θ, n=10) for comparison with treatment groups and to ensure cellular viability at the challenge time point. The log-rank (Mantel-Cox) and Gehan-Breslow-Wilcoxon tests were performed using GraphPad Prism version 9.2.0 for Windows, GraphPad Software, San Diego, California USA, www.graphpad.com, and the null hypothesis (†) was significant, $p< 0.0001$. The family-wise significance level of 5%, using the Bonferroni-corrected threshold method for p-values, indicated significance between groups (*), $p<0.005$.

The survival ratios and percentages were also examined after treatment and after the challenge for the B16-F10 GET-NPS model (Table 6). The NPS and GET-NPS treatments were most efficient at inducing primary tumor clearance as evident by their respective 60% (6:10) and 50% (5:10) survival after treatment. GET treatment alone was less effective than treatment with NPS alone and/or in combination with GET at primary tumor clearance, as evident by the 40% (4:10) survival; although, differences between the treatment groups were not considered significant. Interestingly, treatment with GET was most efficient at inducing immunity, as evident by the 75% (3:4) survival when challenged with the second tumor inoculant despite maintaining stable primary tumor burdens. Furthermore, treatment with NPS was more efficient at inducing immunity than the combined GET-NPS treatment as evident by their 33% (2:6) and 20% (1:5) survival, respectively.

Table 6 B16-F10 GET-NPS survival ratios and percentages.

GET-NPS Model	**Survival (Ratio)**		**Survival (%)**	
Treatment Group	*After Treatment*	*After Challenge*	*After Treatment*	*After Challenge*
Untreated	0:5	0:10	0%	0%
NPS	6:10	2:6	60%	33%
GET	4:10	3:4	40%	75%
GET-NPS	5:10	1:5	50%	20%

Section 4.4. In Vivo: The Humanized Mouse Model

HIS reconstitution. Approximately $1x10^5$ viable HCB CD34+ HSC were engrafted in young, 4-6-week-old, female NSGM3 mice, hu-NSGM3, via intraperitoneal and/or interfemoral injection [184]. All NSGM3 mice in an engraftment group were treated at the same time with the appropriate level of γ-irradiation and received HCB CD34+ HSC from the same donor pool. The peripheral blood was collected via mandibular vein bleed every 4-5 weeks to monitor the progress and/or expansion of the human immune cells. A fluorescently labeled human CD45 (hCD45) antibody was used to identify the percentage of human leukocytes circulating in the periphery as this was considered the first indicator that the host was accepting the engrafted HIS. Figure 25 shows the percentage of hCD45+ cells for each hu-NSGM3 mouse (n=10) over the experimental timeframe from the day of HIS engraftment. These results present the findings from two HIS engraftment groups, which initially consisted of six mice each; however, one mouse from each group did not survive until the first blood examination (17%). Despite the extensive efforts made to ensure purity of the engrafted cells, reduce exposure to γ-irradiation, and administer Baytril to circumvent engraftment issues, such early morbidity was attributed to graft-versus-host disease (GVHD) and/or adverse side-effects of γ-irradiation. Nevertheless, about 33% (4:12) of the mice accepted the engrafted HSC (HIS-NSGM3) as evident by the increasing presence of hCD45+ leukocytes in the peripheral blood albeit only 25% (3:12) breached the threshold for adequate HIS reconstitution. HIS rejection was observed in 50% (6:12) of hosts. Therein lies one of the limitations of this humanized mouse model, that although extreme cautions were employed to ensure consistency among hosts, there were still observations of inconsistent HIS reconstitution, including extremes such as complete rejection

(6:12), premature morbidity likely resultant of GVHD (2:12), low HIS expansion (1:12), and high HIS expansion (2:12).

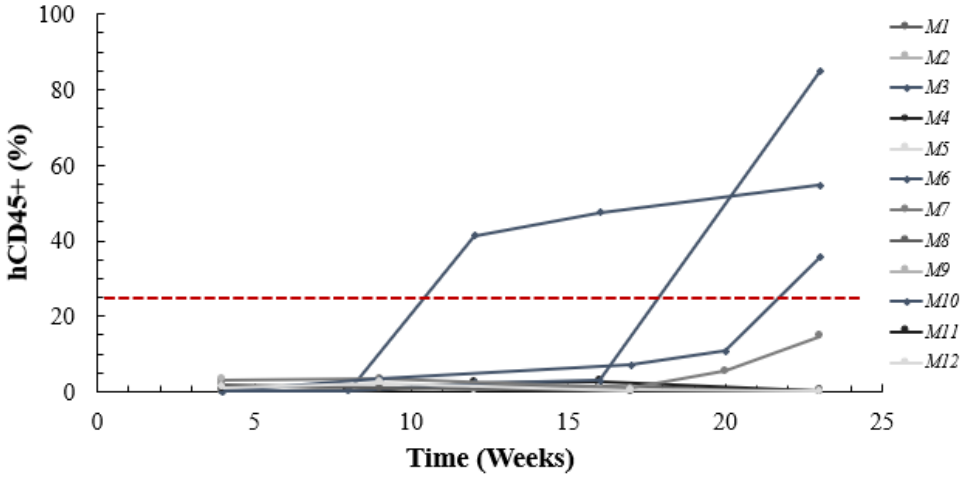

Figure 25. HIS reconstitution variability among NSGM3 mice. Female NSGM3 mice (M) (n=10) were pretreated with sublethal γ-irradiation and engrafted with ~1x10^5 viable HCB CD34+ HSC via IP and/or IF injection at 4-6-weeks-old (day 0). Peripheral blood was routinely monitored for the presence of hCD45+ leukocytes and plotted over time. Adequate HIS reconstitution was considered as >25% hCD45+ (dashed line). The NSGM3 mice that breached this HIS reconstitution threshold are displayed as blue lines with diamond markers, while the grey color scheme was used to display the results of those that did not. Flow cytometry was used for data acquisition and FlowJo™ Software (Windows) Version 10 (Ashland, OR: Becton, Dickinson and Company; 2019) was used for data analysis.

Potential correlations for GVHD. Adequate HIS engraftment was considered when the percentage of hCD45+ cells in the peripheral blood was greater than 25%, while less was considered insufficient; however, higher percentages of hCD45+ cells were found to coincide with weight loss, indicative of GVHD [185,186]. The hu-NSGM3 mice were routinely weighed (~1/week) and examined for maladies associated with their strain as well as the humanization process, such as malocclusions. The weights of hu-NSGM3 mice (n=6) were plotted over time from their date of birth (Figure 26). The hu-NSGM3 mice with stable weights were also those with the lowest percentages of hCD45+ cells, or rather those that rejected the HIS. Weight loss was observed in hu-NSGM3 mice with the highest percentages (>40%) of hCD45+ cells (HIS-NSGM3). Thus, a correlation between weight loss and the percentage of hCD45+ cells was observed.

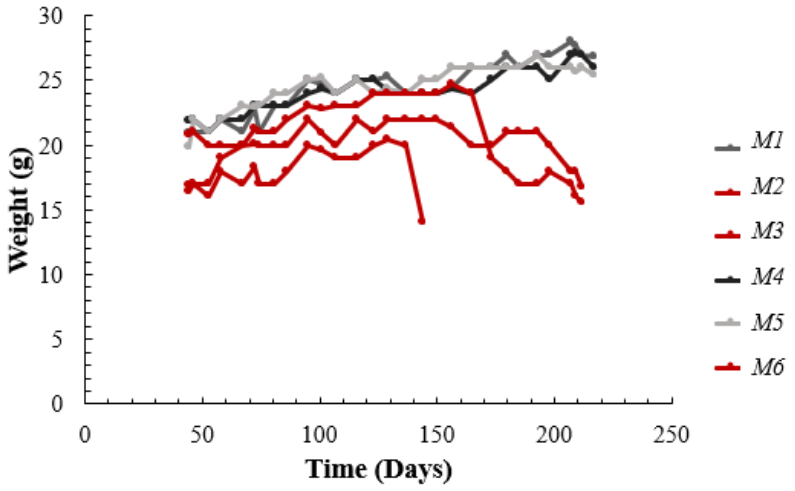

Figure 26. Weight loss in hu-NSGM3 mice. Female NSGM3 mice were pretreated with sublethal γ-irradiation and engrafted with approximately $1x10^5$ viable HCB CD34+ HSC via intraperitoneal and/or interfemoral injection at 4-6-weeks-old. Weights (g) of hu-NSGM3 mice (M) (n=6) were obtained weekly and plotted over time from their date of birth (day 0). Those with steadily increasing weights are displayed in the grey monochromatic scheme, while those with weight loss are displayed in red.

Survival. The survival of hu-NSGM3 mice was also examined. Kaplan-Meier survival curves (Figure 27) were constructed with GraphPad Prism software for two HIS engraftment groups (HIS-1 and HIS-2) of NSGM3 mice (n=6/group) from the day of HIS engraftment (day 0). The results of the log-rank (Mantel-Cox) and Gehan-Breslow-Wilcoxon tests were not considered significant as anticipated, since both groups of hu-NSGM3 mice were engrafted with the same method for HIS reconstitution; however, the survival curves were plotted using the transformation method to plot the asymmetrical confidence intervals with 95% confidence. Only 50% survival was observed for the first HIS engraftment group (HIS-1) over the experimental period of about 26-weeks. The second HIS engraftment group (HIS-2) had 67% survival over the experimental period of about 20-weeks. These results indicated the impermanence of this HIS mouse model, with mortality occurrences after about 1-2 months, 3-months, and 5-months.

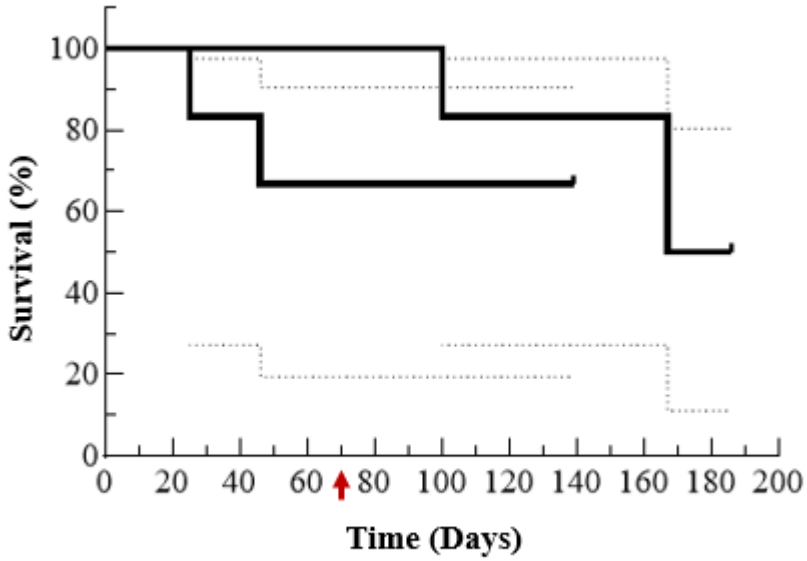

Figure 27. Kaplan-Meier survival curves of HIS engrafted NSGM3 mice. Two groups of female NSGM3 mice were pretreated with sublethal γ-irradiation and engrafted with approximately $1x10^5$ viable HCB CD34+ HSC via intraperitoneal and/or interfemoral injection for reconstituting a human immune system (HIS) at 4-6-weeks-old (day 0). Triple negative breast cancer patient derived xenografts (TNBC-PDX) were implanted into the left mammary fat pad (MFP) about 10-weeks later, as indicated by the red arrow. GraphPad Prism version 9.2.0 for Windows, GraphPad Software, San Diego, California USA, www.graphpad.com., was used to construct the survival curves with 95% confidence intervals using the transformation method to plot the asymmetrical confidence intervals. Log-rank (Mantel-Cox) and Gehan-Breslow-Wilcoxon tests, also analyzed with GraphPad Prism software, indicated no significant differences between the two groups of hu-NSGM3 mice.

TNBC-PDX tumor burden and humanized mice. Hu-NSGM3 mice were implanted with TNBC-PDX tumors 10-weeks after HIS engraftment. The initial hypothesis was that in vivo cocultivation of the HIS and PDX would culminate at the same time due to synergism of stimulatory cytokines; however, this was not the case. Instead, these mice either cultivated the HIS, as evident by increasing percentages of hCD45+ leukocytes, or the TNBC-PDX, as evident by increased tumor growth, as shown in Figure 28. Therefore, unfortunately, gaining insights into the effects of NPS on the HIS was negated.

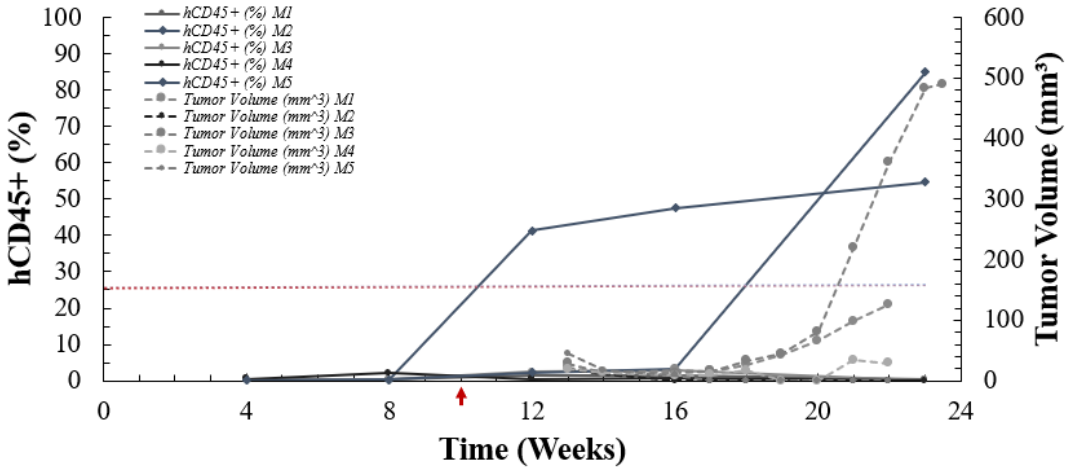

Figure 28. Comparison of HIS and TNBC-PDX development in NSGM3 mice. Female NSGM3 mice (M) (n=10) were pretreated with sublethal γ-irradiation and engrafted with ~1x10^5 viable HCB CD34+ HSC via IP and/or IF injection at 4-6-weeks-old (day 0). Peripheral blood was routinely monitored for the presence of hCD45+ leukocytes and plotted over time. Adequate HIS reconstitution was considered as >25% hCD45+ (dotted red gradient line). TNBC-PDX tumors were implanted into the left mammary fat pad (MFP) about 10-weeks later, as indicated by the red arrow. The NSGM3 mice that breached this HIS reconstitution threshold are displayed as blue lines with diamond markers, while the grey color scheme was used to display the results of those that rejected the HIS and TNBC-PDX. The tumor growth curves (right y-axis) of mice that accepted the TNBC-PDX are displayed as dashed grey lines with round markers. This color scheme was selected since none of the NSGM3 mice accepted both the HIS and TNBC-PDX. Flow cytometry was used for data acquisition and FlowJo™ Software (Windows) Version 10 (Ashland, OR: Becton, Dickinson and Company; 2019) was used for data analysis.

Efficacy of NPS in the human TNBC-PDX and BC-CDX models. NPS was examined for efficacy in clearing human TNBC-PDX tumors in NSG mice. Tumor sections (~2mm^3) were implanted into the MFP of 6-8-week-old female NSG mice. Once the TNBC-PDX tumors measured between about 4-8mm in diameter, they were treated with the 100ns BL NPS parameters (1000 pulses, 50kV/cm) (n=6) or allocated as untreated controls (n=6). Figure 29 shows the resultant TNBC-PDX tumor growth curves for individual NSG mice after treatment with NPS (day 0). As shown, tumors progressed in the untreated NSG mice, while NPS induced complete tumor clearance in five of the six NPS-Tx NSG mice within 3-4-weeks after treatment. In one of the six NPS-Tx mice, the TNBC-PDX appeared to regress during the same timeframe; however, it resurfaced and reached maximum burden around 9-weeks after treatment. That was about 3-weeks slower than the untreated control NSG mice. For this mouse, it was likely that a section of the tumor remained beyond the NPS treatment region. Taken together, these results in an immune-incompetent mouse model indicated that NPS induced cell death mechanisms within the TNBC-PDX tumor cells, rather than inducing an immune response. Regardless of the mechanism(s) at hand, these results corresponded with 83% success and NPS treatment efficacy.

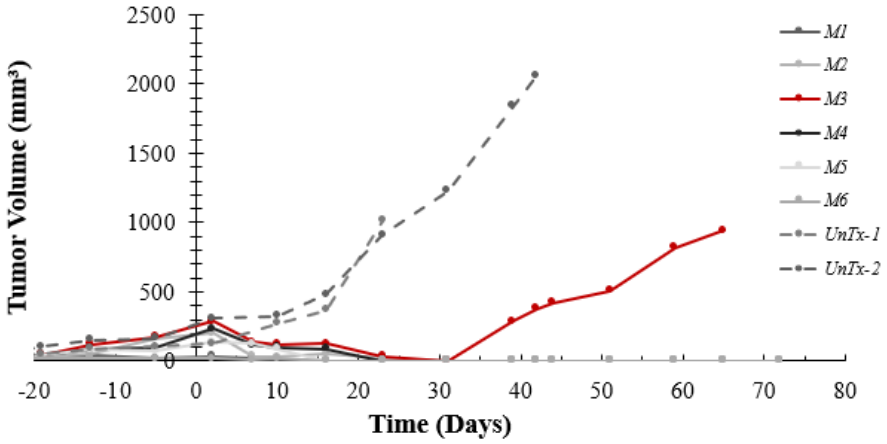

Figure 29. TNBC-PDX tumor volumes in NSG mice after NPS. The left mammary fat pad (MFP) of 6-8-week-old female NSG mice were implanted with TNBC-PDX tumor sections of about $2mm^3$. When the tumors measured 4<8mm in diameter, mice were allocated as untreated (UnTx) controls (n=2) and/or treated (M) with NPS (100ns BL, 1000 pulses, 50kV/cm) (n=6). The resultant tumor growth curves were plotted over time from the day of treatment (day 0). The grey monochromatic color scheme was used to indicate the tumor growth curves of the untreated (dashed lines) and successfully treated (solid lines) NSG mice, while the red solid line indicated tumor progression after treatment with NPS.

NSG mice were also used to examine the efficacy of NPS in the MDA-MB-231 VIM RFP (BC-CDX) tumor model. Tumors were initiated in NSG mice via inoculation of the right MFP with $1x10^6$ MDA-MB-231 VIM RFP cells approximately 4-weeks before treatment (day 0). The resultant BC-CDX tumor volumes for individual NSG mice are shown in Figure 30. Unlike the TNBC-PDX tumor model, these BC-CDX tumors persisted after treatment in all NPS

(100ns BL, 1000 pulses, 50kV/cm) treated (n=3) NSG mice. Additionally, tumor progression appeared to have been unabated in comparison with the untreated (n=2) NSG mice. This was the first-time a cancer has ever been observed to abrogate the effects of NPS to such an extent. Furthermore, these results suggest that the immune system could play a significant role in this BC-CDX cancer model.

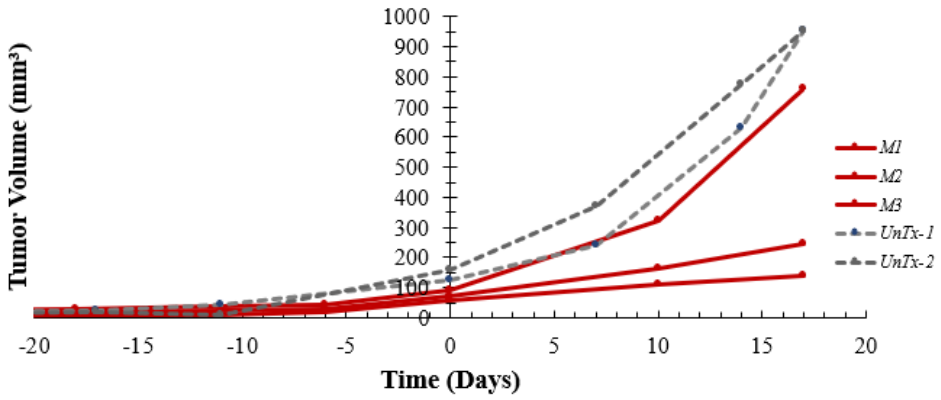

Figure 30. BC-PDX tumor growth curves in NSG mice after NPS. Tumors were initiated in 6-8-week-old female NSG mice via inoculation of the right MFP with $1x10^6$ MDA-MB-231 VIM RFP cells approximately 4-weeks before treatment. Mice were treated with NPS (100ns BL, 1000 pulses, 50kV/cm) (n=3) or allocated as untreated controls (n=2). The resultant BC-CDX tumor growth curves for untreated (dashed lines) and NPS treated (solid red lines) were plotted over time from the day of treatment (day 0).

Section 4.5. Immunity in Murine Melanoma

NPS was investigated for its effects on inducing immunity in the B16-F10 melanoma model. As part of these investigations, peripheral tissues, including the blood and spleen, as well as tissues of the tumor microenvironment (TME), including the tumor and tumor draining lymph node (dLN), were examined in untreated and NPS-Tx BL6 mice on days 1, 3, and 7 after treatment. The tissues were processed into single cell suspensions and stained with fluorescently conjugated antibodies as previously described for acquiring flow cytometric (FC) data. FlowJo™ Software (Windows) Version 10 (Ashland, OR: Becton, Dickinson and Company; 2019) was used for analyses. Figure 31 indicates the preliminary FC gating strategy employed to (a) exclude duplicates, artifacts and/or otherwise illegitimate fluorescence, (b) select the intact cells, excluding cellular debris, and (c) select the CD45+ lymphocytes. This strategy was used as a prelude to subsequent lineage analyses. The number of CD45+ cells of each sample was used to calculate the number of cells per million CD45+ for a given population before calculating the mean and standard error (S.E.).

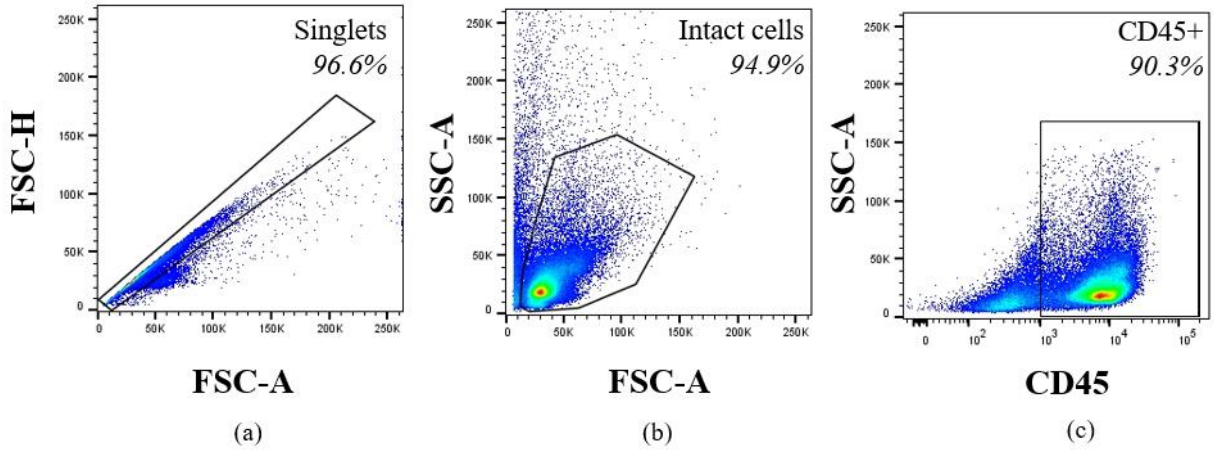

Figure 31. Preliminary leukocyte FC gating strategy. Indicates the initial gating strategy, or parental lineage, used for analyzing all samples. (a) The total number of events were plotted as FSC-A versus FSC-H to gate on the singlet population. The singlet population served as the parent of (b), in which FSC-A was plotted against SSC-A and a gate was drawn around the intact cell population. The intact cell population served as the parent to (c), in which CD45 was plotted against SSC-A and a rectangular gate was used to identify the CD45+ lymphocyte population. The CD45+ population was used as the parent for further classification. FC plots were produced with FlowJo™ Software (Windows) Version 10 (Ashland, OR: Becton, Dickinson and Company; 2019).

Peripheral T cells. NPS induced changes in the memory and effector statuses of CD4+ and CD8+ T cells in the peripheral tissues of B16-F10 tumor bearing BL6 mice. Figure 32 shows the FC gating strategy (a) used to distinguish the effector and memory statuses of the CD4+ (helper) T cells from the CD8+ (cytotoxic) T cells. In this manner, the CD4+ T cells and/or CD8+ T cells served as the parent gates for plotting CD62L (functions as a lymph node adhesion/ homing receptor) versus CD44 (involved in lymphocyte activation) and a quadrant gate was used to indicate the CD62L- CD44+ effector memory (EM), CD62L+ CD44+ central memory (CM), CD62L+ CD44- naïve or stem cell-like memory (N-SCM) T cell phenotypes. The EM (1.2-fold) and N-SCM (3.7-fold) statuses of the CD4+ T cells increased after NPS-Tx, while the CM status decreased (1.75-fold) in the circulating blood. Likewise, the EM and N-SCM (3-fold) statuses of CD8+ T cells increased, while the CM status decreased. The EM status of the CD8+ T cells increased by 1.8-fold within three days albeit the EM CD8+ T cells returned to pre-treatment levels by day 7. The opposite trend was observed for the CM CD8+ T cells, with a modest net loss of 1.2-fold, indicating a shift between effector and central memory statuses. The p-values between groups were calculated and considered significant when p-values were less than 0.01 as indicated by solid black lines.

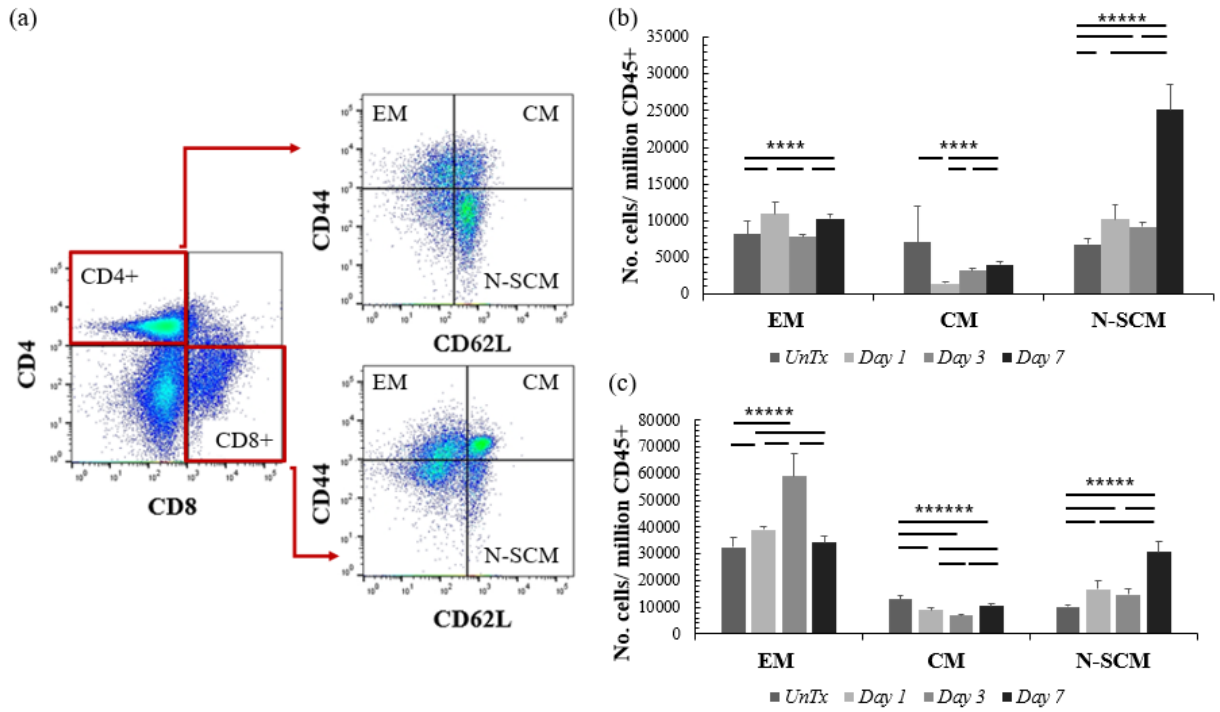

Figure 32. Circulating CD4+ and CD8+ T cells effector and memory statuses. Blood was collected from untreated and NPS-Tx BL6 mice on days 1, 3, and 7 after treatment. Blood aliquots were subjected to ACK RBC lysis buffer for RBC depletion and stained for FC. Representative FC plots (a) indicate the gating strategy. Analyses of the effector memory (EM), central memory (CM), and naïve stem cell-like memory (N-SCM) of CD4+ (a) and CD8+ (b) T cells were conducted. The data represented the results from 6 mice per group with bars representing the mean +S.E. The solid black lines indicate significance, $p<0.01$. FC plots were produced with FlowJo™ Software (Windows) Version 10 (Ashland, OR: Becton, Dickinson and Company; 2019).

In the spleen, Figure 33 the EM (1.5-fold) and N-SCM (1.5-fold) statuses of CD4+ T cells decreased, while the CM status increased by 2.5-fold over the untreated. The CD8+ T cells showed a decrease in CM and EM statuses one day (CM 2.8-fold, EM 1.2-fold) after NPS-Tx but then had an increasing trend from day 1 through day 7 post-treatment (CM 2.4, EM 1.6-fold). The N-SCM status of the CD8+ T cells in the spleen had a decreasing trend within the first three days after NPS-Tx (10-fold) but increased between day 3 and 7 (5-fold).

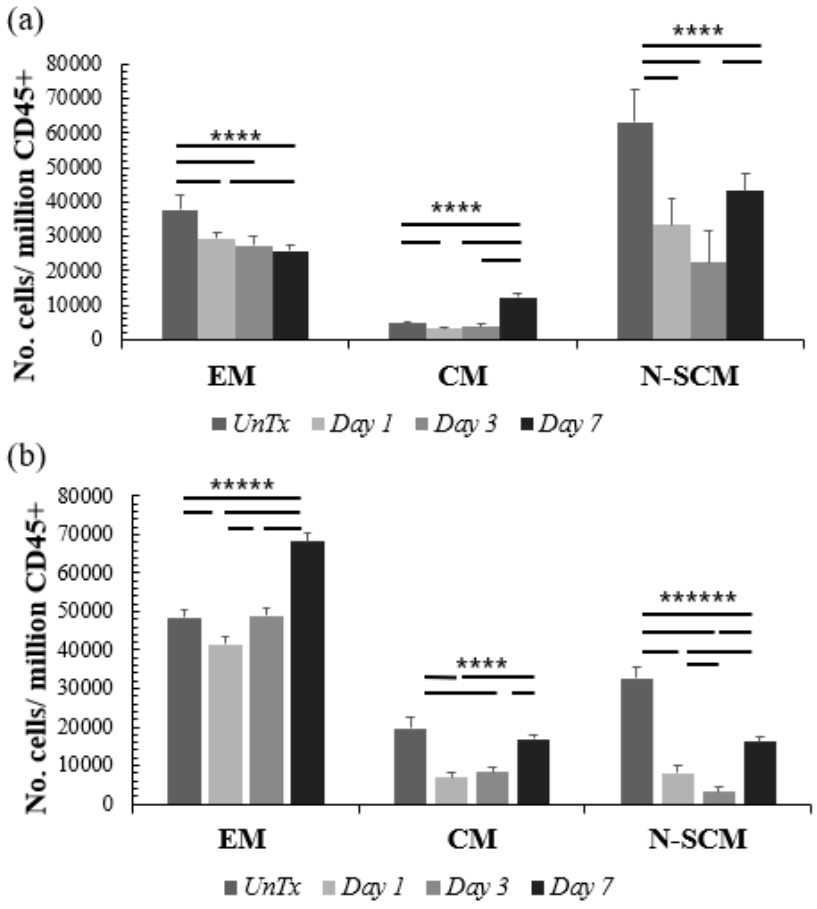

Figure 33. Splenic CD4+ and CD8+ T cells shift effector and memory statuses. Lymphocytes were isolated from the spleens of untreated and NPS-Tx BL6 mice on days 1, 3, and 7 after treatment. Analyses of the effector memory (EM), central memory (CM), and naïve stem cell-like memory (N-SCM) of CD4+ (a) and CD8+ (b) T cells were conducted. The data represented the results from 6 mice per group with bars representing the mean +S.E. The solid black lines indicate significance, $p<0.01$.

The CD4+ and CD8+ T cells in the peripheral tissues were also examined for Interleukin 7 Receptor alpha (IL-7Rα), or CD127, and Programmed Cell Death Protein 1 (PD1) expression as shown in the FC gating strategy in Figure 34. IL-7Rα plays an important role in lymphocyte differentiation, proliferation, and survival [187,188], as well as in the development of lymphoid structures and defensive barriers [189]. The PD1 coinhibitory receptor, checkpoint inhibitor, plays a pivot role in the balancing act of T cell activation [190]. When matched with its ligand, the T cell mediated immune response is down regulated [191]. Thus, detection of IL-7Rα and PD1 T cells were of great interest.

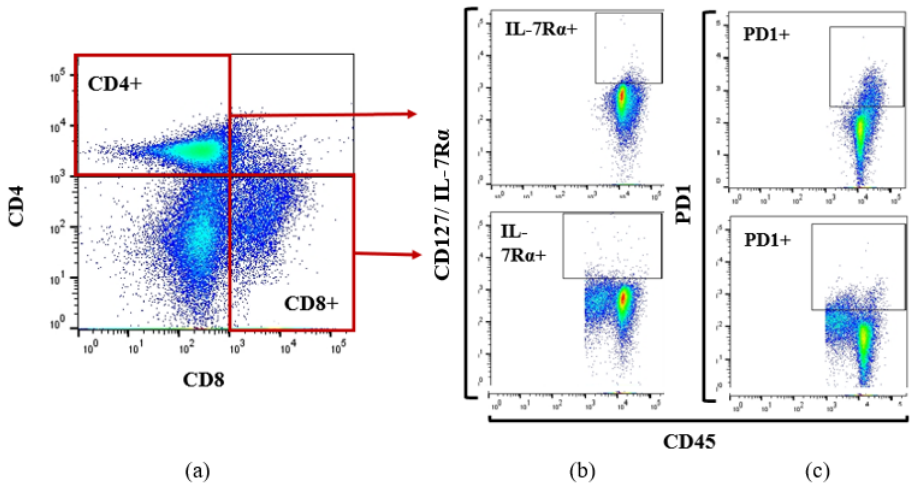

Figure 34. FC gating strategy for IL-7Rα and PD1 expression of T cells. CD4+ and CD8+ T cells (a) served as the parent gates for examining CD127/IL7-Rα (b) and PD1(c). FC plots were produced with FlowJo™ Software (Windows) Version 10 (Ashland, OR: Becton, Dickinson and Company; 2019).

The expression of CD127/IL-7Rα and PD1 were examined in the peripheral tissues of untreated and NPS-Tx BL6 mice on days 1, 3, and 7 after treatment as shown in Figure 35. IL-7Rα+ CD4+ T cells increased in the blood (16-fold) and spleen (4.5-fold). While the number of IL-7Rα+ CD4+ T cells per million were low in these tissues, nearly all differences were significant. IL-7Rα+ CD8+ T cells had an increasing trend in the blood (9-fold) and spleen (5.8-fold). All differences for this population in the peripheral tissues were significant. Interestingly, in the blood, this population increased 22-fold by day 3 and then decreased by 2.3-fold between day 3 and 7. The PD1+ population of CD4+ and CD8+ T cells decreased in the blood (5-fold and 2-fold, respectively) and spleen (1.8-fold and 2.6-fold, respectively) one day after treatment. This was followed by significant increases on day 3 post treatment, with an 8.8-fold increase and 1.3-fold increase for CD4+ T cells and with a 6.7-fold increase and 4.3-fold increase for CD8+ T cells in the blood and spleen, respectively. In the spleen, PD1 expression on CD4+ and CD8+ T cells continued to increase from day 3 to day 7, 1.1-fold and 2.1-fold, respectively; however, in the blood, PD1 expression decreased significantly, with a 2.5-fold decrease in PD1+ CD4+ T cells and 2.1-fold decrease in PD1+ CD8+ T cells. Overall, these fluctuations of IL-7Rα and PD1 indicated that NPS induced dynamic shifts among peripheral CD4+ and CD8+ T cells.

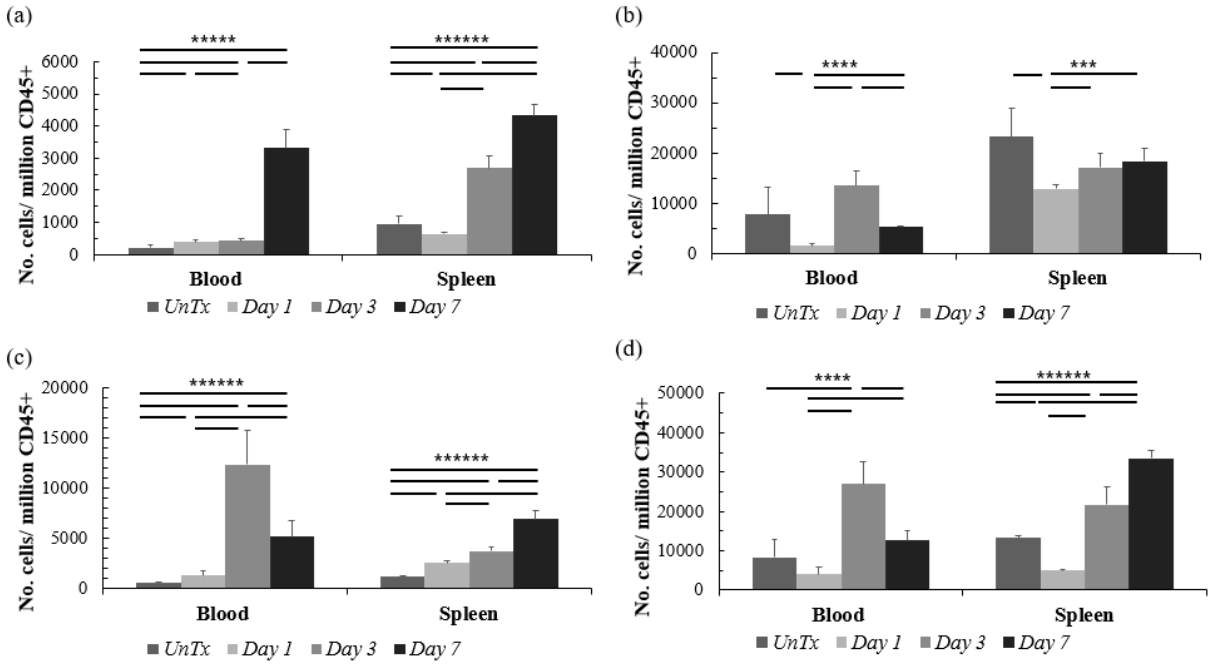

Figure 35. Peripheral IL-7Rα and PD1 expression of T cells after NPS. Lymphocytes were isolated from the blood and spleen of untreated and NPS-Tx BL6 mice on days 1, 3, and 7 after treatment. Analyses of CD127/IL-7Rα+ CD4+ (a) and CD8+ (c) T cells were conducted for the peripheral tissues. Analyses of the PD1+ CD4+ (b) CD8+ (d) T cells were also conducted. The data represented the results from 6 mice per group with bars representing the mean +S.E. The solid black lines indicate significance, $p<0.01$.

T regulatory cells, known for immune suppression, were examined in the peripheral tissues of untreated and NPS-Tx BL6 mice on days 1, 3, and 7 after treatment. As shown in T regulatory cell gating strategy, Figure 36, these T cells are CD4+ and CD25+. These suppressor cells persisted in the blood and spleen after NPS treatment. In the blood, T regulatory cells increased nearly 3-fold by day 7 after NPS. While differences between the untreated and day 1 and day 7 were significant, the expression levels were relatively similar with modest fluctuations between 1.07<1.15-fold. Thus, T regulatory cells persist in the peripheral tissues after NPS.

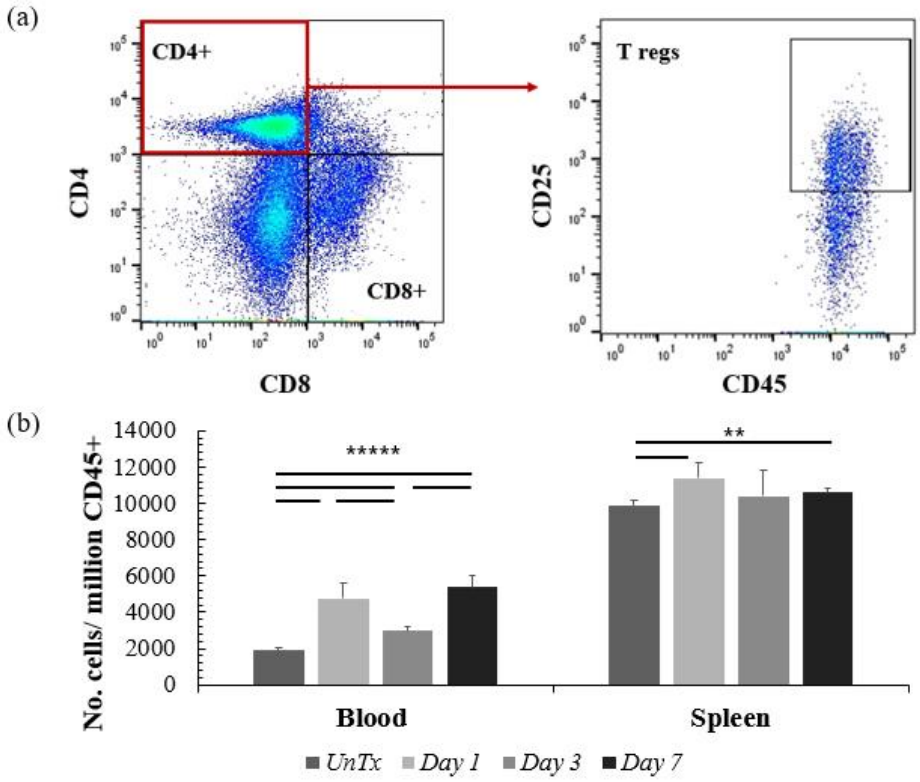

Figure 36. Peripheral regulatory T cells persist after NPS. Lymphocytes were isolated from the blood and spleens of untreated and NPS-Tx BL6 mice on days 1, 3, and 7 after treatment. Representative flow plots (a) indicate the gating strategy for T regulatory cells, CD4+ CD25+. Analyses of the T regulatory cells (b) were conducted for the peripheral tissues. The data represented the results from 6 mice per group with bars representing the mean +S.E. The solid black lines indicate significance, $p<0.01$. FC plots were produced with FlowJo™ Software (Windows) Version 10 (Ashland, OR: Becton, Dickinson and Company; 2019).

Peripheral myelomonocytic cells. The myelomonocytic cells were examined in the in the peripheral tissues of untreated and NPS-Tx BL6 mice after treatment. The flow cytometric gating strategy for analyzing the myeloid subsets is shown in Figure 37. Initially, the dendritic cells (DC) and antigen presenting, macrophages (APC, macs) were distinguished by plotting leukocyte population as CD11b versus CD11c. The CD11c+ CD11b- cells are DC, while the CD11c- CD11b+ cells are APC and macrophages. The APC, macs population served as the parent for identifying the tumor associated macrophages (TAMS) which have the CD11b+ CD11c- F4/80+ phenotype. The F4/80- population served as the parent for identifying the myeloid derived suppressor cells (MDSC), which have the phenotype CD11b+ CD11c- F4/80- Gr-1+. The expression of Major Histocompatibility Complex II (MHC II) and CD86, also known as B7-2, are variably expressed by these myeloid subsets as they play multifaceted roles, especially with respect to the T cell response. Thus, the identified myelomonocytic populations were examined for expression of MHC II and CD86.

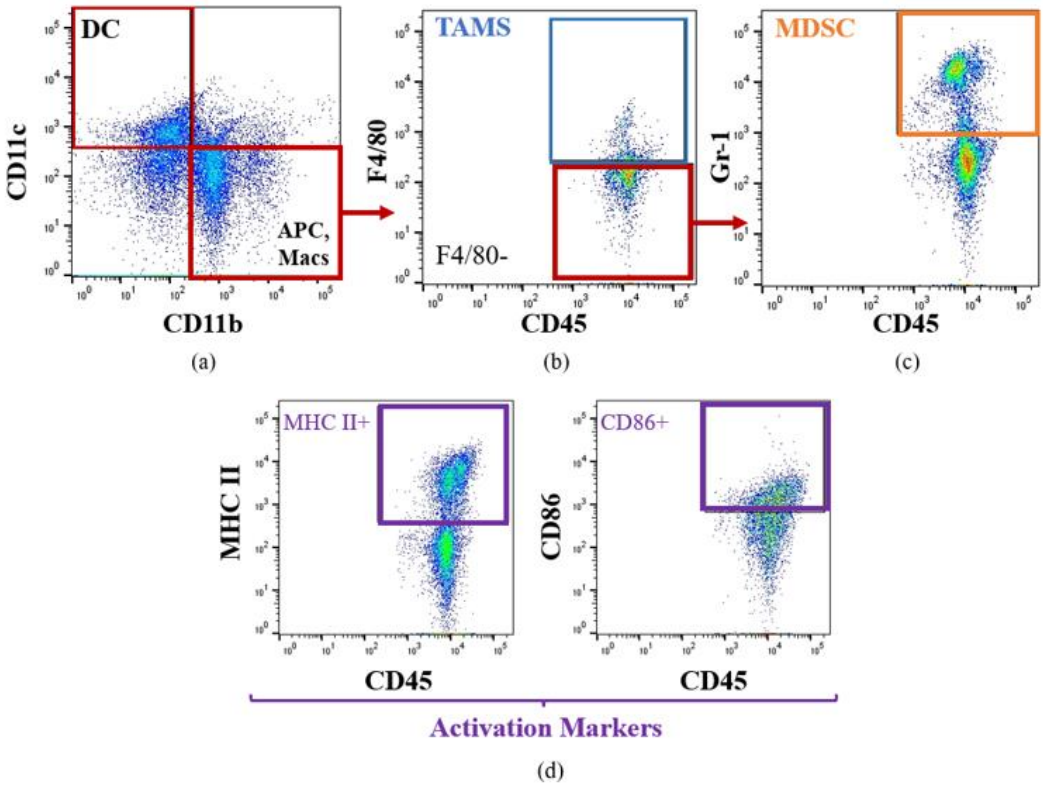

Figure 37. FC gating strategy of myelomonocytic cell populations. (a) Representative FC plot used to distinguish the DC population, CD11b- CD11c+, from the antigen presenting cells (APCs) and macrophages (macs), CD11b+ CD11c-. (b) The CD11b+ CD11c- population was used to distinguish the F4/80+ cells, tumor associated macrophages (TAMS), from the F4/80- cells. (c) The F4/80- cells were examined for Gr-1 expression, indicative of myeloid derived suppressor cells (MDSCs). (d) MHC II and CD86 activation marker were subsequently analyzed for these populations. The FC plots were produced with FlowJo™ Software (Windows) Version 10 (Ashland, OR: Becton, Dickinson and Company; 2019).

The peripheral tissues of untreated and NPS-Tx BL6 mice were examined for myelomonocytic cell populations after NPS. The blood and spleen were examined for DC, APC, macs, TAMS, and MDSC (Figure 38). DC in the blood significantly decreased one day after treatment (1.5-fold), followed by an increasing trend from day 1-7 (1.5-fold) post-treatment, although there was no net difference. DC in the spleen significantly decreased after NPS with a net loss of 6.4-fold. The APC, macs population significantly decreased in the blood (1.3-fold), while they significantly increased in the spleen (1.4-fold). TAMS significantly decreased in the blood (1.7-fold) after NPS. TAMS in the spleen significantly decreased day 1 post-treatment (2.2-fold), then had a significantly increasing trend from day 1-7 (3-fold), resulting in a net increase of 1.3-fold. In the blood, MDSC significantly increased on day 1 (1.4-fold) post-treatment, then significantly decreased from day 1-7(1.3-fold). MDSC in the spleen significantly increased after NPS by 2-fold.

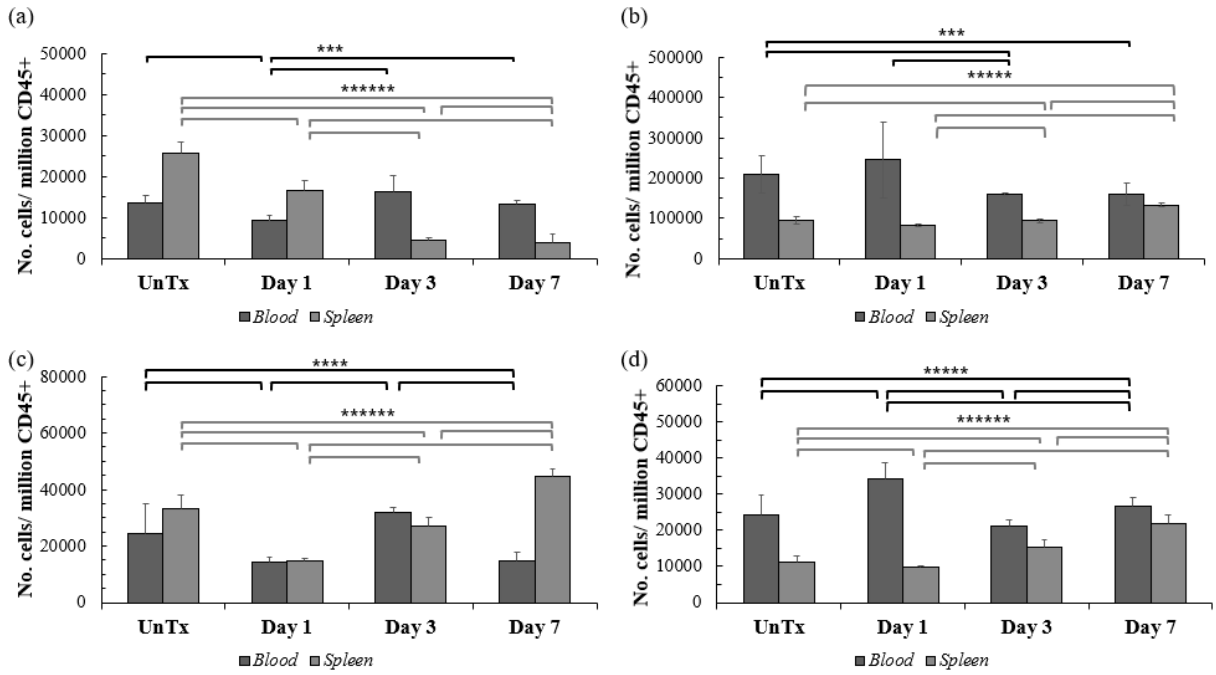

Figure 38. Peripheral myelomonocytic cell populations. Myelomonocytic cell populations were examined in the peripheral tissues, blood and spleen, of untreated and NPS-Tx BL6 mice on day 1, 3, and 7 after treatment. The dendritic cells (a), antigen presenting cells and macs (b), tumor associated macrophages (TAMS) (c), and myeloid derived suppressor cells (MDSC) (d) were analyzed in the blood and spleen. The data represented the results from 6 mice per group with bars representing the mean +S.E. The black and grey brackets indicate significance, $p<0.01$, for the blood and spleen, respectively.

The peripheral APC and MDSC populations were analyzed for CD86 and MHC II activation markers (Figure 39). CD86+ APC, macs significantly increased by about 2-fold after NPS in the blood and spleen. A similar trend was observed for the MDSC populations in the blood (1.7-fold) and spleen (3.4-fold). Analyses of the MHC II+ MDSC showed significant

increasing trends in both the blood and spleen, with net gains of 1.8-fold and 2.8-fold, respectively.

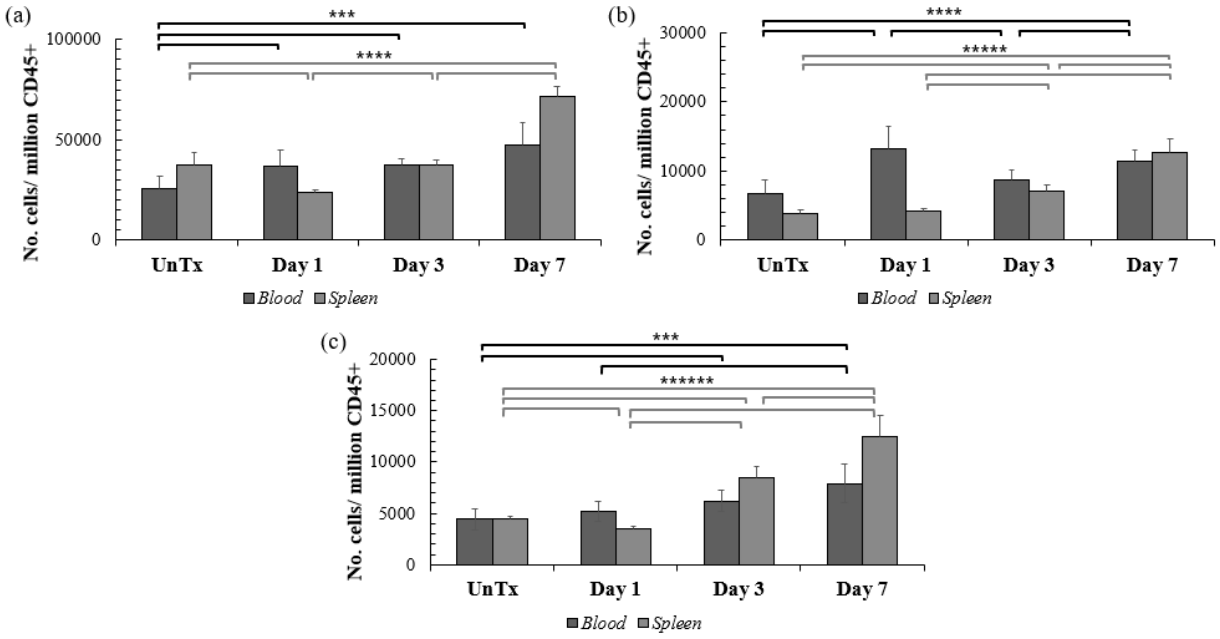

Figure 39. Activation of peripheral myelomonocytic cell populations. CD86 and MHC II activation of myelomonocytic cell populations were examined in the peripheral tissues, blood and spleen, of untreated and NPS-Tx BL6 mice on day 1, 3, and 7 after treatment. CD86+ activation was examined for the antigen presenting cells (APC) and macrophages (macs) (a) and myeloid derived suppressor cells (MDSC) (b) populations. The MDSC population was also examined for MHC II activation (c). The data represented the results from 6 mice per group with bars representing the mean +S.E. The black and grey brackets indicate significance, $p<0.01$, for the blood and spleen, respectively.

Macrophage polarization statuses were also of interest, since they, too, are instrumental in cancer recognition and evasion. Figure 40 shows the FC gating strategy employed for examining the macrophage polarization statuses. Initially, leukocytes were plotted as CD11b versus CD68. A rectangular gate was drawn around the macrophage population, CD11b+ CD68+. This population served as the parent for plotting Erg2 versus CD38. The M1 polarized macrophages are Erg2- CD38+. These pro-inflammatory macrophages play a positive activating role in the immune response, including recognition of atypical cancer cells. The M2 polarized macrophages are Erg2+ CD38-. These anti-inflammatory macrophages play a negative suppressive role in the immune response, often included as a mechanism of cancer evasion. Thus, the yin-yang relationship between macrophage polarization statuses were examined.

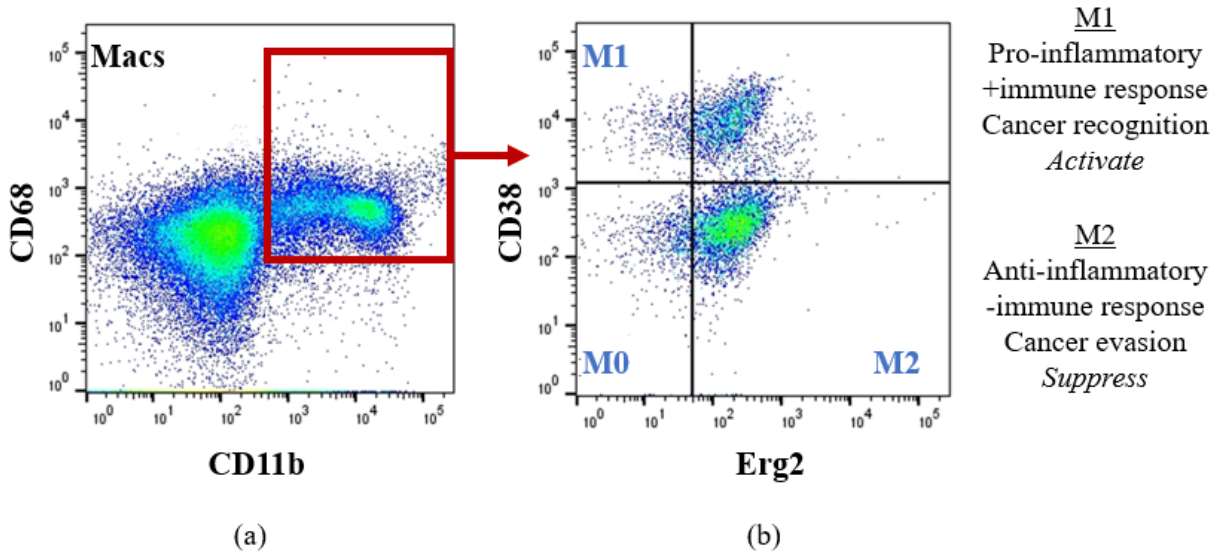

Figure 40. Macrophage polarization FC gating strategy. Macrophages were identified by plotting leukocytes as CD11b versus CD68 (a). The macrophage population, CD11b+ CD68+, served as the parent for plotting Erg2 versus CD38 (b). The M0, M1 and M2 polarization statuses are indicated and important aspects regarding the M1 and M2 statuses are shown to the right. The FC plots were produced with FlowJo™ Software (Windows) Version 10 (Ashland, OR: Becton, Dickinson and Company; 2019).

The peripheral tissues were analyzed for M1 and M2 macrophage polarization statuses in untreated and NPS-Tx BL6 mice. In Figure 41, the blood and spleens of untreated and NPS-Tx BL6 mice were examined for M1 and M2 polarization statuses on day 1, 3, and 7 after treatment. M1 macrophages in the blood had an increasing trend with a net gain of about 1.4-fold. In the spleen, M1 macrophages significantly increased by about 1.6-fold. In the blood, M2

macrophages significantly decreased through day 3 after treatment (2.8-fold), then significantly increased from day 3-7 (2-fold). M2 macrophages in the spleen significantly decreased by 2.2-fold after NPS through day 7.

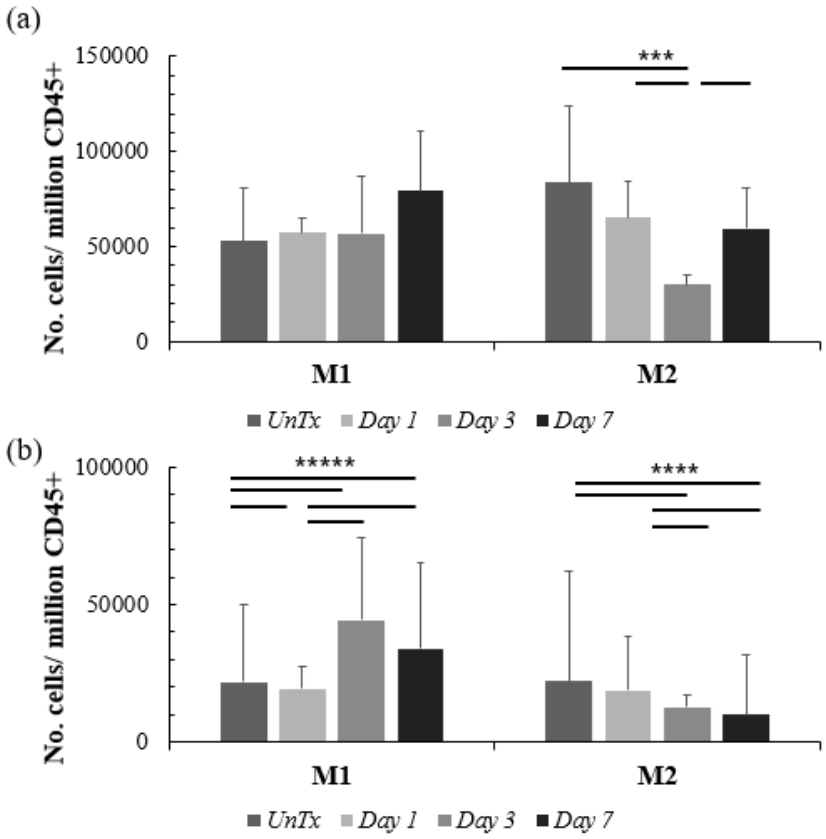

Figure 41. Peripheral M1 and M2 macrophages. The blood (a) and spleen (b) of untreated and NPS-Tx BL6 mice were examined for M1 and M2 macrophages on day 1, 3, and 7 after treatment. The data represented the results from 6 mice per group with bars representing the mean +S.E. The solid black lines indicate significance, $p<0.05$.

Tumor microenvironment: T cells in the B16-F10 tumor and dLN. The effector and memory statuses of CD4+ and CD8+ T cells were examined in the B16-F10 TME of untreated and NPS-Tx BL6 mice on days 1, 3, and 7 after treatment (Figure 42). While NPS-Tx induced tumor death, limiting the tumor examination period to day 1 post-treatment, the dLN served as another means of detecting the NPS induced effects on immunity in the TME. Thus, the effector and memory statuses of CD4+ and CD8+ T cells in the tumor were examined in untreated and NPS-Tx BL6 mice one day post-treatment. The EM status within the tumor decreased by 3.8-fold and 1.2-fold for the CD4+ and CD8+ T cells, respectively. The presence of CM T cells also decreased by 276-fold for the CD4+ T cells and 2.4-fold for the CD8+ T cells, although these differences were not considered significant. Interestingly, the N-SCM status of CD4+ T cells significantly decreased (19-fold), while this population of CD8+ T cells significantly increased (4.5-fold). The effector and memory statuses of CD4+ and CD8+ T cells were also examined in the tumor dLN of untreated and NPS-Tx BL6 mice on day 1, 3, and 7 after treatment. The EM (1.5-fold) and CM (3-fold) statuses of CD4+ T cells significantly decreased one day after treatment, then increased from day 1 through 7, 1.1-fold and 4.7-fold, respectively. The N-SCM CD4+ and CD8+ T cells had a similar trend, with decreases of 1.7-fold and 2.6-fold, respectively, and then increased (CD4+ 2.2-fold, CD8+ 5.5-fold) from day 1 through 7. The EM status of the CD8+ T cells significantly increased, 1.8-fold, within the first day after NPS, then decreased (1.3-fold) by day 7. The CM status of the CD8+ T cells significantly decreased (3.3-fold) one day after NPS-Tx and then had an increasing trend through day 7 post-treatment (5.3-fold).

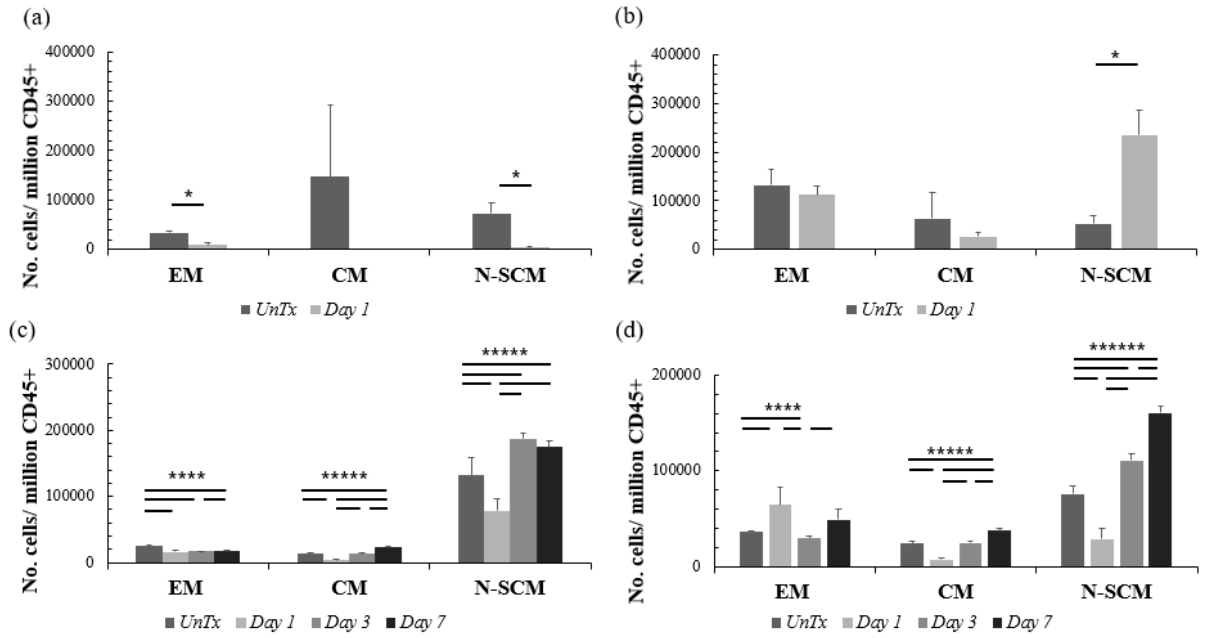

Figure 42. TME effector and memory CD4+ and CD8+ T cells. Lymphocytes were isolated from the tumor and dLN of untreated and NPS-Tx BL6 mice on days 1, 3, and 7 after treatment. Analyses of the effector memory (EM), central memory (CM), and naïve stem cell-like memory (N-SCM) of CD4+ (a) and CD8+ (b) T cells were conducted for the B16-F10 tumor and dLN, as shown in (c) and (d), respectively. The data represented the results from 6 mice per group with bars representing the mean +S.E. The solid black lines indicate significance, $p<0.01$.

The expression of CD127/IL-7Rα and PD1 were examined for the CD4+ T cells in the TME of untreated and NPS-Tx BL6 mice on days 1, 3, and 7 after treatment as shown in Figure 43. IL-7Rα+ CD4+ T cells significantly decreased in the tumor (21-fold) and dLN (3.5-fold) one day post-treatment; however, in the dLN, this was followed by a significant, 10.7-fold increase between day 1 and 7. Regardless of the initial decrease in the CD127/IL-7Rα+ CD4+ T cell

population in the dLN, the presence of this population had a net gain by about 3.1-fold. The PD1+ CD4+ T cells showed a similar trend in the tumor and dLN. Initially, the presence of PD1+ CD4+ T cells significantly decreased in the tumor (17.3-fold) and dLN (2.3-fold). This was followed by a significant increasing trend from day 1 through 7 in the dLN (2.5-fold), albeit the net increase was modest (1.1-fold).

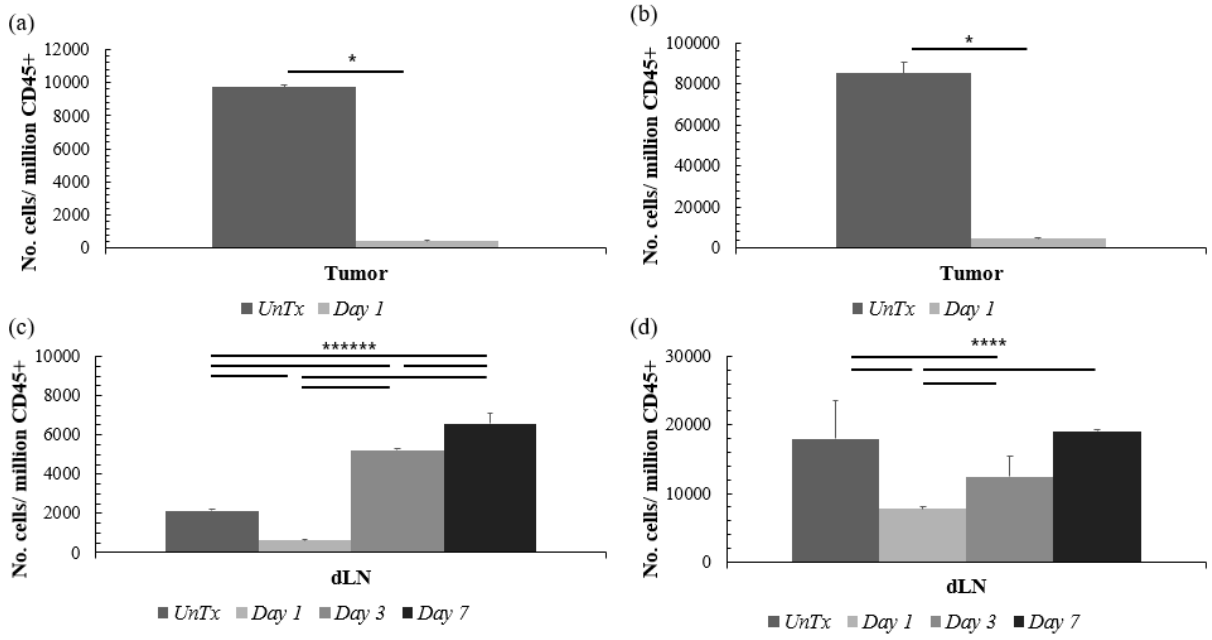

Figure 43. IL-7Rα and PD1 expression of CD4+ T cells in the TME after NPS. Lymphocytes were isolated from the tumor and dLN of untreated and NPS-Tx BL6 mice on days 1, 3, and 7 after treatment. Analyses of CD127/IL-7Rα+ CD4+ T cells were conducted for the tumor (a) and dLN (c). Analyses of the PD1+ CD4+ T cells were also conducted for the tumor (b) and dLN (d). The data represented the results from 6 mice per group with bars representing the mean +S.E. The solid black lines indicate significance, $p<0.01$.

The expression of CD127/IL-7Rα and PD1 were examined for the CD8+ T cells in the TME of untreated and NPS-Tx BL6 mice on days 1, 3, and 7 after treatment as shown in Figure 44. IL-7Rα+ CD8+ T cells significantly increased in the tumor (3.4-fold) and dLN (4.8-fold) after NPS. The PD1+ CD8+ T cells decreased in the tumor (1.2-fold) and significantly decreased in the dLN (2.2-fold) one day after NPS; however, in the dLN, this population significantly increased through day 7 post-treatment (5.8-fold). The PD1+ CD8+ T cells in the dLN had a significant net increase of about 2.6-fold.

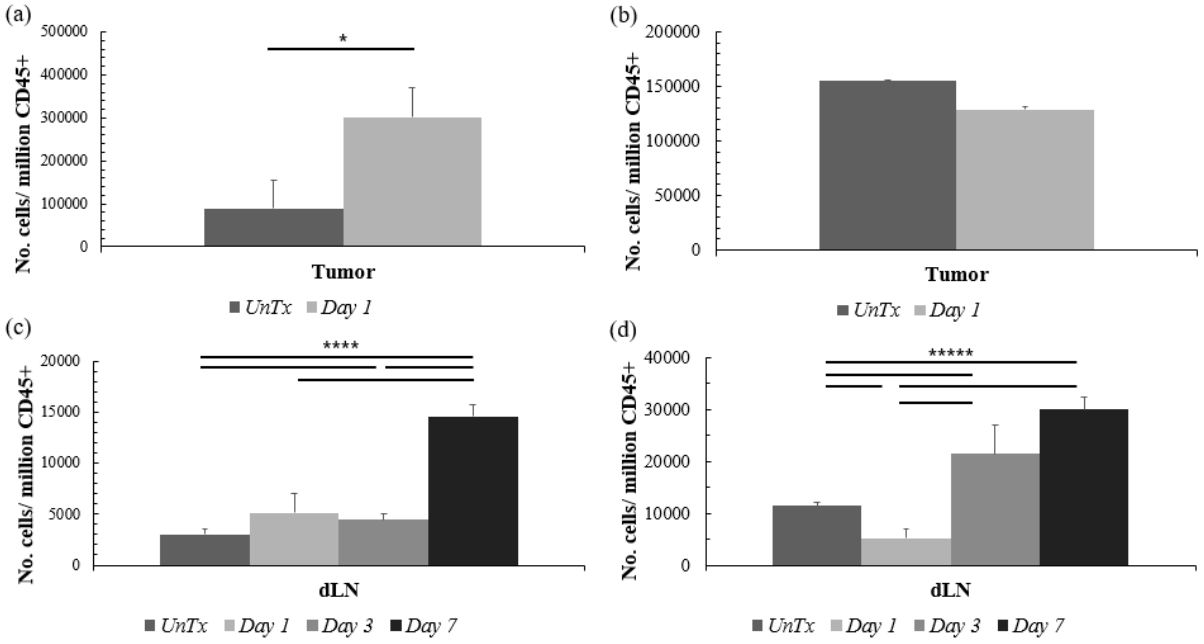

Figure 44. IL-7Rα and PD1 expression of CD8+ T cells in the TME after NPS. Lymphocytes were isolated from the tumor and dLN of untreated and NPS-Tx BL6 mice on days 1, 3, and 7 after treatment. Analyses of CD127/IL-7Rα+ CD8+ T cells were conducted for the tumor (a) and dLN (c). Analyses of the PD1+ CD8+ T cells were also conducted for the tumor (b) and dLN (d). The data represented the results from 6 mice per group with bars representing the mean +S.E. The solid black lines indicate significance, $p<0.01$.

The CD4+ T cells were further examined for regulatory status in the TME. CD4+ T lymphocytes in B16-F10 tumors and dLN were analyzed in untreated and NPS-Tx BL6 mice on days 1, 3, and 7 for CD25 expression, indicative of T regulatory cells (Figure 45). T regulatory cells significantly decreased (3.5-fold) in the tumor one day after NPS. A similar decrease (1.6-fold) was observed in the dLN one day post-treatment; however, regulatory T cells had a significant increasing trend from day 1 through 7, with their presence nearly doubling (1.9-fold).

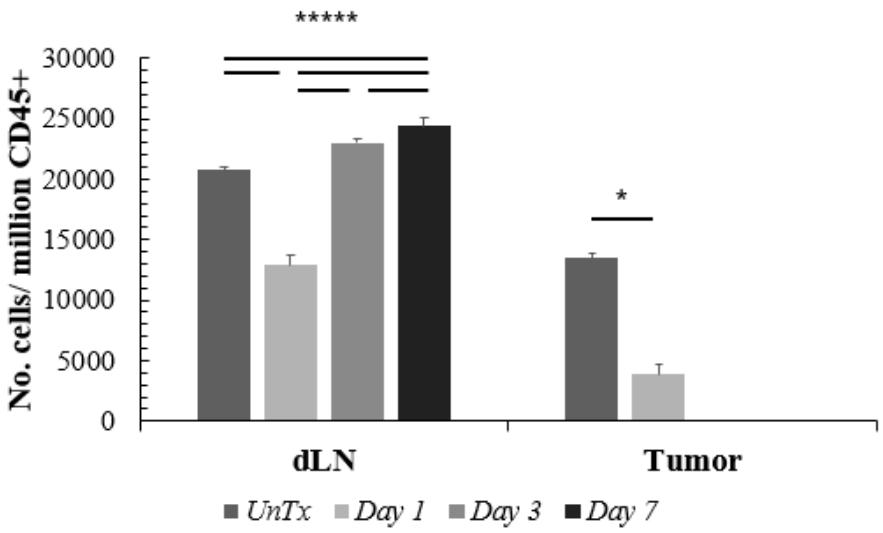

Figure 45. Regulatory T cells persist in the TME after NPS. Lymphocytes were isolated from the tumor and dLN of untreated and NPS-Tx BL6 mice on days 1, 3, and 7 after treatment. Analyses of the T regulatory cells (b) were conducted for the TME. The data represented the results from 6 mice per group with bars representing the mean +S.E. The solid black lines indicate significance, $p<0.01$.

Since intratumoral accumulation of activated T regulatory cells is one of the suppressive mechanisms in which cancers evade the immune system, it was worthwhile to examine them for expression of CD127/ IL-7Rα [191,192]. The T regulatory cells (CD4+ CD25+) were examined for CD127/ IL-7Rα expression in the tumor dLN of untreated and NPS-Tx BL6 mice on days 1, 3, and 7, as shown in Figure 46. IL-7Rα significantly decreased (1.6-fold) one day after NPS; however, this was followed by significant increases on days 3 and 7, 1.9-fold and 2.3-fold. Overall, the presence of IL-7Rα+ T regulatory cells significantly increased by 1.4-fold from the untreated to day 7 post-treatment.

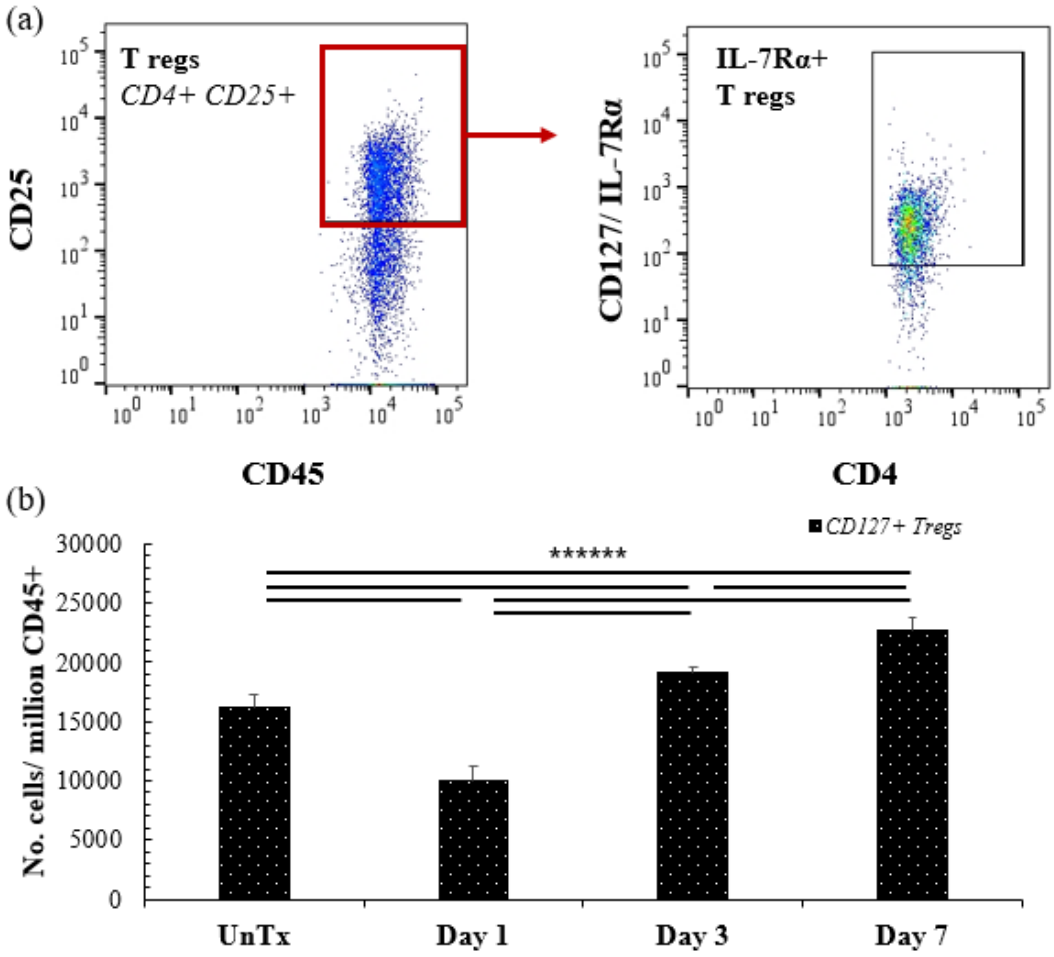

Figure 46. Activated Regulatory T cells persist in the TME after NPS. T regulatory cells (CD4+ CD25+) in the tumor dLN of untreated and NPS-Tx BL6 mice on days 1, 3, and 7 after treatment were examined for CD127/ IL-7Rα expression as shown in the FC gating strategy (a). Analyses of the CD127/ IL-7Rα+ T regulatory cells (b) were conducted for the dLN. The data represented the results from 6 mice per group with bars representing the mean +S.E. The solid black lines indicate significance, $p<0.01$. FC plots were produced with FlowJo™ Software (Windows) Version 10 (Ashland, OR: Becton, Dickinson and Company; 2019).

Tumor microenvironment: myelomonocytic cells in the B16-F10 tumor and dLN.

Myelomonocytic cells were analyzed in the TME. The tumor and dLN of untreated and NPS-Tx BL6 mice were analyzed for dendritic cells and APC, macs after NPS on days 1, 3, and 7. As shown in Figure 47, dendritic cells (7.3-fold) and APC, macs (5.6-fold) populations significantly increased on day 1 post-treatment by 7.3-fold and 5.6-fold, respectively. In the dLN, dendritic cells appeared to have an increasing trend through day 3 post-treatment (1.4-fold) but had an overall significant net decrease of 3.5-fold. The APC, macs population significantly increased (2.2-fold) through day 7.

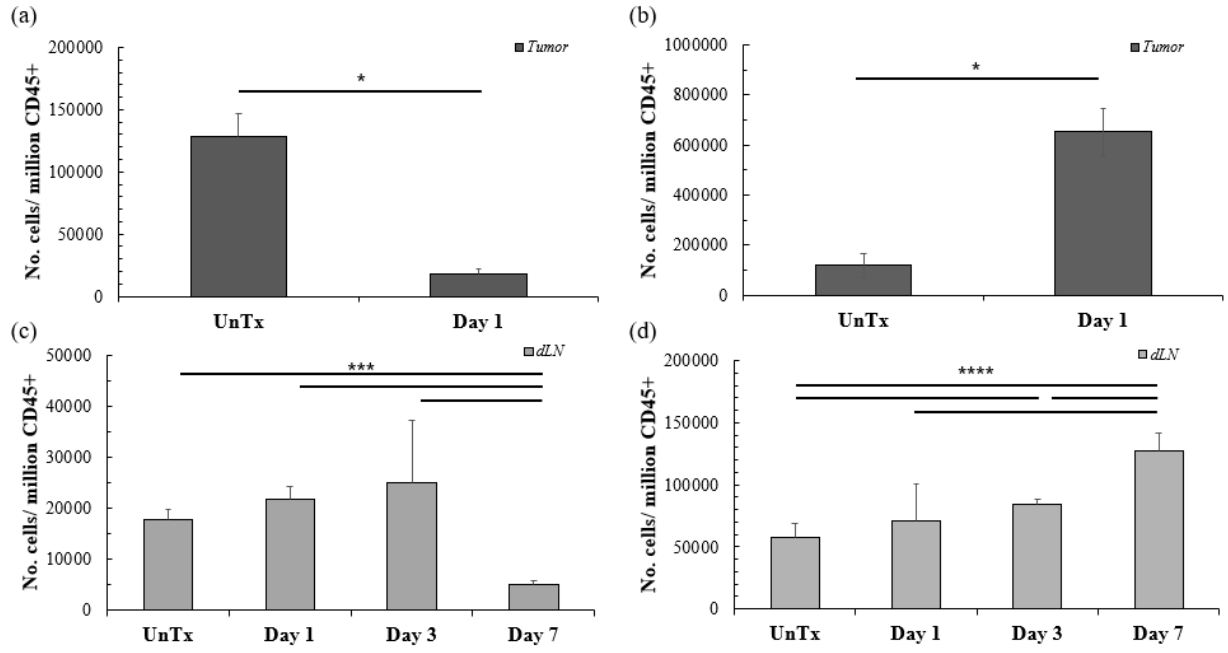

Figure 47. Dendritic cells and antigen presenting cells in the TME. The B16-F10 tumor and dLN of untreated and NPS-Tx BL6 mice were examined for myelomonocytic cell populations on day 1, 3, and 7 after treatment. Dendritic cells (a) and APC, macs (b) populations were examined in the tumor of untreated and NPS-Tx BL6 mice one day after treatment. The dLN were also examined for dendritic cells (c) and APC, macs (d) in untreated and NPS-Tx BL6 mice on day 1, 3, and 7 after treatment. The data represented the results from 6 mice per group with bars representing the mean +S.E. The solid black lines indicate significance, $p<0.05$.

TAMS and MDSC were also analyzed in the tumor and dLN (Figure 48). In the tumor, TAMS and MDSC significantly increased on day 1 post-treatment by 5.6-fold and 7-fold, respectively. TAMS and MDSC also increased by 4-fold and 4.8-fold, respectively, in the dLN through day 7.

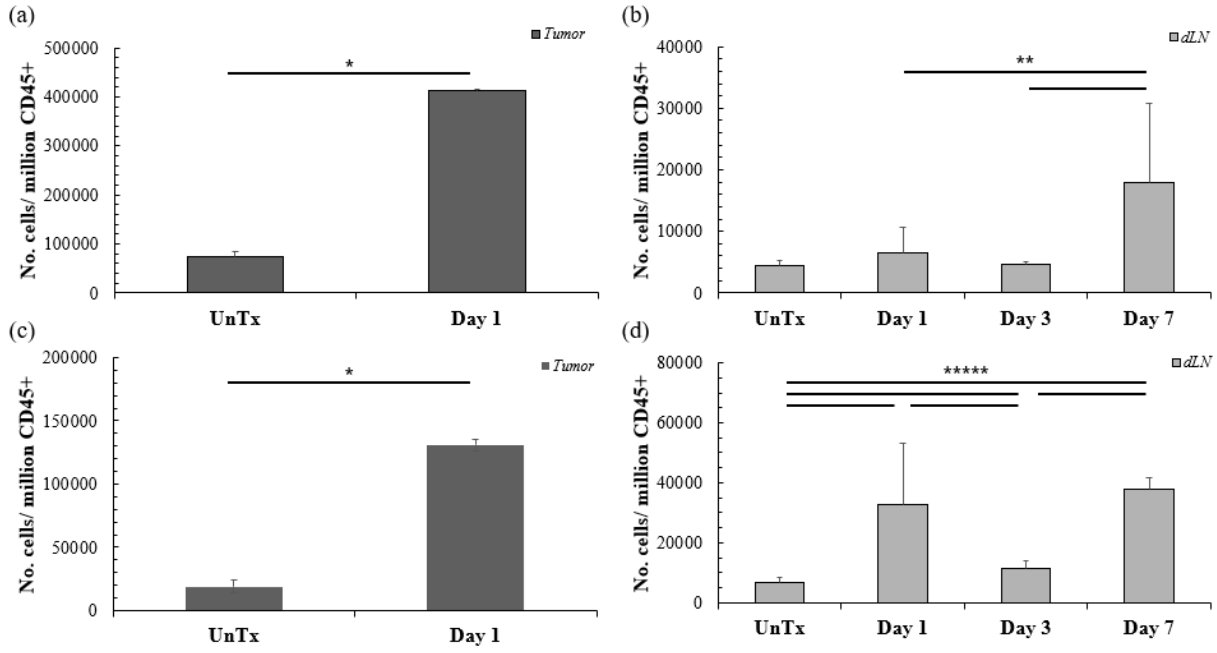

Figure 48. TAMS and MDSC in the TME. The B16-F10 tumor and dLN of untreated and NPS-Tx BL6 mice were examined for myelomonocytic cell populations on day 1, 3, and 7 after treatment. Tumor associated macrophages (TAMS) (a) and myeloid derived suppressor cells (MDSC) (c) populations were examined in the tumor of untreated and NPS-Tx BL6 mice one day after treatment. The dLN were also examined for TAMS (b) and MDSC (d) in untreated and NPS-Tx BL6 mice on day 1, 3, and 7 after treatment. The data represented the results from 6 mice per group with bars representing the mean +S.E. The solid black lines indicate significance, $p<0.05$.

The APC, macs populations in the TME were analyzed for expression of CD86 (Figure 49). The CD86+ APC, macs population significantly increased in the tumor and dLN after treatment with NPS with net gains of 6.5-fold in the tumor after one day and 3.3-fold in the dLN on day 7.

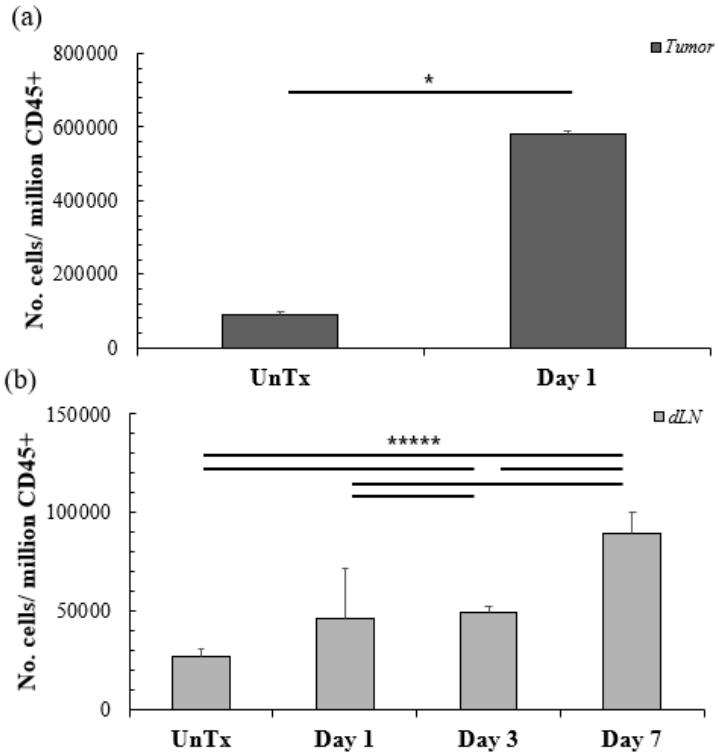

Figure 49. APC, macs activation in the TME. The B16-F10 tumor and dLN of untreated and NPS-Tx BL6 mice were examined for activation of myelomonocytic cell populations on day 1, 3, and 7 after treatment. The APC, macs were examined for CD86+ activation in the tumor (a) and dLN (b). The data represented the results from 6 mice per group with bars representing the mean +S.E. The solid black lines indicate significance, $p<0.05$.

The MDSC population was also analyzed for expression of CD86 and MHC II in the TME (Figure 50). In the tumor, MDSC expression of CD86 (7.6-fold) and MHC II (6.5-fold) significantly increased one day after NPS. MDSC expression of CD86 and MHC II also significantly increased through day 7 post-treatment, with net gains of 7.5-fold and 7-fold, respectively.

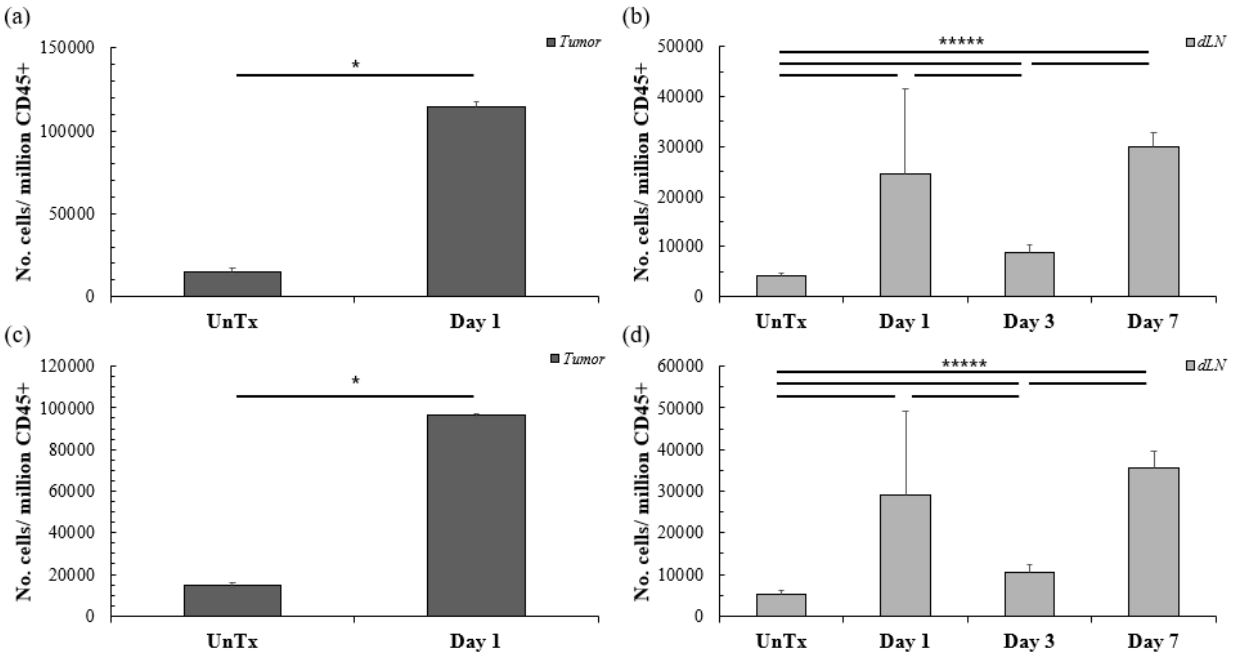

Figure 50. MDSC activation in the TME. The B16-F10 tumor and dLN of untreated and NPS-Tx BL6 mice were examined for activation of myelomonocytic cell populations on day 1, 3, and 7 after treatment. The MDSC were examined for CD86+ activation in the tumor (a) and dLN (b). The MDSC were examined for MHC II+ activation in the tumor (c) and dLN (d). The data represented the results from 6 mice per group with bars representing the mean +S.E. The solid black lines indicate significance, $p<0.05$.

The macrophage polarization statuses were examined in the TME. B16-F10 tumors and dLN from untreated and NPS-Tx BL6 mice were analyzed for M1 and M2 macrophages (Figure 51). M1 macrophages significantly increased by 3.5-fold one day after treatment, while M2 macrophages modestly increased by 1.2-fold. In the dLN, M1 macrophages significantly increased by 3-fold on day 7 after treatment, while M2 macrophages were barely even detectable.

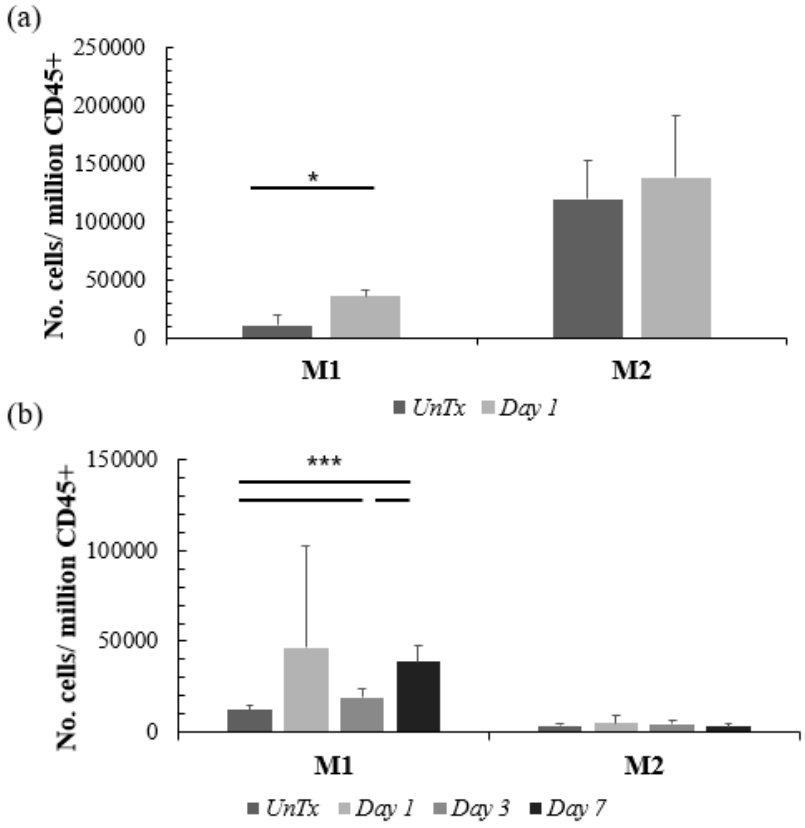

Figure 51. M1 and M2 macrophages in the TME. The B16-F10 tumor (a) and dLN (b) of untreated and NPS-Tx BL6 mice were examined for M1 and M2 macrophages on day 1, 3, and 7 after treatment. The data represented the results from 6 mice per group with bars representing the mean +S.E. The solid black lines indicate significance, $p<0.05$.

NK and NK-T cells in the spleen and TME. The natural killer (NK) and natural killer T lymphocytes (NK-T) were examined in the in the spleens and B16-F10 tumors of untreated and NPS-Tx BL6 mice after treatment. The flow cytometric gating strategy for analyzing the subsets of NK cells is shown in Figure 52. Initially, lymphocytes were plotted as CD335/ NKp46 versus CD161/ NK1.1. The NK cells were defined as the double positive population, CD335/ NKp46+ CD161/ NK1.1+. This population served as the parent for defining NK-T cells, which were also CD3+, and for examining the functional statuses by plotting the NK cells as CD11b versus CD27 [193]. In short, the CD11b- CD27+ NK cells are known for their effector function as they produce cytokines and respond to chemokines [193]. These cells are less cytotoxic and interact with dendritic cells [193]. Likewise, the CD11b+ CD27+ NK cells also interact with dendritic cells and have potent cytotoxic and effector functions [193]. In addition, the Natural Killer Group 2 member D (NKG2D) and Killer cell Lectin-like Receptor subfamily G member 1 (KLRG1) expression was examined as they orchestrate mechanisms of cytotoxicity [193]. The CD11b+ CD27- NK cells also express KLRG1 and are known for their highly cytotoxic functionality despite their mature senescent stature [193]. Thus, KLRG1 expression was examined for the CD11b+ CD27+ and CD11b+ CD27- NK cell populations.

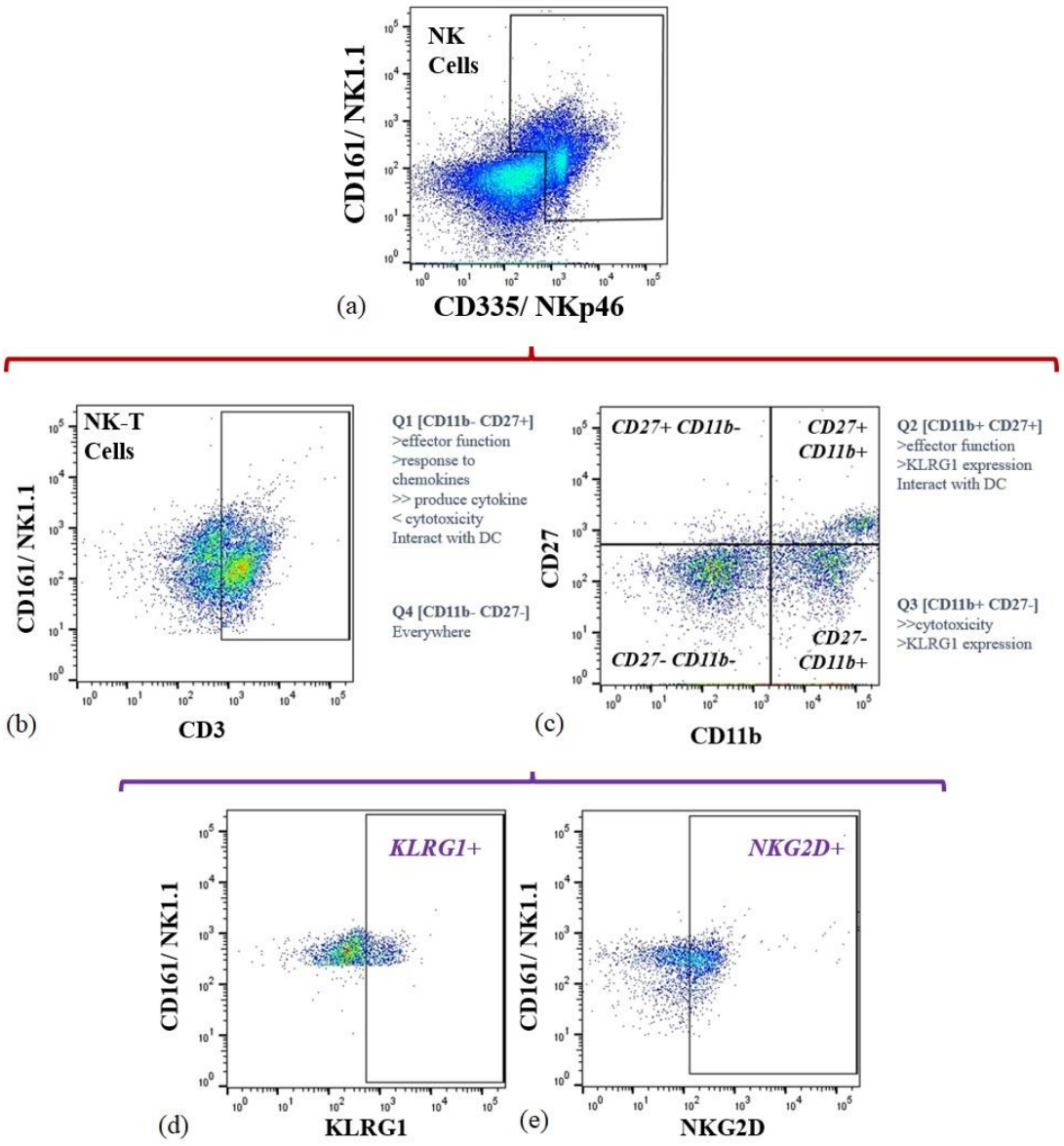

Figure 52. FC gating strategy of NK and NK-T cells. The NK cells (a) were gated as CD335/NKp46+ and CD161/ NK1.1+. This population was used as the parent gate for identifying CD3+ NK-T cells (b) and effector statuses (c) which were plotted as CD11b versus CD27. Populations of NK cells were examined for KLRG1 (d) and NKG2D (e). The FC plots were produced with FlowJo™ Software (Windows) Version 10 (Ashland, OR: Becton, Dickinson and Company; 2019).

Splenocytes from untreated and NPS-Tx BL6 mice were analyzed on days 1, 3, and 7 after treatment for NK cell populations (Figure 53). In the spleen, both NK (1.5-fold) and NK-T cells (1.2-fold) had a significant decreasing trend after treatment. The functional statuses of NK cells were analyzed for CD11b and CD27 expression. After NPS, the CD11b- CD27+ and CD11b+ CD27+ NK cells increased by 1.4-fold and 5-fold, respectively. The more cytotoxic CD11b+ CD27- NK cells had a significant net decrease of about 1.3-fold after treatment, albeit the levels fluctuated by about 1.2-fold between days 1-3 and days 3-7. Expression of KLRG1 was analyzed for the CD11b+ CD27+ and CD11b+ CD27- NK cells. The CD11b+ CD27+ NK cells significantly increased 4-fold after NPS. The increase in the CD11b+ CD27- NK cells was also significant but with a modest net gain by 1.2-fold. Once again, this population had a fluctuating trend, with a peak difference of about 3-fold between day 1-3. Cytotoxic NK cells and NK-T cells were examined for NKG2D expression as an indicator of activation. Interestingly, both CD11b+ CD27- NK cells and NK-T cells significantly decreased their expression of NKG2D by 11-fold and 7-fold, respectively.

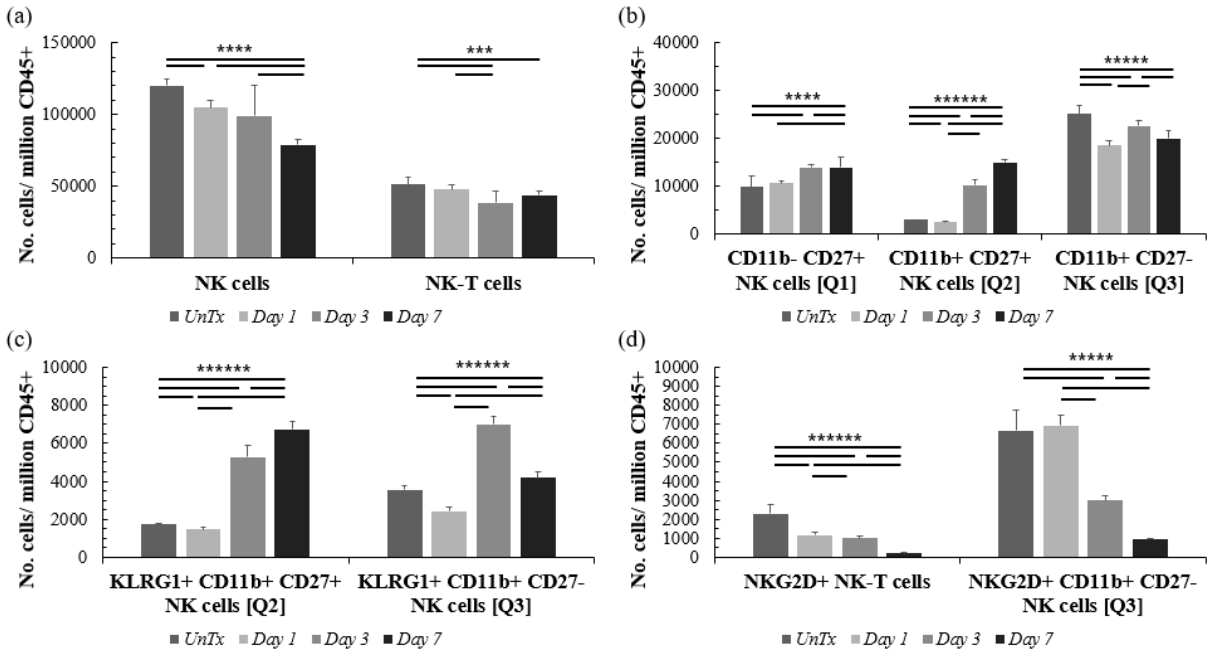

Figure 53. NK cells in the peripheral. NK cell populations were examined in spleens of untreated and NPS-Tx BL6 mice on day 1, 3, and 7 after treatment. Analyses were conducted for NK and NK-T cells (a), CD11b CD27 NK cell statuses (b), and for activation markers, including KLRG1 (c) and NKG2D (d). The data represented the results from 6 mice per group with bars representing the mean +S.E. The solid black lines indicate significance, $p<0.05$.

B16-F10 tumors from untreated and NPS-Tx BL6 mice on day 1 post-treatment were analyzed for NK cell populations (Figure 54). In the tumor, NK cells significantly increased, 1.6-fold, while the NK-T cells decreased 1.3-fold. Functional analyses of the NK cells revealed significant increases in the CD11b+ CD27+ (3-fold) and CD11b+ CD27- (3.5-fold) NK cell populations, while a significant decrease was observed for the CD11b- CD27+ (2.5-fold) NK cell population. KLRG1 expression significantly increased in the CD11b+ CD27+ (4.5-fold) and

CD11b+ CD27- (7-fold) NK cell populations. Cytotoxic NK cells also significantly increased their expression of NKG2D, by 3.3-fold, while the NK-T cells were at a stalemate without detectable difference. All differences analyzed for NK cells within the TME were significant, except for the NK-T cell population(s).

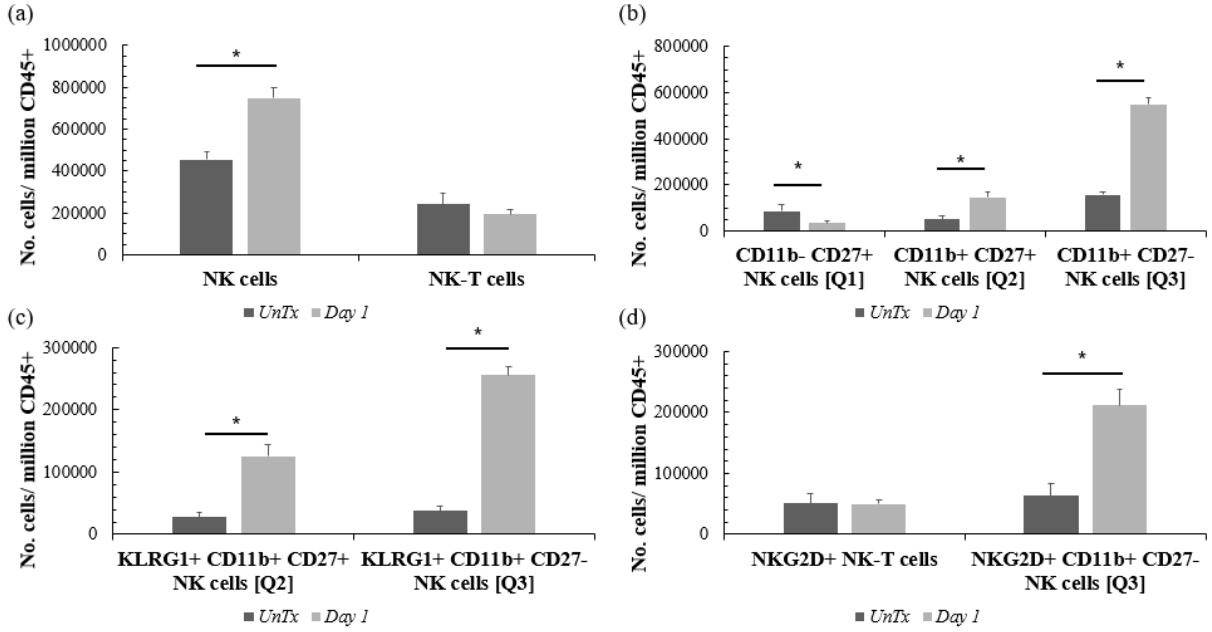

Figure 54. NK cells in the TME. NK cell populations were examined in the B16-F10 tumors of untreated and NPS-Tx BL6 mice one day after treatment. Analyses were conducted for NK and NK-T cells (a), CD11b CD27 NK cell statuses (b), and for activation markers, including KLRG1 (c) and NKG2D (d). The data represented the results from 6 mice per group with bars representing the mean +S.E. The solid black lines indicate significance, $p<0.05$.

Section 4.6. Immunometabolism of CD4+ T Cells

Enriched CD4+ T cells were isolated from LN of naïve and dLN of B16-F10 tumor bearing BL6 mice with untreated and/or NPS treated (NPS-Tx) tumors on days 1 and 3 post-NPS-Tx. The LN/dLN of individual mice were processed independently and were not pooled. The enriched CD4+ T cells were plated at $4x10^5$ cells per well and analyzed using the standard Seahorse XF HS mini protocol for the MitoStress Test kit. The oxygen consumption rates (OCR), correlating with mitochondrial respiration, of CD4+ T cells were measured in real-time under basal conditions and in response to mitochondrial inhibitors as indicated in Figure 55. The respiratory rate of the enriched CD4+ T cells was higher for the cells isolated from NPS treated BL6 mice, as evident by the higher OCR. These results indicated that the in vivo NPS-Tx of B16-F10 tumors induced increased reliance on mitochondrial metabolism of CD4+ T cells. At basal level, prior to the addition of oligomycin, the cells from BL6 mice isolated one day post-NPS-Tx mimicked the low metabolic activity of the naïve mice, while the cells from BL6 mice isolated three days post-NPS-Tx had nearly doubled.

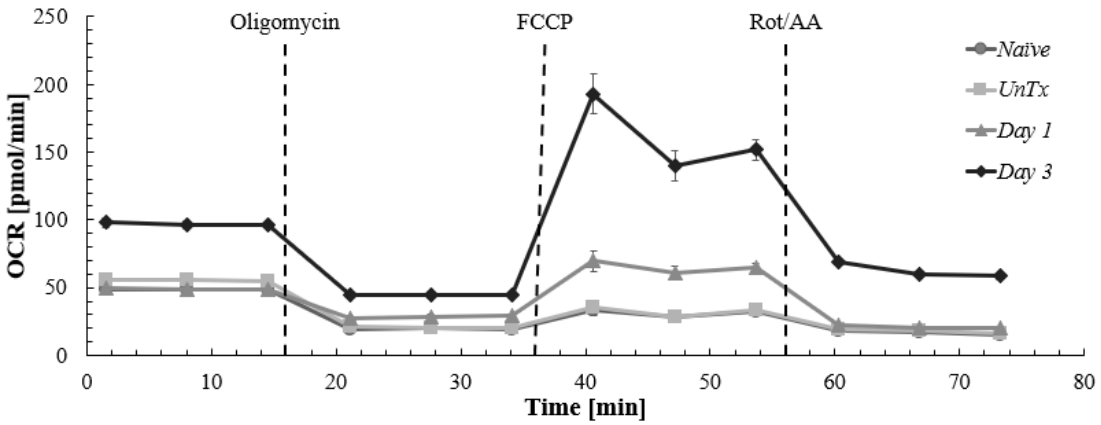

Figure 55. Mitochondrial respiration of enriched CD4+ T cells. CD4+ T cells isolated from dLN of non-tumor bearing and B16-F10 tumor bearing BL6 mice were analyzed using the standard Seahorse MitoStress Test protocol, with stepwise port injections of oligomycin, FCCP and rotenone/ antimycin A. Each well examined contained $4x10^5$ CD4+ T cells from an individual mouse and only one well per mouse was plated. The oxygen consumption rates (OCR) were measured for naïve, untreated, and post-NPS-Tx days 1 and 3. The figure indicates the OCR of the combined results from at least 3 mice per group, with markers representing the mean ±S.E.

To examine the metabolic effects of the B16-F10 tumor bearing status, enriched CD4+ T cells were isolated from naïve and untreated B16-F10 tumor bearing BL6 mice. The mitochondrial respiration was mostly the same as evident by the overlapping OCR curvature; however, the unperturbed basal OCR was slightly lower for the naïve cells (Figure 56). The elevated OCR of the tumor bearing mice indicated that the tumor burden effected CD4+ T cells

by increasing their metabolic activity. These findings also suggest that the tumor burden stressed the metabolism of CD4+ T cells.

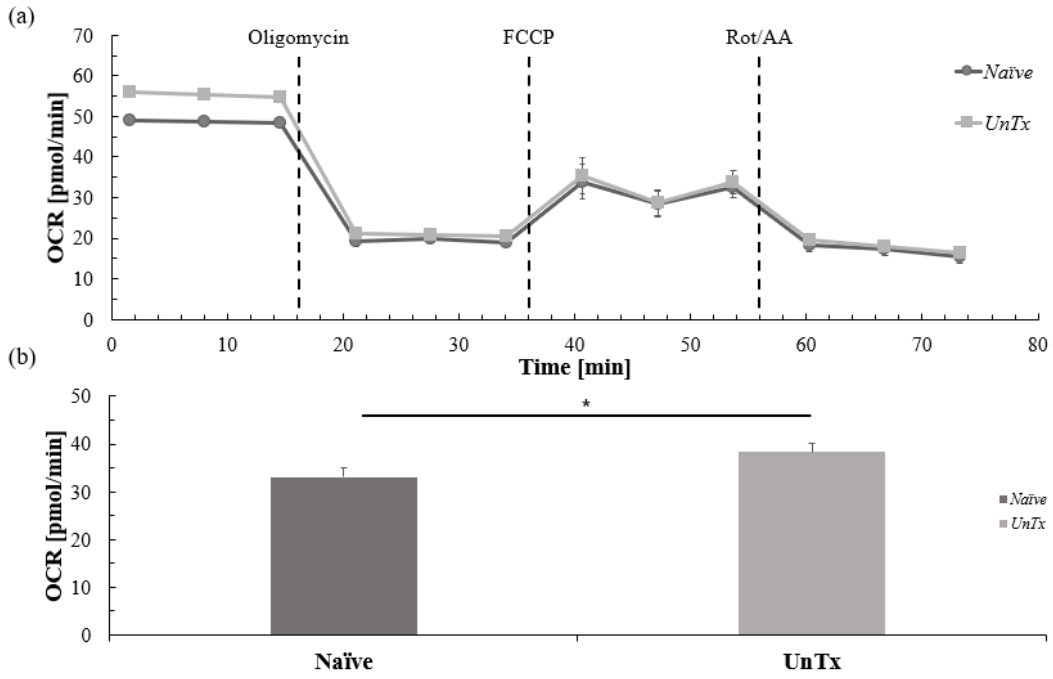

Figure 56. Mitochondrial respiration and basal respiration of enriched CD4+ T cells from naïve and untreated B16-F10 tumor bearing BL6 mice. (a) The OCR of enriched CD4+ T cells isolated from the LN/dLN of naïve and B16-F10 tumor bearing BL6 mice shows that the unperturbed basal respiration varied between these control groups, while other aspects of the OCR curves were nearly the same. (b) The higher basal respiration OCR of the CD4+ T cells in the tumor bearing mice indicated that the metabolism in these cells was more stressed than that of the naïve BL6 mice. The data represented the results from 6 mice per group with markers representing the mean ±S.E. The solid line indicates significance, $p<0.01$(*) ($p=0.0006$).

The extracellular acidification rates (ECAR), correlating with glycolysis, of the enriched CD4+ T cells were analyzed simultaneously with during the same Seahorse MitoStress Test. The stressed ECAR of enriched CD4+ T cells from naïve, untreated, and post-NPS-Tx BL6 mice were examined to determine the effects of NPS on glycolytic metabolism. As shown in Figure 57, the stressed ECAR of enriched CD4+ T cells increased with the additional tumor burden and after NPS-Tx. These results indicated that the in vivo NPS-Tx of B16-F10 tumors induced increased reliance on glycolytic metabolism of CD4+ T cells.

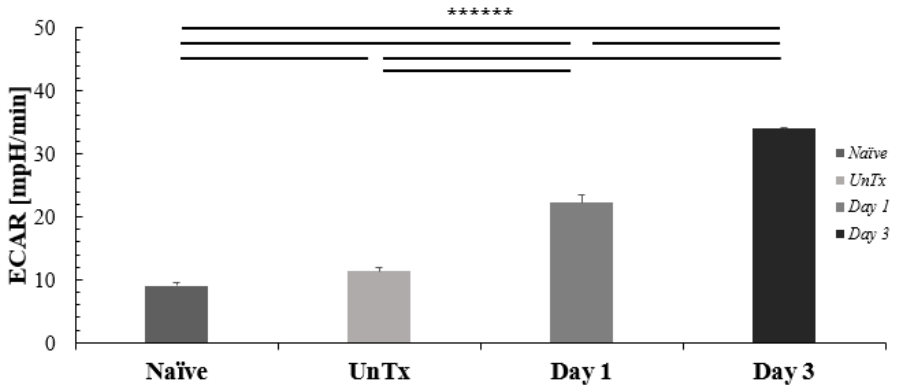

Figure 57. Stressed ECAR of enriched CD4+ T cells. The extracellular acidification rates (ECAR) of enriched CD4+ T cells isolated from the LN/dLN of naïve, untreated, and post-NPS-Tx days 1 and 3 BL6 mice were simultaneously analyzed during the Seahorse MitoStress Test. The figure indicates the stressed ECAR of the combined results from at least 3 mice per group, with bars representing the mean ±S.E. The solid lines indicate significance, $p<0.01$(*).

The metabolic potential OCR and ECAR were examined for the enriched CD4+ T cells from naïve, untreated, and post-NPS-Tx BL6 mice (Figure 58). The metabolic potential OCR and ECAR reflect the cells' ability to meet the energy demands via mitochondrial respiration and glycolysis, respectively. As shown, both OCR and ECAR metabolic potentials increased after in vivo NPS-Tx of B16-F10 tumors indicating that the CD4+ T cells increased mitochondrial and glycolytic metabolism. Taken together, these results indicated that the metabolism of CD4+ T cells shifted towards activation after NPS.

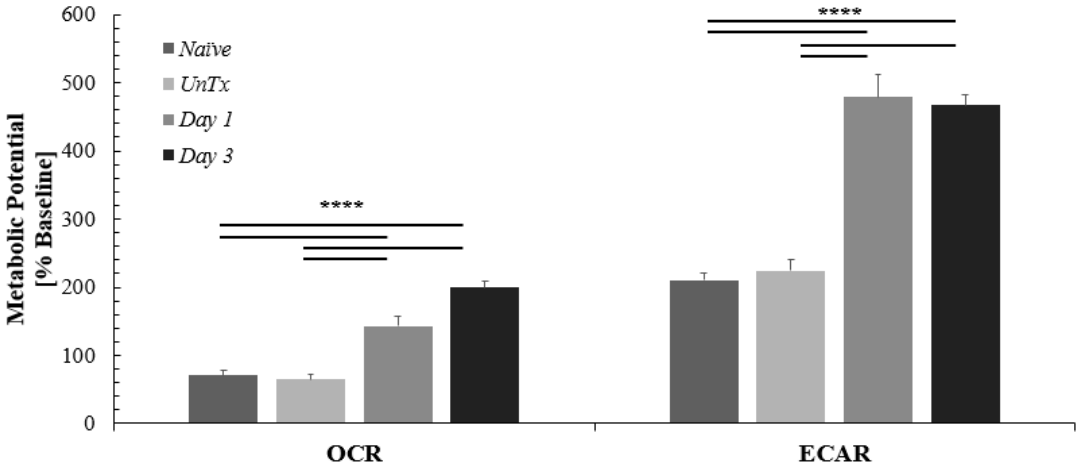

Figure 58. Metabolic potential OCR and ECAR of enriched CD4+ T cells. The metabolic potential OCR and ECAR of enriched CD4+ T cells from LN/dLN of naïve, untreated, and post-NPS-Tx days 1 and 3 were analyzed. The metabolic potentials increased after treatment with NPS. The figure indicates the metabolic potential OCR and ECAR of the combined results from at least 3 mice per group, with bars representing the mean $\pm$S.E. The solid lines indicate significance, $p<0.01(*)$.

CHAPTER V

DISCUSSION

Section 5.1. The mPTP is a Sensor of NPS

The transition of pulsed power, from physical to biological applications, introduced the concept that electric fields could have effects on intracellular structures and functions when the pulse duration and RFT were sufficiently short; however, this did not exclude the plasma membrane nanoporation by NPS. The finding that cells exposed to NPS lost their $\Delta\Psi_m$ suggested that NPS induced a short circuit in the mitochondrial membrane, which implied permeabilization of the IMM, yet it was also possible that NPS could open the mPTP [22,25,32,49,164,194]. The finding that NPS induced loss of $\Delta\Psi_m$ was Ca^{2+}-dependent, and permeabilization of the plasma membrane was not, suggested that NPS most likely did not permeabilize the IMM but likely opened the mPTP [22,25,32].

Although mitochondria are smaller organelles, potentially experiencing reduced effects of NPS than other larger structures, the nanosecond duration and F-RFT voltages superimposed across the high resting IMM $\Delta\Psi_m$ makes them obvious targets for NPS [106,107,195]. The variety of their membrane bound proteins, open the possibilities that events other than IMM permeabilization, could be involved in the NPS-induced loss of $\Delta\Psi_m$ as shown here [195,196]. Furthermore, these mitochondrial proteins are essential to the energy production, metabolic function, calcium homeostasis, and multiple signaling pathways, which endow mitochondria as such vital hubs for regulating processes such as those involved in cell death and proliferation, autophagy, and immunity [74,116,117,197].

In this manuscript, we address aspects of NPS on cellular functions, in part by monitoring the $\Delta\Psi_m$ under conditions that impact cell survival. Here we show that the mechanism whereby

NPS dissipates the $\Delta\Psi_m$ is by acting on CypD, an undisputed, primary regulator of the mPTP and ATP synthase. That NPS acts on CypD to open the mPTP and dissipate $\Delta\Psi_m$ is supported by the observations that NPS-induced loss of $\Delta\Psi_m$ requires calcium and is CsA sensitive, two well-vetted features of CypD. CsA has a well-defined binding site on CypD that inhibits binding to the mPTP complex, and/or other interacting proteins [198-202]. We also supported previous findings that NPS-induced ROS generation is Ca^{2+}-dependent [46]. In actuality, it appears that NPS generates ROS, which sensitizes CypD to calcium to open the mPTP and dissipate the $\Delta\Psi_m$ or that calcium sensitizes the mPTP to ROS to open the mPTP. These observations fit the well-known properties of the mPTP as a nonspecific pore that opens in the presence of elevated calcium concentrations and under oxidative stress [203-205].

We previously considered the 'two-hit' hypothesis that two stimuli are required to open the mPTP, including a noxious stimulus, such as increases in ROS, and elevated levels of calcium [20,179,180]. The studies here, indicate that NPS is responsible for both hits, as an influx of calcium through plasma membrane nanopores and increases in ROS. Given that CypD is Ca^{2+} and ROS dependent, it appears that these events lower the threshold for CypD to activate the mPTP and dissipate the $\Delta\Psi_m$ [90]. Since both, Ca^{2+} and ROS, are necessary, but not individually sufficient, for the $\Delta\Psi_m$ dissipation and pore activation, it begs the question as to which one is the primary instigator. Considering the evidence at hand, it appears that calcium is an enabler and recruit's ROS as an accomplice. Without calcium, the increases in ROS are modest with NPS; however, together, they activate the redox-sensitive, Ca^{2+}-dependent protein, CypD, to open the mPTP. So, how does NPS bring about these two second messengers to accomplish the two hits?

The NPS-induced cellular Ca^{2+}- influx can lead to intramitochondrial calcium increases through electrophoresis driven by the $\Delta\Psi_m$ and the mitochondrial response to calcium overload [206]. The mitochondrial calcium uniporter (MCU) regulates Ca^{2+} influx, while the mitochondrial Na^+/Ca^{2+} exchanger (NCLX) and mitochondrial H^+/Ca^{2+} exchanger, regulate Ca^{2+} efflux [207-211]. The mPTP may also function to maintain mitochondrial homeostasis and minimize mitochondrial calcium overload through brief, low conductance, transient openings [212-214].

Understanding the molecular mechanism(s) for CypD to activate the mPTP complex is complicated by the mystery of the pore constitution. Genetic studies have eliminated many candidates once considered as constituents of the mPTP, including ANT, VDAC, PiC, and the peripheral benzodiazepine receptor, or translocator protein of the outer membrane (TSPO) [202,215]. However, knocking out CypD resulted in complete desensitization to calcium and oxidative stress, demonstrating CypD plays a critical regulatory role in the mPTP [174,216-219].

Recent investigations around the mPTP identity, hypothesize that monomers and/or dimers of ATP synthase form the mPTP [220-223]. Nevertheless, these hypotheses have their distractions [224,225]. The quest to define the mPTP began more than 20 years ago, when the mPTP was proposed to exhibit low and high conductance currents to account for roles calcium played as a physiological regulator and cell death, respectively [212]. Recently, the CRISPR/Cas9 system was used to knockout the c-subunit of ATP synthase, resurrecting the this the two-current concept [226,227]. The investigation found that the clone lacking the c-subunit of ATP synthase exhibited a current much less than the wildtype, both of which were induced by calcium and inhibited by CsA [226,227]. The sensitivity of the smaller pore to ADP and bongkrekic acid suggested that it could be ANT [200]. CypD binds to ANT, and ANT forms a

calcium induced pore that becomes CsA sensitive in the presence of CypD [228]. Furthermore, ATP synthase dimers may dissociate into monomers to form the mPTP [229]. Single monomeric ATP synthases were recently shown to form calcium activated, voltage-gated channels with behaviors like the mPTP when incorporated into giant unilamellar vesicles, suggesting that forming the mPTP may only require ATP synthase monomers [230]. Nevertheless, ATP synthase likely interacts with other mitochondrial proteins to form the mPTP. Such a complex likely includes ANT, PiC and the F_1F_0 ATP synthase, called the ATP synthasome [174,231-234].

One of the least disputed issues regarding the mPTP is its regulation by CypD, the known mitochondrial target for CsA [198,199,235]. Our demonstration that CsA inhibits the Ca^{2+}-dependent decrease in the $\Delta\Psi_m$ is diagnostic for NPS effects on CypD. The CsA binding site on CypD makes CsA an excellent tool for defining CypD functions, many of which relate to the mPTP. The findings that CsA inhibition of CypD resulted in the attenuation of the Ca^{2+} mediated opening of the mPTP, ROS generation, and ATP synthase activity, support current concepts regarding the relationship between ATP synthase and the mPTP [236]. Furthermore, CsA attenuation of ATP synthase activity, demonstrating that CypD binds to and regulates ATP synthase, is consistent with the CypD interactions, later discussed, which could cause conformational changes that modulate the activity of ATP synthase. CypD regulates and CsA inhibits the channel activity of the complete F_1F_0 ATP synthase monomers, including the OSCP subunit in liposomes [220].

In isolated mitochondria, proapoptotic proteins, Bax and Bak, induced a Ca^{2+}-dependent, CsA-sensitive loss of $\Delta\Psi_m$, mitochondrial swelling, and the release of cytochrome c, all of which were inhibited by Bcl-xl. However, Bax and Bak did not affect the IMM component of the mPTP because, in cells that did not express them, there were no altered functions of the mPTP while

OMM permeability decreased [237]. This Ca^{2+}-dependent, CsA-sensitive setting for Bax and Bak, occurs at the OMM when calcium and ROS have activated the IMM components of the mPTP [238]. These findings suggest that these apoptotic protein effects on the mPTP occur as regulatory mechanisms on ATP synthase [239]. In combination with these results, our observations that Bcl-xl did not prevent the NPS-induced loss of $\Delta\Psi_m$, suggest that the NPS-induced mechanism of cell death is not by a Bax or Bak mediated mechanisms. This observation was despite the fact that NPS induced cytochrome c release and both caspase dependent and independent cell death in the Jurkat clones [24,48]. Given the well-known potential for NPS to induce RCD, it may not be surprising that at least one of the NPS mitochondrial sensors, CypD, is an architectural complex at the core of the cell death induction mechanisms [23,24,48,80].

Although NPS has been suggested to directly affect proteins [32,101,102,108], its modulation of calcium and ROS for regulating CypD and the mPTP could be more generalized. The calcium binding site(s) that determines the Ca^{2+}-dependence and ROS affected site(s) that determine the mPTP opening is somewhat obscure. There are a great many calcium binding sites for consideration of the mPTP, such as those of ATP synthase, among others in the mitochondrial matrix. There are Ca^{2+}-dependent interactions between CypD and subunits α, β and e of ATP synthase. Crosslinking studies revealed that CypD binds to the lateral stalk subunits b, d and the oligomycin sensitivity conferral protein (OSCP) [240]. Furthermore, like CypD, OSCP levels are directly proportional to the calcium threshold for mPTP opening, suggesting that OSCP could be a negatively modulating mechanism that is neutralized by CypD [240]. There are also regulatory calcium binding sites in the c subunit and catalytic Ca^{2+}/Mg^{2+} sites in the β subunit of ATP synthase [202,241]. Roles of the OSCP in ATP synthase catalysis correlates with providing access to calcium for opening the mPTP, suggesting a relationship

between ATP synthase and mPTP activation. Although calcium serves as a primary regulator of the mPTP, calcium also tightly regulates ROS, which closely ties it to ETC activity. Like calcium, ROS interacts with a variety of mitochondrial proteins, affecting their function through oxidation. Such redox sensitive proteins include ATP synthase, ANT, VDAC, cardiolipin and CypD, among others [242].

To consider the molecular mechanisms that open the mPTP, CypD has been well characterized by two functional features. We have already discussed the first feature as the sensitivity of CypD to CsA, which consists of a well-defined CsA-binding domain (CsABD) on CypD, including a series of highly conserved amino acids. The inhibitory interaction of CsA has been instrumental for understanding the roles of CypD, as we have also exploited it to define the NPS effects on CypD as a primary regulator of the mPTP. The second CypD feature is its PPIase activity, which, in vitro, catalyzes the isomerization of the peptide bond between a prolyl residue and the neighboring amino acid, frequently a bulky, lipophilic residue such as phenylalanine [243]. The characterization of CypD may be more completely defined based on PPIase activity, as opposed to opening the mPTP. For example, there are two binding pockets on CypD that appear to provide selectivity for substrate binding and enzyme turnover. There is also a less well-defined back face of the CsABD that could accommodate interactions with other proteins [244]. An example of this can be found in the yeast, where cyclophilin was essential to the proper folding of newly imported mitochondrial proteins [245]. While this activity catalyzes a folding reaction, there is scant evidence for CypD to be classified as a chaperone protein [246]. Furthermore, the PPIase activity of CypD has been characterized and assayed, yet its physiological role in mammals remains undefined [246].

Generally, there remain questions about CypD's relationship between PPIase activity and opening the mPTP. CsA competes for the relatively well-defined binding site on CypD and disrupts PPIase activity. CsA also displaces CypD from the mPTP [220]. Modulation of its PPIase activity demonstrated the importance of CypD as a redox-sensitive protein. Oxidation of the cysteine disulfide bridge between two highly conserved residues, Cys157 and Cys203, was crucial for the conformation and enzymatic activity of CypD [247]. In early studies, isolated mitochondria from the liver and heart displayed CsA-sensitive PPIase activity in parallel with Ca^{2+}-induced and CsA-sensitive mitochondrial swelling, suggesting that the (cyclophilin) isomerase could be involved in this response [200]. However, the direct relationship establishing the two activities remains absent.

Mouse embryo fibroblasts, expressing mutated CypD, where Cys203 was exchanged for Ser (C203S), and isolated mitochondria from the liver of mice expressing the CypD C203S mutation in vivo, exhibited attenuated activation of the mPTP [248]. Likewise, S-nitrosylation (SNO) of the CypD Cys203 residue, caused resistance to ROS-induced RCD [248]. These data suggest that mPTP opening depends on the CypD Cys203 residue, which cannot activate the mPTP when nitrosylated [248]. Since oxidation of CypD, such as with elevated levels of ROS, opens the mPTP, the results for S-nitrosylation of this site suggested that Cys203 must be oxidized to open the pore [248]. In contrast, the PPIase activity of CypD with the C203S mutation as well as a C157S mutation, exhibit similar activity to that of the wildtype, and the reduced form of Cys203 exhibited slightly higher activity than that of the wildtype [248]. Thus, PPIase activity slightly favors Cys203 in a reduced redox state, while opening the mPTP requires CypD in the oxidized state [248]. This difference is consistent with the earlier assessment of this issue, that PPIase activity is not required for opening the mPTP [249]. Since the isomerase

activity of CypD is highly conserved within the Cyp family, it may serve an undefined function in nature that is independent of the regulatory role it has on the mPTP [245].

The investigations here, using NPS as an agonist, indicate that NPS generate conditions that promote calcium and ROS collaborate to open the mPTP; however, the molecular mechanisms and sequence of events remain unclear. Thioredoxin reductase 2 (TrxR2) regulates CypD and the mPTP. An altered thiol redox state could be communicated to CypD and other redox-sensitive proteins, including ATP synthase, PiC, ANT, and Bcl-2, among others [250]. Inhibition of TrXR2 causes oxidation of CypD, suggesting redox interactions occur between CypD and the thioredoxin system. In rat heart mitochondria, TrxR2 oxidizes thioredoxin 2 (Trx2) and, subsequently, peroxiredoxin 2 (Prx2). These previously reported observations provide evidence that the thioredoxin system in mitochondria can redox-regulate CypD, and are consistent with our findings, suggesting that ROS may be a more immediate or terminal CypD regulator [250,251]. Furthermore, while the definition of Ca^{2+}-binding sites is more hypothetical, the defined redox regulatory system communicates with CypD. Thus, it is reasonable to suggest that in the presence of calcium, ROS oxidizes CypD to open the mPTP by a mechanism that is independent of PPIase activity.

Section 5.2. Treatment Efficacy of NPS

NPS configurations were investigated for efficacy in murine 4T1-Luc breast cancer and B16-F10 melanoma models. The 100ns BL parameters were previously considered the gold standard; however, the 200ns BL parameters may be more apt. Not only did the 200ns BL parameters induce primary tumor clearance as well as the 100ns BL in the 4T1-Luc model, but it induced immunity more often in both 4T1-Luc and B16-F10 cancer models, with corresponding

survival of 78% and 50%, respectively. This was nearly 10% better in the 4T1-Luc model and 36% better in the B16-F10 model. The 200ns MOSFET parameters were much less efficient at inducing primary tumor clearance in both 4T1-Luc and B16-F10 cancer models, with a 33% and 83% reduction in survival, respectively. Table 7 compares the post-treatment and post-challenge survival results of the two cancer models and NPS parameters. Furthermore, these results indicated that factors beyond matched parameters, like energy and voltage, that impact the successful clearance of tumor burden and induce in situ vaccination.

Table 7 BVM survival comparison of 4T1-Luc and B16-F10.

Treatment Group	**After Treatment**		**After Challenge**	
	4T1-Luc	*B16-F10*	*4T1-Luc*	*B16-F10*
Untreated	NA	NA	0%	0%
100ns BL	100%	64%	67%	14%
200ns BL	100%	50%	78%	50%
200ns MOSFET	67%	17%	67%	0%

In the abscopal effect investigations, the 100ns BL NPS parameters were used to examine the efficacy of NPS at inducing primary and abscopal tumor clearance in the 4T1-Luc breast cancer model. As previously discussed, NPS was most efficient at inducing complete tumor clearance when the abscopal tumor was started three days prior to treatment. In addition to

examining the tumor volumes and survival curves, it was also interesting to consider NPS efficacy with respect to each type of tumor clearance. In Table 8, the ratios of primary, abscopal, and both, primary and abscopal, tumor progression as well as the ratios of complete tumor clearance were tabulated. In this manner, one can see which tumor(s) contributed to the demise of mice within each AE group. In the AE_0 group, three mice succumbed to primary and abscopal tumor burden while one mouse succumbed to primary and/or abscopal tumor burden, only two mice were able to clear both tumors, contributing to 28% NPS treatment success. This suggests that the additional cancer burden on the same day as NPS, overwhelmed the hosts immune system as primary tumor progression after NPS was not typical. As shown in the single tumor model with BVM, complete 4T1-Luc primary tumor clearance was observed in 100% of mice treated with these NPS parameters; however, here, in the AE_0 group, primary tumor progression occurred in four of seven mice, that is 57% NPS failure. In the AE_{-3} group, there was also a high percentage of mice succumbing to tumor burden, with two of twelve mice succumbing to abscopal tumor burden alone (16%) and five of twelve succumbing to primary and abscopal tumor burden (42%). Here, five of twelve mice were also successful at clearing both tumors, contributing to 42% NPS treatment success. These results indicate that while some of the hosts immune systems were likely overwhelmed, others were more capable of tackling both tumors after NPS. Interestingly, the 16% succumbing to abscopal tumor burden alone suggests that the three-day pretreatment duration may have been advantageous for the abscopal tumor, allowing it to develop a secure microenvironment in the interim. This becomes even more valid in the AE_{-7} group since, 90% successfully clear the primary tumor yet succumb to abscopal tumor progression. This implies that the seven-day pretreatment duration was ample time for the abscopal tumors to secure their microenvironments and evade detection after NPS. Only one

mouse in this AE_{-7} group was successful in clearing both tumors, the sole contributor to the 10% NPS treatment success of this group. Taken together, these AE experiments indicate that the 100ns BL NPS parameters were most effective at inducing primary and abscopal tumor clearance when the abscopal tumor was initiated three days prior to treatment. These findings also imply that recent tumor progression, within zero to three days of treatment, negatively impacts NPS treatment success, even with respect to primary tumor clearance, and that well developed abscopal tumor sites can avoid NPS induced immunity.

Table 8 4T1-Luc AE model tumor progression and survival ratios.

Abscopal Treatment Group	**Tumor Progression (Ratio)**			**Survival (Ratio)**
	Primary	*Abscopal*	*Primary & Abscopal*	*Cleared Tumor*
Day 0 [AE_0]	1:7	1:7	3:7	2:7
Day -3 [AE_{-3}]	0:12	2:12	5:12	5:12
Day -7 [AE_{-7}]	0:10	8:10	1:10	1:10

In comparison of the murine breast cancer model and the human TNBC-PDX model, one would think that in addition to the known effects of NPS on extracellular components of the TME, such as disrupting constituents of the ECM and abrogating angiogenesis, that (1) the physical characteristics of the tumor are more suitable for NPS treatment, i.e., they are completely nestled between the pinch electrodes throughout the treatment, which would ensure that all cells, including TILs, within the TME experience stimulation, and/or (2) the TME lacks

immune cell infiltration to some extent and that NPS primarily induces intracellular death mechanisms in the tumor cells. In the murine breast cancer model, 100% of the treated tumors were cleared after treatment, which supports (1) and (2). Either way, the immune system recognizes the tumor, becomes activated, and builds memory, which we saw in 67% of the mice when challenged. The results of the AE investigations may shed some light on this a bit more. Those with abscopal tumors established on day -7 usually cleared the primary tumors but failed to clear the abscopal tumor, while the majority of mice with tumors established on day -3 either cleared or failed to clear both tumors. This suggests that the TME in this model is relatively void of TILs, since it appeared that well established TME were able to avoid detection they must have been keeping the surveilling lymphocytes out, while established yet less developed abscopal TMEs were still penetrable after NPS. Furthermore, the human BC-CDX tumors were unaffected by NPS. This was the first-time a cancer had ever been observed to abrogate the effects of NPS to such an extent, and the lack of immune presence indicated that the immune system likely plays a more significant role in this BC-CDX cancer model.

Section 5.3. The Humanized Mouse Model

The high demand for more predictive preclinical models, especially those compatible with human cancer research, is being tackled from the perspective of the humanized mouse. In an attempt to recapitulate human immune and tumor biology, the oncohu-NSGM3 model was attempted for investigating the effects of NPS on a human TNBC-PDX. The intentions were to examine NPS induced human immunity, however, consistent xenograft alignment was not obtained. Instead, there were mice that accepted the TNBC-PDX yet rejected human immune

reconstitution, while others rejected the TNBC-PDX yet reconstituted the HIS. Nevertheless, some insights were gained with immunocompromised mouse models.

In the hu-NSGM3 model, our observations indicated that HIS engraftment into NSGM3 mice was only successful in about 33%, which was much lower than previous reports. Examining the weights and percentages of hCD45+ cells over time provided correlative insights into GVHD. While this was not part of the original aims, these findings may aid researchers in the future using HIS mouse models.

In the NSG immunocompromised mouse strain, NPS was shown to induce complete tumor regression in 83% of the TNBC-PDX tumors but 0% of the BC-CDX tumors. This indicated that NPS induced different mechanisms of tumor death in vivo. The observations of TNBC-PDX tumor death were likely resultant of intracellularly induced cell death mechanisms, while the lack of BC-CDX tumor death was likely due to the absence of an immune system. Thus, these results indicate that NPS can intersect and/or harness a variety of pathways to defeat cancers.

Section 5.4. NPS Induced Immunity

Cancers are well-known for their evasive tactics and tumor infiltrating leukocytes (TILs) are no stranger to the manipulative prowess of the TME. By manipulating the recruitment, expansion, and functions TILs, such as immunoregulatory T cells and myeloid cells, cancers are able to impair immune-mediated rejection at their primary tumor site as well as egressing tumor cells. This process is referred to as immunoediting and is perhaps one of the most cunning tactics, as the tumor exploits the antitumor immune responses to select for cancer cell clones lacking tumor antigens [64,252]. The significance is, that cancers hijack the immune system and,

thus, is not necessarily restricted to a single region and the whole system should be considered as the TME. Additionally, members of both the innate and adaptive immune system can be exploited by cancers.

Therefore, as part of these investigations, the NPS induced immune response in the B16-F10 melanoma TME was examined. Due to the low treatment efficacy of NPS in this model, it was likely that the suppressive TME persisted. Thus, we analyzed the systemic/ peripheral TME, via the blood and spleen, and the primary TME, via the tumor and tumor dLN, for T cells, dendritic cells (DC), antigen-presenting cells (APC), tumor associated macrophages (TAMs), myeloid derived suppressor cells (MDSC), and natural killer (NK) cells.

The effector and memory statuses of CD4+ and CD8+ T cells were examined as part of investigating the TME. EM CD4+ T cells decreased in the local TME as well as the spleen, while increasing in the blood. This may indicate that NPS revealed the tumor cells to the EM CD4+ T cells in the TME, thus activating them. Since the tumors are typically cleared within a few days after NPS-Tx, the EM CD4+ T cells would no longer be required and thus, the majority would undergo RCD while a few would remain as contributors to the CD4+ T cell memory pool [253]. CM CD4+ T cells decreased in the tumor and blood, while increasing in the dLN and spleen. This indicated that NPS induced a vaccine-like effect with respect to the CM CD4+ T cells, since this correlates with reports that this phenotype persists in the germinal centers of dLN, which regulates the development and maintenance of memory B cells [253]. Thus, upon re-exposure to the antigen, which in this case would be the B16-F10 cancer cells, would support the prompt generation of long-lived plasma B cells [253]. N-SCM CD4+ T cells decreased in the tumor and spleen, while increasing in the dLN and blood. These findings support the resultant shifts in the EM and CM statuses of CD4+ T cells. Since the EM CD4+ T cells were dying after

NPS induced activation, new naïve CD4+ T cells, which normally circulate between the blood and secondary lymphatic tissues like LNs, would be needed [253]. Taken together, NPS induced CD4+ T cells to become activated, aiding in tumor clearance, and generate a vaccine-like effect.

The activation of cytotoxic CD8+ T lymphocytes (CTLs) plays a pivotal role in anticancer immunity [130]. The EM CD8+ T cells decreased in the tumor, while increasing in the dLN and spleen. No net change was observed for these CTLs in the blood; however, the trend was the same as the spleen: a significant increasing trend through day 3 followed by a significant decrease on day 7 post-treatment. A similar trend was reported in response to NPS in rat hepatocellular carcinoma [114]. CM CD8+ T cells increased in the dLN and spleen, while decreasing in the tumor and blood. N-SCM CD8+ T cells increased in the tumor, dLN, and blood, yet decreased in the spleen. The shift observed for the EM and CM statuses of CD8+ T cells in the peripheral tissues indicated that NPS induced CD8+ T cells to take on the effector phenotype, becoming more cytotoxic, within the first few days of treatment, then shift towards lasting memory 7 days later.

The CD4+ and CD8+ T cells in the peripheral tissues were also examined for Interleukin 7 Receptor alpha (IL-7Rα), or CD127, and Programmed Cell Death Protein 1 (PD1) expression. As a member of the hematopoietin receptor superfamily, Il-7Rα plays an important role in lymphocyte differentiation, proliferation, and survival [187,188]. IL-7Rα, along with its hematopoietic growth factor, IL-7, are also required for developing essential lymphoid structures and defensive barriers [189]. High levels of IL-7 and IL-7Rα have been associated with poor prognoses and metastasis in solid tumors [189]. PD1+ T cells are also of interest, since PD1 plays a pivot role in the balancing act of T cell activation [190]. As a member of the immunoglobulin superfamily, this crucial immune checkpoint receptor is primarily expressed on

cytotoxic T cells in peripheral tissues as well as the TME [254-257]. The binding of the PD1 receptor to its inhibitory ligand, PDL, down-regulates the T cell mediated immune response [191]. Thus, detection of IL-7Rα and PD1 T cells were of great interest and provided insights into the dissembling nature of B16-F10 melanoma and the TME.

IL-7Rα+ CD4+ T cells increased in the dLN, blood, and spleen, while decreasing in the tumor. IL-7Rα+ CD8+ T cells increased in all tissues. Since activated T cells lose their expression of IL-7Rα+, these findings coincided with the dominant increasing presence of the N-SCM T cell phenotypes [189]. PD1+ CD4+ T cells generally decreased in all tissues, indicating that activated CD4+ T cells were likely dying, which also supports the previously discussed results. PD1+ CD8+ T cells decreased in the tumor and increased in the dLN, blood, and spleen, indicating that NPS induced CD8+ T cell activation and was consistent with the increased presence of the cytotoxic CD8+ T cell phenotype. However, circulating PD1+ CD8+ T cells have also been associated with exhausted signatures and cancer prognoses [258]. Taken together, the observed changes in IL-7Rα and PD1 expression indicated that NPS induced dynamic shifts in CD4+ and CD8+ T cell activation.

T regulatory cells significantly decreased in the tumor, while increasing in the dLN and blood, yet no net difference was observed in the spleen. The persistence of T regulatory cells in the peripheral tissues after NPS treatment provided a glimpse into the immunosuppressive tactics of this melanoma model. The persistent expression of IL-7Rα by regulatory T cells in the dLN indicated that the B16-F10 TME continued to suppress the immune response despite NPS. Since IL-7Rα is involved in constructing barriers, these T regulatory cells may not only be suppressing the immune response but attempting to rebuild the primary TME [189].

The initial steps in effectuating an anticancer T cell response, requires APC priming of CTLs [130,259,260]. Macrophages, including TAMS, and DCs are capable of antigen presentation within the TME, albeit TAMs have been reported to have a limited capacity[130,261]. Nevertheless, analysis of APCs was used to provide a general idea of the anticancer presence after NPS. APCs increased in the tumor, dLN, and spleen, yet decreased in the blood; however, CD86 expression increased in all tissues. These findings indicated that NPS likely induced activation in APCs.

As superior antigen presenters, DCs play a critical role in the adaptive anticancer immune response, including both the systemic and local TMEs [262,263]. Conventional DCs (cDCs) are a particular subset that can transport tumor antigens to the tumor dLN and activate CTLs through cross-presentation [264]. While maturity of DCs is essential to providing co-stimulatory signals to TILs, should their maturation coincide within the TME their signaling is often insufficient and can be suppressed by regulatory T cells [264]. In these investigations, DCs significantly decreased in the tumor one day after treatment, indicating that they were likely to have matured within the TME and thus, were incapable of sufficient signaling [264]. These findings coincided with decreases in all effector and memory statuses of CD4+ T cells, EM and CM CD8+ T cell statuses, and T regulatory cells, while only the N-SCM CD8+ T cells increased in the tumor. Taken together, this indicated that within the first day after treatment, NPS dismantled the local TME.

Since NPS induced tumor cell death likely involved inflammation and the release of chemokines, cytokines, etc., promoting an influx of immune cells, including DCs, into the TME, it was likely that their frequency may have increased after day 1, which would support our findings that DCs in the dLN increased through day 3 post-treatment. These findings coincided

with increases in CTLs, which indicated that DCs were likely cross-presenting antigens to activate the CD8+ T cells within the first few days after NPS. However, when considering the effects of NPS on DCs and T regs in the dLN, their frequencies were nearly matched through day 3 post-treatment, yet by day 7, the frequency of T regs remained high while the frequency of DCs significantly decreased. This indicated that NPS induced an immune response but the persistence of T regs was likely to have maintained a suppressive TME. This was unlike what was previously seen in rat hepatocellular carcinoma, where the alleviation of immunosuppressive T regulatory cells coincided with DC infiltration, indicating that NPS induced an activated immune response [114]. However, the frequency variability of DCs indicated that in some mice, when the presence of DCs were more dominant than the T regs, NPS was more likely to have flipped the suppressive switch.

MDSCs showed a similar trend, with increases in all tissues except in the blood, where no net change was observed. This was unlike the mouse 4T1-Luc breast cancer where NPS induced decreases within 2-days of treatment [30]. Since the 4T1-Luc tumors are known for their accumulation of MDSCs, we can deduce that B16-F10 tumors may not [30,265,266]. In support of this, the MDSC population in B16-F10 tumors in BL6 mice were shown to decrease over time after implantation [267]. Additionally, CD86 and MHC II expression increased in all tissues. Since expression of these markers are consistent with the classical, proinflammatory, and anticancer M1 polarization state of macrophages, this indicated that NPS elicited an immune response.

TAMs have been reported to aid the TME by suppressing cytotoxic CD8+ T cells either directly through expression of inhibitory ligands or indirectly through recruitment of T regulatory cells [143]. TAMs increased in all tissues except for the blood, in which this

population fluctuated over time. TAMs are further classified as M1 or M2 according to their polarization state. M1 TAMs (CD86+) play a role in anticancer immunity since they produce Th1 cytokines like IFN-γ, which promotes infiltration of CD4+ T helper cells, CTLs, NKs, DCs, as well as macrophages, while inhibiting suppressive T regulatory cells [268]. M2 TAMs are associated with tumor progression, since they produce immunosuppressive cytokines which can aid in metastasis [268]. M1 macrophages increased in all tissues, indicating that NPS induced an immune response. M2 macrophages increased in the tumor (M2 TAMs), while decreasing in the spleen. The increase in M2 TAMs indicated persistent suppression despite NPS-Tx. In the blood, M2 macrophages significantly decreased until day 3, then they significantly increased on day 7 post-treatment. This could indicate that M2 macrophages remained loyal to the tumor since a systemically suppressed TME could aid in metastasis [268]. The polarization status shifts observed indicated that TAMs/ macrophages shifted towards a more activated anti-cancer phenotype; however, systemically, pro-cancer M2 macrophages appeared to regain momentum by day 7. Thus, NPS induced a shift in macrophage polarization status albeit perhaps not enough to inhibit M2 macrophages from sustaining suppression.

NK cells also participate in innate anticancer immunity. NK cells express and respond to signaling molecules, like IFN-γ and tumor necrosis factor (TNF-α) [269]. NK cells are similar to T cells in that they can develop memory, effector functions including cytotoxicity, proliferate upon stimulation, and produce IFN-γ, albeit their activation processes are different [68,270,271]. The maturation of NK cells was reported to have 4-stages according to their phenotypic expression of CD11b and CD27: naïve CD11b- CD27-, CD11b- CD27+, CD11b+ CD27+, and CD11b+ CD27- [193]. Here, we examined populations of NK cells in the tumor and spleen. First, the general statuses of NK and NK-T cells were examined. In the tumor, the NK cells

increased while the NK-T cells had no significant change one day post-treatment. The influx of NK cells in the tumor indicated that NPS induced recruitment of NK cells into the TME. In the spleen, the NK and NK-T cells had a decreasing trend. CD11b- CD27+ NK cells significantly decreased in the tumor but increased in the spleen. While the more mature phenotypes continued to dominate the spleen, this was interesting because the spleen typically has fewer naïve and/or less mature phenotypes of NK cells [193]. This phenotype is associated with decreased cytotoxicity and a limited capacity to differentiate yet has a greater ability to detect and produce cytokines [193]. The CD11b+ CD27+ NK cells increased in both tissues as did their expression of KLRG1. This phenotype of NK cell is considered the most potent effector status since they can kill target cells through NKG2D dependent and non-dependent mechanisms [193]. (NKG2D is normally expressed by all NK cells [272,273].) The CD11b+ CD27- NK cells increased in the tumor as did their expression of KLRG1 and NKG2D. This phenotype represents the more mature, long-lived, senescent NK status and relies on NKG2D mediated cytotoxicity [193]. However, in the spleen, this population significantly decreased along with their expression of NKG2D and their expression of KLRG1 increased. While KLRG1 expression has been identified as a marker of high cytotoxicity, in vivo KLRG1 neutralization studies showed that it supported cancer evasion [274]. Additionally, KLRG1 is often upregulated after treatment with a variety of therapies and may contribute to limited treatment efficacy [274]. It appears that NPS induced a similar response since KLRG1 expression increased post-treatment.

In summary, these findings indicated that NPS induced an immune response in the B16-F10 cancer model. The shifts in DCs, M1 macrophages, and the various effector and memory statuses of T cells indicated that NPS induced an immune response and began to dismantle the TME. Albeit the combined effects of persistent T regulatory cells and M2 TAMs along with the

cohorts of various expression markers, including exhausted expression signatures, potentiated the suppressive TME. Thus, it appeared that every gain towards cancer recovery was met with an equal or greater loss.

Section 5.5. Immunometabolism

Launching an immune response, in addition to the development and maintenance of diverse hematopoietic populations, requires extensive bioenergetic commitments for life [275]. Phenotypically, lymphocytes shift from resting quiescence to highly active statuses within hours of pathogen detection [275]. T cells require extracellular signals from cytokines, antigens, and/or co-stimulatory receptor engagements before they can actively acquire metabolic substrates from their peripheral environment, which are then used to initiate changes in their statuses through protein synthesis [275]. Thus, the recent concept of immunometabolism has prominently risen at the intersection of immunology and biochemistry and refers to the preferential metabolic shift in immune cells for generating energy and metabolites [161,275,276].

Enriched CD4+ T cells were isolated from the LN of naïve and dLN of BL6 mice with untreated and NPS-Tx B16-F10 tumors. The OCR of enriched CD4+ T cells increased 1 and 3 days after in vivo NPS-Tx of B16-F10 tumors in BL6 mice. The additional B16-F10 tumor burden mildly stressed the CD4+ T cells, as evident by the elevated basal OCR and stressed ECAR of the untreated tumor bearing BL6 mice in comparison with the naïve BL6 mice. The stressed ECAR, metabolic potential OCR, and metabolic potential ECAR of the CD4+ T cells increased after in vivo NPS-Tx of the B16-F10 tumors in BL6 mice. These findings indicated that the CD4+ T cells increased their metabolic activity via mitochondrial and glycolytic

pathways which was consistent with activated statuses of previous reports [276-279]. Thus, NPS metabolically activated CD4+ T cells in vivo.

There were several limitations to conducting these investigations. For the NPS-Tx BL6 mice, the enriched CD4+ cells were isolated from a single lymph node, the tumor dLN, which limited the number of enriched CD4+ T cells obtainable per mouse and data was acquired without pooling the enriched cells. Therefore, this led to a reduced n-value for the day 1 and day 3 post-NPS-Tx groups; while the n-values for the naïve and untreated BL6 mice were 6, the n-value for the NPS-Tx groups were 3. Another potential limitation, although not necessarily a factor here in light of the previous limitation, lies with the instrumentation itself. Since the Seahorse XF HS mini can examine only 6-wells per assay, with 2-wells designated as blanks, and each assay taking approximately 1.5-2hr, had enough cells been obtained for triplicate measurements per mouse, with 6 mice per group, that would have consumed 72 plates and 108-144 hours. This would have been extremely inefficient and costly. Instead, this somewhat novel approach of plating cells from individual mice per treatment group sufficiently provided the n-values needed within the constraints of the experimental timeframe.

CHAPTER VI

CONCLUSIONS

Section 6.1. Primary Contributions

The mPTP is a sensor of NPS. The NPS-induced dissipation of the $\Delta\Psi_m$ is codependent on calcium and ROS. A likely scenario for NPS to induce activation of the mPTP is through a nanopore facilitated increase of intracellular calcium, and generation of mROS from Complex I of the ETC, which overload mitochondria, sensitizing CypD to open the mPTP and dissipate $\Delta\Psi_m$. It is likely that Ca^{2+}-dependent CypD becomes oxidized by ROS, increasing the pores open probability. The NPS-induced inhibition of Complex I will also increase the NADH/ NAD^+ ratio that favors activation of Ca^{2+}-dependent α-ketoglutarate dehydrogenase, which causes increased ROS (H_2O_2), thereby supporting $\Delta\Psi_m$ depolarization [280-282]. These studies further demonstrate that the NPS-induced dissipation of the $\Delta\Psi_m$ is independent of caspase activity and insensitive to the protection from the mitochondrial Bcl-2 family of antiapoptotic proteins.

NPS induced immunity and immunometabolism. The in vivo challenge models revealed that (1) treatment efficacy of NPS was cancer type dependent, (2) the establishment of an abscopal tumor impacted the treatment efficacy with respect to primary and abscopal tumor clearance, and (3) the 200ns BL NPS parameters were best at inducing primary tumor clearance and protection. The observed variations of NPS treatment efficacy directed our efforts to the immune system. The TME of the B16-F10 melanoma model was investigated because of the variable treatment efficacy, which indicated something interesting must be occurring immunogenically. Indeed, NPS induced immunogenic shifts towards activation, effector and memory statuses, polarization, infiltration, etc., all favoring cancer recovery, but then the suppressors persisted. This

corroborated the observed treatment efficacy of NPS since tumors generally appeared to regress then progress. Additionally, NPS activated CD4+ T cells in vivo as evident by their metabolic profile which was supported by their phenotypic expression. This was the first time NPS has been investigated for metabolically activating immune cells in vivo.

The humanized mouse project. Cancers are aggressive, evasive, and ruthless killers, claiming millions of lives every year. Cancers are heterogeneous and there is often no single, clearly defined problem as they harness and manipulate a multitude of fundamental mechanisms at the very essence of life. To investigate these mechanisms and vet potential interventive therapies, humanized mice offer a unique model as a prelude to the use of nanosecond pulse stimulation (NPS), a pulse power technology applying nanosecond duration, high electric field pulses, to ablate human tumors. Immunodeficient mouse strains, NSG and NSG-SGM3, were engrafted with human immune cells and human tumors, which would allow us to study the effects of NPS therapy on the human tumor and the human immune system, albeit not without trials and tribulations. Here we show that NSGM3 mice engrafted with HCB CD34+ HSC lack consistency in expansion and chimerism, or variety of immune cell types. Unfortunately, mice that developed the HIS rejected the human tumors, while mice that rejected the immune system developed the human TNBC-PDX tumors. Therefore, we had mice with HIS and no tumor to treat, and mice with tumors to treat yet without a HIS to study. Nevertheless, these investigations were the first attempts at recapitulating human immune and cancer biology for studying the effects of NPS in a more predictable preclinical model, and while these aims were unforeseeably truncated, the correlation between weight and hCD45+ cells was identified in these investigations and may serve as a preliminary method for detecting GVHD in the HIS mouse models. In non-humanized NSG mice, NPS induced tumor death in the TNBC-PDX tumor model in nearly all mice, but not

in the BC-CDX model. The absence of NPS elimination of the BC-CDX is the only known NPS cancer failure and requires further study.

Section 6.2. Widening the Scope

It was proposed to address the significant knowledge gap associated with therapeutically evasive cancers contributing to premature mortality around the world. These investigations broadened our understanding of the immunometabolic mechanisms governing immunity in cancer and provided supportive insights for the translation of pulse power applications into the clinic for treating cancers in human beneficiaries.

Section 6.3. Suggestions for Future Research

While this document serves as a testament to the questions asked and answered, many more have risen and await investigating. There are still some questions remaining around the mPTP, CypD, and ROS. The next experiments should aim to determine the effects of ROS scavengers and mPTP inhibitors on NPS-induced dissipation of $\Delta\Psi_m$, mROS generation, and viability. Regarding the in vivo NPS treatment efficacy studies, outstanding questions around the cancer models with reduced NPS treatment efficacy remain. Specifically, the BC-CDX cancer model could provide some mechanistic insights into NPS induced immunity. Regarding the B16-F10 model immunometabolic studies, additional characterization could be investigated with respect to NKG2D and KLRG1 expression in T cells. It would also be interesting to examine the combined effects of NPS with anti-KLRG1 as a neo-adjuvant therapy in the B16-F10 model [274].

REFERENCES

1. Bertucci, F.; Finetti, P.; Birnbaum, D. Basal breast cancer: a complex and deadly molecular subtype. *Current molecular medicine* **2012**, *12*, 96-110.

2. Foulkes, W.D.; Smith, I.E.; Reis-Filho, J.S. Triple-negative breast cancer. *New England journal of medicine* **2010**, *363*, 1938-1948.

3. Bray, F.; Ferlay, J.; Soerjomataram, I.; Siegel, R.L.; Torre, L.A.; Jemal, A. Global cancer statistics 2018: GLOBOCAN estimates of incidence and mortality worldwide for 36 cancers in 185 countries. *CA: A Cancer Journal for Clinicians* **2018**, *0*, doi:10.3322/caac.21492.

4. ACS. Melanoma Skin Cancer Early Detection, Diagnosis, and Staging. Available online: https://www.cancer.org/cancer/melanoma-skin-cancer/detection-diagnosis-staging.html (accessed on 08/24/2020).

5. Hay, M.; Thomas, D.W.; Craighead, J.L.; Economides, C.; Rosenthal, J. Clinical development success rates for investigational drugs. *Nature Biotechnology* **2014**, *32*, 40-51, doi:10.1038/nbt.2786.

6. Hanahan, D.; Weinberg, R.A. Hallmarks of cancer: the next generation. *Cell* **2011**, *144*, 646-674.

7. Reichle, A. *Evolution-adjusted Tumor Pathophysiology*; Springer: 2013.

8. Flavahan, W.A.; Gaskell, E.; Bernstein, B.E. Epigenetic plasticity and the hallmarks of cancer. *Science* **2017**, *357*, eaal2380.

9. Le Magnen, C.; Shen, M.M.; Abate-Shen, C. Lineage plasticity in cancer progression and treatment. *Annual review of cancer biology* **2018**, *2*, 271-289.

10. Heng, H.H.Q. The genome-centric concept: resynthesis of evolutionary theory. **2009**, *31*, 512-525, doi:10.1002/bies.200800182.

11. Waddington, C. The strategy of the genes: a discussion of some aspects of theoretical biology (London: Gorge Allen and Unwin). **1957**.

12. Henning, A.N.; Klebanoff, C.A.; Restifo, N.P. Silencing stemness in T cell differentiation. *Science* **2018**, *359*, 163-164.

13. Castro-Vega, L.J.; Jouravleva, K.; Ortiz-Montero, P.; Liu, W.-Y.; Galeano, J.L.; Romero, M.; Popova, T.; Bacchetti, S.; Vernot, J.P.; Londoño-Vallejo, A. The senescent microenvironment promotes the emergence of heterogeneous cancer stem-like cells. *Carcinogenesis* **2015**, *36*, 1180-1192, doi:10.1093/carcin/bgv101.

14. Sawant, D.V.; Yano, H.; Chikina, M.; Zhang, Q.; Liao, M.; Liu, C.; Callahan, D.J.; Sun, Z.; Sun, T.; Tabib, T. Adaptive plasticity of IL-10+ and IL-35+ T reg cells cooperatively promotes tumor T cell exhaustion. *Nature immunology* **2019**, *20*, 724.

15. Pribluda, A.; Elyada, E.; Wiener, Z.; Hamza, H.; Goldstein, R.E.; Biton, M.; Burstain, I.; Morgenstern, Y.; Brachya, G.; Billauer, H. A senescence-inflammatory switch from cancer-inhibitory to cancer-promoting mechanism. *Cancer cell* **2013**, *24*, 242-256.

16. Tsoucalas, G.; Karamanou, M.; Lymperi, M.; Gennimata, V.; Androutsos, G. The "torpedo" effect in medicine. *International maritime health* **2014**, *65*, 65-67.

17. Potter, H. Electroporation in biology: Methods, applications, and instrumentation. *Analytical Biochemistry* **1988**, *174*, 361-373, doi:https://doi.org/10.1016/0003-2697(88)90035-8.

18. Schoenbach, K.H.; Peterkin, F.E.; Alden, R.W.; Beebe, S.J. The effect of pulsed electric fields on biological cells: Experiments and applications. *IEEE transactions on plasma science* **1997**, *25*, 284-292.

19. Schoenbach, K.H.; Beebe, S.J.; Buescher, E.S. Intracellular effect of ultrashort electrical pulses. *Bioelectromagnetics: Journal of the Bioelectromagnetics Society, The Society for Physical Regulation in Biology and Medicine, The European Bioelectromagnetics Association* **2001**, *22*, 440-448.

20. Beebe, S.J. Cell responses without receptors and ligands, using nanosecond pulsed electric fields (nsPEFs). *Int J Nanomedicine* **2013**, *8*, 3401-3404, doi:10.2147/IJN.S51357.

21. Beebe, S.J.; Buescher, E.S.; Stark, R.H.; Schoenbach, K.H. Nanosecond pulsed electric field (nsPEF) application effects on human cells: intracellular membrane disruption and apoptosis induction. In Proceedings of the IEEE Conference Record - Abstracts. PPPS-2001 Pulsed Power Plasma Science 2001. 28th IEEE International Conference on Plasma Science and 13th IEEE International Pulsed Power Conference (Cat. No.01CH37, 17-22 June 2001, 2001; p. 251.

22. Beebe, S.J.; Chen, Y.J.; Sain, N.M.; Schoenbach, K.H.; Xiao, S. Transient features in nanosecond pulsed electric fields differentially modulate mitochondria and viability. *PLoS One* **2012**, *7*, e51349, doi:10.1371/journal.pone.0051349.

23. Beebe, S.J.; Fox, P.M.; Rec, L.J.; Somers, K.; Stark, R.H.; Schoenbach, K.H. Nanosecond Pulsed Electric Field (nsPEF) Effects on Cells and Tissues: Apoptosis Induction and Tumor Growth Inhibition. *IEEE Transactions on Plasma Science* **2002**, *30*, 286.

24. Beebe, S.J.; Fox, P.M.; Rec, L.J.; Willis, E.L.K.; Schoenbach, K.H. Nanosecond, high-intensity pulsed electric fields induce apoptosis in human cells. *The FASEB journal* **2003**, *17*, 1493-1495.

25. Beebe, S.J.; Sain, N.M.; Wei, R. Induction of Cell Death Mechanisms and Apoptosis by Nanosecond Pulsed Electric Fields (nsPEFs). *Cells (2073-4409)* **2013**, *2*, 136-162, doi:10.3390/cells2010136.

26. Beebe, S.J.; White, J.; Blackmore, P.F.; Deng, Y.; Somers, K.; Schoenbach, K.H. Diverse effects of nanosecond pulsed electric fields on cells and tissues. *DNA and cell biology* **2003**, *22*, 785-796.

27. Beebe, S.J.; White, J.; Blackmove, P.; Schoenbach, K.H. Nanosecond pulsed electric fields mimic natural cell signal transduction mechanisms. In Proceedings of the Conference Record of the Twenty-Sixth International Power Modulator Symposium, 2004 and 2004 High-Voltage Workshop., 23-26 May 2004, 2004; pp. 220-223.

28. Garner, A.L.; Yang, J.; Chen, N.; Kolb, J.; Loftin, K.C.; Swanson, R.J.; Beebe, S.; Joshi, R.P.; Schoenbach, K.H. Effects of electrical pulses on the dielectric properties of biological cells. In Proceedings of the 2003 Annual Report Conference on Electrical Insulation and Dielectric Phenomena, 19-22 Oct. 2003, 2003; pp. 52-55.

29. Beebe, S.; Fox, P.; Rec, L.; Gellerman, M.; Hall, E.; Willis, L.; Hair, P.; Buescher, E.; Deng, J.; Stark, F.H. High Intensity, Nanosecond Pulsed Electric Fields (nsPEF) Induce Apoptosis In Vitro And In Vivo And Inhibit Tumor Growth in Vivo. *AFOSR/NE*, 21.

30. Beebe, S.; Lassiter, B.; Guo, S. Nanopulse stimulation (NPS) induces tumor ablation and immunity in orthotopic 4T1 mouse breast cancer: A review. *Cancers* **2018**, *10*, 97.

31. Beebe, S.J. Concepts of Cancer and a Novel Cancer Therapy: Treating Tumors as an Aggressive Organ. **2014**.

32. Beebe, S.J. Considering effects of nanosecond pulsed electric fields on proteins. *Bioelectrochemistry* **2015**, *103*, 52-59.

33. Beebe, S.J. Regulated and Apoptotic Cell Death After Nanosecond Electroporation. *Handbook of Electroporation* **2016**, 1-18.

34. Beebe, S.J. Preclinical Studies on Nanosecond Pulses. *Handbook of Electroporation* **2016**, 1-20.

35. Stacey, M.; Stickley, J.; Fox, P.; Statler, V.; Schoenbach, K.; Beebe, S.; Buescher, S. Differential effects in cells exposed to ultra-short, high intensity electric fields: cell survival, DNA damage, and cell cycle analysis. *Mutation Research/Genetic Toxicology and Environmental Mutagenesis* **2003**, *542*, 65-75.

36. Chen, X.; Swanson, R.J.; Beebe, S.J.; Zheng, S.; Kolb, J.F.; Schoenbach, K.H. Nanosecond Pulsed Electric Fields (nsPEFs) Inhibit Melanoma Angiogenesis. In Proceedings of the 2007 International Conference on Electromagnetics in Advanced Applications, 17-21 Sept. 2007, 2007; pp. 1040-1043.

37. Chen, X.; Swanson, R.J.; Kolb, J.F.; Nuccitelli, R.; Schoenbach, K.H. Histopathology of normal skin and melanomas after nanosecond pulsed electric field treatment. *Melanoma research* **2009**, *19*, 361.

38. Chen, X.; Yin, S.; Hu, C.; Chen, X.; Jiang, K.; Ye, S.; Feng, X.; Fan, S.; Xie, H.; Zhou, L. Comparative study of nanosecond electric fields in vitro and in vivo on hepatocellular carcinoma indicate macrophage infiltration contribute to tumor ablation in vivo. *PLoS One* **2014**, *9*, e86421.

39. Chen, X.; Zhang, R.; Aji, T.; Shao, Y.; Chen, Y.; Wen, H. Novel Interventional Management of Hepatic Hydatid Cyst with Nanosecond Pulses on Experimental Mouse Model. *Scientific Reports* **2017**, *7*.

40. Dong, Y.; Yang, W.G.; Weissberg, J.; Goff, C.B.; Chen, W.; Kuwayama, Y.; Leiter, A.; Xing, H.; Meixel, A.; Gaut, D.; et al. Cutaneous Papilloma and Squamous Cell Carcinoma Therapy Utilizing Nanosecond Pulsed Electric Fields (nsPEF). *PLoS ONE* **2012**, *7*, 1-11, doi:10.1371/journal.pone.0043891.

41. Garon, E.B.; Sawcer, D.; Vernier, P.T.; Tang, T.; Sun, Y.; Marcu, L.; Gundersen, M.A.; Koeffler, H.P. In vitro and in vivo evaluation and a case report of intense nanosecond pulsed electric field as a local therapy for human malignancies. *International journal of cancer* **2007**, *121*, 675-682.

42. Gianulis, E.; Labib, C.; Saulis, G.; Novickij, V.; Pakhomova, O.; Pakhomov, A. Selective susceptibility to nanosecond pulsed electric field (nsPEF) across different human cell types. *Cellular & Molecular Life Sciences* **2017**, *74*, 1741-1754, doi:10.1007/s00018-016-2434-4.

43. Hall, E.H.; Schoenbach, K.H.; Beebe, S.J. Nanosecond Pulsed Electric Fields (nsPEF) Induce Direct Electric Field Effects and Biological Effects on Human Colon Carcinoma Cells. *DNA & Cell Biology* **2005**, *24*, 283-291, doi:10.1089/dna.2005.24.283.

44. Hall, E.H.; Schoenbach, K.H.; Beebe, S.J. Nanosecond pulsed electric fields induce apoptosis in p53-wildtype and p53-null HCT116 colon carcinoma cells. *Apoptosis* **2007**, *12*, 1721-1731.

45. Nuccitelli, R.; Chen, X.; Pakhomov, A.G.; Baldwin, W.H.; Sheikh, S.; Pomicter, J.L.; Ren, W.; Osgood, C.; Swanson, R.J.; Kolb, J.F. A new pulsed electric field therapy for melanoma disrupts the tumor's blood supply and causes complete remission without recurrence. *International journal of cancer* **2009**, *125*, 438-445.

46. Nuccitelli, R.; Lui, K.; Kreis, M.; Athos, B.; Nuccitelli, P. Nanosecond pulsed electric field stimulation of reactive oxygen species in human pancreatic cancer cells is Ca 2+-dependent. *Biochemical and biophysical research communications* **2013**, *435*, 580-585.

47. Nuccitelli, R.; Pliquett, U.; Chen, X.; Ford, W.; James Swanson, R.; Beebe, S.J.; Kolb, J.F.; Schoenbach, K.H. Nanosecond pulsed electric fields cause melanomas to self-destruct.

Biochemical and Biophysical Research Communications **2006**, *343*, 351-360, doi:https://doi.org/10.1016/j.bbrc.2006.02.181.

48. Ren, W.; Beebe, S.J. An apoptosis targeted stimulus with nanosecond pulsed electric fields (nsPEFs) in E4 squamous cell carcinoma. *Apoptosis* **2011**, *16*, 382-393.

49. Ren, W.; Sain, N.M.; Beebe, S.J. Nanosecond pulsed electric fields (nsPEFs) activate intrinsic caspase-dependent and caspase-independent cell death in Jurkat cells. *Biochem Biophys Res Commun* **2012**, *421*, 808-812, doi:10.1016/j.bbrc.2012.04.094.

50. Ren, Z.; Chen, X.; Cui, G.; Yin, S.; Chen, L.; Jiang, J.; Hu, Z.; Xie, H.; Zheng, S.; Zhou, L. Nanosecond pulsed electric field inhibits cancer growth followed by alteration in expressions of NF-κB and Wnt/β-catenin signaling molecules. *PLoS One* **2013**, *8*, e74322.

51. Rols, M.-P.; Teissie, J. Electropermeabilization of mammalian cells to macromolecules: control by pulse duration. *Biophysical journal* **1998**, *75*, 1415-1423.

52. Schoenbach, K.H.; Abou-Ghazala, A.; Vithoulkas, T.; Alden, R.W.; Turner, R.; Beebe, S. The effect of pulsed electrical fields on biological cells. In Proceedings of the Digest of Technical Papers. 11th IEEE International Pulsed Power Conference (Cat. No.97CH36127), 29 June-2 July 1997, 1997; pp. 73-78 vol.71.

53. Schoenbach, K.H.; Hargrave, S.J.; Joshi, R.P.; Kolb, J.F.; Nuccitelli, R.; Osgood, C.; Pakhomov, A.; Stacey, M.; Swanson, R.J.; White, J.A. Bioelectric effects of intense nanosecond pulses. *IEEE Transactions on Dielectrics and Electrical Insulation* **2007**, *14*, 1088-1109.

54. Schoenbach, K.H.; Joshi, R.; Kolb, J.; Buescher, S.; Beebe, S. Subcellular effects of nanosecond electrical pulses. In Proceedings of the The 26th Annual International Conference of the IEEE Engineering in Medicine and Biology Society, 1-5 Sept. 2004, 2004; pp. 5447-5450.

55. Schoenbach, K.H.; Katsuki, S.; Stark, R.H.; Buescher, E.S.; Beebe, S.J. Bioelectrics-new applications for pulsed power technology. *IEEE Transactions on Plasma Science* **2002**, *30*, 293-300, doi:10.1109/TPS.2002.1003873.

56. Schoenbach, K.H.; Stark, R.H.; Deng, J.; Aly, R.E.; Beebe, S.J.; Buescher, E.S. Biological/medical pulsed electric field treatments. In Proceedings of the Conference Record of the 2000 Twenty-fourth International Power Modulator Symposium, 26-29 June 2000, 2000; pp. 42-46.

57. Schoenbach, K.H.; Xiao, S.; Camp, J.T.; Heeren, T.; Kolb, J.F.; White, J.A.; Migliaccio, M.; Joshi, R.P.; Nuccitelli, R.; Beebe, S.J.; et al. From Submicrosecond to Subnanosecond Pulses - Entering a New Domain of Electric Field-Cell Interactions. In Proceedings of the 2007 IEEE 34th International Conference on Plasma Science (ICOPS), 17-22 June 2007, 2007; pp. 474-474.

58. Wu, S.; Wang, Y.; Guo, J.; Chen, Q.; Zhang, J.; Fang, J. Nanosecond pulsed electric fields as a novel drug free therapy for breast cancer: an in vivo study. *Cancer letters* **2014**, *343*, 268-274.

59. Yin, S.; Chen, X.; Hu, C.; Zhang, X.; Hu, Z.; Yu, J.; Feng, X.; Jiang, K.; Ye, S.; Shen, K.; et al. Nanosecond pulsed electric field (nsPEF) treatment for hepatocellular carcinoma: A novel locoregional ablation decreasing lung metastasis. *Cancer Letters* **2014**, *346*, 285-291, doi:10.1016/j.canlet.2014.01.009.

60. Guo, S.; Jing, Y.; Burcus, N.I.; Lassiter, B.P.; Tanaz, R.; Heller, R.; Beebe, S.J. Nano-pulse stimulation induces potent immune responses, eradicating local breast cancer while reducing distant metastases. *International journal of cancer* **2018**, *142*, 629-640.

61. Shi, G.; Edelblute, C.; Arpag, S.; Lundberg, C.; Heller, R. IL-12 gene electrotransfer triggers a change in immune response within mouse tumors. *Cancers* **2018**, *10*, 498.

62. Kos, S.; Lopes, A.; Preat, V.; Cemazar, M.; Lampreht Tratar, U.; Ucakar, B.; Vanvarenberg, K.; Sersa, G.; Vandermeulen, G. Intradermal DNA vaccination combined with dual CTLA-4 and PD-1 blockade provides robust tumor immunity in murine melanoma. *PloS one* **2019**, *14*, e0217762.

63. Biswas, S.K. Metabolic reprogramming of immune cells in cancer progression. *Immunity* **2015**, *43*, 435-449.

64. Buck, M.D.; Sowell, R.T.; Kaech, S.M.; Pearce, E.L. Metabolic instruction of immunity. *Cell* **2017**, *169*, 570-586.

65. Giannone, G.; Ghisoni, E.; Genta, S.; Scotto, G.; Tuninetti, V.; Turinetto, M.; Valabrega, G. Immuno-Metabolism and Microenvironment in Cancer: Key Players for Immunotherapy. *International journal of molecular sciences* **2020**, *21*, 4414, doi:10.3390/ijms21124414.

66. Wang, X.; Ping, F.F.; Bakht, S.; Ling, J.; Hassan, W. Immunometabolism features of metabolic deregulation and cancer. *Journal of Cellular and Molecular Medicine* **2019**, *23*, 694-701.

67. Kang, S.; Kumanogoh, A. The spectrum of macrophage activation by immunometabolism. *International Immunology* **2020**, *32*, 467-473, doi:10.1093/intimm/dxaa017.

68. Poznanski, S.M.; Barra, N.G.; Ashkar, A.A.; Schertzer, J.D. Immunometabolism of T cells and NK cells: metabolic control of effector and regulatory function. *Inflammation Research* **2018**, *67*, 813-828.

69. Kobayashi, T.; Mattarollo, S.R. Natural killer cell metabolism. *Molecular Immunology* **2019**, *115*, 3-11, doi:https://doi.org/10.1016/j.molimm.2017.11.021.

70. van der Windt, G.J.W.; Chang, C.-H.; Pearce, E.L. Measuring Bioenergetics in T Cells Using a Seahorse Extracellular Flux Analyzer. *Current protocols in immunology* **2016**, *113*, 3.16B.11-13.16B.14, doi:10.1002/0471142735.im0316bs113.

71. Fan, M.Y.; Turka, L.A. Immunometabolism and PI (3) K signaling as a link between IL-2, Foxp3 expression, and suppressor function in regulatory T cells. *Frontiers in immunology* **2018**, *9*, 69.

72. Ramalho, R.; Rao, M.; Zhang, C.; Agrati, C.; Ippolito, G.; Wang, F.-S.; Zumla, A.; Maeurer, M. Immunometabolism: new insights and lessons from antigen-directed cellular immune responses. In Proceedings of the Seminars in Immunopathology, 2020; p. 1.

73. Alissafi, T.; Kalafati, L.; Lazari, M.; Filia, A.; Kloukina, I.; Manifava, M.; Lim, J.-H.; Alexaki, V.I.; Ktistakis, N.T.; Doskas, T. Mitochondrial Oxidative Damage Underlies Regulatory T Cell Defects in Autoimmunity. *Cell Metabolism* **2020**.

74. Breda, C.N.d.S.; Davanzo, G.G.; Basso, P.J.; Saraiva Câmara, N.O.; Moraes-Vieira, P.M.M. Mitochondria as central hub of the immune system. *Redox biology* **2019**, *26*, 101255-101255, doi:10.1016/j.redox.2019.101255.

75. Monteiro, L.d.B.; Davanzo, G.G.; de Aguiar, C.F.; Moraes-Vieira, P.M.M. Using flow cytometry for mitochondrial assays. *MethodsX* **2020**, *7*, 100938, doi:https://doi.org/10.1016/j.mex.2020.100938.

76. Schoenbach, K.H.; Beebe, S.J.; Buescher, E.S. Intracellular effect of ultrashort electrical pulses. *Bioelectromagnetics* **2001**, *22*, 440-448, doi:10.1002/bem.71.

77. Schoenbach, K.H.; Joshi, R.P.; Stark, R.H.; Dobbs, F.; Beebe, S.J. Bacterial decontamination of liquids with pulsed electric fields. *IEEE Transactions on Dielectrics and Electrical Insulation* **2000**, *7*, 637-645.

78. White, J.A.; Blackmore, P.F.; Schoenbach, K.H.; Beebe, S.J. Stimulation of Capacitative Calcium Entry in HL-60 Cells by Nanosecond Pulsed Electric Fields. *Journal of Biological Chemistry* **2004**, *279*, 22964-22972, doi:10.1074/jbc.M311135200.

79. McDonnell, K.J.; Chemler, J.A.; Bartels, P.L.; O'Brien, E.; Marvin, M.L.; Ortega, J.; Stern, R.H.; Raskin, L.; Li, G.-M.; Sherman, D.H.; et al. A human MUTYH variant linking colonic polyposis to redox degradation of the [4Fe4S]2+ cluster. *Nature Chemistry* **2018**, *10*, 873-880, doi:10.1038/s41557-018-0068-x.

80. Pakhomova, O.N.; Khorokhorina, V.A.; Bowman, A.M.; Rodaitė-Riševičienė, R.; Saulis, G.; Xiao, S.; Pakhomov, A.G. Oxidative effects of nanosecond pulsed electric field exposure in cells and cell-free media. *Archives of Biochemistry and Biophysics* **2012**, *527*, 55-64, doi:https://doi.org/10.1016/j.abb.2012.08.004.

81. Deng, J.; Schoenbach, K.H.; Buescher, E.S.; Hair, P.S.; Fox, P.M.; Beebe, S.J. The effects of intense submicrosecond electrical pulses on cells. *Biophysical journal* **2003**, *84*, 2709-2714.

82. Beebe, S.J.; Fox, P.; Rec, L.; Somers, K.; Stark, R.H.; Schoenbach, K.H. Nanosecond pulsed electric field (nsPEF) effects on cells and tissues: apoptosis induction and tumor growth inhibition. *IEEE Transactions on plasma science* **2002**, *30*, 286-292.

83. Vernier, P.T.; Ziegler, M.J.; Sun, Y.; Gundersen, M.A.; Tieleman, D.P. Nanopore-facilitated, voltage-driven phosphatidylserine translocation in lipid bilayers—in cells andin silico. *Physical Biology* **2006**, *3*, 233-247, doi:10.1088/1478-3975/3/4/001.

84. Sözer, E.B.; Pocetti, C.F.; Vernier, P.T. Transport of charged small molecules after electropermeabilization—drift and diffusion. *BMC biophysics* **2018**, *11*, 1-11.

85. Flewelling, R.F.; Hubbell, W.L. The membrane dipole potential in a total membrane potential model. Applications to hydrophobic ion interactions with membranes. *Biophysical journal* **1986**, *49*, 541-552.

86. Pakhomov, A.G.; Kolb, J.F.; White, J.A.; Joshi, R.P.; Xiao, S.; Schoenbach, K.H. Long-lasting plasma membrane permeabilization in mammalian cells by nanosecond pulsed electric field (nsPEF). *Bioelectromagnetics: Journal of the Bioelectromagnetics Society, The Society for Physical Regulation in Biology and Medicine, The European Bioelectromagnetics Association* **2007**, *28*, 655-663.

87. Gianulis, E.C.; Labib, C.; Saulis, G.; Novickij, V.; Pakhomova, O.N.; Pakhomov, A.G. Selective susceptibility to nanosecond pulsed electric field (nsPEF) across different human cell types. *Cellular and molecular life sciences: CMLS* **2017**, *74*, 1741.

88. Vernier, P.T.; Sun, Y.; Gundersen, M.A. Nanoelectropulse-driven membrane perturbation and small molecule permeabilization. *BMC cell biology* **2006**, *7*, 1-16.

89. Vernier, P.T.; Sun, Y.; Marcu, L.; Craft, C.M.; Gundersen, M.A. Nanoelectropulse-induced phosphatidylserine translocation. *Biophysical journal* **2004**, *86*, 4040-4048.

90. Pakhomov, A.G.; Bowman, A.M.; Ibey, B.L.; Andre, F.M.; Pakhomova, O.N.; Schoenbach, K.H. Lipid nanopores can form a stable, ion channel-like conduction pathway in cell membrane. *Biochemical and biophysical research communications* **2009**, *385*, 181-186.

91. Napotnik, T.B.; Reberšek, M.; Vernier, P.T.; Mali, B.; Miklavčič, D. Effects of high voltage nanosecond electric pulses on eukaryotic cells (in vitro): A systematic review. *Bioelectrochemistry* **2016**, *110*, 1-12.

92. Pakhomova, O.N.; Gregory, B.W.; Semenov, I.; Pakhomov, A.G. Two modes of cell death caused by exposure to nanosecond pulsed electric field. *PloS one* **2013**, *8*, e70278.

93. Morotomi-Yano, K.; Akiyama, H.; Yano, K.-i. Different involvement of extracellular calcium in two modes of cell death induced by nanosecond pulsed electric fields. *Archives of biochemistry and biophysics* **2014**, *555*, 47-54.

94. Rossi, A.; Pakhomova, O.N.; Pakhomov, A.G.; Weygandt, S.; Bulysheva, A.A.; Murray, L.E.; Mollica, P.A.; Muratori, C. Mechanisms and immunogenicity of nsPEF-induced cell death in B16F10 melanoma tumors. *Scientific Reports* **2019**, *9*, 431, doi:10.1038/s41598-018-36527-5.

95. Budi, A.; Legge, F.S.; Treutlein, H.; Yarovsky, I. Electric field effects on insulin chain-B conformation. *The Journal of Physical Chemistry B* **2005**, *109*, 22641-22648.

96. Marracino, P.; Apollonio, F.; Liberti, M.; d'Inzeo, G.; Amadei, A. Effect of High Exogenous Electric Pulses on Protein Conformation: Myoglobin as a Case Study. *The Journal of Physical Chemistry B* **2013**, *117*, 2273-2279, doi:10.1021/jp309857b.

97. Marracino, P.; Paffi, A.; Reale, R.; Liberti, M.; d'Inzeo, G.; Apollonio, F. Technology of high-intensity electric-field pulses: a way to control protein unfolding. *J Phys Chem Biophys* **2013**, *3*, 2161-0398.1000117.

98. Beebe, S.J.; Øyen, O.; Sandberg, M.; Frøysa, A.; Hansson, V.; Jahnsen, T. Molecular cloning of a tissue-specific protein kinase (Cγ) from human testis—representing a third isoform for the catalytic subunit of cAMP-dependent protein kinase. *Molecular Endocrinology* **1990**, *4*, 465-475.

99. Singh, A.; Orsat, V.; Raghavan, V. Soybean hydrophobic protein response to external electric field: a molecular modeling approach. *Biomolecules* **2013**, *3*, 168-179.

100. Manning, G.; Whyte, D.B.; Martinez, R.; Hunter, T.; Sudarsanam, S. The protein kinase complement of the human genome. *Science* **2002**, *298*, 1912-1934.

101. Nesin, V.; Pakhomov, A.G. Inhibition of voltage-gated Na+ current by nanosecond pulsed electric field (nsPEF) is not mediated by Na+ influx or Ca2+ signaling. *Bioelectromagnetics* **2012**, *33*, 443-451.

102. Nesin, V.; Bowman, A.M.; Xiao, S.; Pakhomov, A.G. Cell permeabilization and inhibition of voltage-gated Ca2+ and Na+ channel currents by nanosecond pulsed electric field. *Bioelectromagnetics* **2012**, *33*, 394-404.

103. Hristov, K.; Mangalanathan, U.; Casciola, M.; Pakhomova, O.N.; Pakhomov, A.G. Expression of voltage-gated calcium channels augments cell susceptibility to membrane disruption by nanosecond pulsed electric field. *Biochimica et Biophysica Acta (BBA)-Biomembranes* **2018**, *1860*, 2175-2183.

104. Vernier, P.T.; Sun, Y.; Marcu, L.; Salemi, S.; Craft, C.M.; Gundersen, M.A. Calcium bursts induced by nanosecond electric pulses. *Biochemical and Biophysical Research Communications* **2003**, *310*, 286-295, doi:https://doi.org/10.1016/j.bbrc.2003.08.140.

105. Fauvel, J.; Chap, H.; Roques, V.; Levy-Toledano, S.; Douste-Blazy, L. Biochemical characterization of plasma membranes and intracellular membranes isolated from human platelets using Percoll gradients. *Biochim Biophys Acta* **1986**, *856*, 155-164.

106. Gowrishankar, T.R.; Esser, A.T.; Vasilkoski, Z.; Smith, K.C.; Weaver, J.C. Microdosimetry for conventional and supra-electroporation in cells with organelles. *Biochemical and Biophysical Research Communications* **2006**, *341*, 1266-1276, doi:https://doi.org/10.1016/j.bbrc.2006.01.094.

107. Gowrishankar, T.; Weaver, J.C. Electrical behavior and pore accumulation in a multicellular model for conventional and supra-electroporation. *Biochemical and biophysical research communications* **2006**, *349*, 643-653.

108. Marracino, P.; Havelka, D.; Průša, J.; Liberti, M.; Tuszynski, J.; Ayoub, A.T.; Apollonio, F.; Cifra, M. Tubulin response to intense nanosecond-scale electric field in molecular dynamics simulation. *Scientific reports* **2019**, *9*, 1-14.

109. Schoenbach, K.H.; Joshi, R.P.; Beebe, S.J.; Baum, C.E. A scaling law for membrane permeabilization with nanopulses. *IEEE Transactions on Dielectrics and Electrical Insulation* **2009**, *16*, 1224-1235.

110. Curtis, H.J.; Cole, K.S. Transverse electric impedance of Nitella. *The Journal of general physiology* **1937**, *21*, 189-201.

111. Cole, K. Electric impedance of marine egg membranes. *Transactions of the Faraday Society* **1937**, *33*, 966-972.

112. Semenov, I.; Zemlin, C.; Pakhomova, O.N.; Xiao, S.; Pakhomov, A.G. Diffuse, non-polar electropermeabilization and reduced propidium uptake distinguish the effect of nanosecond electric pulses. *Biochimica et Biophysica Acta (BBA)-Biomembranes* **2015**, *1848*, 2118-2125.

113. Nuccitelli, R.; McDaniel, A.; Anand, S.; Cha, J.; Mallon, Z.; Berridge, J.C.; Uecker, D. Nano-Pulse Stimulation is a physical modality that can trigger immunogenic tumor cell death. *Journal for ImmunoTherapy of Cancer* **2017**, *5*, 32, doi:10.1186/s40425-017-0234-5.

114. Lassiter, B.P.; Guo, S.; Beebe, S.J. Nano-pulse stimulation ablates orthotopic rat hepatocellular carcinoma and induces innate and adaptive memory immune mechanisms that prevent recurrence. *Cancers* **2018**, *10*, 69.

115. Hanahan, D.; Weinberg, R.A. The hallmarks of cancer. *cell* **2000**, *100*, 57-70.

116. Genovese, I.; Vezzani, B.; Danese, A.; Modesti, L.; Vitto, V.A.M.; Corazzi, V.; Pelucchi, S.; Pinton, P.; Giorgi, C. Mitochondria as the decision makers for cancer cell fate: from signaling pathways to therapeutic strategies. *Cell Calcium* **2020**, *92*, 102308, doi:https://doi.org/10.1016/j.ceca.2020.102308.

117. Osellame, L.D.; Blacker, T.S.; Duchen, M.R. Cellular and molecular mechanisms of mitochondrial function. *Best practice & research Clinical endocrinology & metabolism* **2012**, *26*, 711-723.

118. Briston, T.; Selwood, D.L.; Szabadkai, G.; Duchen, M.R. Mitochondrial Permeability Transition: A Molecular Lesion with Multiple Drug Targets. *Trends in Pharmacological Sciences* **2019**, *40*, 50-70, doi:https://doi.org/10.1016/j.tips.2018.11.004.

119. Elrod, J.W.; Molkentin, J.D. Physiologic functions of cyclophilin D and the mitochondrial permeability transition pore. *Circ J* **2013**, *77*, 1111-1122, doi:10.1253/circj.cj-13-0321.

120. Haworth, R.A.; Hunter, D.R. The Ca2+-induced membrane transition in mitochondria: II. Nature of the Ca2+ trigger site. *Archives of biochemistry and biophysics* **1979**, *195*, 460-467.

121. Hunter, D.R.; Haworth, R.A. The Ca2+-induced membrane transition in mitochondria: I. The protective mechanisms. *Archives of biochemistry and biophysics* **1979**, *195*, 453-459.

122. Hunter, D.R.; Haworth, R.A. The Ca2+-induced membrane transition in mitochondria: III. Transitional Ca2+ release. *Archives of biochemistry and biophysics* **1979**, *195*, 468-477.

123. Haworth, R.A.; Hunter, D.R. Control of the mitochondrial permeability transition pore by high-affinity ADP binding at the ADP/ATP translocase in permeabilized mitochondria. *Journal of bioenergetics and biomembranes* **2000**, *32*, 91-96.

124. Crompton, M.; Costi, A. A heart mitochondrial Ca2+-dependent pore of possible relevance to re-perfusion-induced injury. Evidence that ADP facilitates pore interconversion between the closed and open states. *Biochemical Journal* **1990**, *266*, 33-39.

125. McGuinness, O.; Yafei, N.; Costi, A.; Crompton, M. The presence of two classes of high-affinity cyclosporin A binding sites in mitochondria: Evidence that the minor component is involved in the opening of an inner-membrane Ca2+-dependent pore. *European journal of biochemistry* **1990**, *194*, 671-679.

126. Elrod, J.W.; Molkentin, J.D. Physiologic functions of cyclophilin D and the mitochondrial permeability transition pore. *Circulation Journal* **2013**, CJ-13-0321.

127. Baines, C.P.; Gutiérrez-Aguilar, M. The still uncertain identity of the channel-forming unit(s) of the mitochondrial permeability transition pore. *Cell Calcium* **2018**, *73*, 121-130, doi:https://doi.org/10.1016/j.ceca.2018.05.003.

128. Anselmi, C.; Davies, K.M.; Faraldo-Gómez, J.D. Mitochondrial ATP synthase dimers spontaneously associate due to a long-range membrane-induced force. *The Journal of general physiology* **2018**, *150*, 763-770.

129. Virchow, R. An address on the value of pathological experiments. *British medical journal* **1881**, *2*, 198.

130. Garner, H.; de Visser, K.E. Immune crosstalk in cancer progression and metastatic spread: a complex conversation. *Nature Reviews Immunology* **2020**, *20*, 483-497.

131. Ehrlich, P. *Ueber den jetzigen Stand der Karzinomforschung*; 1908.

132. Coley, W.B. The treatment of malignant tumors by repeated inoculations of erysipelas: With a report of ten original cases. 1. *The American Journal of the Medical Sciences (1827-1924)* **1893**, *105*, 487.

133. Coffelt, S.B.; de Visser, K.E. Immune-mediated mechanisms influencing the efficacy of anticancer therapies. *Trends in immunology* **2015**, *36*, 198-216.

134. Paget, S. The distribution of secondary growths in cancer of the breast. *The Lancet* **1889**, *133*, 571-573.

135. Seyfried, T.N.; Huysentruyt, L.C. On the origin of cancer metastasis. *Critical Reviews™ in Oncogenesis* **2013**, *18*.

136. Maman, S.; Witz, I.P. A history of exploring cancer in context. *Nature Reviews Cancer* **2018**, *18*, 359-376.

137. Vogelstein, B.; Kinzler, K.W. The multistep nature of cancer. *Trends in genetics* **1993**, *9*, 138-141.

138. Hersh, E.M.; Mavligit, G.M.; Gutterman, J.U.; Barsales, P.B. Mononuclear cell content of human solid tumors. *Medical and pediatric oncology* **1976**, *2*, 1-9.

139. Tötterman, T.H.; Parthenais, E.; Häyry, P.; Timonen, T.; Saksela, E. Cytological and functional analysis of inflammatory infiltrates in human malignant tumors: III. Further functional investigations using cultured autochthonous tumor cell lines and freeze-thawed infiltrating inflammatory cells. *Cellular immunology* **1980**, *55*, 219-226.

140. Russell, S.W.; Doe, W.F.; Cochrane, C.G. Number of macrophages and distribution of mitotic activity in regressing and progressing Moloney sarcomas. *The Journal of Immunology* **1976**, *116*, 164-166.

141. Whiteside, T. The tumor microenvironment and its role in promoting tumor growth. *Oncogene* **2008**, *27*, 5904-5912.

142. Joyce, J.A.; Pollard, J.W. Microenvironmental regulation of metastasis. *Nature reviews cancer* **2009**, *9*, 239-252.

143. Kitamura, T.; Qian, B.-Z.; Pollard, J.W. Immune cell promotion of metastasis. *Nature Reviews Immunology* **2015**, *15*, 73-86.

144. Beebe, S.J.; Blackmore, P.F.; White, J.; Joshi, R.P.; Schoenbach, K.H. Nanosecond pulsed electric fields modulate cell function through intracellular signal transduction mechanisms. *Physiological measurement* **2004**, *25*, 1077.

145. Schoenbach, K.H.; Joshi, R.P.; Kolb, J.F.; Chen, N.; Stacey, M.; Blackmore, P.F.; Buescher, E.S.; Beebe, S.J. Ultrashort electrical pulses open a new gateway into biological cells. *Proceedings of the IEEE* **2004**, *92*, 1122-1137.

146. Lucas, M.L.; Heller, L.; Coppola, D.; Heller, R. IL-12 Plasmid Delivery by in Vivo Electroporation for the Successful Treatment of Established Subcutaneous B16.F10 Melanoma. *Molecular Therapy* **2002**, *5*, 668-675, doi:10.1006/mthe.2002.0601.

147. Neumann, E.; Schaefer-Ridder, M.; Wang, Y.; Hofschneider, P. Gene transfer into mouse lyoma cells by electroporation in high electric fields. *The EMBO journal* **1982**, *1*, 841-845.

148. Shirley, S.A.; Lundberg, C.G.; Li, F.; Burcus, N.; Heller, R. Controlled gene delivery can enhance therapeutic outcome for cancer immune therapy for melanoma. *Current gene therapy* **2015**, *15*, 32-43, doi:10.2174/1566523214666141121111630.

149. Guo, S.; Jackson, D.L.; Burcus, N.I.; Chen, Y.-J.; Xiao, S.; Heller, R. Gene electrotransfer enhanced by nanosecond pulsed electric fields. *Molecular Therapy - Methods & Clinical Development* **2014**, *1*, 14043, doi:https://doi.org/10.1038/mtm.2014.43.

150. World Health, O. *WHO global coordination mechanism on the prevention and control of noncommunicable diseases: final report: WHO GCM/NCD working group on the alignment of international cooperation with national NCD plans (Working group 3.2, 2016–2017)*; World Health Organization: Geneva, 2018 2018.

151. Wong, C.H.; Siah, K.W.; Lo, A.W. Estimating clinical trial success rates and related parameters in oncology. *Available at SSRN 3355022* **2019**.

152. Wong, C.H.; Siah, K.W.; Lo, A.W. Estimation of clinical trial success rates and related parameters. *Biostatistics* **2018**, *20*, 273-286, doi:10.1093/biostatistics/kxx069.

153. Begley, C.G.; Ellis, L.M. Raise standards for preclinical cancer research. *Nature* **2012**, *483*, 531-533, doi:10.1038/483531a.

154. Hutchinson, L.; Kirk, R. High drug attrition rates—where are we going wrong? *Nature reviews Clinical oncology* **2011**, *8*, 189-190.

155. Vyas, S.; Zaganjor, E.; Haigis, M.C. Mitochondria and cancer. *Cell* **2016**, *166*, 555-566.

156. Kauffman, M.E.; Kauffman, M.K.; Traore, K.; Zhu, H.; Trush, M.A.; Jia, Z.; Li, Y.R. MitoSOX-based flow cytometry for detecting mitochondrial ROS. *Reactive oxygen species (Apex, NC)* **2016**, *2*, 361.

157. Bantug, G.R.; Galluzzi, L.; Kroemer, G.; Hess, C. The spectrum of T cell metabolism in health and disease. *Nature Reviews Immunology* **2018**, *18*, 19.

158. Mills, E.L.; O'Neill, L.A. Reprogramming mitochondrial metabolism in macrophages as an anti-inflammatory signal. *European journal of immunology* **2016**, *46*, 13-21.

159. O'Neill, L.A.; Kishton, R.J.; Rathmell, J. A guide to immunometabolism for immunologists. *Nature Reviews Immunology* **2016**, *16*, 553.

160. van der Windt, G.J.; Chang, C.H.; Pearce, E.L. Measuring bioenergetics in T cells using a seahorse extracellular flux analyzer. *Current protocols in immunology* **2016**, *113*, 3.16 B. 11-13.16 B. 14.

161. Mathis, D.; Shoelson, S.E. Immunometabolism: an emerging frontier. *Nature reviews. Immunology* **2011**, *11*, 81.

162. Breda, C.N.d.S.; Davanzo, G.G.; Basso, P.J.; Saraiva Câmara, N.O.; Moraes-Vieira, P.M.M. Mitochondria as central hub of the immune system. *Redox Biology* **2019**, *26*, 101255, doi:https://doi.org/10.1016/j.redox.2019.101255.

163. Pesta, D.; Gnaiger, E. High-resolution respirometry: OXPHOS protocols for human cells and permeabilized fibers from small biopsies of human muscle. In *Mitochondrial bioenergetics*; Springer: 2012; pp. 25-58.

164. Ford, W.E.; Ren, W.; Blackmore, P.F.; Schoenbach, K.H.; Beebe, S.J. Nanosecond pulsed electric fields stimulate apoptosis without release of pro-apoptotic factors from mitochondria in B16f10 melanoma. *Archives of Biochemistry and Biophysics* **2010**, *497*, 82-89, doi:https://doi.org/10.1016/j.abb.2010.03.008.

165. Kuczma, M.; Podolsky, R.; Garge, N.; Daniely, D.; Pacholczyk, R.; Ignatowicz, L.; Kraj, P. Foxp3-deficient regulatory T cells do not revert into conventional effector CD4+ T cells but constitute a unique cell subset. *The Journal of Immunology* **2009**, *183*, 3731-3741.

166. Chen, R.; Sain, N.M.; Harlow, K.T.; Chen, Y.-J.; Shires, P.K.; Heller, R.; Beebe, S.J. A protective effect after clearance of orthotopic rat hepatocellular carcinoma by nanosecond pulsed electric fields. *European Journal of Cancer* **2014**, *50*, 2705-2713, doi:https://doi.org/10.1016/j.ejca.2014.07.006.

167. McDermott, S.P.; Eppert, K.; Lechman, E.R.; Doedens, M.; Dick, J.E. Comparison of human cord blood engraftment between immunocompromised mouse strains. *Blood* **2010**, *116*, 193-200, doi:10.1182/blood-2010-02-271841.

168. Wunderlich, M.; Chou, F.-S.; Sexton, C.; Presicce, P.; Chougnet, C.A.; Aliberti, J.; Mulloy, J.C. Improved multilineage human hematopoietic reconstitution and function in NSGS mice. *PloS one* **2018**, *13*, e0209034.

169. Futrega, K.; Lott, W.B.; Doran, M.R. Direct bone marrow HSC transplantation enhances local engraftment at the expense of systemic engraftment in NSG mice. *Scientific reports* **2016**, *6*, 23886.

170. Notta, F.; Doulatov, S.; Laurenti, E.; Poeppl, A.; Jurisica, I.; Dick, J.E. Isolation of single human hematopoietic stem cells capable of long-term multilineage engraftment. *Science* **2011**, *333*, 218-221.

171. McKenzie, J.L.; Gan, O.I.; Doedens, M.; Dick, J.E. Human short-term repopulating stem cells are efficiently detected following intrafemoral transplantation into NOD/SCID recipients depleted of CD122+ cells. *Blood* **2005**, *106*, 1259-1261.

172. Notta, F.; Doulatov, S.; Dick, J.E. Engraftment of human hematopoietic stem cells is more efficient in female NOD/SCID/IL-2Rgc-null recipients. *Blood* **2010**, *115*, 3704-3707.

173. Gschweng, E.; De Oliveira, S.; Kohn, D.B. Hematopoietic stem cells for cancer immunotherapy. *Immunological reviews* **2014**, *257*, 237-249.

174. Amanakis, G.; Murphy, E. Cyclophilin D: an integrator of mitochondrial function. *Frontiers in Physiology* **2020**, *11*.

175. Carraro, M.; Checchetto, V.; Szabó, I.; Bernardi, P. F-ATP synthase and the permeability transition pore: fewer doubts, more certainties. *FEBS letters* **2019**, *593*, 1542-1553.

176. Urbani, A.; Giorgio, V.; Carrer, A.; Franchin, C.; Arrigoni, G.; Jiko, C.; Abe, K.; Maeda, S.; Shinzawa-Itoh, K.; Bogers, J.F. Purified F-ATP synthase forms a Ca 2+-dependent high-conductance channel matching the mitochondrial permeability transition pore. *Nature communications* **2019**, *10*, 1-11.

177. Azarashvili, T.; Odinokova, I.; Bakunts, A.; Ternovsky, V.; Krestinina, O.; Tyynelä, J.; Saris, N.-E.L. Potential role of subunit c of F0F1-ATPase and subunit c of storage body in the mitochondrial permeability transition. Effect of the phosphorylation status of subunit c on pore opening. *Cell Calcium* **2014**, *55*, 69-77, doi:https://doi.org/10.1016/j.ceca.2013.12.002.

178. Sobti, M.; Smits, C.; Wong, A.S.; Ishmukhametov, R.; Stock, D.; Sandin, S.; Stewart, A.G. Cryo-EM structures of the autoinhibited E. coli ATP synthase in three rotational states. *eLife* **2016**, *5*, doi:10.7554/eLife.21598.

179. Jacobson, J.; Duchen, M.R. Mitochondrial oxidative stress and cell death in astrocytes—requirement for stored Ca2+ and sustained opening of the permeability transition pore. *Journal of Cell Science* **2002**, *115*, 1175-1188.

180. Brookes, P.S.; Yoon, Y.; Robotham, J.L.; Anders, M.; Sheu, S.-S. Calcium, ATP, and ROS: a mitochondrial love-hate triangle. *American Journal of Physiology-Cell Physiology* **2004**, *287*, C817-C833.

181. Pakhomova, O.N.; Khorokhorina, V.A.; Bowman, A.M.; Rodaitė-Riševičienė, R.; Saulis, G.; Xiao, S.; Pakhomov, A.G. Oxidative effects of nanosecond pulsed electric field exposure in cells and cell-free media. *Archives of Biochemistry & Biophysics* **2012**, *527*, 55-64, doi:10.1016/j.abb.2012.08.004.

182. Robinson, K.; Janes, M.; Pehar, M.; Beckman, J. Searching for Superoxide: Considerations for the Selective Detection of Superoxide Using Hydroethidine and MitoSOX Red: 260. *Free Radical Biology and Medicine* **2006**, *41*.

183. Zielonka, J.; Kalyanaraman, B. Hydroethidine-and MitoSOX-derived red fluorescence is not a reliable indicator of intracellular superoxide formation: another inconvenient truth. *Free Radical Biology and Medicine* **2010**, *48*, 983-1001.

184. Billerbeck, E.; Barry, W.T.; Mu, K.; Dorner, M.; Rice, C.M.; Ploss, A. Development of human CD4+FoxP3+ regulatory T cells in human stem cell factor-, granulocyte-macrophage colony-stimulating factor-, and interleukin-3-expressing NOD-SCID IL2Rgamma(null) humanized mice. *Blood* **2011**, *117*, 3076-3086, doi:10.1182/blood-2010-08-301507.

185. Ishikawa, F.; Yasukawa, M.; Lyons, B.; Yoshida, S.; Miyamoto, T.; Yoshimoto, G.; Watanabe, T.; Akashi, K.; Shultz, L.D.; Harada, M. Development of functional human blood and immune systems in NOD/SCID/IL2 receptor γ chainnull mice. *Blood* **2005**, *106*, 1565-1573.

186. De La Rochere, P.; Guil-Luna, S.; Decaudin, D.; Azar, G.; Sidhu, S.S.; Piaggio, E. Humanized mice for the study of immuno-oncology. *Trends in immunology* **2018**, *39*, 748-763.

187. Mazzucchelli, R.; Durum, S.K. Interleukin-7 receptor expression: intelligent design. *Nature Reviews Immunology* **2007**, *7*, 144-154.

188. Liu, Y.-J.; Soumelis, V.; Watanabe, N.; Ito, T.; Wang, Y.-H.; de Waal Malefyt, R.; Omori, M.; Zhou, B.; Ziegler, S.F. TSLP: an epithelial cell cytokine that regulates T cell differentiation by conditioning dendritic cell maturation. *Annu. Rev. Immunol.* **2007**, *25*, 193-219.

189. Barata, J.T.; Durum, S.K.; Seddon, B. Flip the coin: IL-7 and IL-7R in health and disease. *Nature immunology* **2019**, *20*, 1584-1593.

190. Sharpe, A.H.; Pauken, K.E. The diverse functions of the PD1 inhibitory pathway. *Nature Reviews Immunology* **2018**, *18*, 153-167, doi:10.1038/nri.2017.108.

191. Zhou, G.; Sprengers, D.; Boor, P.P.C.; Doukas, M.; Schutz, H.; Mancham, S.; Pedroza-Gonzalez, A.; Polak, W.G.; de Jonge, J.; Gaspersz, M.; et al. Antibodies Against Immune Checkpoint Molecules Restore Functions of Tumor-Infiltrating T Cells in Hepatocellular Carcinomas. *Gastroenterology* **2017**, *153*, 1107-1119.e1110, doi:10.1053/j.gastro.2017.06.017.

192. Vinay, D.S.; Ryan, E.P.; Pawelec, G.; Talib, W.H.; Stagg, J.; Elkord, E.; Lichtor, T.; Decker, W.K.; Whelan, R.L.; Kumara, H.S. Immune evasion in cancer: Mechanistic basis and therapeutic strategies. In Proceedings of the Seminars in cancer biology, 2015; pp. S185-S198.

193. Hayakawa, Y.; Smyth, M.J. CD27 dissects mature NK cells into two subsets with distinct responsiveness and migratory capacity. *The Journal of Immunology* **2006**, *176*, 1517-1524.

194. Napotnik, T.B.; Wu, Y.H.; Gundersen, M.A.; Miklavčič, D.; Vernier, P.T. Nanosecond electric pulses cause mitochondrial membrane permeabilization in Jurkat cells. *Bioelectromagnetics* **2012**, *33*, 257-264.

195. Kotnik, T.; Miklavčič, D. Theoretical evaluation of voltage inducement on internal membranes of biological cells exposed to electric fields. *Biophysical journal* **2006**, *90*, 480-491.

196. Weaver, J.C.; Schoenbach, K.H. Biodielectrics. *IEEE Transactions on Dielectrics and Electrical Insulation* **2003**, *10*, 715-716, doi:10.1109/TDEI.2003.1237322.

197. Tait, S.W.; Green, D.R. Mitochondria and cell signalling. *Journal of cell science* **2012**, *125*, 807-815.

198. Fournier, N.; Ducet, G.; Crevat, A. Action of cyclosporine on mitochondrial calcium fluxes. *Journal of bioenergetics and biomembranes* **1987**, *19*, 297-303.

199. Crompton, M.; Ellinger, H.; Costi, A. Inhibition by cyclosporin A of a Ca2+-dependent pore in heart mitochondria activated by inorganic phosphate and oxidative stress. *Biochemical Journal* **1988**, *255*, 357.

200. Halestrap, A.P.; Davidson, A.M. Inhibition of Ca2+-induced large-amplitude swelling of liver and heart mitochondria by cyclosporin is probably caused by the inhibitor binding to mitochondrial-matrix peptidyl-prolyl cis-trans isomerase and preventing it interacting with the adenine nucleotide translocase. *Biochemical Journal* **1990**, *268*, 153-160.

201. Hurst, S.; Gonnot, F.; Crola Da Silva, C.; Gomez, L.; Sheu, S.-s. GSK3β-Dependent Phosphorylation of CypD and PTP Regulation During Myocardial Infarction. *Circulation* **2019**, *140*, A14362-A14362.

202. Bernardi, P.; Di Lisa, F. The mitochondrial permeability transition pore: molecular nature and role as a target in cardioprotection. *Journal of molecular and cellular cardiology* **2015**, *78*, 100-106.

203. Duchen, M.R.; McGuinness, O.; Brown, L.A.; Crompton, M. On the involvement of a cyclosporin A sensitive mitochondrial pore in myocardial reperfusion injury. *Cardiovascular research* **1993**, *27*, 1790-1794.

204. Halestrap, A.P.; Woodfield, K.-Y.; Connern, C.P. Oxidative stress, thiol reagents, and membrane potential modulate the mitochondrial permeability transition by affecting nucleotide binding to the adenine nucleotide translocase. *Journal of Biological Chemistry* **1997**, *272*, 3346-3354.

205. Broekemeier, K.M.; Krebsbach, R.J.; Pfeiffer, D.R. Inhibition of the mitochondrial Ca 2+ uniporter by pure and impure ruthenium red. *Molecular and cellular biochemistry* **1994**, *139*, 33-40.

206. Pakhomova, O.N.; Gregory, B.W.; Khorokhorina, V.A.; Bowman, A.M.; Xiao, S.; Pakhomov, A.G. Electroporation-induced electrosensitization. *PloS one* **2011**, *6*, e17100.

207. Baughman, J.M.; Perocchi, F.; Girgis, H.S.; Plovanich, M.; Belcher-Timme, C.A.; Sancak, Y.; Bao, X.R.; Strittmatter, L.; Goldberger, O.; Bogorad, R.L. Integrative genomics

identifies MCU as an essential component of the mitochondrial calcium uniporter. *Nature* **2011**, *476*, 341-345.

208. De Stefani, D.; Raffaello, A.; Teardo, E.; Szabò, I.; Rizzuto, R. A forty-kilodalton protein of the inner membrane is the mitochondrial calcium uniporter. *Nature* **2011**, *476*, 336-340.

209. Palty, R.; Silverman, W.F.; Hershfinkel, M.; Caporale, T.; Sensi, S.L.; Parnis, J.; Nolte, C.; Fishman, D.; Shoshan-Barmatz, V.; Herrmann, S. NCLX is an essential component of mitochondrial Na+/Ca2+ exchange. *Proceedings of the National Academy of Sciences* **2010**, *107*, 436-441.

210. Jiang, J.; Stoyanovsky, D.A.; Belikova, N.A.; Tyurina, Y.Y.; Zhao, Q.; Tungekar, M.A.; Kapralova, V.; Huang, Z.; Mintz, A.H.; Greenberger, J.S. A mitochondria-targeted triphenylphosphonium-conjugated nitroxide functions as a radioprotector/mitigator. *Radiation research* **2009**, *172*, 706-717.

211. Tsai, J.-H.; Chi, M.M.-Y.; Schulte, M.B.; Moley, K.H. The fatty acid beta-oxidation pathway is important for decidualization of endometrial stromal cells in both humans and mice. *Biology of reproduction* **2014**, *90*, 34, 31-12.

212. Ichas, F.; Mazat, J.-P. From calcium signaling to cell death: two conformations for the mitochondrial permeability transition pore. Switching from low-to high-conductance state. *Biochimica et Biophysica Acta (BBA)-Bioenergetics* **1998**, *1366*, 33-50.

213. Bernardi, P.; von Stockum, S. The permeability transition pore as a Ca2+ release channel: new answers to an old question. *Cell calcium* **2012**, *52*, 22-27.

214. Zorov, D.B.; Juhaszova, M.; Sollott, S.J. Mitochondrial reactive oxygen species (ROS) and ROS-induced ROS release. *Physiological reviews* **2014**, *94*, 909-950.

215. Mishra, J.; Jhun, B.S.; Hurst, S.; Jin, O.; Csordás, G.; Sheu, S.-S. The mitochondrial Ca 2+ uniporter: Structure, function, and pharmacology. *Pharmacology of Mitochondria* **2017**, 129-156.

216. Nakagawa, T.; Shimizu, S.; Watanabe, T.; Yamaguchi, O.; Otsu, K.; Yamagata, H.; Inohara, H.; Kubo, T.; Tsujimoto, Y. Cyclophilin D-dependent mitochondrial permeability transition regulates some necrotic but not apoptotic cell death. *Nature* **2005**, *434*, 652-658, doi:10.1038/nature03317.

217. Baines, C.P.; Kaiser, R.A.; Purcell, N.H.; Blair, N.S.; Osinska, H.; Hambleton, M.A.; Brunskill, E.W.; Sayen, M.R.; Gottlieb, R.A.; Dorn, G.W. Loss of cyclophilin D reveals a critical role for mitochondrial permeability transition in cell death. *Nature* **2005**, *434*, 658-662.

218. Devalaraja-Narashimha, K.; Diener, A.M.; Padanilam, B.J. Cyclophilin D gene ablation protects mice from ischemic renal injury. *American Journal of Physiology-Renal Physiology* **2009**, *297*, F749-F759.

219. Elrod, J.W.; Wong, R.; Mishra, S.; Vagnozzi, R.J.; Sakthievel, B.; Goonasekera, S.A.; Karch, J.; Gabel, S.; Farber, J.; Force, T. Cyclophilin D controls mitochondrial pore–dependent Ca 2+ exchange, metabolic flexibility, and propensity for heart failure in mice. *The Journal of clinical investigation* **2010**, *120*, 3680-3687.

220. Giorgio, V.; Von Stockum, S.; Antoniel, M.; Fabbro, A.; Fogolari, F.; Forte, M.; Glick, G.D.; Petronilli, V.; Zoratti, M.; Szabó, I. Dimers of mitochondrial ATP synthase form the permeability transition pore. *Proceedings of the National Academy of Sciences* **2013**, *110*, 5887-5892.

221. Bonora, M.; Bononi, A.; De Marchi, E.; Giorgi, C.; Lebiedzinska, M.; Marchi, S.; Patergnani, S.; Rimessi, A.; Suski, J.M.; Wojtala, A. Role of the c subunit of the FO ATP synthase in mitochondrial permeability transition. *Cell cycle* **2013**, *12*, 674-683.

222. Bernardi, P. Why F-ATP synthase remains a strong candidate as the mitochondrial permeability transition pore. *Frontiers in physiology* **2018**, *9*, 1543.

223. Carraro, M.; Bernardi, P. Measurement of membrane permeability and the mitochondrial permeability transition. In *Methods in cell biology*; Elsevier: 2020; Volume 155, pp. 369-379.

224. Richardson, A.P.; Halestrap, A.P. Quantification of active mitochondrial permeability transition pores using GNX-4975 inhibitor titrations provides insights into molecular identity. *Biochemical Journal* **2016**, *473*, 1129-1140.

225. Halestrap, A.P. The C ring of the F1Fo ATP synthase forms the mitochondrial permeability transition pore: a critical appraisal. *Frontiers in oncology* **2014**, *4*, 234.

226. Neginskaya, M.A.; Solesio, M.E.; Berezhnaya, E.V.; Amodeo, G.F.; Mnatsakanyan, N.; Jonas, E.A.; Pavlov, E.V. ATP synthase C-subunit-deficient mitochondria have a small cyclosporine A-sensitive channel, but lack the permeability transition pore. *Cell reports* **2019**, *26*, 11-17. e12.

227. He, J.; Ford, H.C.; Carroll, J.; Ding, S.; Fearnley, I.M.; Walker, J.E. Persistence of the mitochondrial permeability transition in the absence of subunit c of human ATP synthase. *Proceedings of the National Academy of Sciences* **2017**, *114*, 3409-3414.

228. Brustovetsky, N.; Klingenberg, M. Mitochondrial ADP/ATP carrier can be reversibly converted into a large channel by Ca2+. *Biochemistry* **1996**, *35*, 8483-8488.

229. Bonora, M.; Morganti, C.; Morciano, G.; Pedriali, G.; Lebiedzinska-Arciszewska, M.; Aquila, G.; Giorgi, C.; Rizzo, P.; Campo, G.; Ferrari, R. Mitochondrial permeability transition involves dissociation of F1 FO ATP synthase dimers and C-ring conformation. *EMBO reports* **2017**, *18*, 1077-1089.

230. Mnatsakanyan, N.; Llaguno, M.C.; Yang, Y.; Yan, Y.; Weber, J.; Sigworth, F.J.; Jonas, E.A. A mitochondrial megachannel resides in monomeric F 1 FO ATP synthase. *Nature communications* **2019**, *10*, 1-11.

231. Karch, J.; Molkentin, J.D. Identifying the components of the elusive mitochondrial permeability transition pore. *Proceedings of the National Academy of Sciences* **2014**, *111*, 10396-10397.

232. Halestrap, A.P. What is the mitochondrial permeability transition pore? *Journal of molecular and cellular cardiology* **2009**, *46*, 821-831.

233. Bonora, M.; Wieckowski, M.R.; Chinopoulos, C.; Kepp, O.; Kroemer, G.; Galluzzi, L.; Pinton, P. Molecular mechanisms of cell death: central implication of ATP synthase in mitochondrial permeability transition. *Oncogene* **2015**, *34*, 1475.

234. Chen, C.; Ko, Y.; Delannoy, M.; Ludtke, S.J.; Chiu, W.; Pedersen, P.L. Mitochondrial ATP synthasome: three-dimensional structure by electron microscopy of the ATP synthase in complex formation with carriers for Pi and ADP/ATP. *Journal of Biological Chemistry* **2004**, *279*, 31761-31768.

235. Davidson, A.M.; Halestrap, A.P. Partial inhibition by cyclosporin A of the swelling of liver mitochondria in vivo and in vitro induced by sub-micromolar [Ca2+], but not by butyrate. Evidence for two distinct swelling mechanisms. *Biochemical Journal* **1990**, *268*, 147-152.

236. Halestrap, A.P.; Clarke, S.J.; Javadov, S.A. Mitochondrial permeability transition pore opening during myocardial reperfusion—a target for cardioprotection. *Cardiovascular research* **2004**, *61*, 372-385.

237. Karch, J.; Kwong, J.Q.; Burr, A.R.; Sargent, M.A.; Elrod, J.W.; Peixoto, P.M.; Martinez-Caballero, S.; Osinska, H.; Cheng, E.H.; Robbins, J. Bax and Bak function as the outer membrane component of the mitochondrial permeability pore in regulating necrotic cell death in mice. *eLife* **2013**, *2*, e00772.

238. Kwong, J.Q.; Molkentin, J.D. Physiological and pathological roles of the mitochondrial permeability transition pore in the heart. *Cell metabolism* **2015**, *21*, 206-214.

239. Narita, M.; Shimizu, S.; Ito, T.; Chittenden, T.; Lutz, R.J.; Matsuda, H.; Tsujimoto, Y. Bax interacts with the permeability transition pore to induce permeability transition and cytochrome c release in isolated mitochondria. *Proceedings of the National Academy of Sciences* **1998**, *95*, 14681-14686.

240. Carraro, M.; Jones, K.; Sartori, G.; Schiavone, M.; Antonucci, S.; Kucharczyk, R.; Di Rago, J.-P.; Franchin, C.; Arrigoni, G.; Forte, M. The Unique Cysteine of F-ATP Synthase OSCP Subunit Participates in Modulation of the Permeability Transition Pore. *Cell Reports* **2020**, *32*, 108095.

241. Bernardi, P.; Lippe, G. Channel formation by F-ATP synthase and the permeability transition pore: an update. *Current Opinion in Physiology* **2018**, *3*, 1-5, doi:https://doi.org/10.1016/j.cophys.2017.12.006.

242. Tajeddine, N. How do reactive oxygen species and calcium trigger mitochondrial membrane permeabilisation? *Biochimica et Biophysica Acta (BBA)-General Subjects* **2016**, *1860*, 1079-1088.

243. Fischer, G.; Bang, H.; Mech, C. Determination of enzymatic catalysis for the cis-trans-isomerization of peptide binding in proline-containing peptides. *Biomedica biochimica acta* **1984**, *43*, 1101-1111.

244. Davis, T.L.; Walker, J.R.; Campagna-Slater, V.; Finerty Jr, P.J.; Paramanathan, R.; Bernstein, G.; MacKenzie, F.; Tempel, W.; Ouyang, H.; Lee, W.H. Structural and biochemical characterization of the human cyclophilin family of peptidyl-prolyl isomerases. *PLoS Biol* **2010**, *8*, e1000439.

245. Matouschek, A.; Rospert, S.; Schmid, K.; Glick, B.S.; Schatz, G. Cyclophilin catalyzes protein folding in yeast mitochondria. *Proceedings of the National Academy of Sciences* **1995**, *92*, 6319-6323.

246. Porter, G.A., Jr.; Beutner, G. Cyclophilin D, Somehow a Master Regulator of Mitochondrial Function. *Biomolecules* **2018**, *8*, 176, doi:10.3390/biom8040176.

247. Linard, D.; Kandlbinder, A.; Degand, H.; Morsomme, P.; Dietz, K.-J.; Knoops, B. Redox characterization of human cyclophilin D: identification of a new mammalian mitochondrial redox sensor? *Archives of Biochemistry and Biophysics* **2009**, *491*, 39-45.

248. Nguyen, T.T.; Stevens, M.V.; Kohr, M.; Steenbergen, C.; Sack, M.N.; Murphy, E. Cysteine 203 of cyclophilin D is critical for cyclophilin D activation of the mitochondrial permeability transition pore. *Journal of Biological Chemistry* **2011**, *286*, 40184-40192.

249. Scorrano, L.; Nicolli, A.; Basso, E.; Petronilli, V.P. Two modes of activation of the permeability transition pore: the role of mitochondrial cyclophilin. *Molecular and cellular biochemistry* **1997**, *174*, 181-184.

250. Folda, A.; Citta, A.; Scalcon, V.; Calì, T.; Zonta, F.; Scutari, G.; Bindoli, A.; Rigobello, M.P. Mitochondrial thioredoxin system as a modulator of cyclophilin D redox state. *Scientific reports* **2016**, *6*, 1-11.

251. Scalcon, V.; Bindoli, A.; Rigobello, M.P. Significance of the mitochondrial thioredoxin reductase in cancer cells: An update on role, targets and inhibitors. *Free Radical Biology and Medicine* **2018**, *127*, 62-79.

252. Vesely, M.D.; Schreiber, R.D. Cancer immunoediting: antigens, mechanisms, and implications to cancer immunotherapy. *Annals of the New York Academy of Sciences* **2013**, *1284*, 1-5, doi:10.1111/nyas.12105.

253. Raphael, I.; Joern, R.R.; Forsthuber, T.G. Memory CD4+ T Cells in Immunity and Autoimmune Diseases. *Cells* **2020**, *9*, doi:10.3390/cells9030531.

254. Wang, X.; Yang, X.; Zhang, C.; Wang, Y.; Cheng, T.; Duan, L.; Tong, Z.; Tan, S.; Zhang, H.; Saw, P.E. Tumor cell-intrinsic PD-1 receptor is a tumor suppressor and mediates resistance to PD-1 blockade therapy. *Proceedings of the National Academy of Sciences* **2020**, *117*, 6640-6650.

255. Pardoll, D.M. The blockade of immune checkpoints in cancer immunotherapy. *Nature Reviews Cancer* **2012**, *12*, 252-264.

256. Zou, W.; Wolchok, J.D.; Chen, L. PD-L1 (B7-H1) and PD-1 pathway blockade for cancer therapy: Mechanisms, response biomarkers, and combinations. *Science translational medicine* **2016**, *8*, 328rv324-328rv324.

257. Cheng, X.; Veverka, V.; Radhakrishnan, A.; Waters, L.C.; Muskett, F.W.; Morgan, S.H.; Huo, J.; Yu, C.; Evans, E.J.; Leslie, A.J. Structure and interactions of the human programmed cell death 1 receptor. *Journal of Biological Chemistry* **2013**, *288*, 11771-11785.

258. Ma, J.; Zheng, B.; Goswami, S.; Meng, L.; Zhang, D.; Cao, C.; Li, T.; Zhu, F.; Ma, L.; Zhang, Z.; et al. PD1Hi CD8+ T cells correlate with exhausted signature and poor clinical outcome in hepatocellular carcinoma. *Journal for ImmunoTherapy of Cancer* **2019**, *7*, 331, doi:10.1186/s40425-019-0814-7.

259. Chen, D.S.; Mellman, I. Oncology meets immunology: the cancer-immunity cycle. *immunity* **2013**, *39*, 1-10.

260. Palucka, A.K.; Coussens, L.M. The basis of oncoimmunology. *Cell* **2016**, *164*, 1233-1247.

261. Lewis, C.E.; Pollard, J.W. Distinct role of macrophages in different tumor microenvironments. *Cancer research* **2006**, *66*, 605-612.

262. Almand, B.; Resser, J.R.; Lindman, B.; Nadaf, S.; Clark, J.I.; Kwon, E.D.; Carbone, D.P.; Gabrilovich, D.I. Clinical significance of defective dendritic cell differentiation in cancer. *Clinical Cancer Research* **2000**, *6*, 1755-1766.

263. Tang, M.; Diao, J.; Cattral, M.S. Molecular mechanisms involved in dendritic cell dysfunction in cancer. *Cellular and Molecular Life Sciences* **2017**, *74*, 761-776.

264. Gardner, A.; Ruffell, B. Dendritic Cells and Cancer Immunity. *Trends in immunology* **2016**, *37*, 855-865, doi:10.1016/j.it.2016.09.006.

265. Bunt, S.K.; Sinha, P.; Clements, V.K.; Leips, J.; Ostrand-Rosenberg, S. Inflammation induces myeloid-derived suppressor cells that facilitate tumor progression. *The Journal of Immunology* **2006**, *176*, 284-290.

266. Gabrilovich, D.I.; Nagaraj, S. Myeloid-derived suppressor cells as regulators of the immune system. *Nature reviews immunology* **2009**, *9*, 162-174.

267. Potez, M.; Trappetti, V.; Bouchet, A.; Fernandez-Palomo, C.; Güç, E.; Kilarski, W.W.; Hlushchuk, R.; Laissue, J.; Djonov, V. Characterization of a B16-F10 melanoma model locally implanted into the ear pinnae of C57BL/6 mice. *PLOS ONE* **2018**, *13*, e0206693, doi:10.1371/journal.pone.0206693.

268. Chen, C.; Bandarchuk, A.; Wong, C.; Gotlieb, V.K.; Minhas, H.; Joseph, G.; Tribie, S.; Wang, J.-C. Monocytic Myeloid-Derived Suppressor Cells (Mo-MDSC) Are Increased but Not M1 or M2 TAM Macrophages in the Bone Marrow of Patients with BCR-ABL Negative Myeloid Neoplasm (MPN). *Blood* **2017**, *130*, 5266, doi:https://doi.org/10.1182/blood.V130.Suppl_1.5266.5266.

269. Fehniger, T.A.; Cooper, M.A. Harnessing NK cell memory for cancer immunotherapy. *Trends in immunology* **2016**, *37*, 877-888.

270. Cooper, M.A.; Elliott, J.M.; Keyel, P.A.; Yang, L.; Carrero, J.A.; Yokoyama, W.M. Cytokine-induced memory-like natural killer cells. *Proceedings of the National Academy of Sciences* **2009**, *106*, 1915-1919.

271. Pearce, E.L.; Mullen, A.C.; Martins, G.A.; Krawczyk, C.M.; Hutchins, A.S.; Zediak, V.P.; Banica, M.; DiCioccio, C.B.; Gross, D.A.; Mao, C.-a. Control of effector CD8+ T cell function by the transcription factor Eomesodermin. *Science* **2003**, *302*, 1041-1043.

272. Jamieson, A.M.; Diefenbach, A.; McMahon, C.W.; Xiong, N.; Carlyle, J.R.; Raulet, D.H. The role of the NKG2D immunoreceptor in immune cell activation and natural killing. *Immunity* **2002**, *17*, 19-29.

273. Spear, P.; Wu, M.-R.; Sentman, M.-L.; Sentman, C.L. NKG2D ligands as therapeutic targets. *Cancer Immun* **2013**, *13*, 8-8.

274. Greenberg, S.A.; Kong, S.W.; Thompson, E.; Gulla, S.V. Co-inhibitory T cell receptor KLRG1: human cancer expression and efficacy of neutralization in murine cancer models. *Oncotarget* **2019**, *10*, 1399-1406, doi:10.18632/oncotarget.26659.

275. Fox, C.J.; Hammerman, P.S.; Thompson, C.B. Fuel feeds function: energy metabolism and the T-cell response. *Nature Reviews Immunology* **2005**, *5*, 844-852.

276. Zhao, L.; Wu, Q.; Wang, X.; Wang, S.; Shi, X.; Shan, Z.; Teng, W. Reversal of Abnormal CD4+ T Cell Metabolism Alleviates Thyroiditis by Deactivating the mTOR/HIF1a/Glycolysis Pathway. *Frontiers in endocrinology* **2021**, *12*, 659738-659738, doi:10.3389/fendo.2021.659738.

277. Chang, Y.-L.; Rossetti, M.; Vlamakis, H.; Casero, D.; Sunga, G.; Harre, N.; Miller, S.; Humphries, R.; Stappenbeck, T.; Simpson, K.; et al. A screen of Crohn's disease-associated microbial metabolites identifies ascorbate as a novel metabolic inhibitor of activated human T cells. *Mucosal Immunology* **2018**, *12*, doi:10.1038/s41385-018-0022-7.

278. Cao, Y.; Rathmell, J.; Macintyre, A. Metabolic Reprogramming towards Aerobic Glycolysis Correlates with Greater Proliferative Ability and Resistance to Metabolic

Inhibition in CD8 versus CD4 T Cells. *PloS one* **2014**, *9*, e104104, doi:10.1371/journal.pone.0104104.

279. Milam, A.A.V.; Bartleson, J.M.; Buck, M.D.; Chang, C.-H.; Sergushichev, A.; Donermeyer, D.L.; Lam, W.Y.; Pearce, E.L.; Artyomov, M.N.; Allen, P.M. Tonic TCR signaling inversely regulates the basal metabolism of CD4+ T cells. *ImmunoHorizons* **2020**, *4*, 485-497.

280. Luongo, T.S.; Lambert, J.P.; Yuan, A.; Zhang, X.; Gross, P.; Song, J.; Shanmughapriya, S.; Gao, E.; Jain, M.; Houser, S.R. The mitochondrial calcium uniporter matches energetic supply with cardiac workload during stress and modulates permeability transition. *Cell reports* **2015**, *12*, 23-34.

281. Chouchani, E.T.; Pell, V.R.; James, A.M.; Work, L.M.; Saeb-Parsy, K.; Frezza, C.; Krieg, T.; Murphy, M.P. A unifying mechanism for mitochondrial superoxide production during ischemia-reperfusion injury. *Cell metabolism* **2016**, *23*, 254-263.

282. Di Lisa, F.; Bernardi, P. Modulation of mitochondrial permeability transition in ischemia-reperfusion injury of the heart. Advantages and limitations. *Current medicinal chemistry* **2015**, *22*, 2480-2487.

VITA

BRITTNEY L. RUEDLINGER
Brued001@odu.edu
The Frank Reidy Research Center for Bioelectrics
Old Dominion University
Norfolk, VA 23508

EDUCATION

Old Dominion University	**Norfolk, VA**
PhD, Biomedical Sciences	December 2021
Old Dominion University	**Norfolk, VA**
Master of Science, Chemistry	December 2018
Old Dominion University	**Norfolk, VA**
Bachelor of Science, Biochemistry	May 2017
Tidewater Community College	**Norfolk, VA**
Associate of Science	December 2015

PUBLICATIONS AND PRESENTATIONS

Ruedlinger, Brittney, *et al*., *NPS Induced Immunity and Immunometabolism of CD4+ T cells in Murine Melanoma.* (forthcoming)
Ruedlinger, Brittney, *et al*., *The Mitochondrial Permeability Transition Pore is a Sensor of Nano-Pulse Stimulation.* (forthcoming)
Ruedlinger, Brittney, and Beebe, Stephen. *Minireview*. *Intracellular Effects of Nanosecond Pulsed Electric Fields.* (forthcoming)
Ruedlinger, Brittney, *et al*., "Trials and Tribulations of Humanizing Mice for Cancer Research" (2021). The Graduate School Posters. 1. https://digitalcommons.odu.edu/gradposters2021_gradschool/1
Ruedlinger, Brittney, *et al*., "Cyclophilin D Is a Sensor of Nano-Pulse Stimulation" (2021). The Graduate School Posters. 2. https://digitalcommons.odu.edu/gradposters2021_gradschool/2
Ruedlinger, Brittney, *et al*., "Humanizing Mice for Cancer Treatment. Biomedical Research" Retreat Tuesday, October 15, 2019. Webb Center, Old Dominion University.
Ruedlinger, Brittney, *et al*., "How Sequence Directs Structure: My First Steps to Unlock the Protein Folding Code in GB1" (2016) Atrium N. Old Dominion University Undergraduate Research Symposium, Learning Commons, Perry Library.

AWARDS

ODU Honors College Undergraduate Research Supply Grant 2016 ($500)
ODU Honors College Undergraduate Research Fellowship 2015 ($1500)